Water confined in hydrophobic nanopores Towards a new phase diagram

Oriana Osta-Rangel

Thèse de doctorat

NNT : 2021UPASF041

université PARIS-SACLAY

Water confined in hydrophobic nanopores: Towards a new phase diagram

L'Eau confinée en milieu hydrophobe : Vers un nouveau diagramme de phase

Thèse de doctorat de l'université Paris-Saclay

École doctorale n° 571
Sciences Chimiques : Molécules, Matériaux, Instrumentation et Biosystèmes (2MIB)
Spécialité de doctorat : Chimie
Unité de recherche : Université Paris-Saclay, CEA, CNRS, LLB, 91191, Gif-sur-Yvette, France.
Référent : Faculté des sciences d'Orsay,

Thèse présentée et soutenue à Paris-Saclay, le 22 octobre 2021, par

Oriana OSTA-RANGEL

Composition du Jury

Mehran MOSTAFAVI Professeur, Université Paris-Saclay	Président
Jean-Pierre BELLAT Professeur, Université de Bourgogne Franche-Comté	Rapporteur & Examinateur
Denis MORINEAU Directeur de Recherche, Université de Rennes 1	Rapporteur & Examinateur
Anne BOUTIN Directrice de Recherche, ENS, Paris	Examinatrice
Elisabeth CHARLAIX Professeur, Université de Grenoble-Alpes	Examinatrice

Direction de la thèse

Christiane ALBA-SIMIONESCO Directrice de Recherche, Université Paris-Saclay	Directrice de thèse
Nancy BRODIE-LINDER Maître de conférences Émérite, U. Cergy-Pontoise	Co-directrice de thèse
Hynd REMITA Directrice de Recherche, Université Paris-Saclay	Invitée

université PARIS-SACLAY

ÉCOLE DOCTORALE
Sciences Chimiques: Molécules, Matériaux, Instrumentation et Biosystèmes (2MIB)

Titre : L'Eau confinée en milieu hydrophobe: Vers un nouveau diagramme de phase

Mots clés : confinement, nanomatériaux, amphiphile, hydrophobicité, diffraction des neutrons.

Résumé: L'eau confinée dans des nanopores amphiphiles et hydrophobes joue un rôle vital dans la nature. Ici, nous avons étudié l'effet de différents niveaux d'hydrophobicité sur le comportement de phase de l'eau confinée. Tout d'abord, nous avons synthétisé des organosilices nanoporeux (de type MCM-41) avec différentes densités de groupes organiques à la surface pour les utiliser comme matériaux de confinement modèles. Nous avons utilisé une approche de synthèse directe pour les matériaux amphiphiles et de post-greffage pour les hydrophobes. Nous avons ensuite réalisé une caractérisation complète de la structure des pores, de la morphologie et de la chimie de surface des matériaux, en utilisant l'IRTF, l'ATG, l'adsorption d'azote et de vapeur d'eau, la diffusion des neutrons à petits angles, et la microscopie électronique en transmission. Les matériaux amphiphiles présentent des pores cylindriques indépendants avec des diamètres d'environ 4,5 nm et de grandes capacités d'adsorption d'eau à la pression atmosphérique. Les matériaux hydrophobes présentent des pores légèrement plus petits (D ~4 nm) où l'eau ne se condense pas à basse pression.

Nous avons constaté que le niveau d'hydrophobicité des matériaux amphiphiles amplifie les effets du confinement, en abaissant sa densité et son point de fusion au-delà de l'attendu pour les nanopores hydrophiles. En mesurant la structure cristalline de la glace à la pression atmosphérique par diffraction des neutrons, nous avons trouvé de la glace à défauts d'empilement (I_{SD}) avec environ 30 % de couches hexagonales (I_h) et 70 % de couches cubiques (I_c). Les résultats de la calorimétrie différentielle à balayage (DSC) et de la diffraction des neutrons indiquent la présence d'une fraction d'eau non congelable allant de 45 % à près de 80 %, augmentant avec le niveau d'hydrophobicité. Nous proposons que cette eau liquide et amorphe présente une distribution non-homogène autour des grains de glace, en particulier à proximité des groupes organiques à la surface des nanopores amphiphiles. Nos résultats préliminaires d'écho de spin neutronique, indiquent que les groupes organiques à la surface sont responsables du ralentissement des molécules d'eau qui les entourent, empêchant la croissance des grains de glace.

La pression d'intrusion de l'eau dans les nanopores hydrophobes, déterminée par imagerie neutronique, était d'environ 400 bars, et une hystérésis significative a été trouvée pour l'extrusion, qui s'est produite à une pression presque atmosphérique. En utilisant la diffraction des neutrons à haute pression, nous avons découvert que l'eau confinée dans des nanopores hautement hydrophobes cristallise en formes de glace de densité plus élevée (glaces II et III) à des pressions significativement plus basses que prévu. Les transitions de phase de la glace II confinée à la glace III puis à l'eau liquide sont réversibles et reproductibles. Ces résultats nous ont permis de tracer de nouvelles lignes de transition dans le diagramme de phase pression-température de l'eau lourde confinée dans des nanopores hydrophobes.

université PARIS-SACLAY

ÉCOLE DOCTORALE
Sciences Chimiques: Molécules, Matériaux, Instrumentation et Biosystèmes (2MIB)

Title : Water confined in hydrophobic nanopores: Towards a new phase diagram

Keywords : confinement, nanomaterials, amphiphilic, hydrophobicity, neutron diffraction.

Abstract: Water confined in hydrophobic cavities is ubiquitous in nature, but the effect of hydrophobicity on its phase transitions is still debated. Herein we have studied this effect on the liquid-solid transitions of confined water. First, we synthesized nanoporous organosilicas (MCM-41-type), with different densities of organic groups at the surface, to use them as model confining materials. We used a direct synthesis approach for the amphiphilic materials and post-grafting for hydrophobic. Then, we performed a comprehensive characterization of the materials' pore structure, morphology, and surface chemistry, using FTIR, TGA, N_2 and H_2O adsorption, SAXS, TEM, and neutron backscattering. Results show that the amphiphilic materials present cylindrical, independent pores with diameters around 4.5 nm and large water adsorption capacities at atmospheric pressure. On the other hand, the hydrophobic materials present slightly smaller pores (D ~4 nm) where water does not condense at low pressures.

We found that higher hydrophobicity levels in amphiphilic materials enhance the effects of confinement, lowering its density and melting point beyond the expected for hydrophilic nanopores. We measured the crystalline structure of the confined ice at atmospheric pressure using neutron diffraction, and we found stacking-disordered ice (I_{SD}) with around 30 % hexagonal (I_h) and 70 % cubic (I_c) layers. DSC and neutron diffraction results indicate the presence of a non-freezable fraction of water ranging from 45 % to nearly 80 %, increasing with the hydrophobicity level. We propose that this liquid-like, amorphous water presents a non-homogeneous distribution around the ice grains, especially neighboring the organic groups at the surface of the amphiphilic nanopores. From our preliminary neutron spin echo results, we conclude that the organic groups at the surface are responsible for slowing down the water molecules that surround them, hindering the ice grain growth.

The water intrusion pressure in hydrophobic nanopores, determined by neutron imaging, was around 400 bar, and a significant hysteresis was found for the extrusion, which occurred at nearly atmospheric pressure. Using neutron diffraction at high pressures, we found that water confined in highly hydrophobic nanopores crystallizes into higher density ice forms (ices II and III) at pressures significantly lower than expected. The phase transitions from confined ice II to ice III and then to liquid water are reversible and reproducible. These results allowed us to draw new transition lines to the pressure-temperature phase diagram of water confined in hydrophobic nanopores.

Acknowledgements

I want to thank all the people that made this thesis possible. Starting with my Ph.D. supervisors Christiane Alba-Simionesco and Nancy Brodie-Linder, I could not have found a better team. Thank you for all your guidance, for your professional and personal support. It was easy to enjoy this journey next to you.

Then, to all the LLB team, in especial to: Marianne Bombled, thank you for introducing me to so many experimental techniques and for being the best office-mate that ever existed! To Annie Brûlet for teaching me how to use the SAXS instrument, for always being available for my questions, and for even performing the experiments when I couldn't do it. Thanks to Burkhard Annighofer for the high-quality technical and scientific support regarding the high-pressure sample environment for neutron diffraction, for being open to performing modifications to the set-up for the experiments we had designed. Thanks to Jacques Dapertigny for the efforts invested in the diffraction experiments in 7C2, including long hours on the weekends! I appreciate your kindness and scientific rigor. Thanks to Frédéric Ott for his valuable contributions in neutron imaging experiments and data treatment. I'm especially grateful to Florence Porcher for being tremendously helpful in the design and execution of neutron diffraction experiments at high pressure in G4.4 and for the fantastic data treatment and analysis support with FullProf. Some of the most important findings of this thesis would not have been possible without your help. All my appreciation and gratefulness to Stephane Longeville for training me in neutron spin-echo and for helping me obtain the best possible accuracy in every measurement. Besides the results shown here for water dynamics in amphiphilic nanopores, a whole study on the dynamics of water-glycerol mixtures was produced thanks to your kind help. I truly appreciated all our discussions on scientific and cultural topics. Thanks to Jose Texeira and Marie-Claire Bellissent-Funel for all those valuable discussions on the neutron experiments and confined water. Thanks to Arnaud Helary, Frederic Legendre, Sebastien Gautrot, and Xavier Guillou for your valuable help with the neutron experiments' sample environment. I'm grateful to Aurore Verdier and Olivier Sineau for all the administrative work.

Thanks to my family in Venezuela for all your support. You keep me strong through every challenge. To my awesome husband and to my beautiful son, I am extremely lucky to have you. Finally, to the one that has always been my rock, Father, thanks for everything!

Table of contents

CHAPTER 1
INTRODUCTION

In nature, water is often trapped in small cavities, in between layers, or in the vicinity of macromolecules. This type of water has been called *confined water*, and it is of vital importance for biological, geological, and industrial processes. The behavior of confined water, as for any fluid, varies from that of the bulk. For instance, confinement at the nanoscale triggers changes in the fluid's density, mobility, freezing and melting temperatures, and crystalline structure.

In order to study such properties of confined water, it is necessary to have model porous systems, called *confining materials*. Those properties strongly depend on the pore size of the confining material and the pore surface's chemical nature (hydrophilic, amphiphilic, or hydrophobic).

Another crucial parameter relies on the mechanism by which water enters the nanopores. For example, if water is *adsorbed* in vapor form, or if it enters the pore as a liquid, through *imbibition* or forced *intrusion*, this might modify the thermodynamic properties of the confined fluid, which will then affect its phase transitions. Therefore, it is essential to study the pore filling mechanisms to precisely define the confining condition.

This chapter aims to present relevant scientific advances in confining materials, the different methods to fill the pores with water, and summarize some key elements involved in the behavior of confined fluids, giving special attention to the case of confined water. Finally, the impact of the modulations of water's properties in confinement on industrial applications will be discussed.

1.1. Confining materials

Confining materials contain cavities that are small enough to observe a difference in the physical properties of the fluid in bulk. Such porous solids have a broad spectrum of applications in water treatment, gas separation, and heterogeneous catalysis.

Porous materials have been classified by the International Union of Pure and Applied Chemistry (IUPAC) according to their pore size into microporous, mesoporous, and macroporous (Figure 1.1). With the rising of nanosciences, the term *nanoporous* made its appearance, being applied to all three categories for materials which pores go up to 100 nm.

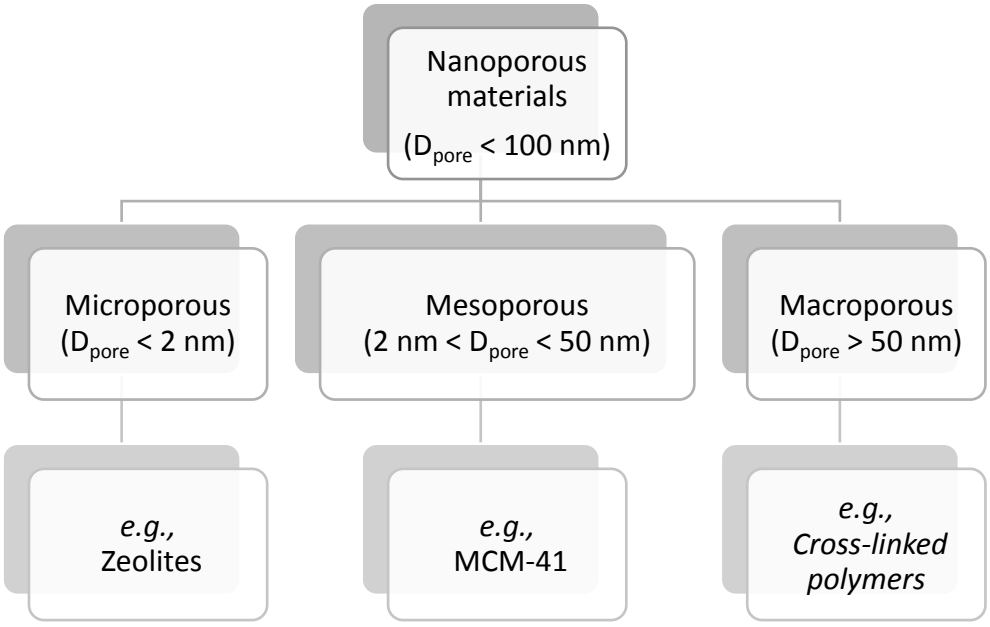

Figure 1.1: Classification of porous materials, according to their pore width, by the IUPAC[1]. The more recent term *nanoporous* includes all three categories.

Nanoporous solids, such as carbon nanotubes, zeolites, and silicas, are excellent model systems to study confined fluids. They have been investigated for their multiple applications as well. Their surface properties maximize the interactions with the targeted molecules and take advantage of confinement effects for better performance in their applications.

Carbon nanotubes (CNT), for example, have a large surface area, high conductivity, and mechanical strength, which is why they are used for biomedical applications,[2] energy storage,[3] and polymer reinforcement,[4] among others. Moreover, the dynamic properties of fluids in carbon nanotubes have gained much interest in fundamental and applied

research.[5]

Another example of confining systems are the zeolites, which are broadly used for catalysis, gas separation, and ion exchange,[6] due to their reactive surfaces and to their interconnected pore network with cages sized from 0.3 to 1 nm.[7,8]

Nanoporous silica materials, like SBA-15 (Santa Barbara Amorphous No. 15)[9] and MCM-41 (Mobil Composition of Matter No. 41),[10] present an organized pore structure with cylindrical pores arranged in a 2D-hexagonal geometry. They have characteristic pore sizes going from 2 to 10 nm. Compared with other nanoporous materials, they have been less extensively used for industrial applications due to high cost and low hydrothermal stability.[6] Nevertheless, this range of pore sizes is suitable for molecular confinement studies, as such effects become significant in pores with diameters around 5 - 20 molecular sizes.[11,12]

Besides the pore size, other factors that can influence the properties of fluids in confinement are the pore shape, surface roughness, and interpore connections (like those present in SBA-15.[13], MCM-48, or Vycor glass). In order to perform systematic studies in confinement, these parameters should be controlled.

Taking this into account, MCM-41, with appropriate pore size, a uniform pore structure, reproducible surface, and the absence of interpore connections, represents a suitable alternative for water confinement studies. Furthermore, MCM-41 admits many surface chemistry modifications that allow transforming a hydrophilic (water-loving) surface, rich in hydroxyl groups (1.6 silanol groups/ nm^2)[14] into a hydrophobic (water-hating) one, abundant in non-polar organic groups.

Water confinement studies in hydrophilic and hydrophobic nano-environments are found in the literature and will be discussed in the next section. However, the effect of amphiphilic confinement (*i.e.*, confinement in nanocavities containing hydrophilic and hydrophobic moieties at the surface) has been less studied.

Periodic mesoporous organosilicas (PMOs) surged in 1999 as an organic-inorganic alternative to mesoporous silicas. New functionalities were explored in catalysis, environmental applications (water treatment), and biomolecule adsorption by expanding the framework composition. These materials are synthesized using bridged silanes ($(R'O)_3Si\text{-}R\text{-}Si(OR')_3$ (R'=methyl or ethyl, R=the bridged organic groups)) as precursors. The precursors are condensed using a surfactant's liquid crystal as a template, similar to mesoporous silica materials.[15–17]

Another way to produce amphiphilic nanoporous materials is to use a co-condensation or direct synthesis method with alkyl-trialkoxysilanes ($(R'O)_3Si\text{-}R$), as methyl-triethoxysilane,

for instance. In this way, the hydrophobicity of the product can be easily tailored by changing the percentage of organosilane in the precursors' mixture.

These last two methods have the advantage of being a one-step approach, eliminating the time-consuming and laborious task of post-synthesis modifications and producing a homogeneously functionalized surface across the pore.

MCM-41-type of materials has been selected to study water confining in this thesis. Using a direct synthesis modification with organosilanes has made it possible to synthesize materials with a controlled hydrophilic-hydrophobic balance. A later grafting of extra organic groups on these materials has been used to obtain highly hydrophobic nanopores. These synthetic methods, detailed in Chapter 2, have allowed the novel study of the thermodynamic states of water in amphiphilic and hydrophobic nanopores presented in Chapters 6 and 7 of this work. Seen in another way, we have used water as a local probe to study the subtle effects of amphiphilic and hydrophobic confinement.

1.2. Filling the nanopores with water

The three well-known processes for pore filling are imbibition, vapor adsorption/condensation, and intrusion. In hydrophilic or even amphiphilic nanopores, water vapor adsorption and imbibition are efficient pore-filling techniques. However, the amount of water introduced in hydrophobic nanopores using such techniques is significantly lower. Compression of the system at pressures of a few hundred bars is required to achieve water intrusion in hydrophobic nanopores.

Imbibition and vapor adsorption

Water imbibition in hydrophilic (or amphiphilic) nanoporous materials takes place due to capillary forces. In this case, water is in its liquid state, and it displaces the air inside the nanopores. The same principle is used, for example, in oil extraction when water is used as the "wetting phase" to push oil, the "non-wetting phase" out of porous media.[18]

For adsorption, instead, water is required in its vapor form. Water molecules will first be adsorbed at the surface of the nanoporous material, and at a certain pressure, a phase transition (liquefaction) takes place due to the capillary condensation.[19]

Water adsorption, described in detail in Chapter 3, has been used in this work as a characterization technique for the synthesized materials and confined water. Important information as the number of silanol groups (Si-OH) at the surface and the density of confined water (Chapters 5 and 6) was extracted from these experiments.

Intrusion and extrusion in heterogeneous lyophobic systems

The intrusion and extrusion processes in heterogeneous lyophobic systems (HLS), like water and hydrophobic nanoporous organosilica, have been (and still are) broadly studied due to their applications in energy storage.[20–30]

The energy conversion process occurs when water is forced, by an external pressure, to enter the hydrophobic nanopores. The mechanical energy is transformed into surface energy, creating a new interface between the liquid and the pore walls. When the pressure is reduced to a critical value, this energy is released by the extrusion process.

In the case of hydrophobic cylindrical nanopores (post-grafted MCM-41), Lefevre *et al.* (2004) have found that the intrusion pressure (P_{int}) as a function of the pore size can be described with standard capillarity theory.[20] According to the Laplace-Washburn equation, (P_{int}) can be written as a function of the liquid-vapor surface tension (γ_{LV}), the advancing contact angle (θ_a) and the pore radius (r_p):

$$P_{int} = -2\frac{\gamma_{LV}}{r_p}cos\theta_a$$

However, the description of the extrusion pressure is somehow more complex. The limiting step in this process is the formation of a vapor bubble within the nanopore. Thus, nucleation theory is needed to describe this phenomenon. In addition, line tension effects have to be considered to obtain a good fit of the data.[20] This last contribution is associated with the elongation of the triple line (*i.e.*, the line where the solid, liquid, and vapor coexist) along the nucleation process.

The extrusion pressure (P_{ext}) can be then calculated as a function of the thermal energy (k_BT), the extrusion time (t_e), the characteristic time (τ_n), the interfacial tension (γ_{LV}) and area (A), the line length (λ) and tension (L_t) and the volume of the bubble (V_n):

$$P_{ext} = \frac{k_BT}{V_n}ln\frac{t_e}{\tau_n} - \left(\gamma_{LV}\frac{A}{V_n} + \lambda\frac{L_t}{V_n}\right)$$

P_{ext} is typically lower than P_{int}, giving rise to an intrusion/extrusion hysteresis. This energy storage behavior is called *shock absorber* (SA, in Figure 1.2). For small nanopores (~1 nm) or at high enough temperatures, nucleation is no longer the limiting factor, and the hysteresis disappears, forming a *spring* (S). If there is water remaining in the nanopores after the pressure has been released, the system is called a *bumper* (B).[20,21,23,24]

On the reversibility of the intrusion/extrusion process, Karbowiak *et al.* (2009) found that the water intrusion process triggers modifications on the material's surface (this is the case for silicalite-1), transforming it into a more hydrophilic surface through the formation of

silanol defects.[31] This is another reason why the extrusion process does not follow the same pathway as the intrusion in most cases.

In this work, the intrusion/extrusion process was followed by neutron imagery. The results and discussion are presented in Chapter 7.

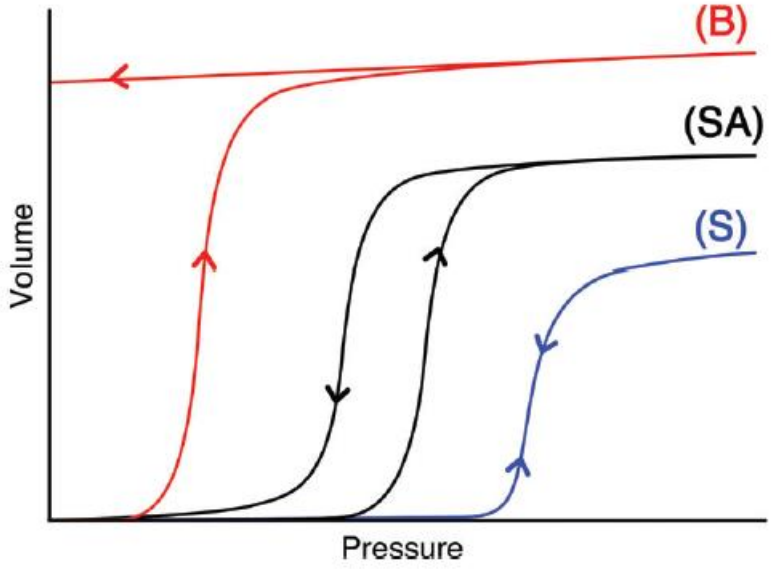

Figure 1.2: Schematic representation of the three different types of energy storage behavior: Spring (S), Shock Absorber (SA), and Bumper (B). Taken from Fraux et al. (2017)[23]:

1.3. Freezing and melting of confined water

The behavior of confined fluids deviates, sometimes dramatically, from that of the bulk. Confinement is known to modify the crystallization and melting behavior[13,32], the glass transitions,[33] density,[34], and dynamics[35] of fluids.

On the effect of confinement on crystallization, the melting point depression in a cavity of radius r is governed by the Gibbs-Thomson Equation:

$$\Delta T_m(r) = T_m - T'_m(r) = \frac{2\gamma_{sl}\overline{V}_m T_m}{r\Delta_m H(r)}$$

where ΔT_m is the melting temperature depletion, Tm is the melting temperature of the bulk, T'_m is the melting temperature of the confined fluid, γ_{sl} is the surface tension between the surface and the fluid, $\overline{V}_m$ is the molar volume of the fluid, r is the radius of the confining cavity $\Delta_m H$ is the melting enthalpy of the fluid.

In practice, as the size dependence of γ_{sl}, $\overline{V}_m$, and $\Delta_m H$ is difficult to take into account, the bulk analogs can be used to approximate the size dependence of the melting temperature.

Usually, $\left[\frac{2\gamma_{sl}\overline{V}_m T_m}{\Delta_m H(r)}\right]$ is considered a prefactor (C_{GT}) of the 1/r law and fixed as a constant. This equation is not supposed to be valid for small pore sizes, and a deviation from linearity (see figure 1.3) is observed. For fitting convenience, and because the role of the surface (over the volume) becomes predominant, a liquid-like layer thickness *t* (usually around two molecular sizes), adjacent to the surface, is considered in addition to the crystal grain and then subtracted to *r:*

$$\Delta T_m(r) \cong \frac{C_{GT}}{r - t}$$

According to the Gibbs-Thomson equation, the melting temperature depression is inversely proportional to the pore size. However, numerous cases of deviations from the Gibbs-Thomson equation have been reported in the literature, like in the case of CCl_4 in activated carbon fibers[36]. In another study, Dosseh *et al.* (2003) found that benzene and cyclohexane confined in SBA-15 and MCM-41 also deviate from this behavior, as shown in the nonlinearity of their curves in Figure 1.3.[11] They conclude that the fewer the interactions between the liquid and the surface, the more pronounced the deviation from this thermodynamic model. This would explain why the behavior of cyclohexane deviates more than the one of benzene, which can interact with the surface via polar-π interactions. In the same way, the behavior of water, which can interact with the surface hydroxyl groups by H-bonds, can be fairly described using this equation.

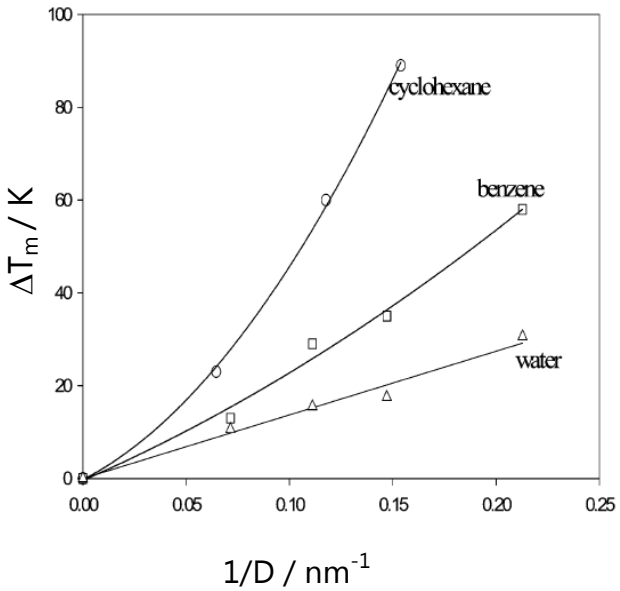

Figure 1.3: Melting temperature depression of cyclohexane, benzene, and water confined in SBA-15 vs. the inverse of the pore diameter. The line is a guide for the eye to remark linearity deviations in the cases of benzene and cyclohexane[11]

An important source of uncertainty that may influence the adequacy of the Gibbs-

Thomson equation is the pore size determination method used.[37] Indeed, it is not unusual to find discrepancies in the pore size value at the nanometer scale. One reason for this is the variety of available models and formulas to calculate the pore diameter of nanoporous materials. Among the most frequently used are:

- the Brunauer–Emmett–Teller (BET) method,
- the Barrett-Joyner-Halenda (BJH) method,
- the Kruk-Jaroniec-Sayari (KJS) and improved KJS (iKJS) methods,
- the NL-DFT method based on Monte-Carlo simulations, and
- a combination of nitrogen adsorption and SAXS data.

A more detailed description of the pore size determination methods will be presented in Chapter 3.

The case of water

Even though deviations from the predictions of the melting point depression, given by the Gibbs-Thomson equation, are abundant in the literature, in the case of water confined in cylindrical nanopores, it has been reported a good agreement of this simple model with experimental data.

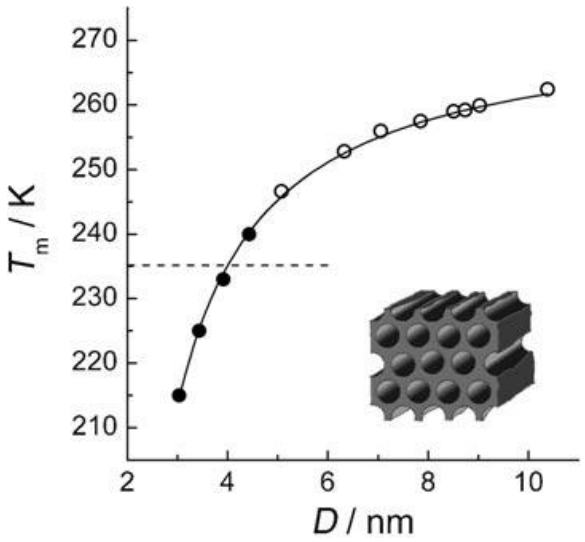

Figure 1.4: Effect of the pore size (D = pore diameter) of cylindrical silica nanopores (MCM-41, filled dots, and SBA-15, empty dots) on the melting temperature of water. The dashed line marks the limit for (bulk) water's homogeneous nucleation. Confinement in silica nanopores allows to supercool water at temperatures well below this limit.[38]

Freezing and melting of water confined in hydrophilic SBA-15 and MCM-41 nanopores have been previously studied using DSC,[39,40,38] NMR, X-Rays, and Neutron Diffraction[41] techniques. Findenegg *et al.* (2008) found a systematic decrease of the melting

temperature of water with the pore size in agreement with the Gibbs-Thomson equation (Figure 1.4).[38] In this case, the fit of the melting point depression of water as a function of the pore size yields a liquid layer thickness of t ~ 0.6 nm.[38,39]

The melting point is preferred for confinement studies because the freezing temperature of water confined in MCM-41 depends on the nucleation and growth probabilities, and it changes with the scan rate. On the other hand, the melting process is thermodynamically controlled; as a result, the melting point is more reproducible.

Due to the geometric constraints that reduce the probability of crystal growth, the freezing point of water in cylindrical nanopores is always lower than its melting point, giving place to a melting/freezing hysteresis.[42] For a fixed scan rate, this hysteresis has been found to decrease for smaller nanopores until it disappears at a certain critical diameter[39,42], as shown in Figure 1.5. This crossing point is a specific feature of water, as it has not been reported for other fluids.

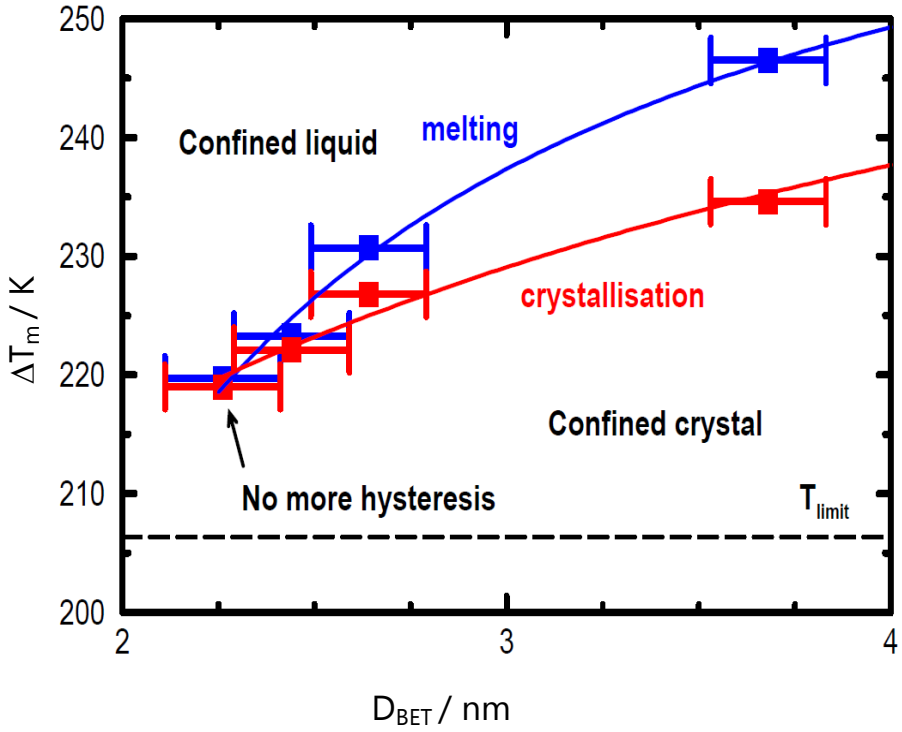

Figure 1.5: Melting (blue) and freezing (red) point depression of water in MCM-41 materials. The melting/freezing hysteresis disappears at the point marked with an arrow. The crossing point was found in an MCM-41 C12 D_{BET} =2.3 nm at 0.5 K/min [42]

Jähnert *et al.* (2008) also determined the point where the freezing/melting hysteresis disappears (by extrapolation). They obtained a KJS pore size value of D^*_{hys} ~ 2.8 nm. This result agrees with Deschamps *et al.* (2010)[42], knowing that D_{KJS} estimates higher pore diameters than the BET method (D_{KJS} ~ D_{BET} + 0.6 nm).

A thermodynamic limit for crystallization

The point of zero hysteresis is crucial for studies on confined water because, from that point, no crystallization or melting signals are observed within the resolution limits of neutron diffraction, DSC, or NMR cryoporometry[43].

Jähnert *et al.* (2008)[39] estimated the molar melting enthalpy of water (ΔH) in the pores from the DSC curves, correcting the amount of water by subtracting the liquid layer t adjacent to the pore walls. They found a systematic decrease in the molar melting enthalpy of confined water in pores of decreasing pore sizes. By extrapolation to $\Delta H = 0$ (the thermodynamic limit of crystallization inside the nanopores), they obtained a critical KJS pore size of $D^*_{\Delta H} \sim 2.7$ nm, in close agreement with the value obtained at the point of zero hysteresis.

The effect of the surface chemistry

Besides changing the size of the cavity where water is confined, one can modify the interactions of the pore wall with water by changing its surface chemistry. The behavior of confined water in hydrophobic and amphiphilic environments has a vast impact on cell biology, geology, and mechanical energy storage.

A remarkable example was given by Agrawal et al. (2017). They found a freezing phase transition of water in carbon nanotubes of 1.05 nm at 138 °C. The ice-like structure of water in those smooth, perfectly cylindrical nanopores is significantly stabilized.[44]

Unlike carbon nanotubes, the surface of nanoporous silica is rather rough, especially when a post-grafting treatment is performed to transform the material into hydrophobic. Deschamps *et al.* (2010) confined water in hydrophilic and hydrophobic MCM-41 (for which a high pressure of water is needed to fill the pores) (Figure 1.6). This research showed that the melting temperature of water decreases further when it is confined in hydrophobic nanopores, obtained by post-grafting silica materials with trimethyl silane groups (this method will be explained in Chapter 2). A thermodynamic limit for water melting inside hydrophobic cylindrical nanopores was then established at a diameter BET of $D_{\text{phobe}} = (2.3 \pm 0.2)$ nm, the melting temperature of this confined ice being 206 K.[42]

This significant difference in the melting temperature of water confined in hydrophilic vs. hydrophobic environments raises questions regarding the intermediate condition, water in amphiphilic nanopores: How does the melting temperature evolve with different levels of hydrophobicity? And, how is the crystalline structure of confined ice affected by this parameter?

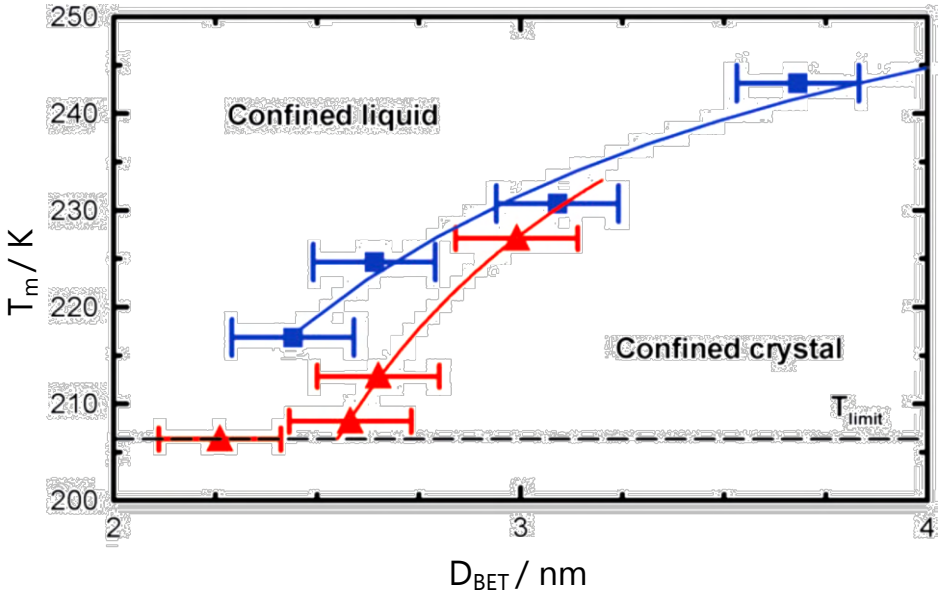

Figure 1.6: Melting temperatures of water confined in hydrophilic (blue) and hydrophobic (red) cylindrical silica nanopores. The dashed line marks the thermodynamic limit under which confined water does not crystallize.[42]

Morishige et al. (2018)[45] approached this problem using mesoporous carbons (CMK-type), concluding that the wall surface nature did not significantly alter the melting point of confined water when using materials with relatively large pore diameters (> 6.4 nm). Our experimental studies on the behavior of water confined in amphiphilic MCM-41-type materials of smaller pore diameters (~ 4.5 nm) will be the topic of Chapter 6 of this work.

1.4. Confined ice structure

Besides the impact of confinement in water's freezing and melting temperatures, confined conditions also influence the crystalline structure of ice. Details on the influence of confinement on the different aspects of crystallization are provided in the literature.[46]

In bulk water, the thermodynamically stable form of ice at normal pressures is hexagonal ice (I_h). However, the first diffraction experiments on confined water shown what seemed to be the crystallographic signature of cubic ice (I_c)[47], a structure proposed the first time by König in 1943[48].

An example is provided by Dore *et al.* (2002) in Figure 1.7. They measured the neutron diffraction pattern of D_2O in MCM-48 (nanoporous silica with an interconnected, cubic pore structure). In the figure, the temperature difference functions (S(Q, T) - S(Q, T0)) for a reference temperature T0 = 292 K are shown. This function is helpful to eliminate many of the experimental corrections to the raw dataset when the studied material (water) is contained in a matrix whose diffraction pattern does not change with temperature.

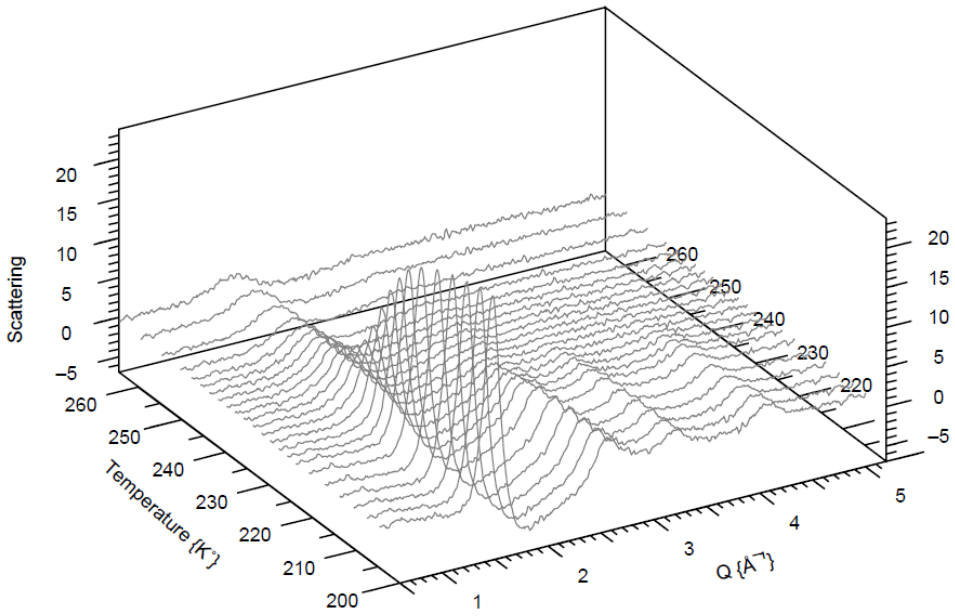

Figure 1.7: Neutron diffraction temperature difference functions (S (Q, T) - S (Q, T0)) for liquid (D_2O) water and ice in MCM-48 with a pore size of 3.5 nm (f ~0.25).[49]

In agreement with previous observations, their results showed the apparition of diffraction peaks at 1.75, 2.83, 3.46, and 4.39 A^{-1}, corresponding to the known crystallographic signature of cubic ice.

Later experiments revealed that the measured structure was a combination of hexagonal and cubic ice.[50] This structure, consisting of randomly mixed I_h and I_c planes with numerous growth defects, now receives the name of stacking-disordered ice I_{SD}.[51–54]

On the other hand, the observed phenomenon is somewhat different when water is confined below the critical pore diameter D^*. A clear example is provided by Audonnet *et al.* (Figure 1.8).[55] They performed neutron diffraction measurements on water confined in pores of D_{BET} = 1.5 nm. The absence of clear Bragg peaks at low temperatures confirms that no crystallization has taken place in this sample. However, structural changes are observed upon cooling. The position of the maximum of the diffraction peak (Q_0) shifts to lower values suggesting a transformation of the confined liquid water to a lower density structure,[56] similar to the low density amorphous form of water (LDA).

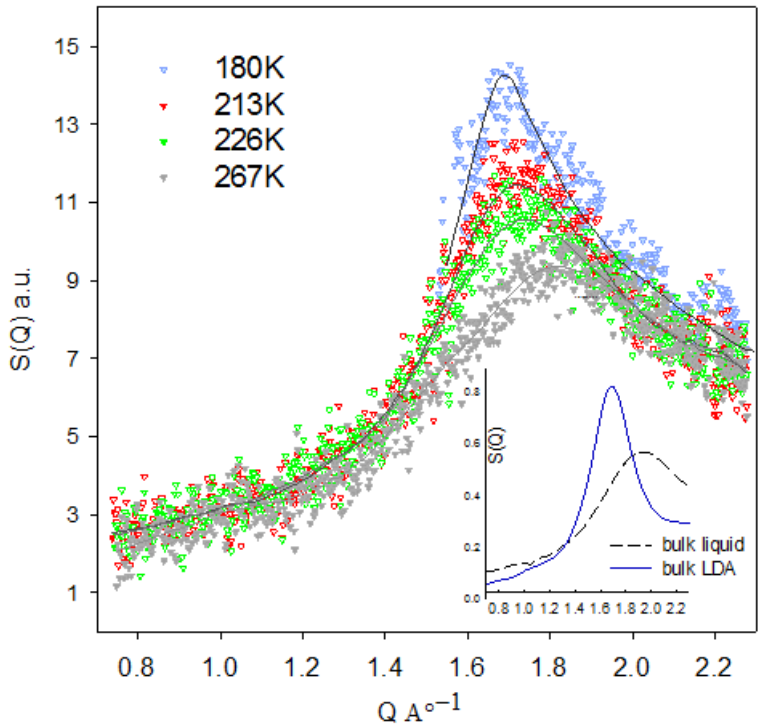

Figure 1.8: Evolution of the shape of the main peak of the static structure factor of confined water: Effect of the temperature decrease in water confined in nanopores of D_{BET} = 1.5nm. Insert: the behavior of bulk water.[55]

A computational approach

Computational studies have played an essential role in the study of the structure of confined water. The variety of methods used includes the density functional theory (DFT), molecular dynamics (MD), and Monte Carlo (MC) simulations. In particular, Molinero *et al.* have developed a method to reproduce most of water's anomalous properties: The mW potential for MC simulations.

The mW potential is a monatomic model of water that uses tetrahedral short-range interactions to model hydrogen bonding. It comes from the modification of the tetrahedrality parameter of the Stillinger-Weber (SW) potential for Silicon[57]. This coarse-grained model can efficiently reproduce the structures of liquid, crystal, and solid amorphous water, its energetics, its liquid anomalies, and its phase transitions. Through its validation, *Molinero and Moore*[58] conclude that these anisotropic, tetrahedral interactions define water behavior.

The mW potential has been used to study the freezing and melting of water confined in 3 nm hydrophilic nanopores[59] and deeply supercooled bulk water,[51] among other systems. Simulations are carried out in the NPT ensemble (constant number of moles, pressure, and temperature). From these simulations, the authors have shown that even though the

crystallographic signature of confined water resembles that of cubic ice, the actual structure is a stacking of hexagonal and cubic layers, called stacking disorder ice (I_{SD}).

Figure 1.9 shows the diffraction patterns of I_h, I_c, and confined water (simulation of water crystallized at 180 K in a 10^3 nm^3 box). The S(Q) of confined water was calculated as the Fourier transform of the radial correlation function, g(r), to obtain the diffraction patterns. It can be noted that the only distinguishable peaks are those which are common for hexagonal and cubic ice (111, 220, 311). The authors explain that the broadening of these peaks may be due to the small size of the crystallites. This broadening prevents the resolution of the (100) peak from hexagonal ice. Their results indicate a ratio of hexagonal to cubic layers of 1 to 2. However, the characteristic hexagonal peaks do not appear in the calculated diffraction pattern. The authors conclude that the absence of pure I_h crystallites explains the lack of high-order hexagonal peaks (as 102 and 103).

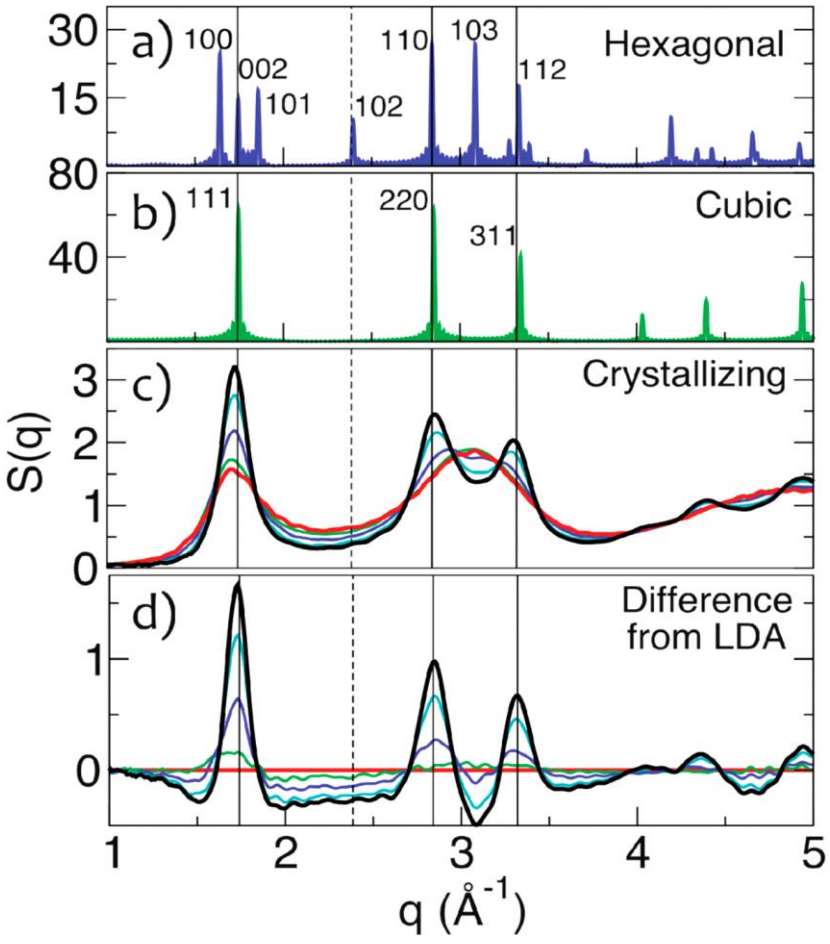

Figure 1.9: MD simulations of diffraction patterns of I_h, I_c, and water crystallized at 180 K in a 103 nm^3 box. Their results indicate a ratio of hexagonal to cubic layers of 1 to 2. LDA: Low-density amorphous water.[51]

Using the same mW potential for MD simulations, Moore *et al.* (2010) studied the specific case of water confined in a 3 nm cylindrical, hydrophilic nanopore. This particular study reproduces the experimental results obtained with 3 nm silica nanopores: A melting temperature at 223 K (51 K under the melting temperature of the simulated bulk water) and the presence of a layer of liquid water adjacent to the pore wall. Additionally, the authors have found that the critical size of the nucleus of ice contains ~75 to 100 water molecules, which agrees with the established thermodynamic limit for crystallization in the pores.[59,60]

1.5. Applications of confined water

Water properties in hydrophobic confinement can be used to enhance the solubility of otherwise immiscible solutes for applications like catalysis and gas storage (among others). This is a consequence of the modulation of water's polarity due to the distortion of the H-Bond network. This concept has been recently named water as a Tuneable Solvent (Wa-TuSo). [61]

In this sense, altering the nanoconfinement environment can have consequences on how water behaves, having a significant impact on the performance of nanoporous materials at countless applications.

As we have seen before, there are mainly two ways to modulate the behavior of water by changing the properties of the nanopores: the first one is to change the size of the pore, and the second one is to modify the interactions between water and the pore wall surface, i.e., by changing its surface chemistry.

In this work, the effort has been focused on controlling the surface chemistry of the materials. We have recently published an article on the effects of these modifications on the materials' performance on applications like catalysis and protein trapping.[62] Our results are in total agreement with the WaTuSo concept.

Furthermore, it is worth noting that the variety of crystalline phases makes water an excellent probe for nano-environments. While a simpler substance like hydrocarbons might form the same crystalline structure at all pressures, the crystalline structure of water changes depending on the confining conditions. Therefore it gives information about the local organization of water, its density, ratio amorphous/crystal, and possible and effective pressure inside the nanopores and can be a powerful tool for the characterization of nanomaterials.

1.6. Conclusion

In this thesis, we have selected materials of the type MCM-41, modified by direct synthesis or post-synthesis grafting to control the level of hydrophobicity inside the pores. This has allowed the experimental study of the phase transitions of confined water, not only in hydrophilic and hydrophobic but also in amphiphilic nano-environments. The synthesis and characterization of these confining materials (Chapters 2, 3, and 5) was a major part of this thesis.

The studies mentioned in this chapter show that the melting point of water in hydrophilic nanopores decreases with the pore size, this behavior can be fitted with the Gibbs-Thomson model and the structure of the confined ice in these hydrophilic nanopores corresponds to stacking disordered ice. This thesis addresses the effect of different levels of hydrophobicity on the melting point of water and its crystalline structure (Chapter 6).

We have also seen the advances of recent investigations on the intrusion and extrusion processes for water in hydrophobic nanopores at high pressures. However, an experimental study using neutron diffraction on the ice structure inside the nanopores at high pressures has not been reported before. Our results on the intrusion of water in hydrophobic nanopores and the crystalline structure of confined water at high pressures are exposed in Chapter 7.

In summary, the objectives of this work were:

- To study the effect of the pore wall hydrophobicity on the properties of confined water (density, Tm, crystalline structure of ice…)
- To study the structure of water intruded into hydrophobic nanopores at high pressures.

References

1. Sing, K. S. W. Reporting physisorption data for gas/solid systems with special reference to the determination of surface area and porosity (Recommendations 1984). *Pure and Applied Chemistry* **57**, 603–619 (1985).
2. Merum, S., Veluru, J. B. & Seeram, R. Functionalized carbon nanotubes in bio-world: Applications, limitations and future directions. *Materials Science and Engineering: B* **223**, 43–63 (2017).
3. Wang, B., Hu, C. & Dai, L. Functionalized carbon nanotubes and graphene-based materials for energy storage. *Chem. Commun.* **52**, 14350–14360 (2016).
4. Coleman, J. N., Khan, U. & Gun'ko, Y. K. Mechanical Reinforcement of Polymers Using Carbon Nanotubes. *Adv. Mater.* **18**, 689–706 (2006).
5. Whitby, M. & Quirke, N. Fluid flow in carbon nanotubes and nanopipes. *Nature Nanotech* **2**, 87–94 (2007).
6. Lehman, S. E. & Larsen, S. C. Zeolite and mesoporous silica nanomaterials: greener syntheses, environmental applications and biological toxicity. *Environ. Sci.: Nano* **1**, 200–213 (2014).
7. Rashed, M. N. & Palanisamy, P. N. Introductory Chapter: Adsorption and Ion Exchange Properties of Zeolites for Treatment of Polluted Water. in *Zeolites and Their Applications* (eds. Rashed, M. N. & Palanisamy, P. N.) (InTech, 2018). doi:10.5772/intechopen.77190.
8. Flanigen, E. M. Chapter 2 Zeolites and molecular sieves: An historical perspective. in *Studies in Surface Science and Catalysis* vol. 137 11–35 (Elsevier, 2001).
9. Zhao, D. Triblock Copolymer Syntheses of Mesoporous Silica with Periodic 50 to 300 Angstrom Pores. *Science* **279**, 548–552 (1998).
10. Beck, J. S. *et al.* A new family of mesoporous molecular sieves prepared with liquid crystal templates. *Journal of the American Chemical Society* **114**, 10834–10843 (1992).
11. Dosseh, G., Xia, Y. & Alba-Simionesco, C. Cyclohexane and Benzene Confined in MCM-41 and SBA-15: Confinement Effects on Freezing and Melting. *The Journal of Physical Chemistry B* **107**, 6445–6453 (2003).
12. Audonnet, F., Brodie–Linder, N., Morineau, D., Frick, B. & Alba-Simionesco, C. From the capillary condensation to the glass transition of a confined molecular liquid: Case of toluene. *Journal of Non-Crystalline Solids* **407**, 262–269 (2015).
13. Alba-Simionesco, C. *et al.* Effects of confinement on freezing and melting. *Journal of Physics: Condensed Matter* **18**, R15–R68 (2006).
14. Kocherbitov, V. & Alfredsson, V. Hydration of MCM-41 Studied by Sorption Calorimetry. *J. Phys. Chem. C* **111**, 12906–12913 (2007).

15. Descalzo, A. B., Martínez-Máñez, R., Sancenón, F., Hoffmann, K. & Rurack, K. The Supramolecular Chemistry of Organic–Inorganic Hybrid Materials. *Angew. Chem. Int. Ed.* **45**, 5924–5948 (2006).

16. Asefa, T., MacLachlan, M. J., Coombs, N. & Ozin, G. A. Periodic mesoporous organosilicas with organic groups inside the channel walls. *Nature* **402**, 867–871 (1999).

17. Inagaki, S., Guan, S., Fukushima, Y., Ohsuna, T. & Terasaki, O. Novel Mesoporous Materials with a Uniform Distribution of Organic Groups and Inorganic Oxide in Their Frameworks. *J. Am. Chem. Soc.* **121**, 9611–9614 (1999).

18. Li, Y., Mason, G., Morrow, N. R. & Ruth, D. W. Capillary Pressure at the Imbibition Front During Water–Oil Counter-Current Spontaneous Imbibition. *Transp Porous Med* **77**, 475–487 (2009).

19. Llewellyn, P. L. *et al.* Water Sorption on Mesoporous Aluminosilicate MCM-41. *Langmuir* **11**, 574–577 (1995).

20. Lefevre, B. *et al.* Intrusion and extrusion of water in hydrophobic mesopores. *The Journal of Chemical Physics* **120**, 4927–4938 (2004).

21. Eroshenko, V. & Grosu, Y. Thermodynamic and operational properties of heterogeneous lyophobic systems. *Int. J. Thermo* **16**, 1–9 (2012).

22. Grosu, Y. G. Thermodynamics and operational properties of nanoporous heterogeneous lyophobic systems for mechanical and thermal energy storage/dissipation. (2015).

23. Fraux, G., Coudert, F.-X., Boutin, A. & Fuchs, A. H. Forced intrusion of water and aqueous solutions in microporous materials: from fundamental thermodynamics to energy storage devices. *Chem. Soc. Rev.* (2017) doi:10.1039/C7CS00478H.

24. Loic, M. Etude macroscopique dynamique et microscopique des systèmes hétérogènes lyophobes. (2019).

25. Michelin-Jamois, M., Picard, C., Vigier, G. & Charlaix, E. Giant Osmotic Pressure in the Forced Wetting of Hydrophobic Nanopores. *Phys. Rev. Lett.* **115**, 036101 (2015).

26. Eroshenko, V. A. A new paradigm of mechanical energy dissipation. Part 1: Theoretical aspects and practical solutions. *Proceedings of the Institution of Mechanical Engineers, Part D: Journal of Automobile Engineering* **221**, 285–300 (2007).

27. Eroshenko, V. A., Piatiletov, I., Coiffard, L. & Stoudenets, V. A new paradigm of mechanical energy dissipation. Part 2: Experimental investigation and effectiveness of a novel car damper. *Proceedings of the Institution of Mechanical Engineers, Part D: Journal of Automobile Engineering* **221**, 301–312 (2007).

28. Coiffard, L., Eroshenko, V. A. & Grolier, J.-P. E. Thermomechanics of the variation of interfaces in heterogeneous lyophobic systems. *AIChE J.* **51**, 1246–1257 (2005).

29. Popyk, A. & Eroshenko, V. Current Status and Perspectives of the Thermomolecular Engine Developing. *Int. J. Thermo* **17**, 33–41 (2014).

30. Laouir, A., Luo, L., Tondeur, D., Cachot, T. & Le Goff, P. Thermal machines based on surface energy of wetting: Thermodynamic analysis. *AIChE J.* **49**, 764–781 (2003).

31. Karbowiak, T., Paulin, C., Ballandras, A., Weber, G. & Bellat, J.-P. Thermal Effects of Water Intrusion in Hydrophobic Nanoporous Materials. *J. Am. Chem. Soc.* **131**, 9898–9899 (2009).

32. Christenson, H. K. Confinement effects on freezing and melting. *J. Phys.: Condens. Matter* **13**, R95–R133 (2001).

33. Alcoutlabi, M. & McKenna, G. B. Effects of confinement on material behaviour at the nanometre size scale. *Journal of Physics: Condensed Matter* **17**, R461–R524 (2005).

34. Knight, A. W., Kalugin, N. G., Coker, E. & Ilgen, A. G. Water properties under nanoscale confinement. *Sci Rep* **9**, 8246 (2019).

35. Morineau, D. Molecular Dynamics in Confinement Probed by Neutron Scattering Methods. in 341–375 (2020). doi:10.1142/9789811217968_0010.

36. Radhakrishnan, R., Gubbins, K. E., Watanabe, A. & Kaneko, K. Freezing of simple fluids in microporous activated carbon fibers: Comparison of simulation and experiment. *The Journal of Chemical Physics* **111**, 9058–9067 (1999).

37. Lu, Y., Liu, Y., Xu, Y., Wang, L. & Li, J. Size-dependent melting of ice in mesoporous silica. *Philosophical Magazine* **93**, 1827–1842 (2013).

38. Findenegg, G. H., Jähnert, S., Akcakayiran, D. & Schreiber, A. Freezing and Melting of Water Confined in Silica Nanopores. *ChemPhysChem* **9**, 2651–2659 (2008).

39. Jähnert, S. *et al.* Melting and freezing of water in cylindrical silica nanopores. *Physical Chemistry Chemical Physics* **10**, 6039 (2008).

40. Schreiber, A., Ketelsen, I. & Findenegg, G. H. Melting and freezing of water in ordered mesoporous silica materials. *Physical Chemistry Chemical Physics* **3**, 1185–1195 (2001).

41. Webber, B. & Dore, J. Structural and dynamic studies of water in mesoporous silicas using neutron scattering and nuclear magnetic resonance. *J. Phys.: Condens. Matter* **16**, S5449–S5470 (2004).

42. Deschamps, J., Audonnet, F., Brodie-Linder, N., Schoeffel, M. & Alba-Simionesco, C. A thermodynamic limit of the melting/freezing processes of water under strongly hydrophobic nanoscopic confinement. *Phys. Chem. Chem. Phys.* **12**, 1440–1443 (2010).

43. Petrov, O. & Furó, I. A study of freezing–melting hysteresis of water in different porous materials. Part II: surfactant-templated silicas. *Phys. Chem. Chem. Phys.* **13**, 16358 (2011).

44. Agrawal, K. V., Shimizu, S., Drahushuk, L. W., Kilcoyne, D. & Strano, M. S. Observation of extreme phase transition temperatures of water confined inside isolated carbon nanotubes. *Nature Nanotech* **12**, 267–273 (2017).

45. Morishige, K. Influence of Pore Wall Hydrophobicity on Freezing and Melting of Confined Water. *J. Phys. Chem. C* **122**, 5013–5019 (2018).

46. Meldrum, F. C. & O'Shaughnessy, C. Crystallization in Confinement. *Adv. Mater.* 2001068 (2020) doi:10.1002/adma.202001068.

47. Bellissent-Funel, M. -C., Lal, J. & Bosio, L. Structural study of water confined in porous glass by neutron scattering. *The Journal of Chemical Physics* **98**, 4246–4252 (1993).

48. König, H. Eine kubische Eismodifikation. *Zeitschrift für Kristallographie - Crystalline Materials* **105**, 279–286 (1943).

49. Dore, J., Webber, B., Hartl, M., Behrens, P. & Hansen, T. Neutron diffraction studies of structural phase transformations for water–ice in confined geometry. *Physica A: Statistical Mechanics and its Applications* **314**, 501–507 (2002).

50. Morishige, K. & Uematsu, H. The proper structure of cubic ice confined in mesopores. *The Journal of Chemical Physics* **122**, 044711 (2005).

51. Moore, E. B. & Molinero, V. Is it cubic? Ice crystallization from deeply supercooled water. *Physical Chemistry Chemical Physics* **13**, 20008 (2011).

52. Malkin, T. L., Murray, B. J., Brukhno, A. V., Anwar, J. & Salzmann, C. G. Structure of ice crystallized from supercooled water. *Proceedings of the National Academy of Sciences* **109**, 1041–1045 (2012).

53. Malkin, T. L. *et al.* Stacking disorder in ice I. *Physical Chemistry Chemical Physics* **17**, 60–76 (2015).

54. Morishige, K., Yasunaga, H. & Uematsu, H. Stability of Cubic Ice in Mesopores. *J. Phys. Chem. C* **113**, 3056–3061 (2009).

55. Audonnet, F. & Alba-Simionesco, C. Experiments performed on the diffractometer G6.1 at the LLB (manuscript in preparation).

56. Yoshida, K., Yamaguchi, T., Kittaka, S., Bellissent-Funel, M.-C. & Fouquet, P. Thermodynamic, structural, and dynamic properties of supercooled water confined in mesoporous MCM-41 studied with calorimetric, neutron diffraction, and neutron spin echo measurements. *The Journal of Chemical Physics* **129**, 054702 (2008).

57. Stillinger, F. H. & Weber, T. A. Computer simulation of local order in condensed phases of silicon. *Physical Review B* **31**, 5262–5271 (1985).

58. Molinero, V. & Moore, E. B. Water Modeled As an Intermediate Element between Carbon and Silicon †. *The Journal of Physical Chemistry B* **113**, 4008–4016 (2009).

59. Moore, E. B., de la Llave, E., Welke, K., Scherlis, D. A. & Molinero, V. Freezing, melting and structure of ice in a hydrophilic nanopore. *Physical Chemistry Chemical Physics* **12**, 4124 (2010).

60. Moberg, D. R. *et al.* The end of ice I. *Proc Natl Acad Sci USA* **116**, 24413–24419 (2019).

61. Breynaert, E. *et al.* Water as a tuneable solvent: a perspective. *Chem. Soc. Rev.* 10.1039.C9CS00545E (2020) doi:10.1039/C9CS00545E.

62. Osta, O. *et al.* Direct Synthesis of Mesoporous Organosilica and Proof-of-Concept Applications in Lysozyme Adsorption and Supported Catalysis. *ACS Omega* (2020) doi:10.1021/acsomega.0c01996.

CHAPTER 2

SYNTHESIS METHODS OF THE CONFINING MATERIALS

This chapter presents practical information on the synthesis of amphiphilic and hydrophobic nanoporous materials of the MCM-41-type. We herein provide details on the silica condensation, surface chemistry control (by direct synthesis and post-grafting), and surfactant removal (calcination and washing) methods, as well as the product yields and recommendations on possible complications that can arise during the synthesis.

2.1. Vocabulary

MCM-41

MCM-41 belongs to the M41S family of molecular sieves, discovered in 1992 by Mobil researchers[1]. They developed a *templated synthesis* for mesoporous materials. This approach is based on forming a lyotropic liquid crystal by a surfactant used as a template for condensing a silica precursor (here, tetraethoxysilane, also known as TEOS) catalyzed by either an acid or a base (Equation 2.1).

$$Si(OCH_2CH_3)_4 + 2\ H_2O \xrightarrow{\text{acid/base}} SiO_2 + 4\ CH_3CH_2OH \qquad (2.1)$$

After this condensation occurs, the pores are opened by removing the surfactant using calcination or solvent extraction.

MCM-41 has a hexagonal phase and is the best-known member of the M41S family. Other members are MCM-48 and MCM-50 with a cubic and lamellar phase, respectively (Figure 2.1).

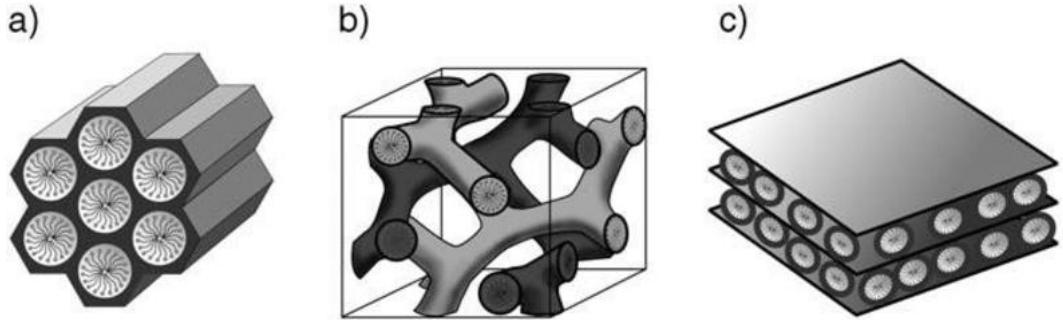

Figure 2.1: Schematic representation of M41S materials: a) MCM-41, with a 2D hexagonal structure, b) MCM-48, with a cubic structure, and c) MCM-50 with a lamellar structure.[2]

In the previous chapter, we discussed that MCM-41-type materials meet all the requirements for being used as model materials for confinement studies: They have an appropriate pore diameter (2 – 5 nm) for the study of confined water (approx. the size of 7 to 17 water molecules), an uniform pore structure, no inter-pore connections, and admit surface chemistry modifications.

Differences with SBA-15

In 1998, a similar family of materials denominated Santa Barbara Amorphous (SBA) was conceived by a group of researchers at the University of California, Santa Barbara, using the same principle[3]. SBA-15 is analogous to MCM-41, with a hexagonal pore structure.

There are several differences in the synthesis of SBA-15 and MCM-41, one of the most

important is the type of surfactant used as a template. For SBA-15, a non-ionic surfactant (P123) is used, while for MCM-41, we use a cationic surfactant (alkyltrimethylammonium bromide). This difference is crucial because it defines the pore size of the product. For SBA-15, the typical pore diameter is around 7 nm, while the pore size for MCM-41-like materials can be modulated between 2 and 5 nm by using surfactants with different chain lengths varying from 8 to 18 carbons.[1]

Besides, the hydrophilic chain of P123 can penetrate the aqueous channels where the silica condensation takes place. The subsequent removal of the surfactant will open a certain amount of micropores that interconnect the cylindrical mesopores of SBA-15. These micropores are not found in MCM-41. Therefore independent cylindrical pores (ideal for confinement studies) are obtained.

Another essential difference between the two synthetic methods concerns the pH. The P123 polymer in *very acidic conditions* or the alkyltrimethylammonium bromide salt in *very basic media* are necessary conditions for the success of the two synthetic methods. These conditions are required for two reasons. First, to accelerate the polymerization process of the TEOS (highly acid or highly basic conditions catalyze the polymerization process). Second, an acidic pH guarantees a strong interaction between the silica precursors and the negatively charged P123 micelles, in the same way that a basic pH does it for the positively charged alkyltrimethylammonium micelles.

Surfactant removal methods

The removal of the template is usually done by one of the following methods:

Calcination:

It consists of heating the sample to temperatures higher than 550 °C for up to 8 hours. This will burn out the organic template, opening the pores of the material. Such thermal treatment also has effects on the silica phase. In this step, dehydration, dehydroxylation, and siloxane bridge formation take place due to the high temperature, yielding a more condensed silica framework.[4–7]

Washing:

It is a softer method to remove the surfactant from the nanopores. The ideal washing method will vary for the type of material. In the case of MCM-41, the material is suspended in an acidic ethanol solution and stirring at temperatures around 35° C. The acidic solution will positively charge the silica surface, repelling the cationic template and making it easier to extract with ethanol. For SBA-15, Pasternak *et al.* have developed a non-ionic template

extraction method using a basic copper II solution and diluted nitric acid. In this case, copper II forms a complex with the surfactant removing it from the SBA-15 nanopores.[8]

After removing the template, the resulting silica surface is composed of silanol (Si-OH) and siloxane (Si-O-Si) groups. The proportion of these two groups will strongly depend on the method used for template removal: Calcination causes dehydration of silanol groups to form more siloxane groups, while solvent extraction at lower temperatures yields a silanol-rich surface.[9]

Surface chemistry control

In the context of confinement studies, a material like MCM-41 is ideal for studying water in hydrophilic nanopores, but one might be interested in studying water in hydrophobic or amphiphilic nano-environments. Fortunately, silica admits many surface modifications that allow controlling the hydrophobicity of the surface.

Two methods are commonly used to modify the surface chemistry of silica-based nanoporous materials: post-synthesis grafting (or simply post-grafting) and co-condensation (or direct synthesis). Both methods have advantages and disadvantages, and the use of one or the other will depend on the purpose of the desired material.

Post-synthesis grafting

It consists of a chemical reaction between the silanol groups at the surface and a functionalized organosilane, holding at least one leaving group, such as -Cl or ethoxy.[10–12]

The reaction efficiency depends on this leaving group. Chloro- organosilanes have been proven to be much more reactive than ethoxy-organosilanes (67% vs. 22% in MCM-41), and yet a random distribution along the surface can be achieved for appropriate pore sizes. This is the key to obtain a homogeneous surface and avoiding pore blockage.[13]

A successful reaction with this method will produce completely functionalized, hydrophobic surfaces, and the pore size will decrease on account of the grafted groups (trimethyl-silane or dimethyl-octyl-silane, for example). However, a partial functionalization with this method, in the attempt to obtain a weaker grafting density that would yield to an amphiphilic surface, actually leads to a non-uniform distribution of the grafted groups, mostly placed at the external surface and at the entrance of the pores.[14]

The direct synthesis or co-condensation method

It consists of including in the precursor mixture an organosilane that will condense together with the silica precursor (TEOS, for example). In this way, the organic groups will

be part of the material's framework, distributed among the internal part of the walls and the surface. This method produces a surface in which the organic groups are distributed inside and outside of the nanopores.[15,16] The direct synthesis allows obtaining partially modified surfaces and controlling the organic groups' surface density.

However, the direct synthesis presents a downside: the degree of hydrophobicity obtained by this method is limited by the percentage of organosilane that can be introduced in the precursor mixture without altering the pore structure. Previous research shows that a loss of the 2D-hexagonal pore structure is obtained for percentages higher than 20%, with a significant decrease in the surface area and pore volume.[17,18]

For the reasons explained above, in the design of confining materials, one would prefer a direct synthesis for amphiphilic materials, preserving the post-grafting method for highly hydrophobic nanopores.

2.2. Experimental protocol for the direct synthesis

For the direct synthesis of mesoporous organosilica, the aim was to obtain amphiphilic materials with a highly ordered pore structure. To avoid the disruption of the honeycomb-like structure, the organosilane percentage in the precursor mixture was kept under 20 mol%. This high limit of organosilane for ordered cylindrical nanopores was established in previous research work. Larger percentages of organosilane in the mixture were proved to cause disruptions in the hexagonal order of the product[19]

Materials

- Template: Octadecyltrimethylammonium bromide ($C_{21}H_6NBr$) or dodecyltrimethylammonium bromide ($C_{15}H_6NBr$)
- Tetraethyl orthosilicate **(TEOS)**
- Methyltriethoxysilane **(MTES)**
- Phenyltriethoxysilane **(PTES)**
- Ammonia (30%)
- Hydrochloric acid (37%)
- Ethanol (99.98%) Sigma-Aldrich.

Procedure

MCM-41-type materials with different percentages of MTES or PTES were prepared. For each one, 4 mmol of the cationic surfactant C_nTAB was dissolved in 72.0 ml of ultrapure

water at 50 °C and was stirred vigorously for 1.5 h for complete dissolution, then the temperature was decreased to 35 °C, and 4.8 ml of ammonia (30%) were added, the mixture was stirred for further 5 min. After, the precursors' mixture was added, keeping a constant number of moles of silicon (26.33 mmol). The final molar composition of the reaction mixture was:

$$(1 - x)\ TEOS: x\ MTES\ (or\ ETES, PTES): 2.4\ NH_3: 0.15\ C_nTAB: 152\ H_2O$$

where x is the fraction of methyl-, ethyl- or phenyl-triethoxysilane (MTES, ETES, or PTES, respectively) that spans a range from 0 to 0.20 and n is the length of the alkyl chain of the surfactant.

Samples were named according to the template used and their fraction of organosilane in the precursor mixture, as follows:

C18-M7-Me for 0.93 TEOS/ 0.07 MTES

C18-M15-Me for 0.85 TEOS/ 0.15 MTES

C18-M7-Ph for 0.93 TEOS/ 0.07 PTES, all of them using C_{18}TAB as template, and C12-M7-Me for 0.93 TEOS/ 0.07 MTES using C_{12}TAB as template. Standard MCM-41 C_{18} and C_{12} were synthesized and washed under the same conditions for comparison.

The precise quantities of each substance for the synthesis of the different materials are shown in Table 1. As an example, for C18-M15-Me, 1.570 g of C_{18}TAB, 5.13 mL of TEOS, and 0.81 mL of MTES were used.

The reaction was allowed to stir, at a rate of 300 rpm, for 3.5 h. The obtained white solid was washed twice with 40 ml of HCl 2%v/v and then with ultrapure water until reaching neutral pH.

Table 2.1: Quantity of the different substances for the synthesis of nanoporous organosilica (MCM-41-type).

Substance		**Quantity**
Water (ml)		72.0
Ammonia (30%) (ml)		4.8
Template (g)		
C_{12}TAB		1.230
C_{18}TAB		1.570
Precursor mixture (ml)		
0% MTES	TEOS	6.04
	MTES	0
7% MTES	TEOS	5.62
	MTES	0.38
10% MTES	TEOS	5.43
	MTES	0.54
15% MTES	TEOS	5.13
	MTES	0.81
20% MTES	TEOS	4.83
	MTES	1.08
7% PTES	TEOS	5.62
	PTES	0.46
7% ETES	TEOS	5.62
	ETES	0.40

The typical reaction yield for the direct synthesis was (85 $\pm$ 5)%.

Template Removal

The conditions of template removal were adjusted to obtain a clean material without causing damages to the surface. For this purpose, two steps were needed: first, an acidification step, followed by an ethanol extraction step. The acidification step has the objective to protonate the hydroxyl groups of the material, creating repulsion between the surface and the positively charged surfactant. During the subsequent ethanol extraction step, the removal of the surfactant from the nanopores takes place.

Procedure

The procedure was the following: 100 ml of an aqueous solution of HCl (2%v/v) were added per gram of product, and it was stirred for 25 min at room temperature. The solid was filtered and re-dispersed in a mixture of 200 ml of Ethanol 99% and 10ml of ultrapure water. This mixture was stirred at 50 °C for three hours. Then, the solid was filtered and dried for 24h in an oven at 60 °C.

Critical parameters for a successful washing were the concentration and time of exposure to the acidic solution and the presence of 5 %v/v of water mixed with ethanol in the extraction step. The template extraction was verified through FTIR. In some cases, the procedure had to be repeated to remove all the surfactant from the pores due to either an inefficient acidification step or the absence of water in the extraction mixture.

Due to the presence of residual surfactant in the material, an additional thermal treatment was required for the sample C18-M7-Ph to accomplish total surfactant removal. This sample was additionally heated at 350 °C for 1 hour under a nitrogen atmosphere. At this temperature, the phenyl groups at the surface are not affected, and the entire residual template is eliminated.

The typical reaction yield for the template removal was (75 $\pm$ 20)%. The primary source of inefficiency was the filtration steps with a Duran funnel #4. The losses were depending on the grain size of the material. For example, for C18-M20-Me, there were significant losses of product (%yield ~55%). The supernatant was later centrifuged, and the solid was analyzed using transmission electron microscopy. We found that the grain size of this product was around 120 nm, more than five times smaller than the other samples. Filtering with a Duran funnel of porosity 4 (nominal max pore size 1.0-1.6 μm) entailed the loss of nearly half the synthesized product.

2.3. Experimental protocol for the post-synthesis grafting

The degree of hydrophobicity obtained by the direct synthesis described above is limited if we aim to obtain an ordered hexagonal pore structure. Therefore, in this post grafting experiment, we have decided to modify the surface of the methyl-containing mesoporous materials C18-M7-Me and C18-M15-Me with trimethylsilane groups. Additionally, this experiment allowed us to study the effect of the existent methyl groups at the surface on the silylation reaction's efficiency and homogeneity. For additional details on this procedure, see Appendix 1.

The products are C18-M7-Me $SiMe_3$ and C18-M15-Me $SiMe_3$

The reaction between the hydroxyl groups on the surface and chlorotrimethylsilane is shown in equation 2.2.

(2.2)

Materials

- Nanoporous organosilica C18-M7-Me and C18-M15-Me
- Chloroform ($CHCl_3$)
- Chlorotrimethylsilane ($ClSi(CH_3)_3$)
- Triethyl-amine ($N(CH_2CH_3)_3$)
- Molecular Sieve 0.3 nm, from Merk.

Preparation steps

The primary source of error for this reaction is the presence of water in the reactants. If any of the substances is not properly dry, the remaining water will react with $ClSi(CH_3)_3$, which will reduce the amount of this reagent available for reaction at the surface and form secondary products inside and outside of the pore network.

- For this reason, before the reaction, the following preparation steps were necessary:
- Activate molecular sieves (0.3 nm, Merck) by heating them to 110 °C in the oven for 24h. Then place them with the $CHCl_3$ in a container with a screw cap for 24 h before commencing the reaction.
- Distill $N(CH_2CH_3)_3$.
- Cleaning and drying a round-bottom flask and a double vacuum line.
- Outgassing the set-up (See Apendix 1)

Procedure

650 mg of dry nanoporous organosilica were placed in a clean round-bottom flask. The solvent and reagents were added in this order: first 20 ml of chloroform, followed by 3.5 ml of triethylamine, and finally 3.5 ml of chlorotrimethylsilane. The flask was covered with aluminum foil, and the reaction was stirred for one hour under argon flow. After this time, the argon bottle was closed, and the reaction was allowed to stir overnight. The next day, extra 50 ml of chloroform were added to dissolve the subproduct triethylamine hydrochloride. The solid was filtered with a Buchner funnel (Porosity 4) and rinsed three times with chloroform. The obtained product was dried in the oven at 80 °C for 24 h. The quantities of material used for the reaction are summarized in Table 2. The set-up is shown in Figure 2.2.

Figure 2.2: Apparatus for the post-grafting reaction under an inert atmosphere.

Table 2.2: Quantity of the different substances for the post-grafting of nanoporous organosilica materials.

Substance	**Quantity**
Nanoporous organosilica (mg)	650
Chloroform (ml)	20
Triethyl-amine (ml)	3.5
Trimethyl-chloro-silane (ml)	3.5

The reaction yield for the post-grafting was (95 ± 5)%.

2.4. Conclusion

In this chapter, we have discussed the mechanism and methods used to synthesize MCM-41-type nanoporous organosilica and template removal. Two surface modification approaches to control the hydrophobicity of the materials were exposed: direct synthesis and post rafting. The direct synthesis or co-condensation method was used to prepare the amphiphilic materials. Using the solvent extraction method enabled us to prepare the direct synthesis products without the danger of burning off the organic groups at the surface.

Our approach for the synthesis of hydrophobic materials consisted of a combination of co-condensation and post-grafting.

The methods used to characterize the products will be presented in the next chapter.

References

1. Beck, J. S. *et al.* A new family of mesoporous molecular sieves prepared with liquid crystal templates. *Journal of the American Chemical Society* **114**, 10834–10843 (1992).
2. Hoffmann, F., Cornelius, M., Morell, J. & Fröba, M. Silica-Based Mesoporous Organic–Inorganic Hybrid Materials. *Angewandte Chemie International Edition* **45**, 3216–3251 (2006).
3. Zhao, D. Triblock Copolymer Syntheses of Mesoporous Silica with Periodic 50 to 300 Angstrom Pores. *Science* **279**, 548–552 (1998).
4. He, N. Y., Ge, S. X., Yang, C., Cao, J. M. & Gu, M. Effects of calcination and synthetic conditions on the photoluminescence of hexagonal mesoporous materials. *Materials Letters* **58**, 3304–3307 (2004).
5. Basso, A. M., Nicola, B. P., Bernardo-Gusmão, K. & Pergher, S. B. C. Tunable Effect of the Calcination of the Silanol Groups of KIT-6 and SBA-15 Mesoporous Materials. *Applied Sciences* **10**, 970 (2020).
6. Ding, Y., Zhao, C., Lia, Y., Ma, Z. & Lv, X. EFFECT OF CALCINATION TEMPERATURE ON THE STRUCTURE AND CATALYTIC PERFORMANCE OF THE CU-MCM-41 CATALYSTS FOR THE SYNTHESIS OF DIMETHYL CARBONATE. *Quim. Nova* (2018) doi:10.21577/0100-4042.20170291.
7. Bagshaw, S. A. & Bruce, I. J. Rapid calcination of high quality mesostructured MCM-41, MSU-X, and SBA-15 silicate materials: A step towards continuous processing? *Microporous and Mesoporous Materials* **109**, 199–209 (2008).
8. Pasternak, N., Nancy, L. & Alba-Simionesco, C. Procédé d'extraction de tensioactif d'un matériau nanoporeux. (2015).
9. Tiemann, M. & Weinberger, C. Selective Modification of Hierarchical Pores and Surfaces in Nanoporous Materials. *Adv. Mater. Interfaces* **8**, 2001153 (2021).
10. Zhao, X. S. & Lu, G. Q. Modification of MCM-41 by surface silylation with trimethylchlorosilane and adsorption study. *The Journal of Physical Chemistry B* **102**, 1556–1561 (1998).
11. Wouters, B. H., Chen, T., Dewilde, M. & Grobet, P. J. Reactivity of the surface hydroxyl groups of MCM-41 towards silylation with trimethylchlorosilane. *Microporous and Mesoporous Materials* **44–45**, 453–457 (2001).

12. Schoeffel, M., Brodie–Linder, N., Audonnet, F. & Alba–Simionesco, C. Wall thickness determination of hydrophobically functionalized MCM-41 materials. *J. Mater. Chem.* **22**, 557–567 (2012).

13. Deschner, T., Liang, Y. & Anwander, R. Silylation Efficiency of Chorosilanes, Alkoxysilanes, and Monosilazanes on Periodic Mesoporous Silica. *J. Phys. Chem. C* **114**, 22603–22609 (2010).

14. Yokoi, T., Yoshitake, H. & Tatsumi, T. Synthesis of amino-functionalized MCM-41 via direct co-condensation and post-synthesis grafting methods using mono-, di- and tri-amino-organoalkoxysilanes. *Journal of Materials Chemistry* **14**, 951 (2004).

15. Macquarrie, D. J. Direct preparation of organically modified MCM-type materials. Preparation and characterisation of aminopropyl–MCM and 2-cyanoethyl–MCM. *Chemical Communications* 1961–1962 (1996).

16. Macquarrie, D., Jackson, D., Mdoe, J. G. & Clark, J. Organomodified hexagonal mesoporous silicates. *New journal of chemistry* **23**, 539–544 (1999).

17. Rabbani, M. M., Oh, W.-T. & Nam, D.-G. Synthesis and Characterization of Methyltrieth-oxysilyl-Mediated Mesoporous Silicalites. *Transactions on Electrical and Electronic Materials* **12**, 119–122 (2011).

18. Putz, A.-M. *et al.* Mesoporous silica obtained with methyltriethoxysilane as co-precursor in alkaline medium. *Applied Surface Science* **424**, 275–281 (2017).

19. Burkett, S. L., Sims, S. D. & Mann, S. Synthesis of hybrid inorganic–organic mesoporous silica by co-condensation of siloxane and organosiloxane precursors. *Chemical Communications* **11**, 1367–1368 (1996).

CHAPTER 3

TECHNIQUES FOR THE CHARACTERIZATION OF NANOPOROUS MATERIALS

In order to perform confinement studies in nanopores of controlled hydrophobicity, a significant part of the experimental efforts were focused on the synthesis of amphiphilic and hydrophobic nanoporous materials and the determination of their physical and chemical properties. A comprehensive characterization of the synthesized nanoporous materials was performed in order to answer the following questions:

- How are the pores organized within the material? (Nitrogen adsorption, SAXS, TEM)
- Has the surfactant been efficiently removed from the pores? (FTIR, TGA)
- What are the surface area, pore-volume, and pore size of the material? (Nitrogen adsorption, SAXS)
- What is the density of hydroxyl groups at the surface? (Water adsorption)
- For amphiphilic materials, have the organic groups been incorporated into the material by the co-condensation method? (FTIR, TGA)
- Has the surface modification by post-grafting been efficient? (FTIR, TGA)
- Can the material be qualified as hydrophobic? (Water adsorption)

Each of the techniques described below contributed valuable information to obtain a detailed description of the confining materials. Often, several techniques were combined to answer one question.

This chapter aims to explain why each experimental technique was chosen, its limitations, and what kind of information can be extracted from the data.

3.1. Fourier Transform Infrared Spectroscopy (FTIR)

FTIR was the first technique used after each synthesis. FTIR enables to follow chemical changes on the materials: Integration of organic moieties during the direct synthesis, template removal from the pores, and surface chemistry modification by post-grafting.

The principle of FTIR is well described in the literature [1–3]. In short, when electromagnetic radiation in the infrared region interacts with matter, changes in molecular dipolar moment associated with vibrations and rotations occur. Molecules absorb infrared radiation if their frequency corresponds to one of the fundamental modes of vibration of the molecule. As these frequencies are dependent on the mass of the atoms bonded and on the strength of those bonds, an infrared spectrum is helpful to study the chemical structure of a sample.

Attenuated Total Reflection (ATR) was used due to the easy sample preparation and reproducible measurements. The principle of ATR is that the IR beam is directed to a high optical density crystal above which the sample is located; then, an evanescent wave is formed, extending to the sample. According to the sample's chemical structure, the evanescent wave is attenuated and passed back to the beam, exiting the opposite extreme of the crystal, towards a detector[4].

In this work, FTIR spectra from the samples were taken 4000 to 400 cm^{-1} with a Bruker TENSOR equipped with a Platinum ATR at room temperature and atmospheric pressure.

Figure 3.1 shows an FTIR spectrum of MCM-41 as-synthesized (before template removal). The typical absorption bands for silica materials correspond to the SiO-H stretching (at 3300 cm^{-1}), SiO-H bending (at 1650 cm^{-1}), and the Si-O stretching mode (1050 cm^{-1}).

For MCM-type of materials, the template contains a carbonated chain which can be detected by the absorption bands between 2800 and 3000 cm^{-1} from the C-H stretching modes. After washing or calcination, the absence of these peaks in the FTIR spectrum confirms the efficient template removal.

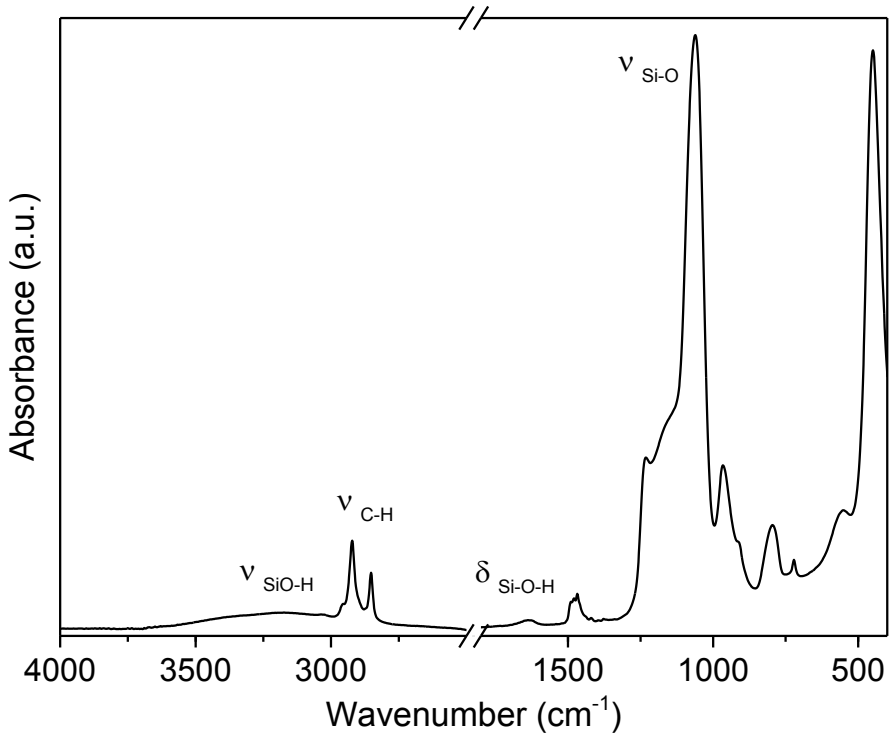

Figure 3.1: Example of an FTIR spectrum for MCM-41 as synthesized.

3.2. Thermogravimetric Analysis (TGA)

TGA consists of the measurement of the mass of a sample as a function of temperature. The particularity of this technique is its high precision for the temperature and weighing, 0.1ºC and 0.001 mg, respectively.

TGA was used to follow the adsorbed water evaporation, surfactant loss, and the loss of the organic groups of the functionalized materials. The measurements were performed with a Q050 from TA Instruments, in an inert atmosphere (nitrogen flow), from ambient temperature to 850 ºC with a temperature ramp of 10 ºC/min.

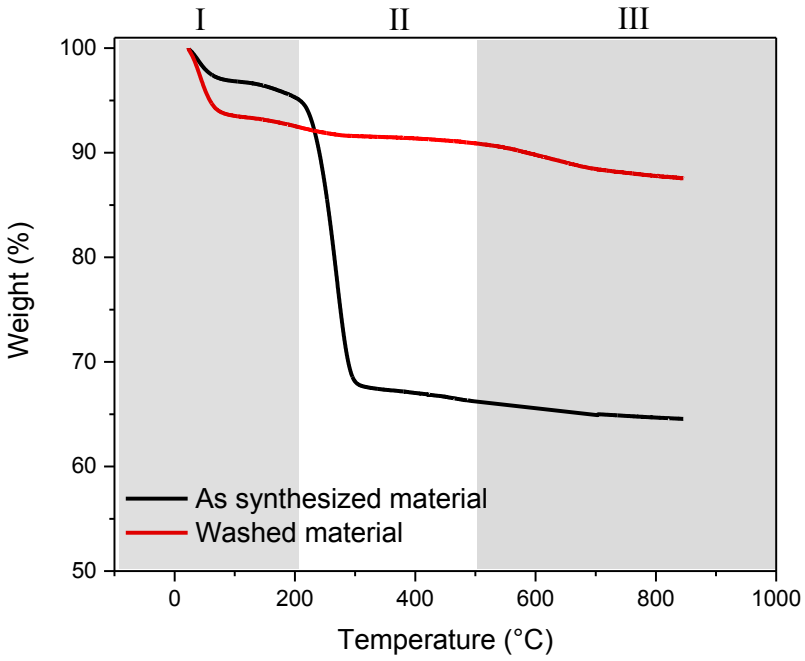

Figure 3.2: Example of TGA curves of an as-synthesized material (with surfactant) and a washed material, between 20 and 850 °C.

The typical TGA curves for organosilica materials are shown in Figure 3.2. Several weight loss steps can be identified. First, up to 200 °C (Zone I, in the figure), we observe the loss of water adsorbed both inside the nanopores and at the external surface. Naturally, the quantity of water adsorbed in a washed material will be greater than in an "as-synthesized" one, where the pores are blocked by surfactant. Around 300 °C (Zone II), a mass loss of approx. 30 % is expected for the as-synthesized, corresponding to the mass of surfactant. Finally, from 500 °C (Zone III), the loss of the organic groups attached to the material's framework, together with the condensation of silanol (Si-OH) groups to form siloxane (Si-O-Si) bridges.

3.3. Transmission Electron Microscopy (TEM)

TEM confirmed the presence of a 2D-hexagonal arrangement of cylindrical nanopores and provided morphologic information like the grain size distribution of the material. An example of a TEM image is shown in Figure 3.3.

This technique uses a sharp, accelerated electron beam as a probe to image a sample with sub-nanometric resolution. When such a beam illuminates a thin sample, several phenomena are produced, e.g., backscattering, secondary or Auger electrons, X-Rays or visible light generation, Bremsstrahlung X-Rays generation, inelastic and elastic scattering, and electron transmission[5].

The images were recorded in bright field mode, *i.e.*, after illuminating the sample, the transmitted electrons were detected by placing the objective aperture below the incident electron beam.

For the sample preparation, one to two drops of suspensions of the materials in ethanol were placed on square mesh TEM support grids made of copper. Images were taken with a JEOL JEM-2010 high-resolution transmission electron microscope.

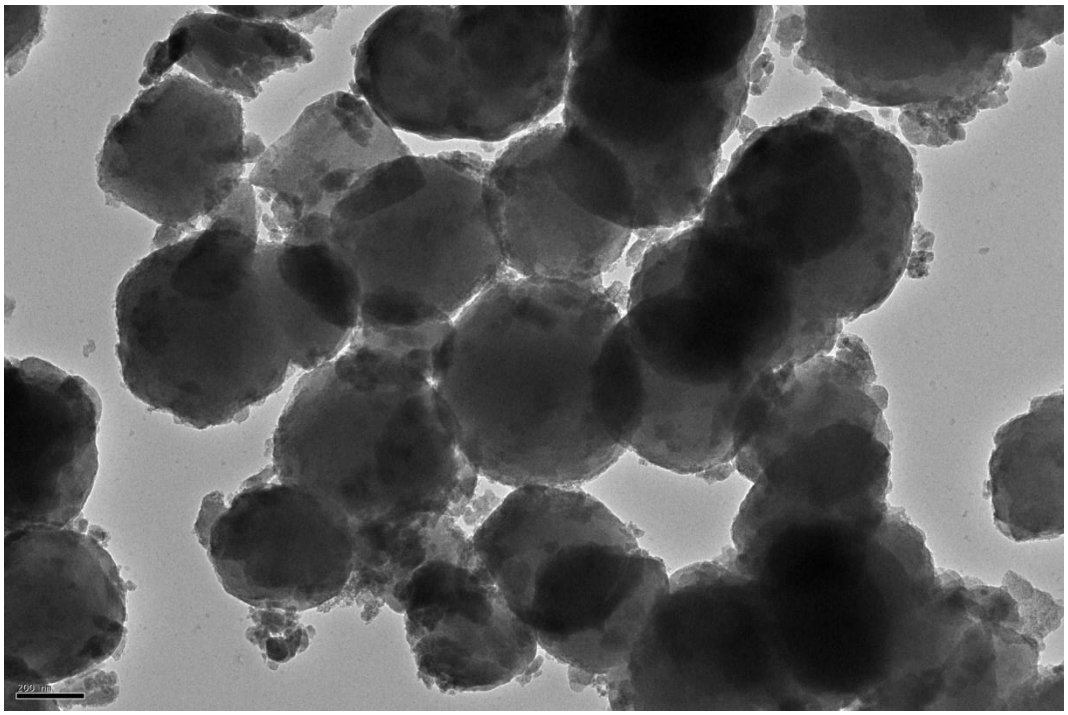

Figure 3.3: Example of a transmission electron microscopy image (C18M15Me).

3.4. Small-Angle X-Ray Scattering (SAXS)

This technique is used in combination with nitrogen adsorption to characterize the pore structure of the materials. In SAXS experiments, a collimated beam of X-Rays interacts with the sample, and light is scattered according to the local electronic density. The scattered intensity is collected as a function of the magnitude of the wave vector (Q).

The scattered intensity I(Q) is the Fourier Transform of the correlation function of the electronic density. The scattered vector amplitude (Q) of the Bragg peaks is related to the lattice spacing (d), or cell parameters of the structure:

$$d = \frac{2\pi}{Q_{Bragg}} \tag{3.5}$$

The lattice spacing is used to calculate the pore diameter, combined with the results

from nitrogen adsorption (see the KJS method in section 3.5).

An example of the SAXS curve obtained for MCM-41-like materials is shown in Figure 3.4. The 2D-hexagonal structure of MCM-41 materials can be identified by an intense peak followed by two less intense ones, indexable to the (10), (11), and (20) distances of the hexagonal geometry[6].

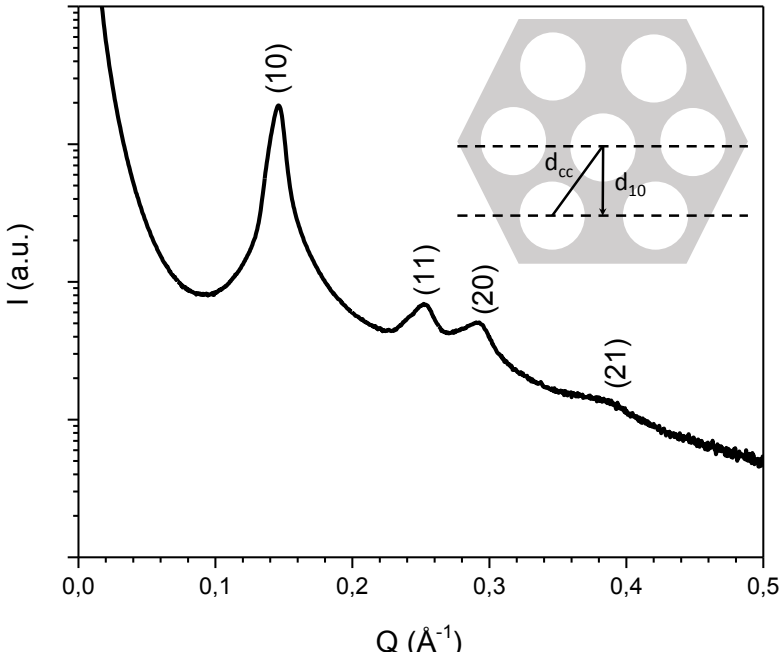

Figure 3.4: Example of SAXS curve for C18M15Me at room temperature.

The instrument used is located at the Laboratoire Léon Brillouin. A copper rotating anode with a fine focus filament serves as an X-Ray generator. The beam passes through a Xenocs collimating multilayer mirror, coupled with homemade hybrid crystal slits. Then, the beam interacts with the sample, followed by a vacuum chamber containing a beam-stop with a calibrated photodiode.

3.5. Nitrogen Adsorption

The physisorption of gas on the surface of a solid is helpful to characterize the surface of porous solids. The relationship between the adsorbed amount of gas and its pressure at constant temperature is known as the adsorption isotherm. Adsorption isotherms were determined point-by-point, measuring the volume of gas adsorbed, introducing a gas dose, and allowing time for the system to reach equilibrium.

Nitrogen adsorption experiments were performed with ASAP 2020 Surface Area and

Porosity Analyzer from micromeritics. Approx. 50 mg of nanoporous silica samples were degassed under vacuum at 90 °C for 24 h to remove adsorbed water, and then the nitrogen adsorption and desorption isotherms were taken at 77 K, the typical duration for completion of adsorption and desorption is between 5 to 8 hours.

Our nanoporous materials present a nitrogen adsorption isotherm of type IV from the IUPAC classification[7] (Figure 3.5). The adsorption consists on a monolayer-multilayer formation (these two processes are more or less overlapped depending on the difference between the adsorbate-adsorbate and the adsorbate-adsorbent affinities) followed by pore condensation, which represents a shifted vapor-liquid phase transition. For narrow mesopores (cylindrical pores less than ~5 nm diameter) the isotherm is completely reversible; for larger pore sizes or for other fluids with stronger intermolecular interactions (such as water), an hysteresis between adsorption and desorption appears (see section 2.6).

In type IV isotherms, three different adsorption zones can be identified. Each one of them gives different information about the physical properties of the material.

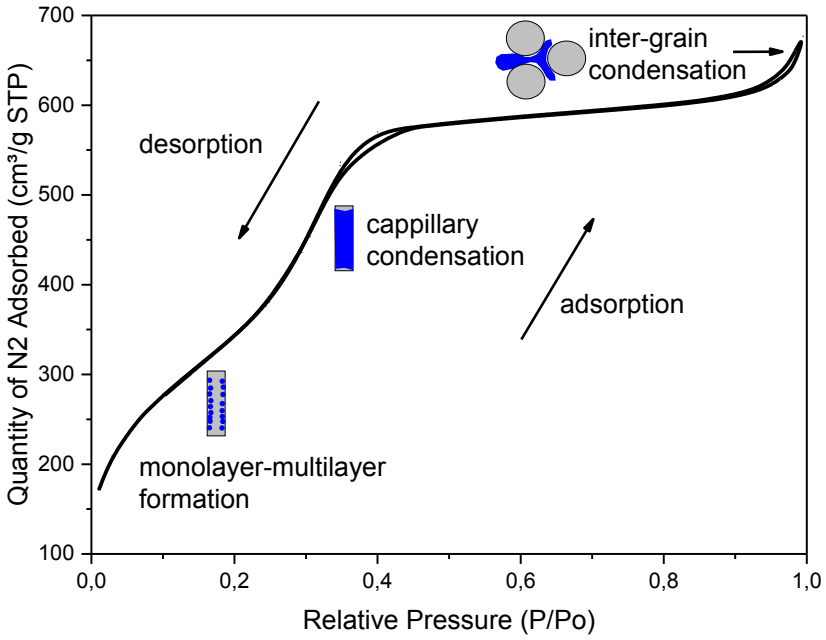

Figure 3.5: Example of a type IV nitrogen adsorption/desorption isotherm for an amphiphilic nanoporous material (C18M15Me) at 77 K.

At low relative pressures (P/P_0 < 0.2), the monolayer-multilayer formation can be observed; this zone is also called the "knee" of the isotherm. For hydrophilic materials, the knee of the isotherm tends to be more pronounced; this is due to enhanced polar-induced polar interactions between the surface and nitrogen molecules. On the contrary, more

hydrophobic materials present lower quantities of nitrogen adsorbed in this zone and a less pronounced knee of the isotherm.

After the material's surface has been saturated with nitrogen, a second zone called the capillary condensation is observed. Then, a plateau that indicates saturation can be observed. The plateau is the appropriate zone to determine the pore volume (V_{pore}) of the material; one would usually take the value of the quantity of nitrogen adsorbed at:

$$P/P_0 = (P/P_0)^* + 0.1 \quad (3.1)$$

The pressure chosen for the determination of the total pore volume should be specified with the results. The wrong choice of this pressure is a common source of error for determining the pore volume and pore sizes of nanoporous materials. For example, if we take the isotherm in Figure 3.5, choosing P > 0.95 would overestimate the pore volume. This is because the increase in the quantity of nitrogen adsorbed at high pressures corresponds to the inter-granular condensation and not the available volume inside the pores.

To calculate the surface area, the Brunauer-Emmett-Teller (BET) method[8], applied to the knee of the isotherm ($P/P_0 < 0.2$), is used. The BET equation in the linear form is:

$$\frac{P}{V\,(P_0-P)} = \frac{1}{V_m C} + \frac{C-1}{V_m C}\frac{P}{P_0} \quad (3.2)$$

where V is the volume of gas adsorbed at the relative pressure P/P_0, V_m is the volume of monolayer capacity, and C is a constant dependent on the isotherm shape.

By plotting $P/(V(P_0 - P))$ vs. P/P_0, the values of Vm and C can be obtained. The BET surface area can be calculated from Vm and the area occupied by each molecule in the monolayer (0.162 nm^2 for nitrogen at 77 K).

The BET method assumes that the enthalpy of desorption ($\Delta_{des}H$) of the first layer is much greater than the enthalpy of desorption of the second layer (approx. enthalpy of liquefaction ($\Delta_{vap}H$)). The C value, which formula is shown in Equation (3.3), is a measure of that difference.[9]

$$C = e^{\frac{\Delta_{des}H - \Delta_{vap}H}{RT}} \quad (3.3)$$

where R is the universal gas constant ant T is the temperature.

A high C value (C > 100) is obtained when the gas molecule has a strong affinity towards the surface, like in MCM-41 (hydrophilic). The C value decreases when organic groups are present at the surface (amphiphilic or hydrophobic). This is because the intermolecular forces between nitrogen molecules and the surface of silica are mainly due to dipole-induced dipole interactions and the organic groups decrease the polarity of the

surface.

In the case of low C values (C < 20), the formation of the monolayer and multilayer occur simultaneously, causing an overestimation of the BET surface area (A)[9,10].

Pore size calculation

There exist several methods to calculate the pore size of nanoporous materials from the nitrogen adsorption data, the values obtained depend on the selected method.

The Brunauer–Emmett–Teller (BET) method[8]:

Using the values of total pore volume (V_{pore}) and BET surface area (A), one can calculate the diameter of cylindrical pores:

$$D = \frac{4V_{pore}}{A} \tag{3.4}$$

The main disadvantage of this method is that, for amphiphilic and hydrophobic materials, like the ones synthesized for this work, the relative error in the BET surface area, due to the overlap of the monolayer/multilayer adsorption, is propagated to the calculation of the pore size.

The Barrett-Joyner-Halenda (BJH) method[11]:

This method is based on the Kelvin equation (Equation 3.5):

$$r_K(P/P_0) = \frac{2\gamma V_m cos\theta}{RTLn(P/P_0)} \tag{3.5}$$

Where P/P_0 is the relative pressure, γ is the liquid/vapor surface tension, V_m is the molar volume of the liquid, r_K is the kelvin radius, R is the universal gas constant, θ is the contact angle, and T is the temperature.

Besides considering the Kelvin radius (r_K), the BJH method considers the thickness of the adsorbed layer, $t(P/P_0)$, formed before capillary condensation.

$$r_{BJH} = r_K + t(P/P_0) \tag{3.6}$$

The thickness $t(P/P_0)$ is calculated with the Halsey equation:

$$t(P/P_0) = 3.54[-5/\ln(P/P_0)]^{1/3} \tag{3.7}$$

Finally, the pore size distribution according to the BJH model can be written as:

$$D_{BJH(P/P_0)} = \frac{4\gamma V_m cos\theta}{RTLn(P/P_0)} + 7.08[-5/\ln(P/P_0)]^{1/3} \tag{3.8}$$

Two different values are obtained corresponding to the adsorption and desorption branch

due to the hysteresis caused by the formation of the meniscus. For cylindrical nanopores, the value of the pore size obtained using the desorption branch is considered more accurate. This is because desorption is an equilibrium phase transition, where a sudden emptying of the pores occurs, while adsorption is associated with metastable states of the pore fluid that progressively lead to condensation.

The BJH method is commonly used to determine the pore size of SBA-15-type materials, with a pore size greater than 7 nm. For smaller pores, like in MCM-41-type materials, this method has been found to underestimate the pore diameter by approximately one nanometer.[12]

The nonlocal density functional theory (NLDFT) method[13]:

This model has been used to calculate pore size distributions in nanoporous materials, including MCM-41, from the desorption branches of experimental Nitrogen and Argon isotherms. Neimark *et al.* (1998) set the fluid-fluid interaction parameters to reproduce the bulk fluid thermodynamic properties, such as equilibrium densities and pressures, liquid-gas interfacial tensions at low temperatures, and a set of standard adsorption isotherms on nonporous surfaces in the multilayer adsorption region (also known as "kernel"). These parameters are then used to solve the general adsorption isotherm equation, where the experimental isotherm is described as a superposition of isotherms in individual pores (Equation 3.9).

$$N_{exp}\left(\frac{P}{P_0}\right) = \int_{Dmin}^{Dmax} \varphi(D) N_V\left(D, \frac{P}{P_0}\right) dD \qquad (3.9)$$

Where $N_{exp}(P/P_0)$ is the experimental isotherm, $N_V(D, P/P_0)$ is the theoretical isotherm in pores of size *D*, and $\varphi(D)$ is the pore size distribution.[13]

In order to perform this calculation, commercial software is provided by instrumental manufacturers with kernels for the particular adsorbate-adsorbent system at different temperatures.

It is important to note that the NLDFT method is only recommended if appropriate model isotherms are available for adsorbate, adsorbent, and pore geometry.[14]

The Kruk-Jaroniec-Sayari (KJS)[15] and improved Kruk-Jaroniec-Sayari (iKJS)[16] methods:

Kruk, Jaroniec, and Sayari (1997) introduced a method to calculate pore diameters for MCM-41 samples from adsorption and X-ray diffraction data. Combining these two techniques makes the KJS method more robust than the previously discussed methods for

MCM-41-type materials.[17] The calculation considers the pore volume (*Vp*) and the lattice spacing (*d*).

$$D_{SAXS} = cd\left(\frac{\rho V_p}{1+\rho V_p}\right)^{1/2} \quad (3.10)$$

Where $c = (8/(3^{1/2}\pi))^{1/2}$ and ρ is the density of the pore walls. It is assumed that the density of the adsorbate (nitrogen) inside the pore is the same as the density of the liquid adsorbate at 77.4 K. The density of amorphous silica (2.2 g/cm^3) was set as the density of the pore walls (ρ).

Using this method, Kruk *et al.* (1997)[10] found that the BJH method underestimated the pore size of MCM-41 molecular sieves by approx. 0.6 nm. They proposed then the following correction to the calculation of the BJH pore size distribution for MCM-41 materials in the range from 2 to 6.5 nm:

$$D_{KJS(P/P_0)} = \frac{4\gamma V_m cos\theta}{RTLn(P/P_0)} + 2t(P/P_0) + 0.6\,nm \quad (3.11)$$

Later, Jaroniec and Solovyov (2006)[16] proposed an improvement of Equation (3.11) by including the best-fit coefficients of X-Ray modeling of MCM-41 and extending to larger pore SBA-15 materials. The improved KJS method in Equation 3.12 can be used for pore sizes from 2 to 12 nm.

$$D_{iKJS} = -1.15\left[\log\left(0.875\frac{P}{P_0}\right)\right] + 0.2\left[\frac{60.65}{0.03-\log\left(\frac{P}{P_0}\right)}\right]^{0.397} + 0.27\,nm \quad (3.12)$$

Due to the particularities of the nanoporous materials synthesized for this work (pores diameters ~4 nm with an amphiphilic or hydrophobic surface), D_{SAXS} from Kruk-Jaroniec-Sayari has been selected as the most precise method for pore size determination. Nevertheless, the pore size calculated by the different models will be reported as means of comparison with previous research work.

3.6. Water adsorption

Similar to the nitrogen adsorption experiments described in the previous section, water vapor adsorption experiments were performed with ASAP 2020 Surface Area and Porosity Analyzer from micromeritics.

This technique was helpful to determine the silanol (-Si-OH) surface density[18] and for the characterization of the degree of hydrophobicity of the materials. Furthermore, it allowed the determination of water's density inside the nanopores (see section 4.1).[18–21]

Figure 3.6 shows an example of the water adsorption/desorption isotherms obtained

for amphiphilic nanoporous materials. According to its shape, it can be classified as a type IV isotherm (like the nitrogen adsorption), but a hysteresis loop H1 is observed in this case. The presence of this hysteresis loop is due to the different mechanisms taking place in the adsorption and desorption bands. In the adsorption, multilayer adsorption plays an important role, while for desorption, the pressure has to be low enough to overcome the meniscus formed by water inside the pores.[22]

By combining water adsorption and nitrogen adsorption experiments, Kocherbitov and Alfredson (2007) determined the density of hydroxyl groups on the surface of MCM-41 C16. Assuming that the monolayer formation corresponds to one molecule of water per hydroxyl group, the number of hydroxyl groups at the surface (in nm^{-2}) is given by the equation 3.13:

$$n_{OH} = \frac{hw * N_A * S}{M_w} x10^8 \tag{3.13}$$

where h_W is the mass of water adsorbed of water molecules that form the monolayer (from the BET equation, see section 3.4), N_a is the Avogadro number and S is the BET surface area of the material from nitrogen adsorption. They found a value of $n_{OH} = 1.6\ nm^{-2}$ for calcined MCM-41 C16.

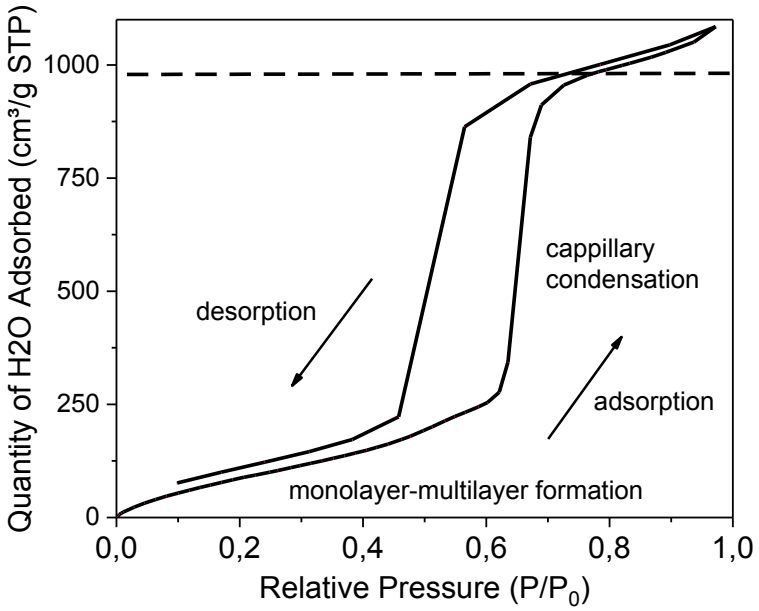

Figure 3.6: Example of H_2O adsorption/desorption isotherm for C18M15Me of a nanoporous material at 298.15 K.

For these experiments, the same equipment for nitrogen adsorption was used, an ASAP 2020 Surface Area and Porosity Analyzer from micromeritics. A temperature-controlled water vapor source accessory was used. For a typical water adsorption/desorption

experiment, 50 mg of the nanoporous material were degassed under vacuum for 24 h at 90 °C. Then the sample was weighed, and the water adsorption/desorption isotherms were taken; this last procedure typically took 1 day for hydrophilic or amphiphilic materials and 3 days for hydrophobic ones.

The experiment duration was observed to be exceptionally long for hydrophobic materials. Furthermore, the total quantity of water adsorbed per gram was significantly lower (> 10% m/m), and no capillary condensation occurred (see Chapter 7). This low and slow water adsorption defines a truly hydrophobic material and sets them apart from the amphiphilic ones.

3.7. Conclusion

A precise determination of the physical and chemical properties of the newly synthesized materials was necessary before the confinement studies. Therefore, in this chapter, we have presented the experimental techniques that allowed a comprehensive characterization of such materials.

The methods used to study their surface chemistry, specific pore volume and surface area, pore geometry, and pore size were discussed. The results of the characterization are presented in Chapter 5.

The determination of this last parameter received special attention due to the large variety of methods available. Here, we have presented the arguments behind our selection of the value of D_{SAXS} from the Kruk-Jaroniec-Sayari method.

We have included the study of the materials' surface by water vapor adsorption in this chapter because this method allowed determining the hydroxyl group density at the surface, and it was helpful to assess the materials' hydrophobicity. However, we will see in the next chapter how the same experiments were used to determine the density of confined water.

References

1. Stuart, B. H. *Infrared spectroscopy fundamentals and applications*. (J. Wiley & Sons, 2009).
2. Smith, B. C. *Fundamentals of Fourier transform infrared spectroscopy*. (CRC Press, 1996).
3. Doyle, W. M. Principles and applications of Fourier transform infrared (FTIR) process analysis. *Process control and quality* **2**, 50 (1992).
4. Perkin Elmer, Inc. Technical Note. FT-IR Spectroscopy Attenuated Total Reflectance (ATR). (2006).
5. Williams, D. B. & Carter, C. B. *Transmission electron microscopy: a textbook for materials science*. (Springer, 2009).
6. Zienkiewicz-Strzałka, M., Skibińska, M. & Pikus, S. Small-angle X-ray scattering (SAXS) studies of the structure of mesoporous silicas. *Nuclear Instruments and Methods in Physics Research Section B: Beam Interactions with Materials and Atoms* (2017) doi:10.1016/j.nimb.2017.03.028.
7. Sing, K. S. W. Reporting physisorption data for gas/solid systems with special reference to the determination of surface area and porosity (Recommendations 1984). *Pure and Applied Chemistry* **57**, 603–619 (1985).
8. Brunauer, S., Emmett, P. H. & Teller, E. Adsorption of Gases in Multimolecular Layers. *Journal of the American Chemical Society* **60**, 309–319 (1938).
9. Peter Klobes, Klaus Meyer and Ronald G. Munro. *Porosity and Specific Surface Area Measurements for Solid Materials*. (NIST (National Institute of Standards and Technology), 2006).
10. Kruk, M., Jaroniec, M. & Sayari, A. Application of Large Pore MCM-41 Molecular Sieves To Improve Pore Size Analysis Using Nitrogen Adsorption Measurements. *Langmuir* **13**, 6267–6273 (1997).
11. Barrett, E. P., Joyner, L. G. & Halenda, P. P. The determination of pore volume and area distributions in porous substances. I. Computations from nitrogen isotherms. *Journal of the American Chemical society* **73**, 373–380 (1951).
12. Ravikovitch, P. I., Wei, D., Chueh, W. T., Haller, G. L. & Neimark, A. V. Evaluation of Pore Structure Parameters of MCM-41 Catalyst Supports and Catalysts by Means of Nitrogen and Argon Adsorption. *J. Phys. Chem. B* **101**, 3671–3679 (1997).

13. Neimark, A. V., Ravikovitch, P. I., Grün, M., Schüth, F. & Unger, K. K. Pore Size Analysis of MCM-41 Type Adsorbents by Means of Nitrogen and Argon Adsorption. *Journal of Colloid and Interface Science* **207**, 159–169 (1998).

14. Weidenthaler, C. Pitfalls in the characterization of nanoporous and nanosized materials. *Nanoscale* **3**, 792 (2011).

15. Kruk, M., Jaroniec, M. & Sayari, A. Adsorption Study of Surface and Structural Properties of MCM-41 Materials of Different Pore Sizes. *The Journal of Physical Chemistry B* **101**, 583–589 (1997).

16. Jaroniec, M. & Solovyov, L. A. Improvement of the Kruk−Jaroniec−Sayari Method for Pore Size Analysis of Ordered Silicas with Cylindrical Mesopores. *Langmuir* **22**, 6757–6760 (2006).

17. Schoeffel, M., Brodie–Linder, N., Audonnet, F. & Alba–Simionesco, C. Wall thickness determination of hydrophobically functionalized MCM-41 materials. *J. Mater. Chem.* **22**, 557–567 (2012).

18. Kocherbitov, V. & Alfredsson, V. Hydration of MCM-41 Studied by Sorption Calorimetry. *J. Phys. Chem. C* **111**, 12906–12913 (2007).

19. Kocherbitov, V. Properties of Water Confined in an Amphiphilic Nanopore. *J. Phys. Chem. C* **112**, 16893–16897 (2008).

20. Rother, G. *et al.* Water Uptake by Silica Nanopores: Impacts of Surface Hydrophilicity and Pore Size. *J. Phys. Chem. C* **124**, 15188–15194 (2020).

21. Takei, T. *et al.* Changes in density and surface tension of water in silica pores. *Colloid & Polymer Science* **278**, 475–480 (2000).

22. Sing, K. S. W. & Williams, R. T. Physisorption Hysteresis Loops and the Characterization of Nanoporous Materials. *Adsorption Science & Technology* **22**, 773–782 (2004).

CHAPTER 4

TECHNIQUES FOR THE STUDY OF CONFINED WATER

This chapter presents the different experimental techniques used to describe the thermodynamic state of confined water. Properties such as the freezing and melting temperatures and enthalpies, intrusion pressure in hydrophobic nanopores, the crystalline structure of confined ice at different pressures, and dynamics of confined water were studied employing differential scanning calorimetry, and neutron techniques such as neutron scattering, neutron spin-echo, and neutron imaging.

4.1. Density of confined water

Water adsorption experiments, described in section 3.6, allowed the determination of the average density of water in the nanopores.

For this purpose, the adsorption curves are transformed into a density vs. P/P_0 using the molar mass of water and the material's pore volume, provided by the nitrogen adsorption isotherms. Then, we define a molecular density in number of molecules per nm^3 regardless of its isotopic character (D_2O or H_2O) (Figure 4.1). This was useful for the different experiments performed involving heavy or light water (D_2O was mainly used for neutron diffraction experiments, where we filled the materials with ~80 % of the capacity of the materials to avoid external water. When changing from light to heavy water, one should also consider the isotope effect on the transition temperatures and dynamic properties of water[1]).

The density of water confined in the nanopores can then be compared to that of bulk water, namely 33,4 molecules/nm^3 at 1 bar and 298.15 K. However, given that the water distribution is likely to be non-uniform within the pore, ρ_{pore} must be taken to be an effective density that only partially defines the thermodynamic state of the liquid in the pore. The results of the density of water confined in amphiphilic materials are discussed in Chapter 6.

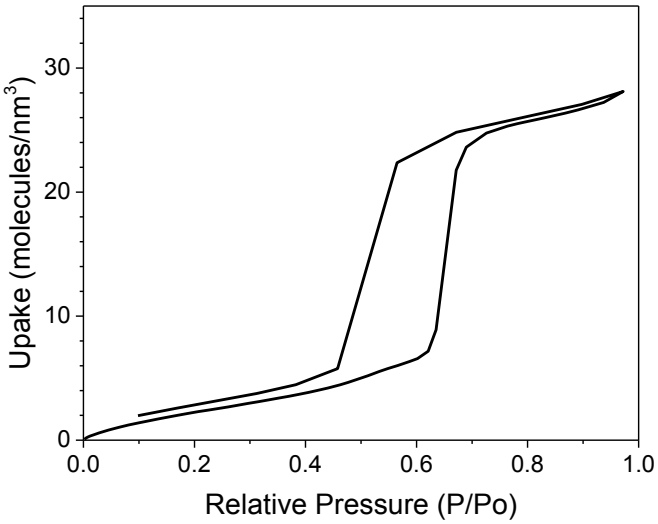

Figure 4.1: Density of water confined in C18M15Me at 298.15 K. The saturation pressure of water is P_0 = 0.0313 bar.

4.2. Differential Scanning Calorimetry (DSC)

DSC is a thermal analysis that measures heat flow associated with material transitions as a function of time and temperature in a controlled atmosphere. In our case, DSC has been used to determine the temperature of the melting/freezing phase transitions of confined and excess bulk water, the fraction of confined water that crystallizes inside the pore, and by subtraction, the thickness of the liquid layer of water at the vicinity of the pore wall.

DSC measures the temperature difference between the sample and a reference. This quantity is transformed in heat flow using Ohm's law.

$$dQ/dt = \Delta T/R \tag{4.1}$$

where dQ/dt is the heat flow in mW, ΔT is the temperature difference between the sample and the reference in ºC, and R is the thermal resistance in ºC/mW.

For this work, two DSC Q-100 from TA instruments were used. One of them is equipped with a compressor, able to go down to -80 ºC, and the second one is equipped with a liquid nitrogen cooling system (LNCS), able to achieve temperatures as low as -130 ºC. In a typical DSC experiment, a mixture of approx. 10 mg of the nanoporous material and the corresponding pore volume of ultrapure liquid water placed in an aluminum hermetic capsule and weighted in a precision balance. The sample was left for 15 minutes at 20 ºC inside the DSC chamber before starting the measurement. After this time, several temperature cycles were performed at scan rates between 0.5 K/min and 10 K/min.

The typically obtained curve is illustrated in Figure 4.2. Usually, two exothermic peaks (freezing) and two endothermic peaks (melting) are observed, corresponding to the external excess water and the confined water.

The melting temperature was reproducible at the selected scan rates. In contrast, freezing, being a process dominated by nucleation and growth kinetics, its temperature varied depending on the scan rate used. Two relevant temperatures related to the melting process are shown in the figure: The onset of the melting temperature peak and its maximum. Our reported melting temperature corresponds to the maximum, as this is more representative of the overall melting process inside the nanopores.

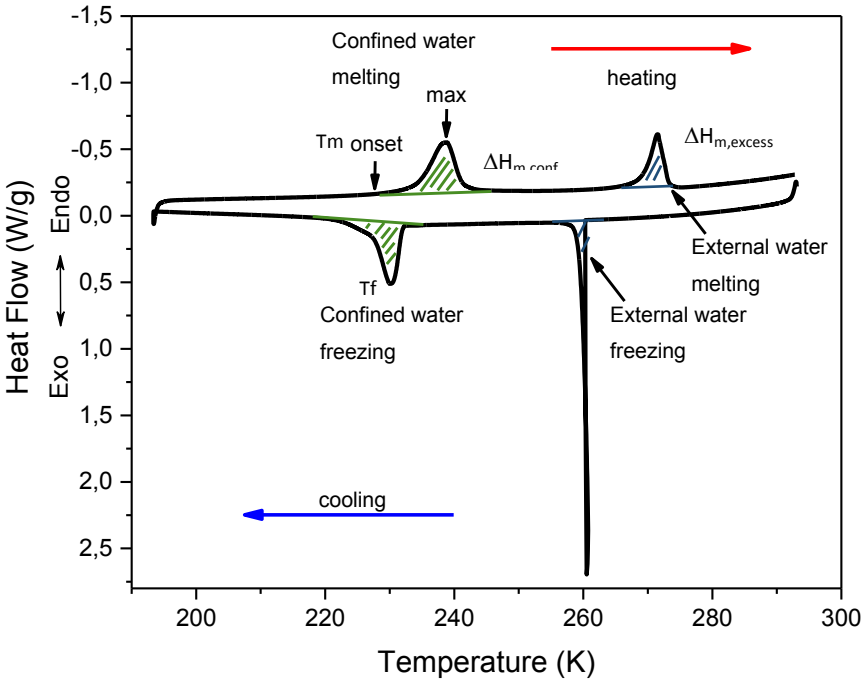

Figure 4.2: Example of a DSC measurement: H_2O confined in C18M15Me at 2 K/min.

The percentage of water that crystallizes inside the pores was determined as follows. First, the amount of excess water was calculated from the external melting enthalpy ($\Delta H_{m,\,excess}$), using the molar enthalpy of hexagonal ice ($\Delta H_{m,\,Ih}$):

$$mass_{H2O,excess}\,(mg) = \frac{\Delta H_{m,excess}}{\Delta H_{m,Ih}} \tag{4.2}$$

Then, by difference to the total amount of water weighted, we obtained the total amount of water inside the pores at melting:

$$mass_{H2O,confined\ total}\,(mg) = mass_{H2O,total}\,(mg) - mass_{H2O,excess}\,(mg) \tag{4.3}$$

Due to the presence of a liquid-like layer adjacent to the pore surface, not all of the confined water will crystallize (and melt). The amount of water that crystallizes was calculated from the melting enthalpy of confined water ($\Delta H_{m,\,conf}$) and the molar melting enthalpy of cubic ice ($\Delta H_{m,\,Ic}$).

$$mass_{H2O,confined\ cryst}\,(mg) = \frac{\Delta H_{m,conf}}{\Delta H_{m,Ic}} \tag{4.4}$$

Then, the percentage of crystalized water is:

$$\%H_2O_{confined\ cryst} = \frac{mass_{H2O,confined\ cryst}}{mass_{H2O,confined\ total}} * 100\% \quad (4.5)$$

More precise measurements were achieved when we avoided external water ($mass_{H2O,excess} = 0$). Our strategy to avoid excess water was to use only 80 to 90% of the corresponding pore volume from nitrogen adsorption. The reason for this is that water expands upon cooling, which means that if the pore volume is 100% filled with liquid water at room temperature, some water will be expulsed out of the nanopores. Another important experimental hack was to mix the sample carefully with a spatula before the measurement. In such cases, the external water signals are not observed. Regardless of the presence of external water, the melting temperature of confined water remained the same.

To further improve the precision of the measurement, a thermogravimetric analysis (TGA) was performed after DSC measurements. In this case, a TGA measurement up to 200 °C was helpful to obtain the total amount of water adsorbed (see section 3.2).

4.3. Neutron Diffraction (ND)

Neutron scattering measurements provide information on the structure and dynamics of a sample at the atomic level. The neutron-matter interaction has a unique property: unlike X-Rays, which interact with the electronic cloud of the atoms in the sample, neutrons interact with the nuclei of the atoms. In this section, we will discuss only a few relevant aspects of neutron scattering, and more precisely, neutron diffraction, used here to determine the crystalline structure of ice confined in the nanopores.

Since neutrons interact with nuclei rather than with the electrons of an atom, this interaction is dependent on the isotope. This interaction can be described in terms of the coherent and incoherent scatterings. For example, deuterium (^{2}H) has a higher *coherent* scattering cross-section compared to that of ^{1}H (5.592 barn and 1.7583 barn, respectively) and a much lower *incoherent* scattering cross-section (2.05 barn vs. 80.27 barn, respectively). As the incoherent scattering does not contain any structural information and increases the multiple scattering and attenuation effects, it is then preferable to use D_2O instead of H_2O to study the structure of water.[2]

The analysis of the scattered intensity of the neutron beam as a function of the scattering angle (θ) gives access to the local structure of the sample. This scattering can be expressed as a function of the modulus of the scattering wave vector (Q):

$$Q = \left(\frac{4\pi}{\lambda}\right) sin\theta \quad (4.6)$$

where λ is the wavelength of the neutrons.

The coherent differential scattering cross section of a liquid is given in the static approximation by:

$$\left(\frac{d\sigma}{d\Omega}\right)_{coh} = \sum_{ij} b_i\, b_j \exp(iQ.r_{ij}) \tag{4.7}$$

where *bi* and *bj* are the coherent scattering lengths of atoms *i,j*.

The structure factor of N molecules is then given by:

$$S_M(Q) = \frac{1}{(\sum_i b_i)^2}\left(\frac{d\sigma}{d\Omega}\right)_{coh} \tag{4.8}$$

For a molecular liquid the structure factor is usually split into an intramolecular form factor $f_1(Q)$ and an intermolecular contribution $D_M(Q)$, $S_M(Q) = f_1(Q) + D_M(Q)$. The form factor may be calculated for a known molecular geometry which allows relating the structure factor to the intermolecular pair correlation function $g_L(r)$:

$$S_M(Q) = f_1(Q) + \frac{4\pi}{Q}\rho_M \int (g_L(r) - 1) r sin(Q_r) dr \tag{4.9}$$

where ρ_M is the molecular density of the liquid, and $f_1(Q)$ *is*:

$$f_1(Q) = \frac{1}{(\sum_i b_i)^2}\sum_{ij} b_i\, b_j \left(\frac{\sin(Qr_{ij})}{Qr_{ij}}\right)\exp(-\gamma_{ij}Q^2) \tag{4.10}$$

where r_{ij} is the distance between atoms *i* and *j* of the same molecule and $\gamma_{i\,j}$ is a Debye-Waller factor proportional to the square of the mean square displacement of atoms *i* and *j* in the direction r_{ij} . At large Q-values, $D_M(Q)$ goes to zero and the main contribution to the structure factor comes from *fi(Q)*. We have adopted an empirical method for the correction of inelastic effects due to the difference between the energy-integrated intensity at constant angle (equation (4.11)) and the static scattering function *S,(Q)*: the so-called Placzek corrections were evaluated with a polynomial function , $P(Q)=A+BQ^2+CQ^4+DQ^6$, where *A, B, C, D* are adjustable parameters[3,4].

Two different neutron diffraction instruments were used for the experiments at atmospheric pressure and under high pressures.

Diffractometer 7C.2 (@LLB, Saclay, France)

The spectrometer 7C2 is a two-axis diffractometer located on the hot source of the reactor Orphée. Using different monochromators, the wavelength could be set to approx. 0.58 Å, 0.7 Å, or 1.11 Å. The scattering vector (Q) range will depend on the selected wavelength. We have selected to work at 1.11 Å in order to obtain a better resolution from

1.0 $Å^{-1}$ to 5.0 $Å^{-1}$. The Q-range in these experiments was from 0.3 $Å^{-1}$ to 10 $Å^{-1}$, which allowed us to study both the structure and the form factor of confined water during the crystallization process.

Two different sample preparation protocols were tested. First, around 300 mg of the nanoporous material ware introduced in a vanadium cell (diameter = 6 mm), and the spectrum of the empty matrix was taken. Then, the amount of D_2O corresponding to a complete filling of the pores was added directly to the cell. The obtained diffraction curves clearly show diffraction peaks at 1.6 $Å^{-1}$, 1.7$Å^{-1}$ and 1.9 $Å^{-1}$ from hexagonal ice at 260 K, corresponding to external water (Figure 4.3).

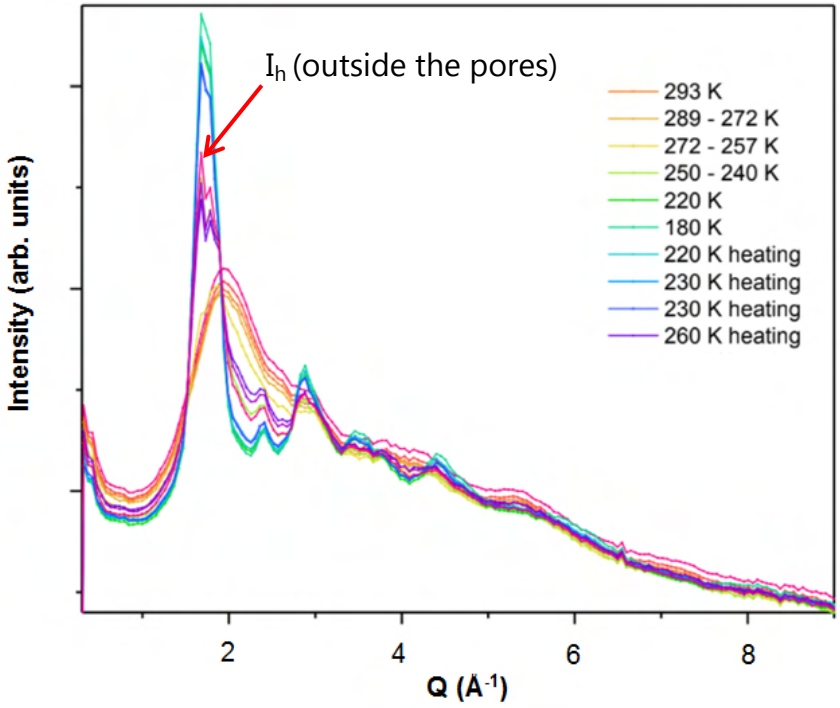

Figure 4.3: Raw diffraction spectra of a mixture of D_2O and C18-M15-Me. The diffraction peaks at 1.6 $Å^{-1}$, 1.7$Å^{-1}$, and 1.9 $Å^{-1}$ indicate the presence of hexagonal ice outside the pores.

Therefore, a different procedure was carried out to avoid external water. This time, we chose a filling factor smaller than 100% to avoid having external water due to the decrease in the density upon cooling. The powder was carefully transferred to a 10 ml glass sample bottle, where it was mixed with the amount of D_2O corresponding to a filling factor between 80% and 90%, hermetically closed, and left to settle for one hour. This procedure allowed to obtain clean spectra of D_2O confined in amphiphilic materials.

The data treatment, illustrated in figure 4.4, consisted of the empty matrix subtraction (cell with dry nanoporous material), a Cadmium correction to account for sample attenuation effects, and an inelastic correction using the value of I (Q→∞) as described in

the literature.[5]

The corrected intensity $I'(Q)$ was calculated using the equation:

$$I'(Q) = \frac{I(Q)-(1-b)I_{EM}(Q)-bI_{Cd}(Q)}{I(Q\to\infty)} \quad (4.11)$$

where $I_{EM}(Q)$ is the diffraction intensity of the empty matrix (dry nanoporous material), $I_{Cd}(Q)$ is the diffraction intensity of a Cadmium cylinder of ø = 6mm, b is an attenuation coefficient in the range of (0.02 to 0.10) and $I(Q \to \infty)$ is the value of the diffraction intensity at high Q (10 $Å^{-1}$).

It is important to note that such corrections do not consider the crossed terms between the material and confined water. For this reason, the corrected neutron scattering curves are not meant to be used to obtain a pair correlation function of pure water but to compare the different changes in the structure of liquid water and ice confined in nanopores of different surface chemistry.

Once the main phases on confined ice were identified, the corrected spectra were fitted, using the software FullProf to perform a Rietveld refinement to determine the crystalline structure of the confined ice.

The main disadvantage of this instrument for our experiments was the relatively low resolution, which made it challenging to identify complex combinations of crystalline ice structures. For this reason, a more resolved instrument was required for confinement studies at high pressures.

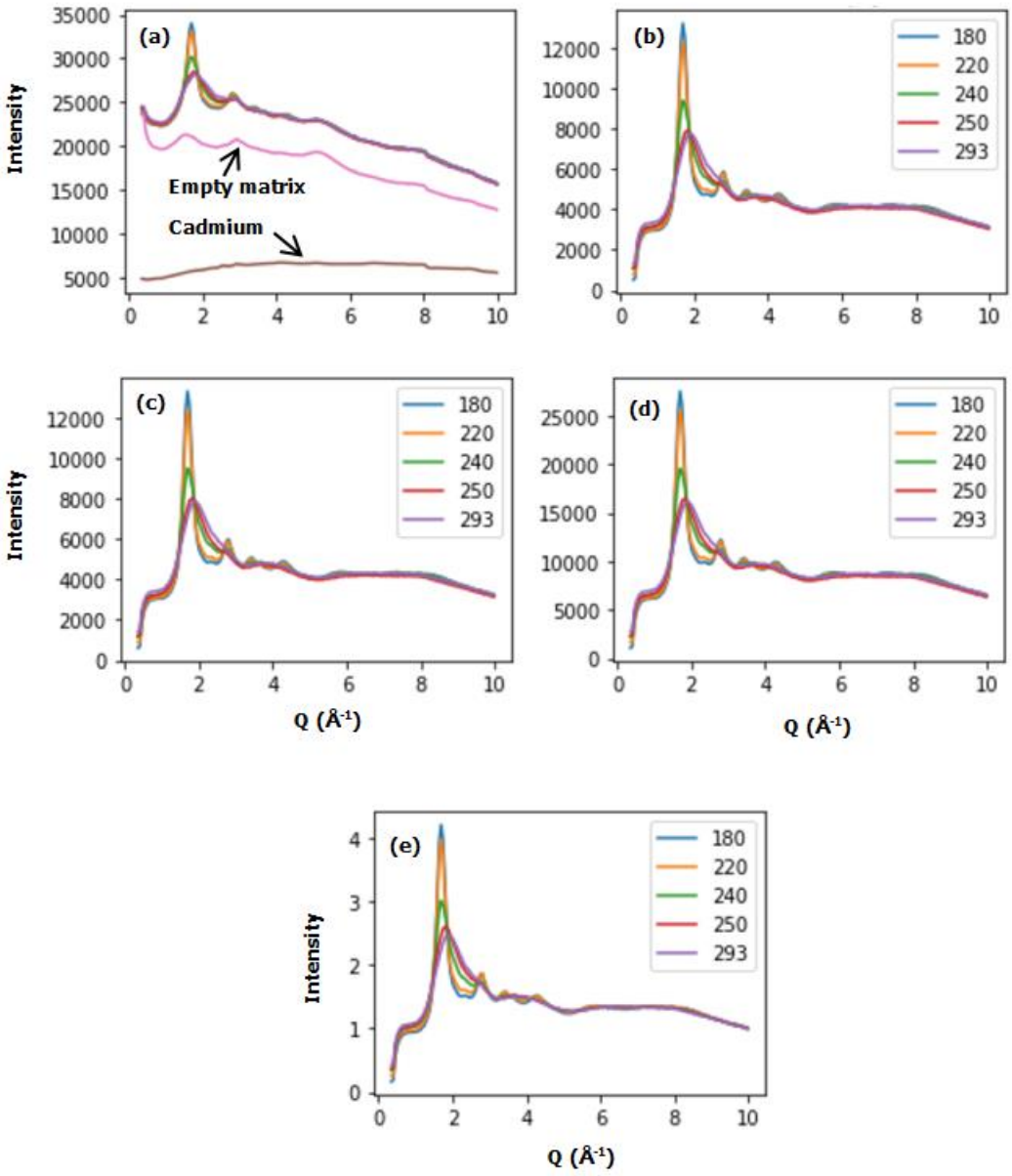

Figure 4.4: Corrections applied to the neutron diffraction curves of D_2O@C18M15Me (*f ~0.8*) at atmospheric pressure and different temperatures (7C2@LLB). (a) Raw data, (b) subtraction empty matrix in a vanadium cell, (c) Cadmium subtraction, (d) Normalization mass D_2O and (e) Normalization I(Q→∞).

The wavelength and detector zero-angle were obtained from standard calibration measurements using a nickel powder. At atmospheric pressure, a thin walled cylindrical vanadium cell with an inner diameter of 6.0 mm was used for these samples.

Diffractometer G4.4 (@LLB, Saclay, France)

G44 is a cold neutron, high-resolution powder two-axis diffractometer. Using a monochromator, the wavelength can be set as 1.800 Å, 1.960 Å, 2.401 Å, or 2.8935 Å. We have selected to work with λ = 2.8935 Å, in order to have access to lower Q values and

better isolation of the peaks of the different phases of ice, starting at 1.0 $Å^{-1}$. The Q-range obtained in these experiments was from 0. to 4 $Å^{-1}$. The instrument's high resolution allowed us to discriminate between the different phases of ice formed under confinement at high pressures.

For high-pressure experiments, we have used a cell made of steel with an external diameter of 6 mm and a height of 80 mm, connected by a 3.2 mm capillary to an external liquid compressor charged with D_2O. Inside this cell, we located a capsule made of aluminum with an internal diameter of 4.4 mm and two holes that allow the transit of water. The material (powder) was introduced in the capsule to prevent that the material passed to the capillary and cause damages to the high-pressure equipment.

Due to the temperature and pressure evolution of the diffraction coming from the pressure cell, the complete subtraction of the background was not possible. The data analysis was focused on the indexation of the Bragg peaks, like it is shown in figure 4.5, comparing our results with simulations of the neutron diffraction curves of the different phases of ice.

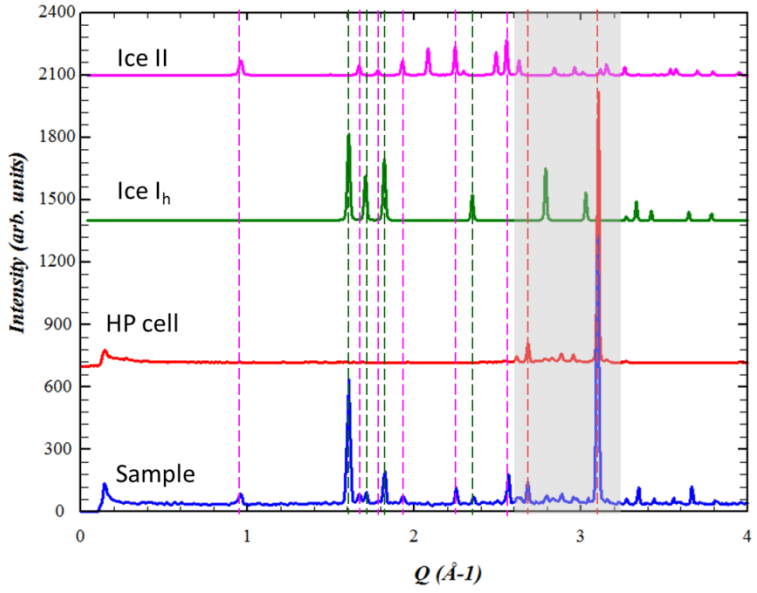

Figure 4.5: Peak indexation of the neutron diffraction curves of confined ice at high pressure and low temperature (G4.4@Orphée). The grey rectangle highlights the area of the high-pressure cell peaks. The dashed lines show the peaks corresponding to ice II (pink), ice I_h (green), and the high-pressure cell (red). The curves have been Y-shifted for clarity. The neutron diffraction curves of Ice II and Ice I_h shown here are simulations from crystallographic data.

4.4. Neutron (Resonance) Spin Echo (NSE, NRSE)

Neutron scattering can also be used to study the dynamic properties of a system when energy is exchanged upon the scattering process. When inelastic neutron scattering (INS) or quasi-elastic neutron scattering (QENS) occurs, the exchanged energy analysis can be used to study relaxation processes, rotational, vibrational, or diffusive processes taking place in the sample.

In traditional INS and QENS techniques, both the incident and scattered wavevectors have to be defined. To enhance the resolution of the measurement, the wavelength distribution of the neutron beam, $\Delta\lambda$, has to be reduced by using a monochromator, causing a decrease in the intensity of the signal.

Neutron spin echo is a powerful QENS technique used in this work to study the dynamics of water confined in nanoporous materials and water in soft-confinement using water-glycerol mixtures. The particularity of this technique is that it overcomes the inverse relationship between intensity and resolution present in traditional inelastic or quasi-elastic neutron scattering techniques.

Neutron spin echo uses the neutron spin polarization property to directly measure the difference in energy between the incident and the scattered wavevectors. This difference is independent of the wavelength used, which means that NSE can use a wide distribution of wavelength, keeping its resolution and boosting the signal intensity.[7]

Diffractometer MUSES (@LLB)

This instrument combines conventional and resonance neutron spin echo. The conventional NSE spectrometer is used for measurements at short Fourier times ($\tau < 200$ ps), and the NRSE option gives access to measurements at longer times (200 ps $< \tau <$ 2000 ps).

The principle: In conventional NSE, the polarized neutron beam will enter the first coil (see Figure 4.6), and a counterclockwise Larmor precession takes place. Then, the neutrons will interact with the sample, gaining or losing a certain amount of energy. In MUSES, a π-flipper will reverse the precessing angle of neutrons, and they will enter the second coil, where the opposite Larmor precession of neutrons will occur. If the neutron's velocity has changed due to its interaction with the sample, its spin will not return to the initial orientation. The polarization is then a measure of the change in the neutron's energy. In NRSE mode, the two precession coils are replaced by four radiofrequency coils. The typical neutron spin-echo experiment consisted of measuring the polarization at Fourier times

from t=0 ps to 2000 ps. These values were then normalized by the signal at t=0 and divided by the normalized resolution. As shown in Figure 4.7, a decay curve was obtained for the different temperatures (200 to 280 K).

A time-temperature superposition curve (Figure 4.8) was then built and fitted with a stretched exponential function (also known as Kohlrausch–Williams–Watts function, equation 4.8) to obtain a more precise value of the stretching parameter β_{KWW}.

$$f(t) = A * \exp(-(t/\tau)\hat{}\beta_{KWW}) + y_0 \quad (4.8)$$

The characteristic time τ was then obtained for each temperature. Several wavevectors going from 1 $Å^{-1}$ to 1.9 $Å^{-1}$ were studied around the maximum peak of the structure factor for chosen samples.

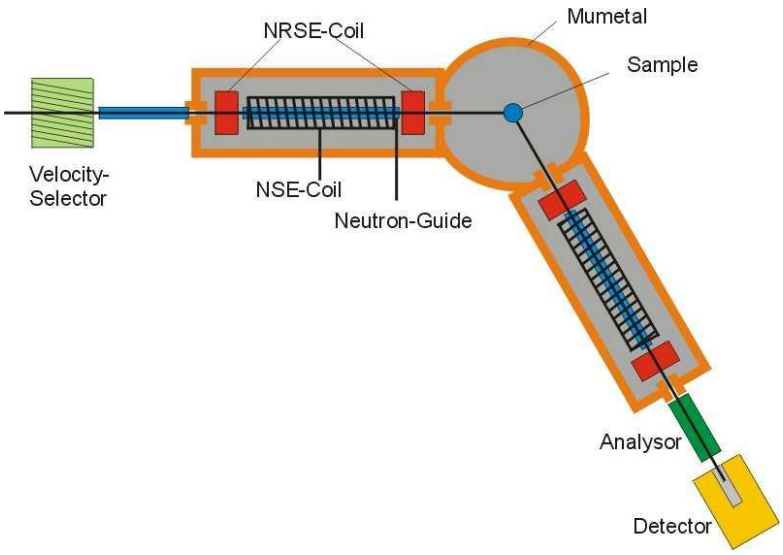

Figure 4.6: General set-up of the spin-echo spectrometer MUSES. Figure taken from the LLB website.

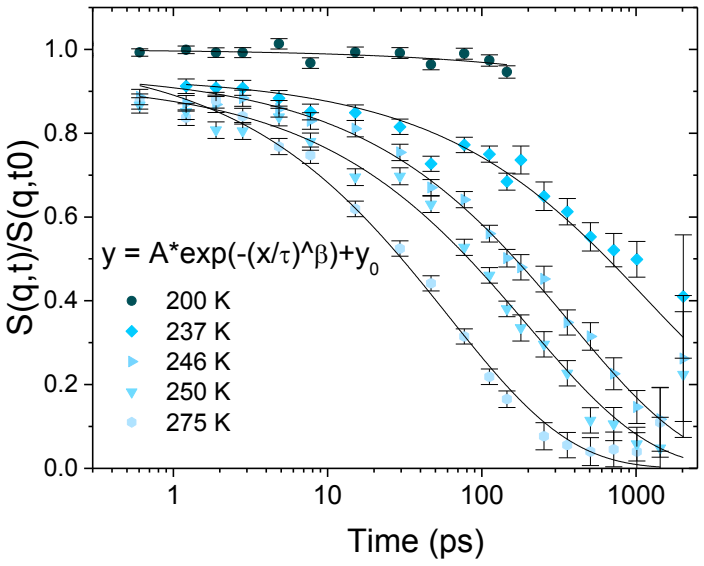

Figure 4.7: Example of neutron spin-echo decay curves for the same sample (a water-glycerol mixture of molar fraction Xgly = 0.4) at different temperatures. At Q = 1.7 $Å^{-1}$.

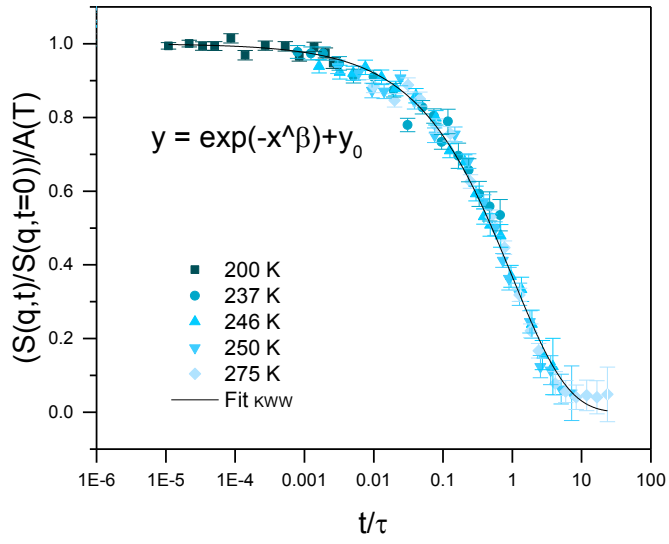

Figure 4.8: Example of a time-temperature superposition curve. Same data as for figure 4.7.

Note that the data presented above are part of a submitted manuscript on the interplay of vitrification and ice formation in a cryoprotectant aqueous solution at low temperature. This topic is not developed here but similar experiments were performed with water in the amphiphilic materials, presented in chapter 6.

4.5. Neutron Imaging (NI)

Different mechanisms for pore-filling with water were studied in this thesis using neutron imaging. Thanks to its high sensitivity to hydrogen, neutron imaging is the appropriate technique to assess in a macroscopic manner the imbibition in hydrophilic/amphiphilic nanoporous materials and the intrusion in hydrophobic ones by measuring the amount of water present in the sample as a function of external parameters such as pressure and time.

Beamline IMAGINE (@LLB)

Located in a cold neutron guide, IMAGINE allows performing neutron radiography and tomography. The neutron flux was $2x10^7$ neutrons/s/$cm^{2,}$ and the detector used was a CDD camera coupled with a scintillator.

The sample environment consisted of the same high-pressure cell used for G4.4 experiments, connected through a 3.2 mm capillary to a liquid compressor, located outside the restricted area in order to be able to monitor and continuously modify the pressure from 1 to 4000 bar at room temperature (298.15 K). A series of images were recorded for each sample with 60 s acquisition time and around 20 s of processing time between images. The data was then treated with ImageJ and homemade macros. The treatment consists of a normalization using an empty beam image, subtraction of the flat field, filtering, and systematic selection of the same interest area for each image of the same sample. Examples of the treated images are shown in Figure 4.9.

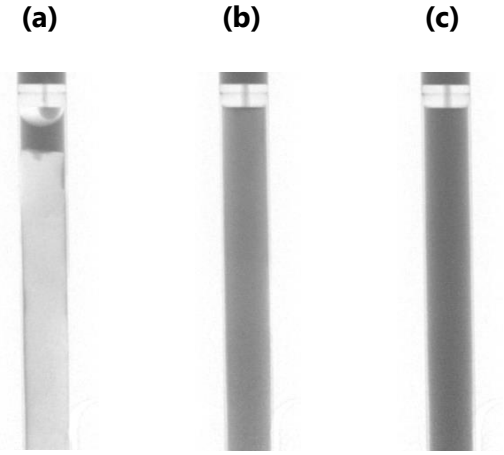

Figure 4.9: Example images from IMAGINE after subtraction of the empty high pressure (HP) cell. (a) A hydrophobic powder, in white, surrounded by water within the HP cell and around the capsule containing the powder, in black. (b) The powder and water are mixed. A sudden decrease of intensity from (b) to (c) is a sign of water intrusion into the nanopores.

As water absorbs neutrons better than the silica material, the intensity decreases when the amount of water inside the capsule increases. The total intensity of each image is plotted against the pressure of water (Figure 4.10). A sudden step around 450 bar indicates the intrusion of water into the nanopores.

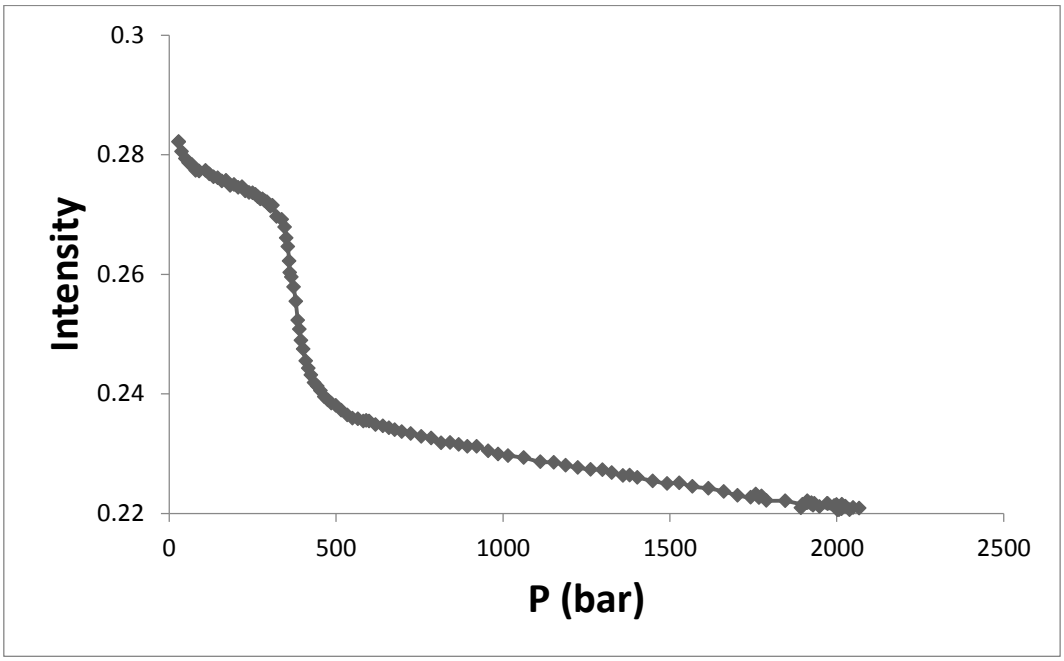

Figure 4.10: Total neutron intensity versus pressure of water.

For a stack of images, the total intensity in the selected area is related to the amount of water present using an established calibration curve from the instrument. The relationship between the transmittance and the water depth in the image is the following:

$$T = (1 - 0.13)e^{(-x/1.85)} + 0.13 \tag{4.9}$$

where T is the normalized transmittance in the zone of interest, and *x* is the depth of water in millimeters. Using this information and the geometry of the cylindrical cell, we calculated the volume of water. Then we transformed the volume to mass of water, using the density of water at the temperature of calibration (equation 4.9). We obtained a plot of the water mass vs. pressure (Figure 4.11) that allowed us to identify the characteristic times and pressures for pore filling.

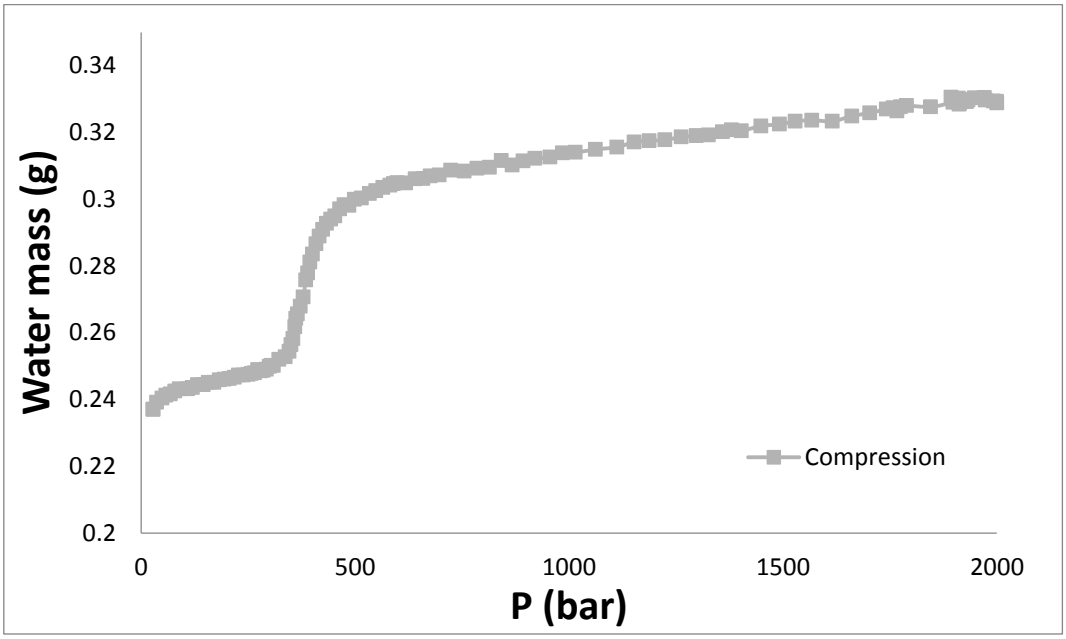

Figure 4.11: Volume of water from neutron imagery versus pressure.

4.6. Conclusion

The different techniques used in this thesis for studying confined water, its mechanisms to enter the nanopores, its phase transitions, its structure, and dynamics have been presented in this chapter. The use of water adsorption and neutron imaging allowed us to follow the filling of the nanopores with water via vapor adsorption, imbibition, and intrusion. Differential scanning calorimetry was used to determine the freezing and melting of confined water at atmospheric pressure, while neutron diffraction served to determine the structure of liquid water and ice at pressures going from 1 to 4000 bar. Additionally, neutron spin-echo was used to study the dynamics of selected samples of water confined in amphiphilic nanopores.

References

1. Gainaru, C. *et al.* Anomalously large isotope effect in the glass transition of water. *Proc Natl Acad Sci USA* **111**, 17402–17407 (2014).
2. Amann-Winkel, K. *et al.* X-ray and Neutron Scattering of Water. *Chem. Rev.* **116**, 7570–7589 (2016).
3. Bellissent-Funel, M.-C., Bosio, L. & Teixeira, J. The inelasticity correction for liquid water in neutron scattering. *J. Phys.: Condens. Matter* **3**, 4065–4074 (1991).
4. Placzek, G. The Scattering of Neutrons by Systems of Heavy Nuclei. *Phys. Rev.* **86**, 377–388 (1952).
5. Eibl, S. The highly fragile glass former Decalin. (2009).
6. Rietveld, H. M. A profile refinement method for nuclear and magnetic structures. *J Appl Crystallogr* **2**, 65–71 (1969).
7. Mezei, F. The principles of neutron spin echo. in *Neutron Spin Echo* (ed. Mezei, F.) vol. 128 1–26 (Springer Berlin Heidelberg, 1980).

CHAPTER 5

PHYSICAL PROPERTIES OF THE NANOPOROUS ORGANOSILICA MATERIALS

An accurate description of the structure and surface chemistry of the nanopores is essential for confinement studies. Keeping in mind that the objective of this thesis is to study the effect of the surface chemistry on the properties of confined water, it was necessary to determine the density of organic and silanol groups at the surface, but also to ensure that the synthesized confining materials were uniform in pore geometry with a well-defined pore size and resistant to hydrolysis upon contact with water.

This chapter's objective is to provide validation of the co-condensation and postgrafting syntheses described in Chapter 2 and to present a comprehensive characterization of the amphiphilic and hydrophobic materials (listed in table 5.1) that were later used for our studies in water confinement. The discussions here focus mainly on the materials C18-M7-Me, C12-M7-Me, C18-M15-Me, and C18-M7-Ph, whose properties are compared to their hydrophilic equivalent, MCM-41 C18 and C12. Additional materials, as C18-M10-Me and C18-M7-Et, were synthesized and characterized by another chemist, following the same procedures as the rest of the materials.

Table 5.1: List of synthesized nanoporous (organo)silica materials.

Material	Template	Precursor mixture (mol%)	Post-grafting modification
MCM-41 C18	C_{18}TAB	100 % TEOS	-
C18-M7-Me		7 % MTES – 93 % TEOS	-
C18-M10-Me*		10 % MTES – 90 % TEOS	-
C18-M15-Me		15 % MTES – 85 % TEOS	-
C18-M7-Et*		7 % ETES – 93 % TEOS	-
C18-M7-Ph		7 % PTES – 93 % TEOS	-
MCM-41 C12	C_{12}TAB	100 % TEOS	-
C12-M7-Me		7 % MTES – 93 % TEOS	-
C18-M7-Me $SiMe_3$	C_{18}TAB	7 % MTES – 93 % TEOS	-Si-$(CH_3)_3$
C18-M15-Me $SiMe_3$		15 % MTES – 85 % TEOS	-Si-$(CH_3)_3$

*synthesized by Aurelie Doira. TEOS = tetraethoxysilane, MTES = methyltriethoxysilane, ETES = ethyltriethoxysilane, PTES = phenyltriethoxysilane.

5.1. Physical and chemical properties of amphiphilic materials

The first step after the synthesis of amphiphilic materials, was to verify the template removal and incorporation of the organic groups in the mesoporous silica using FTIR (Figure 5.1).

Typical absorption bands at 1060, 796, and 445 cm^{-1} associated with Si-O stretching and bending modes of condensed silica were found in all the materials, and a band at 953 cm^{-1} associated with the Si-OH groups at the surface[1].

In the spectra of C18-M7-Me and C18-M15-Me, we find an absorption band at 1276 cm^{-1}. This band is attributed to the C-H bending of the carbon bonded to a Si atom, indicating the incorporation of the methyl group in the framework. This was ratified by elemental analysis, where we quantified the percentage of carbon, which showed an efficient incorporation (> 80%) of the organosilane in the material's framework (*i.e.*, more than 80% of the organosilane present in the precursors' mixture was incorporated to the material).

The intensity of this band increases when the fraction of MTES used is increased. The incorporation of the phenyl group in sample C18-M7-Ph was identified by the peaks at 695 – 740 cm^{-1} from the aromatic C-H bend.

The absorption bands at 2921, 2852, and 1480 cm^{-1}, from C-H, stretching and bending of the alkyl chain of C_{18}TAB, are only present in the as-synthesized material, indicating that the washing method has been efficient to remove the template.

Table 5.2: Physical properties of selected nanoporous materials determined by nitrogen adsorption.

Sample	**S_{BET}, N_2 (m^2/g)**	**q_{ads}, N_2 gas† (cm^3/g)**	**V_{pore} (cm^3/g)**	**D_{BET} (nm)**	**C**
MCM-41 C18	1007	461	0.712	2.8	89
C18-M7-Me	1130	581	0.899	3.2	76
C18-M15-Me	1284	635	0.982	3.1	78
C18-M7-Ph	989	406	0.628	2.5	44

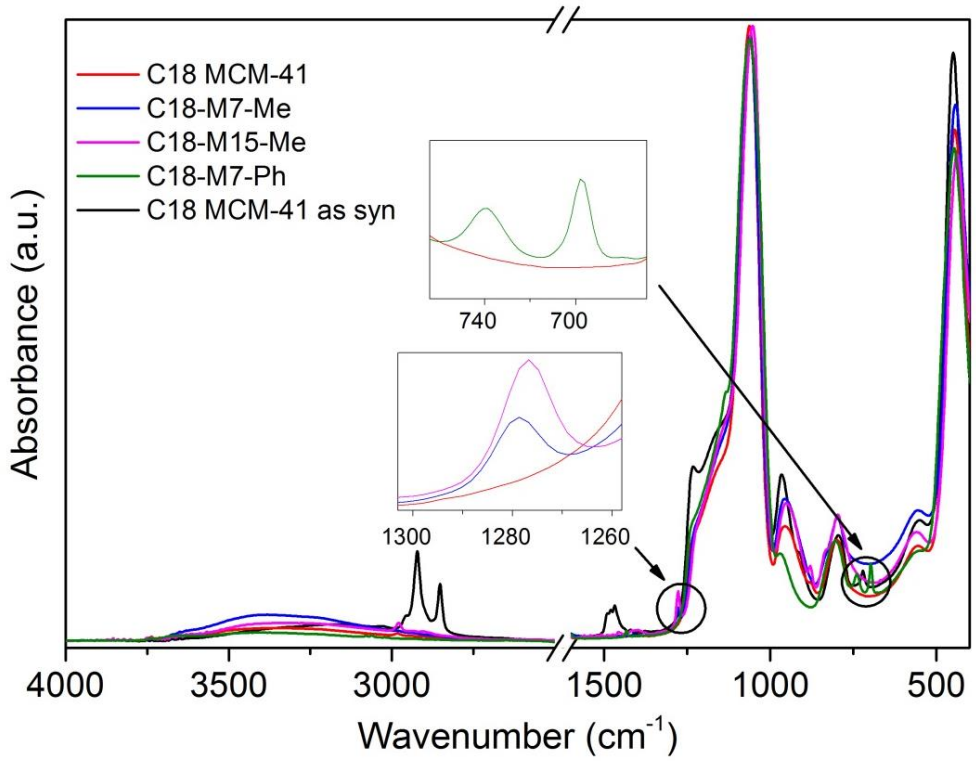

Figure 5.1: FTIR spectra of (a) MCM-41 C18, (b) C18-M7-Me, (c) C18-M15-Me, and (d) C18-M7-Ph and (e) MCM-41 as synthesized (before template removal).

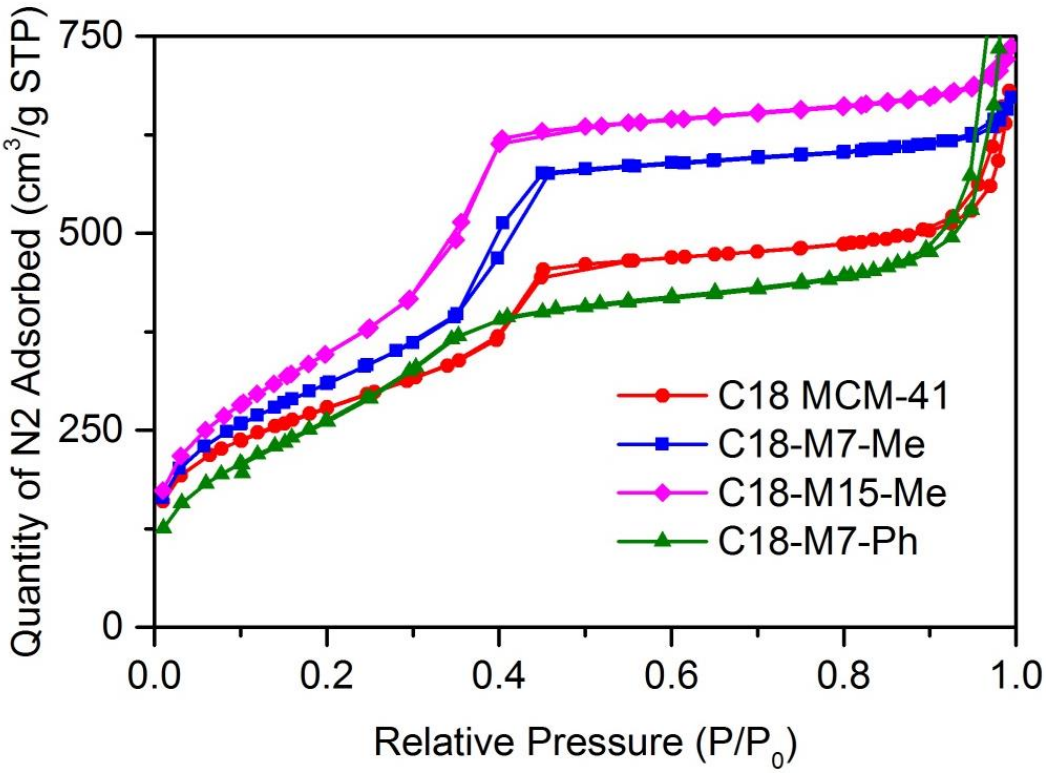

Figure 5.2: Nitrogen adsorption-desorption isotherms at 77 K of MCM-41 C18 and mesoporous organosilica materials.

Nitrogen adsorption and desorption isotherms at 77 K for these samples are shown in Figure 5.2. For standard and methyl-modified MCM-41 C18, results show a regular type IV adsorption isotherm. We observed an increase in the surface area and pore volume for C18-M7-Me and C18-M15-Me with respect to MCM-41 C18 (See Table 5.2). From transmission electron microscopy (Figure 5.3), we observed the hexagonal pore structure of C18-M15-Me and a mean grain size of 415 nm.

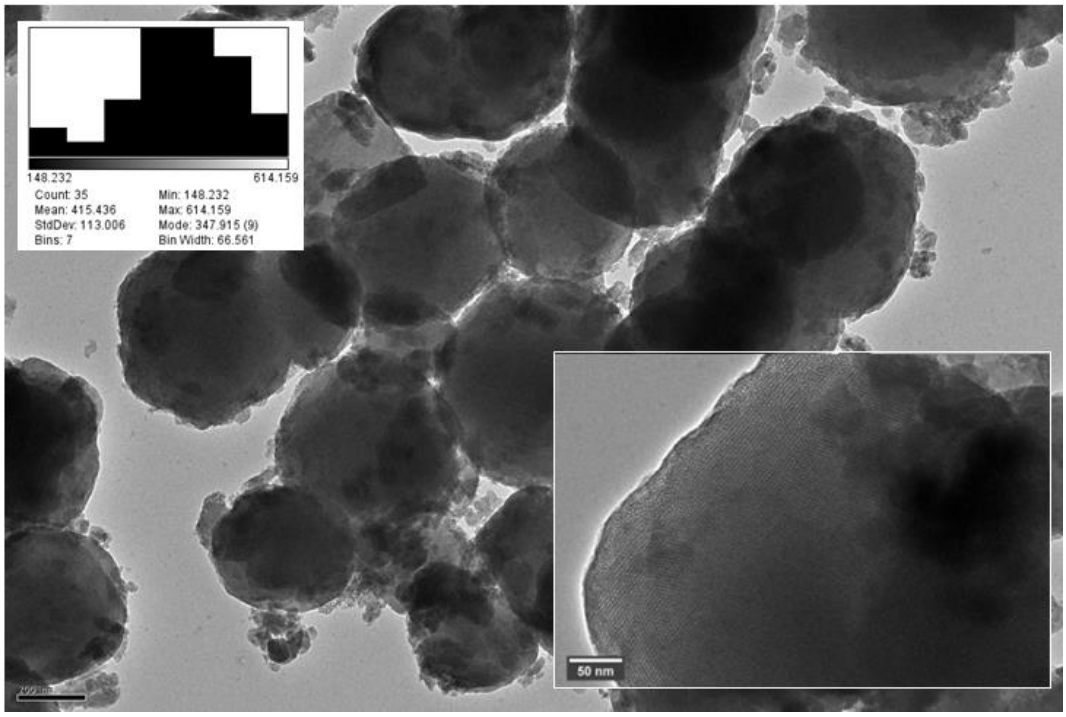

Figure 5.3: Transmission electron microscopy image of C18-M15-Me. Inserts: Grain size distribution with a mean value of 415 nm and zoomed image of a grain.

On the other hand, the co-condensation with PTES produced a less organized material (C18-M7-Ph), evidenced by a spread capillary condensation, slightly lower surface area, and pore volume than MCM-41 C18. C18-M7-Ph can be compared to benzene-PMO[2].

Benzene-PMO uses 1,4-bis(triethoxysilyl)benzene as a precursor and yields an organosilane with a periodic distribution of aromatic groups. This material has a slightly lower pore volume (0.50 cm^3/g) and a lower surface area (~600 m^2/g) than C18-M7-Ph[2].

The late condensation at $P/P_0 > 0.9$ in samples MCM-41 C18 and C18-M7-Ph was attributed to condensation in the interparticle cavities when the size of the mesoporous silica grains are small (< 100 nm)[3], as it was evidenced for C18-M7-Ph by TEM (Figure 5.4).

It is worth noting that the affinity constant, C, calculated from the BET equation, shows a significant decrease with respect to the value of MCM-41 C18 (C = 89) for all the modified materials. This parameter is directly correlated to the adsorbent-adsorbate affinity. Since induced dipole-dipole interactions govern this adsorption, the introduction of organic groups decreases the affinity of nitrogen towards the surface. Then, the

observed drop of the C value within the same family of materials is another evidence of their increasing hydrophobicity.

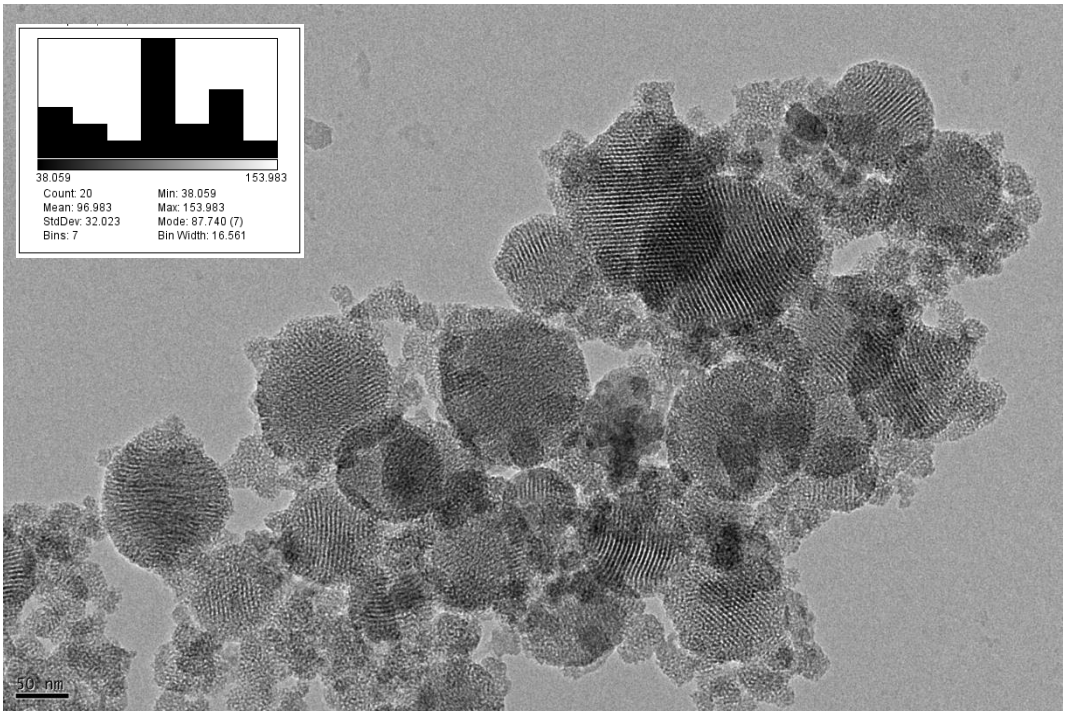

Figure 5.4: Transmission electron microscopy image of C18-M7-Ph. Insert: Grain size distribution with a mean value of 97 nm. This picture cannot assess the dimensions of the intergranular porosity in dried conditions because the sample preparation for TEM requires the suspension of the nanoparticles in ethanol.

These results indicate that, upon introducing MTES at percentages up to 15%, the obtained organosilica maintain an ordered pore structure while increasing their hydrophobic character.

Small-Angel X-Ray Scattering

Figure 5.5 shows the Small-angle X-Ray scattering patterns for the synthesized materials. The observation of three Bragg peaks indexed as (10), (11), and (20) confirm the 2D hexagonal structure p6mm of the standard and methyl modified materials. The broadening of the (10) peak of the phenyl modified sample could suggest a higher polydispersity in the d_{10} lattice plane spacing.

The lattice plane spacing d_{10} (Table 5.3) was calculated from the SAXS patterns. In combination with the pore volume obtained by nitrogen adsorption, this parameter allowed the calculation of the pore diameter (D_{SAXS}). This method is more precise for determining the size of small hydrophobic pores than the BET model that only uses nitrogen adsorption data[4] (see Chapter 3).

We found that the pore diameter does not change significantly up to 15% MTES or 7% PTES, while the post-grafting method always induces a decreasing pore size. However, the

pore wall thickness shows a 16% increase in C18-M7-Ph compared to MCM-41 C18. On the contrary, we found a decrease of 20% in the pore wall thickness of C18-M7-Me and 30% in C18-M15-Me. Such structural changes probably have their origin in the interactions of MTES/PTES with the template, disrupting the hexagonal order for higher fractions of organosilane in the precursors' mixture.[5]

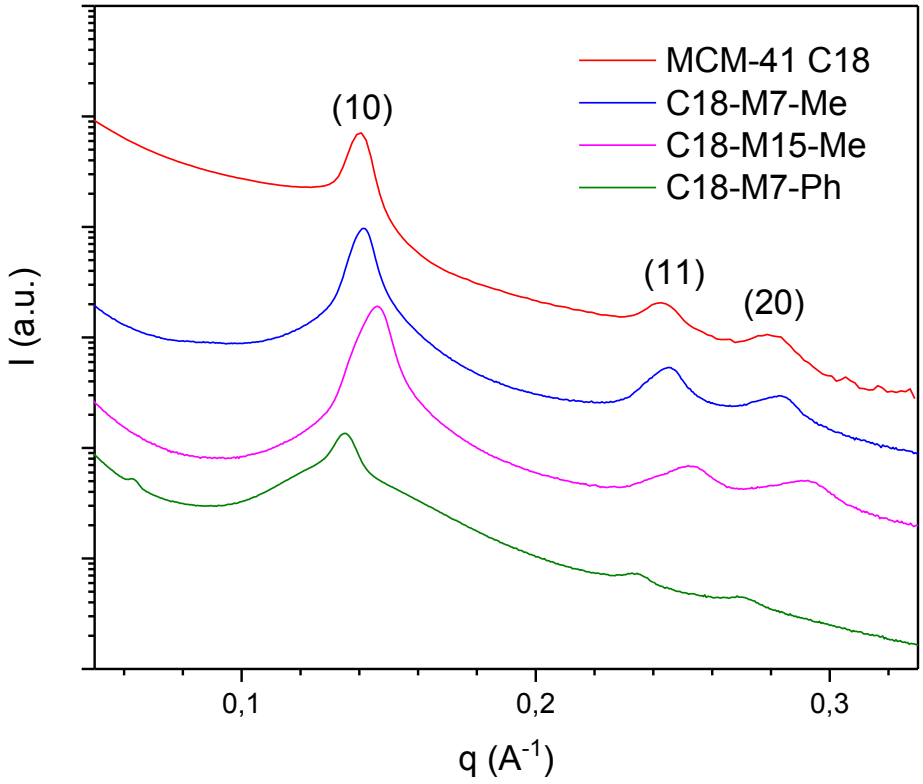

Figure 5.5: Small-angle scattering curves of MCM-41 C18 and mesoporous organosilica materials.

Table 5.3: Physical properties of selected nanoporous materials determined by SAXS. d_{10} is the lattice plane spacing and d_{cc} is the distance between two pore centers. The pore size D_{SAXS} and the pore wall thickness (ε_{wall}) were calculated using the pore volume determined by nitrogen adsorption.

Material	Q_{10} ($Å^{-1}$)	d_{10} (nm)	dcc (nm)	D_{SAXS} (nm)	ε_{wall} (nm)
MCM-41 C18	0.1407	4.466	5.16	4.2	1.0
C18-M7-Me	0.1415	4.440	5.13	4.4	0.7
C18-M15-Me	0.1460	4.304	4.97	4.3	0.7
C18-M7-Ph	0.1350	4.654	5.37	4.3	1.1

Neutron Backscattering Experiments: Elastic and Inelastic Fixed Window Scans

We have investigated the rotational dynamics of methyl groups at the surface and inside the wall of C18-M15-Me using neutron backscattering. This characterization allowed us to assess the methyl groups distribution at the surface and inside the pore wall of the material.

The experiment aimed to distinguish the onset of the free rotation of methyl groups around the threefold axis as the temperature increased from 7K to 292K. Incoherent Neutron Backscattering is particularly well suited for this task because of its high sensitivity to Hydrogen atoms and its possibility to operate in Elastic and Inelastic Fixed Window temperature Scans (EFWS and IFWS), which allows the identification of the onset of motions faster than a few nanoseconds.

With the high-resolution backscattering spectrometer IN16B at the ILL (Grenoble, France)[6], we have performed two sets of experiments[7,8] on two different samples. The first sample is C18-M15-Me, compared to its partly calcined homolog, the latter being heated up to 550°C at atmospheric pressure in order to remove a large part of the methyl groups attached at the surface.

$$SiO_2(\text{-}CH_3)_x \rightarrow SiO_2(\text{-}CH_3)_{x-y} + y(^{\bullet}CH_3) \qquad (5.1)$$

The results are presented in Figure 5.6 (a, b), where respectively the two EFWS normalized at 2K and the two IFWS and their intensity difference are reported.

At very low temperatures, all motions of the materials are frozen, and the elastic scattered intensity slightly decreases with temperature because of the Debye-Waller factor. However, local motions such as methyl group rotation can occur,[8] and the EFWS in Figure 5.6a decays in two steps indicating that above 100 K and 250 K, the methyl group rotation enters the dynamical window of the spectrometer.

The EFWS in two steps demonstrates that the methyl groups interact with two distinct environments: the less constraining one (at lower temperatures) corresponds to the groups at the surface, while the most constraining one is at higher temperatures and corresponds to groups inside the pore wall. The slight difference between the two curves, in intensity above 100 K, is due to the most rigid character of the partly calcined sample.

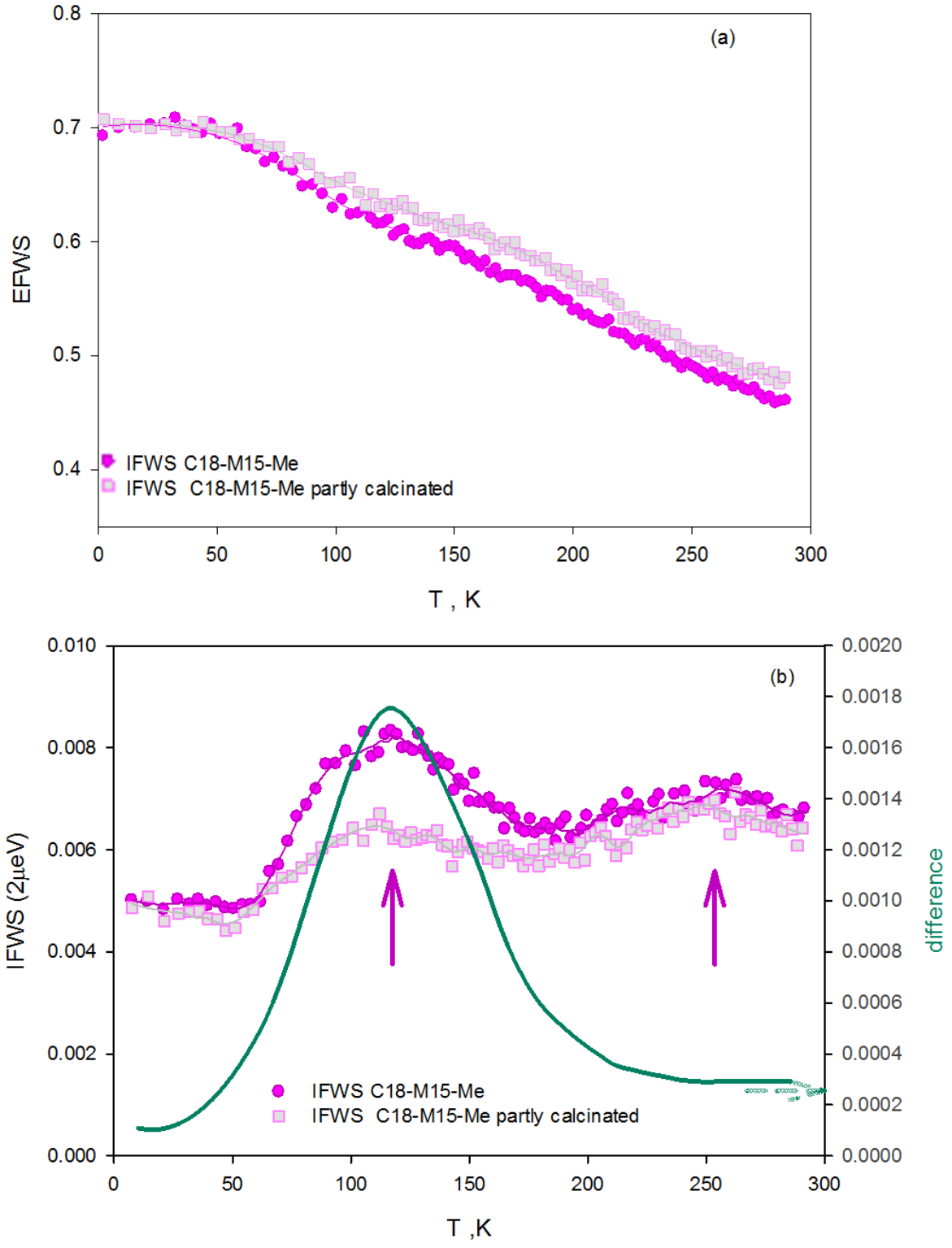

Figure 5.6: (a) Elastic intensity measured with the fixed window mode, EFWS, as a function of temperature on the spectrometer IN16B at the ILL, for the two samples C18-M15-Me, as defined in the main text, and its partly calcined homolog (C18-M15-Me partly calcined); (b) Inelastic intensity measured in the IFWS mode at 2µeV; pink arrows indicate the temperatures at which the methyl group rotations cross the energy of 2µeV, the difference between the two samples in green illustrates how the methyl groups at the surface are affected by the thermal treatment.

These results are confirmed in Figure 5.6b with the IFWS. As the temperature increases,

the frequency of the rotation shifts to a lower value and enters the elastic line, causing a quasi-elastic broadening. Detected at a fixed frequency of 2 meV, the inelastic signal increases in amplitude. As the temperature continues to increase, the motion becomes faster and the inelastic signal even broader, inducing an amplitude decrease at a fixed frequency. We observe two maxima in the IFWS corresponding to the two steps in EFWS (pink arrows in the figure). At 117 K, the amplitude difference between the two samples evidences the presence of methyl groups at the surface that is affected by the thermal treatment of the calcined sample. The second important feature is the lowest inelastic intensity of the peak at 255 K, illustrating the lowest amount of mobile H inside the pore walls, which remain the same in the two samples.

In short, these experiments allowed us to identify two distinct populations of methyl groups, the first one has been assigned to the free groups at the surface (rotation peak at 117 K), and the second one corresponds to those trapped inside the pore walls (rotation peak at 255 K). Using the area under the curve, we estimated the fraction of each population, obtaining that 30-35% of methyl groups are trapped in the walls, while the rest (70 – 65 %) are at the surface (among them, 80% were removed by the calcination at 550 °C).

Limit cases: C18-M20-Me and C12-M7-Me

The synthesis of C18-M20-Me had a significantly lower reaction yield than the rest of the materials (~55%). The main loss was identified in the filtration step. Figure 5.7 shows the nitrogen adsorption isotherms of two different samples of this material. The first one was filtered by a Duran funnel # 4 (nominal max pore size 1.0-1.6 µm) and the second one from the supernatant, which was centrifuged and dried later.

In contrast with the materials C18-M7-Me and C18-M15-Me that had a lower fraction of MTES in the precursors' mixture, the isotherms of C18-M20-Me do not show a marked capillary condensation. Furthermore, there is a striking difference between filtered and the supernatant samples. The filtered material presented a significantly lower BET surface area (256 m^2/g versus 903 m^2/g for the supernatant) and pore volume (0.151 cm^3/g versus 0.486 cm^3/g for the supernatant). The significant late condensation on the supernatant sample is attributed to the inter-granular cavities of a small grain material, which explains why it was not filtered by the Duran funnel. This was confirmed using transmission electron microscopy (Figure 5.8), where we distinguished two different populations, one with an average grain size of around 120 nm and larger grains of around 350 nm.

Even though the samples are still porous, these results show a non-homogeneous porosity and a disordered structure. This is a consequence of the disruption of the liquid crystal structure, due to interactions with the organosilane that modify the packing

parameter of the surfactant. Our results confirm the 20 mol% limit that has been observed before in the co-condensation of organosilanes and TEOS.[5,9] Such a disordered pore structure makes C18-M20-Me non-compiling for our confinement studies.

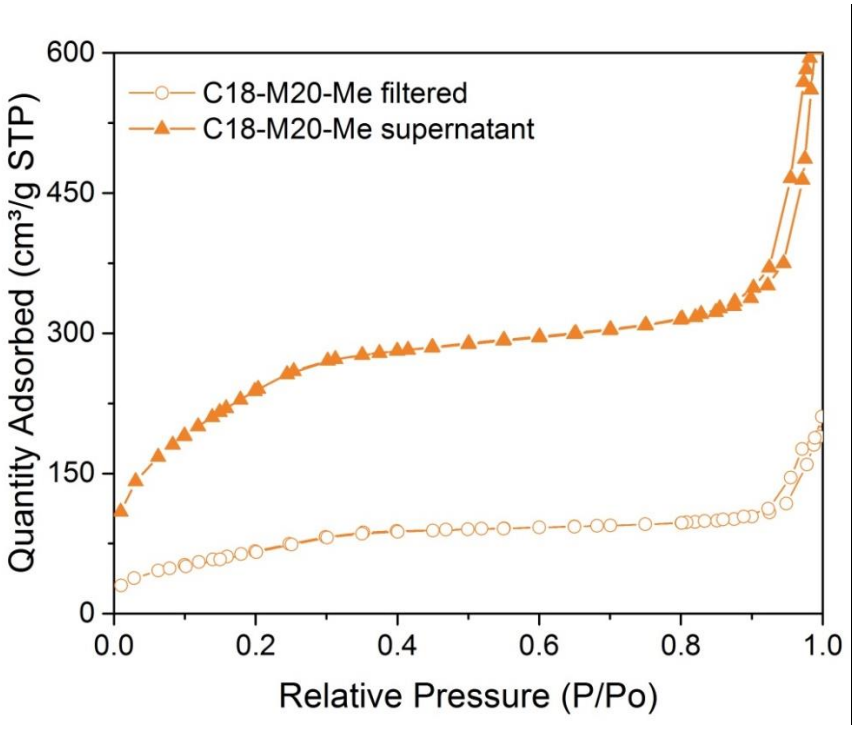

Figure 5.7: Nitrogen adsorption-desorption isotherms at 77 K of two samples of C18-M20-Me, one taken from the filtered power and the second one taken from the supernatant, which was later centrifuged and dried.

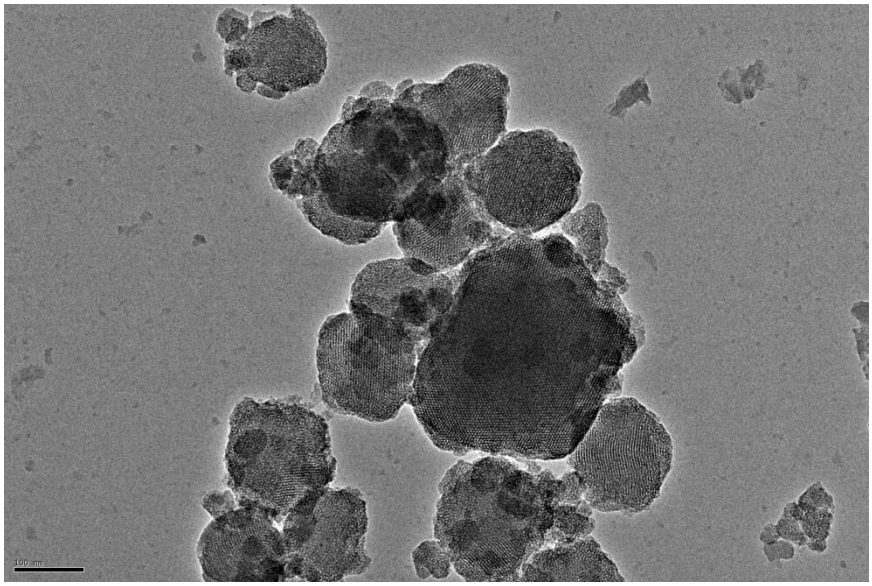

Figure 5.8: Transmission electron microscopy image of C18-M20-Me. The scale bar corresponds to 100 nm.

Figure 5.9 shows the nitrogen adsorption isotherms of MCM-41 C12 and C12-M7-Me. This last material was synthesized in order to explore the organic modification of small pore mesoporous silica, which is difficult to obtain by post-grafting methods. In this case,

we obtained a high surface area material, with pore volume slightly lower than the MCM-41 C12 (0.505 cm^3/g and 0.539 cm^3/g, respectively) but with an ordered, homogeneous pore structure confirmed by transmission electron microscopy (Figure 5.10). Even though the addition of methyl triethoxysilane seems to have a greater effect on the structure of this smaller pore size material, both products meet the required standards for our confinement studies.

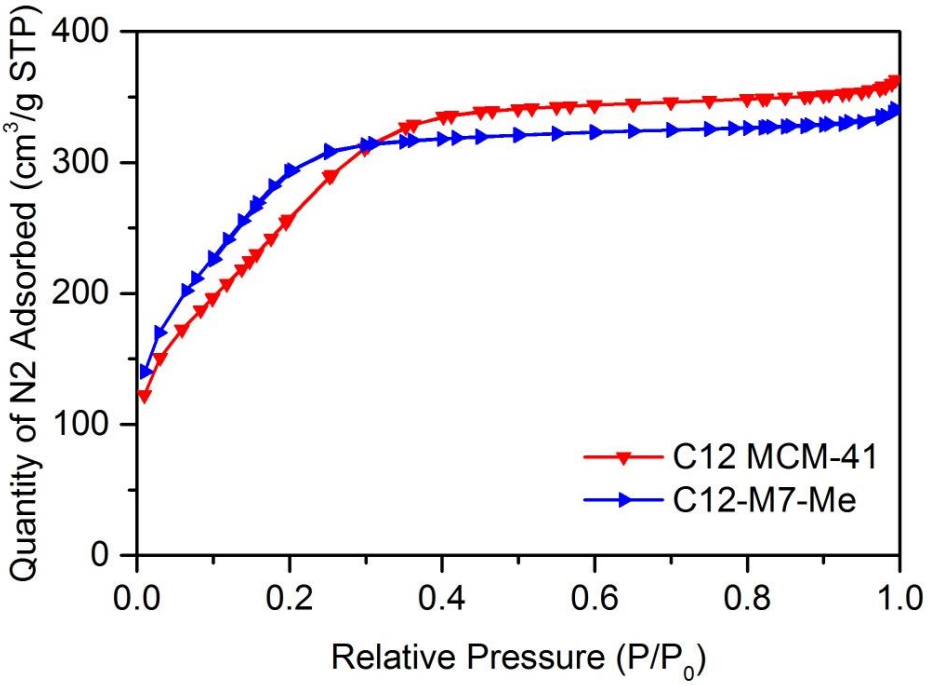

Figure 5.9: Nitrogen adsorption-desorption isotherms at 77 K of MCM-41 C12 and C12-M7-Me.

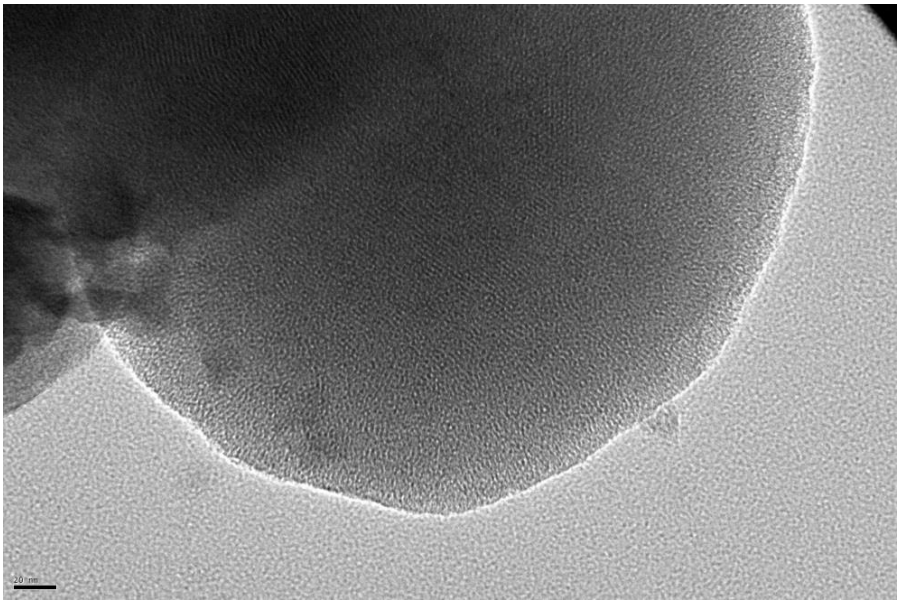

Figure 5.10: Transmission electron microscopy image of C12-M7-Me. The scale bar corresponds to 20 nm.

Water adsorption isotherms and hydrothermal resistance of the amphiphilic materials

Figure 5.11 shows the water adsorption isotherms of the hydrophilic MCM-41 C18 and amphiphilic materials. As discussed in chapter 3, we find type IV isotherms with an H1 hysteresis loop for this kind of material. We observe that the total quantity of water increases with the material's pore volume, regardless of their organic functionalization. These results show that the hydrophobicity of the materials is not strong enough to avoid water vapor condensation in the pores.

As in nitrogen adsorption experiments, a late condensation present in C18-M7-Ph could be a consequence of the small grain size. Compared to this material, benzene PMO presents a water adsorption isotherm of similar shape, but with a slightly lower total amount of water adsorbed (~600 cm^3/g STP).[10]

We performed three consecutive water adsorption-desorption isotherms for C12-M7-Me. The desorption isotherms do not join the adsorption isotherm, probably because some water molecules remain in the material, opening siloxane (Si-O-Si) bridges and generating new silanol (Si-OH) groups at the surface. The total quantity of water adsorbed decreases slightly on account of those water molecules that have been incorporated into the material.

This experiment allowed us to estimate the density of silanol groups at the surface (see details in section 3.6). The value obtained for the washed hydrophilic material was 3.0 nm^{-2}, almost double that of Kocherbitov and Alfredsson (2007) for a calcined MCM-41 C16 material.[11] n_{OH} decreases for all the amphiphilic materials. A 20% decrease is observed for C18-M7-Me, 27 % for C18-M15-Me and a 43 % decrease is obtained for C18-M7-Ph.

Table 5.4: Apparent BET surface area calculated from water adsorption isotherms, corresponding C value, and hydroxyl group densities for selected materials. The organic group density is shown for reference.

Material	$S_{BET,H2O}$ (m^2/g)	$C_{BET, H2O}$	n_{OH} (nm^{-2})	n_{Org} (nm^{-2})
MCM-41 C18	128	7.1	3.0	0.00
C18-M7-Me	166	6.7	2.4	0.18
C18-M15-Me	172	8.3	2.2	0.34
C18-M7-Ph	99.4	3.4	1.7	0.20
C12-M7-Me 1st cycle	148	7.2	2.2	0.18
C12-M7-Me 2nd cycle	161	6.3	2.4	0.18
C12-M7-Me 3rd cycle	154	7.4	2.3	0.18

C12-M7-Me initially presents 27 % fewer hydroxyl groups at the surface than MCM-41

C18. The number of –OH groups seems to increase slightly with the consecutive water adsorption and desorption cycles, which agrees with the incorporation of water molecules to the surface that we mentioned before.

The water vapor adsorption data shown here was also used for the determination of the density of confined water in amphiphilic nanopores (Chapter 6).

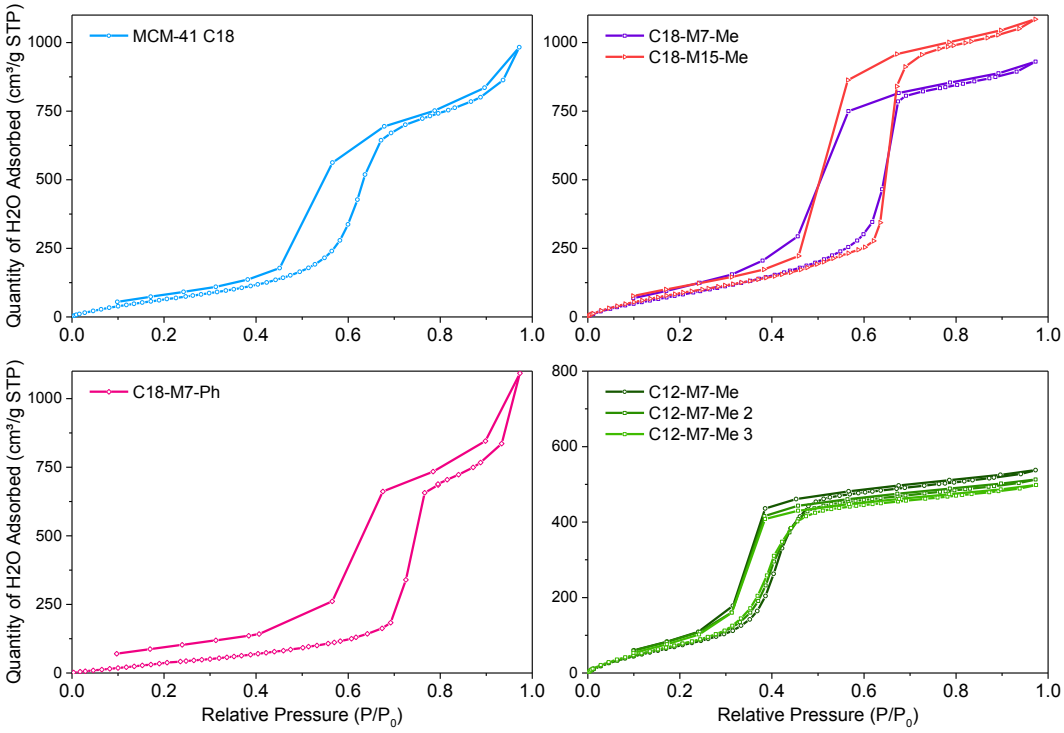

Figure 5.11: Water adsorption and desorption isotherms on C18 materials (pore sizes between 4.3 and 4.5 nm) and three consecutive cycles on C12-M7-Me (3 nm pore size) at 298 K. (P_0 =0.0317 bar at 298.15 K)

We have studied the surface degradation of the organosilica materials after contact with water. During water adsorption experiments, the materials were in contact with water at neutral pH and 25 °C. Afterward, they were heated to 90°C under vacuum for 24 h to ensure the elimination of any residual water molecule.

Figure 5.12 shows nitrogen adsorption-desorption isotherms for the same organosilica samples before and after water adsorption (and desorption). The total quantity of N_2 adsorbed after capillary condensation is directly related to the pore volume. This quantity decreases due to the pore structure degradation upon contact with water. In the case of C18-M7-Me, the quantity of N_2 adsorbed at P/P_0 = 0.5 decreases by 11.8 % of its initial value. A smaller difference (4.22 %) is observed in the case of C18-M15-Me, while for C18-M7-Ph, the pore volume is roughly constant (a small negative value of 3.16 %, attributable to the experimental error). These results indicate an increasing surface stabilization towards hydrolysis when the hydrophobicity of the surface increases, due to the presence of methyl or phenyl groups.

Knowing the extent of the pore surface degradation is important for the planning of confinement experiments. Whenever possible, the measurements should be performed within a 24 hour window from the moment the materials are put in contact with water.

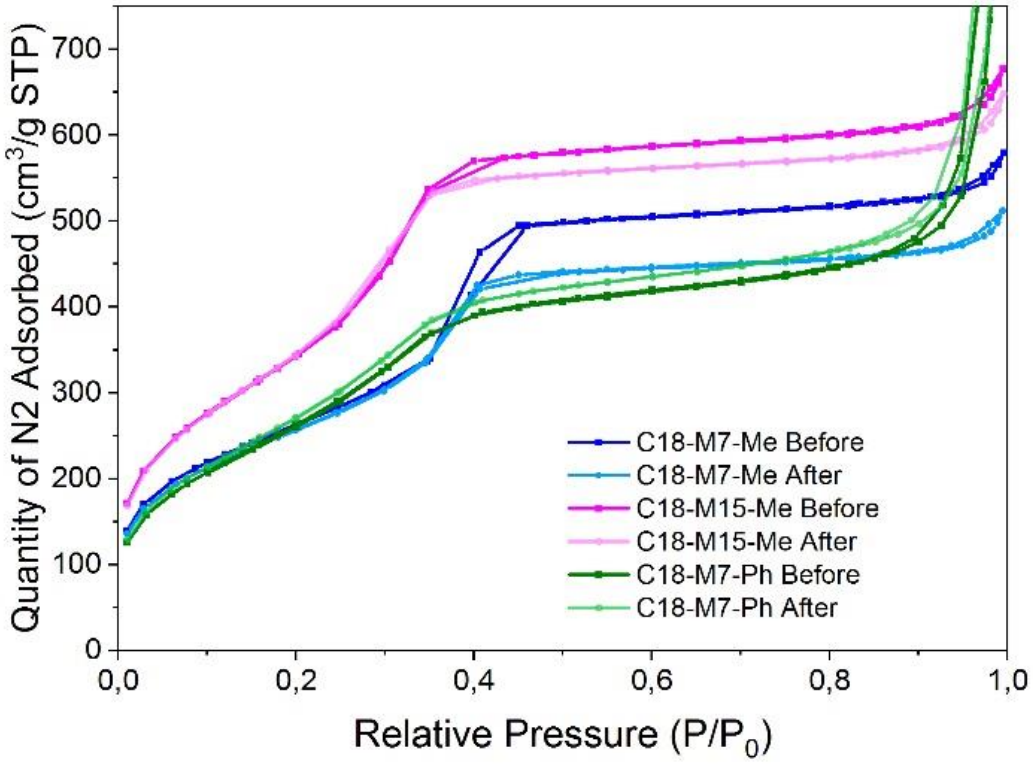

Figure 5.12: Nitrogen adsorption and desorption isotherms at 77 K of selected materials before and after water adsorption.

5.2. Physical and chemical properties of the post-grafted materials

We modified the surface of two amphiphilic materials (C18-M7-Me and C18-M15-Me) with chlorotrimethylsilane (Cl-Si(CH_3)$_3$). FTIR Spectra of the modified materials (Figure 5.13) show new bands at 1255 and 2964 cm^{-1}, corresponding to C-H bend and stretching, respectively. This serves as confirmation that the –$SiMe_3$ has been grafted to the surface.

A redshift of the Si-CH_3 bending peak of pre-existent methyl groups is observed after the surface modification (insert in Figure 5.13). In this case, the pre-existent –CH_3 acts as an infrared probe of the local environment, indicating a decrease of electronegativity in the nanoenvironment. This concept of introducing certain organic groups (usually nitriles) as a probe of electronegativity has been broadly exploited to investigate the binding and folding of proteins.[12]

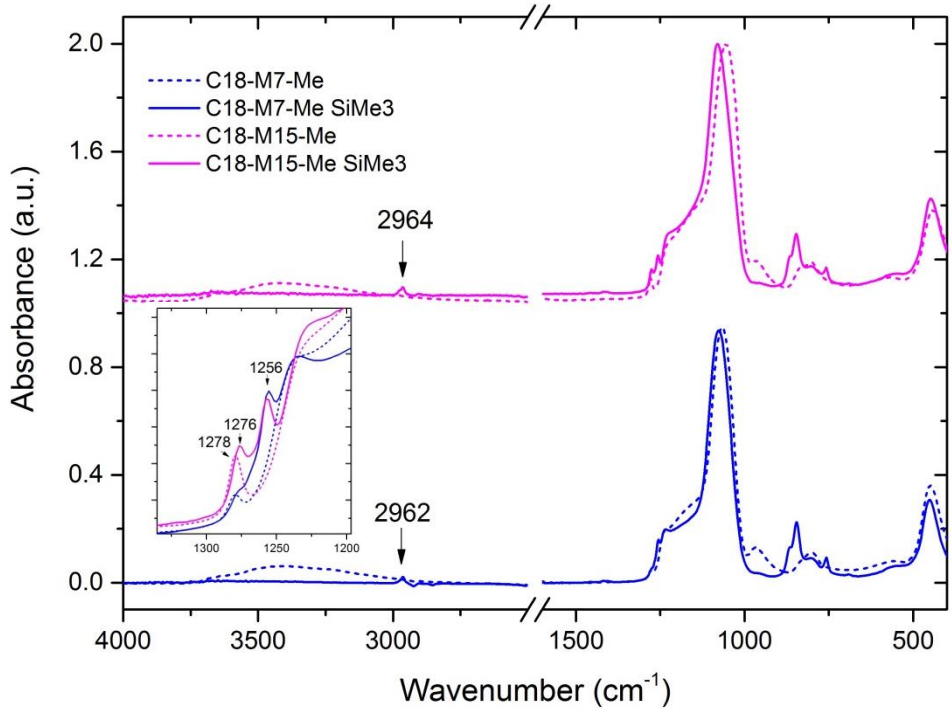

Figure 5.13: FTIR spectra of the postgrafted materials and the original amphiphilic materials. Insert: Zoom between 1200 cm^{-1} and 1350 cm^{-1} to show the redshift produced to the pre-existent $–CH_3$ bands due to a decrease in the polarity of the nanoenvironment.

Nitrogen adsorption/desorption isotherms are shown in Figure 5.14 for the materials before and after silylation. Physical properties such as pore volume, surface area, pore size, wall thickness, and functionalization layer thickness were calculated from these data and are shown in Table 5.5.

Results show that the pore volume, surface area, pore diameter, and C value have significantly decreased upon functionalization, while the wall thickness has increased. The pore volume is around 40 % smaller for both samples, and the surface area has decreased by approx. 29 % of its initial value. These results confirm that the -$SiMe_3$ groups have been effectively grafted to the internal surface of the pores.

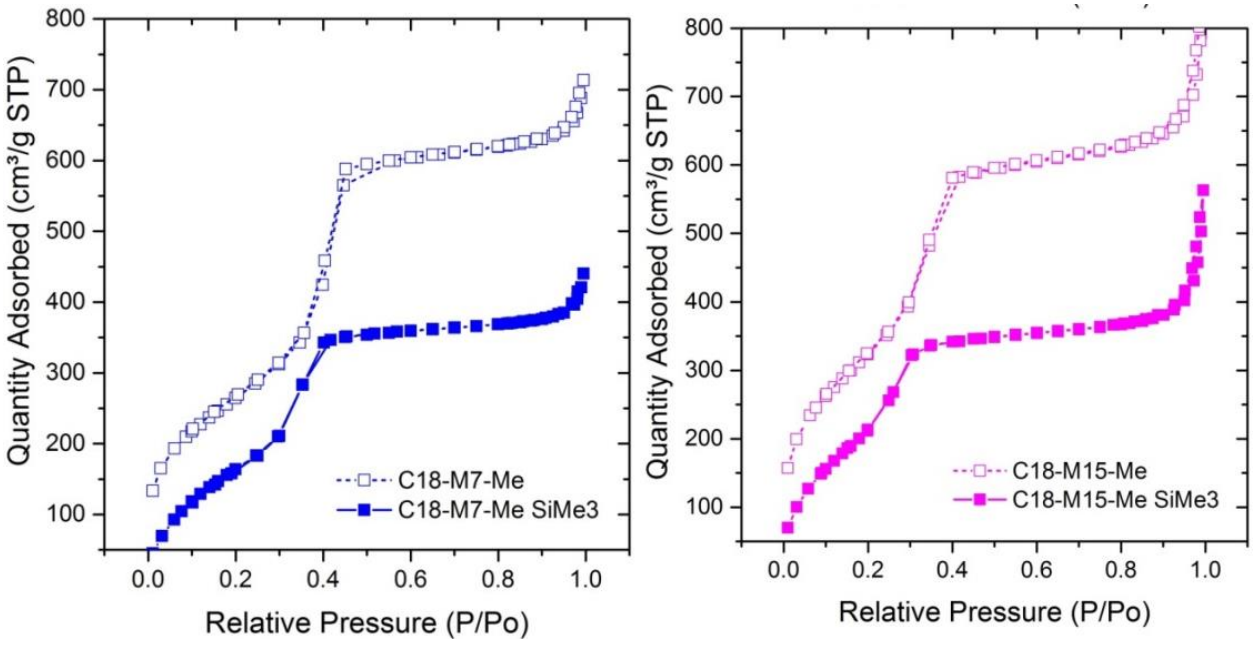

Figure 5.14: Nitrogen adsorption and desorption isotherms at 77 K before and after silylation.

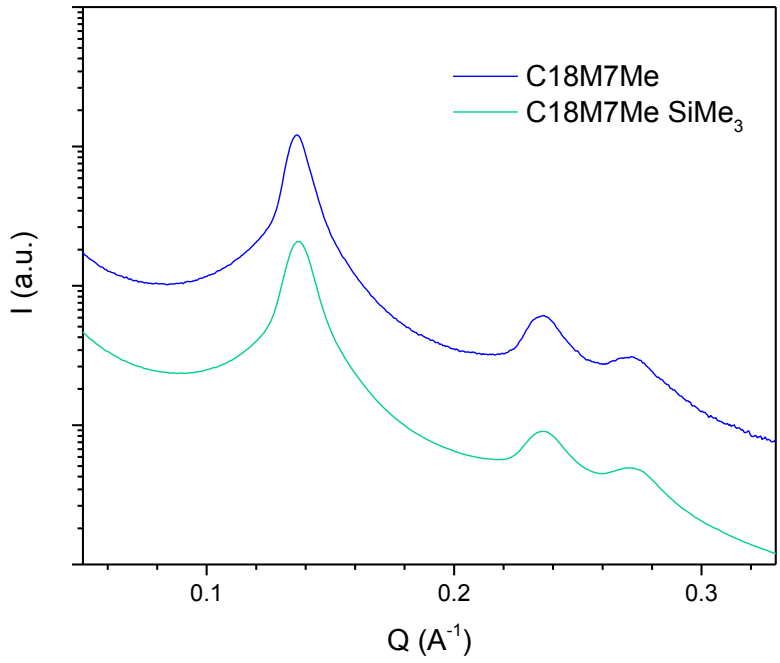

Figure 5.15: Small-angle scattering curves of the postgrafted material C18-M7-Me SiMe3 and C18-M7-Me

We performed a SAXS measurement to C18-M7-Me $SiMe_3$ (Figure 5.15), which allowed us to confirm that the hexagonal structure of the material was unaltered by the surface treatment, as the position of the Bragg peaks (10), (11), and (20) did not change.

We obtained the wall thickness for both original and modified materials using the inter-pore distance calculated from SAXS. Results show in both cases that a hydrophobic layer of 0.2 nm has been grafted to the pore surface.

Table 5.5: Physical properties of the materials before and after surface modification.

Material	V_p (cm3/g)	S_{BET} (m^2/g)	C	D_{SAXS} (nm)	ε_{wall} (nm)	ε_{SiMe3} (nm)
C18-M7-Me*	0.920	979	62	4.6	0.8	0.2
C18-M7-Me $SiMe_3$	0.547	688	19	4.0	1.2	
C18-M15-Me*	0.921	1208	53	4.3	0.7	0.2
C18-M15-Me $SiMe_3$	0.539	856	23	3.9	1.1	

*synthesized by Aurelie Doira

We performed a thermal-gravimetrical analysis of the hydrophobic materials (Figure 5.16) to determine the grafting density of the materials. The mass loss observed between 350 °C and 800 °C corresponds to the sum of the grafted $SiMe_3$ + the $–CH_3$ from the direct synthesis. Then, the grafting density (τ) has been calculated as shown below, subtracting the loss of $–CH_3$ from the original material before surface modification. Results are shown in Table 5.6.

$$\tau = \frac{\frac{\Delta m_2}{m_2} - \frac{\Delta m_1}{m_1}}{M_{silane} * S_{BET}} * N_A \qquad (5.2)$$

where $\Delta m_2 / m_2$ is the relative mass loss for the modified material, $\Delta m_1 / m_1$ is the relative mass loss for the original material, M_{silane} is the molar mass of $SiMe_3$ (73.192 g/mol), S_{BET} is the Surface Area of the initial material, and N_A is the Avogadro's number**.**

Table 5.6: Calculation of the grafting density of modifies materials.

Material	$\Delta m_1/m_1$ $-CH_3$	$\Delta m_2/m_2$ CH_3 + $Si(CH_3)_3$	$\Delta m/m$ $Si(CH_3)_3$	S_{BET} (m^2/g)	τ (nm^{-2})
C18-M7-Me $SiMe_3$	0.0391	0.1058	0.0667	979	0.56
C18-M15-Me $SiMe_3$	0.0500	0.0986	0.0486	1208	0.33

During the silylation, $Cl\text{-}Si(CH_3)_3$ reacts with silanol active sites at the surface. It is natural that a higher grafting density was found in C18-M7-Me $SiMe_3$ because C18-M7-Me has a higher silanol surface density than C18-M15-Me.

The grafting densities found here are much lower than in MCM-41 (between 2.5 and 3.0 nm^{-2})[13,14], even though the silanol surface density of C18-M7-Me and C18-M15-Me is not so far from MCM-41. This is probably an effect of the steric hindrance caused by the pre-existent methyl groups at the surface.

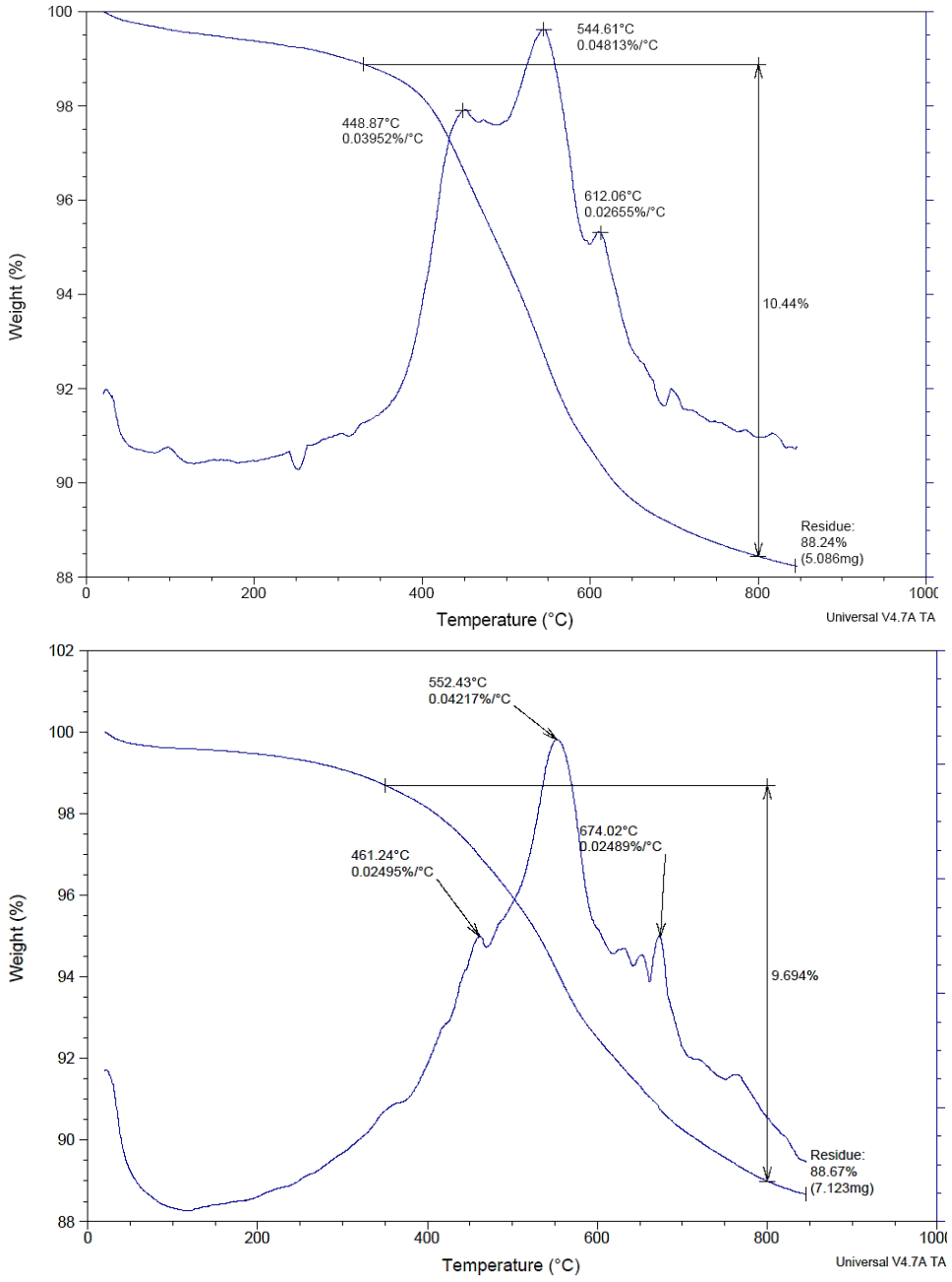

Figure 5.16: TGA of C18-M7-Me $SiMe_3$ and C18-M15-Me $SiMe_3$ at 10 K/min.

Regardless, the high hydrophobicity of these materials was confirmed by a very low water adsorption capacity. The results of water vapor adsorption experiments are discussed in detail in section 7.1.

Table 5.7 presents a summary of the structural and chemical characterization of the synthesized material. Other compositions (C18-M10-Me and C18-M7-Et), synthesized by another chemist (Aurelie Doira), were added to the table, as they were later used for the confinement experiments.

Table 5.7: Structural and chemical characterization of the synthesized materials

Material	$S_{BET, N2}$ (m^2/g)	V_{pore} (cm^3/g)	D_{BET} (nm)	C	Q_{10} ($Å^{-1}$)	d_{10} (nm)	dcc (nm)	D_{SAXS} (nm)	ε_{wall} (nm)	n_{OH} (nm^{-2})	n_{Org} (nm^{-2})
MCM-41 C18	1007	0.712	2.8	89	0.1407	4.466	5.16	4.2	1.0		0.00
MCM-41 C18 (2)	717	0.679	3.8	75	0.1301	4.830	5.58	4.5	1.0	3.0	0.00
MCM-41 C12	979	0.539	2.1	35	0.1768	3.554	4.10	3.2	0.9		0.00
C18-M7-Me	1130	0.899	3.2	76	0.1415	4.440	5.13	4.4	0.7	2.4	0.18
C18-M7-Me*	979	0.920	3.8	62	0.1365	4.603	5.32	4.6	0.8		0.21
C18-M10-Me*	1032	0.881	3.4	58	0.1378	4.560	5.27	4.5	0.8		0.28
C18-M15-Me	1284	0.982	3.1	78	0.1460	4.304	4.97	4.3	0.7	2.2	0.34
C18-M15-Me*	1208	0.921	3.0	53	0.1464	4.292	4.96	4.3	0.7		0.36
C18-M20-Me	903	0.447	2.0	37	0.1550	4.054	4.68	3.5	1.2		
C18-M7-Et*	1114	0.911	3.3	47	0.1509	4.164	4.81	4.1	0.7		0.18
C18-M7-Ph	989	0.628	2.5	44	0.1350	4.654	5.37	4.3	1.1	1.7	0.20
C12-M7-Me	1134	0.505	1.8	35	0.1862	3.370	3.89	3.0	0.9	2.2	0.18
C18-M7-Me $SiMe_3$	688	0.547	3.2	19	0.1404	4.475	5.17	4.0	1.2		0.21 (-CH3) + 0.56 (-SiMe3)
C18-M15-Me $SiMe_3$	856	0.539	2.5	23	0.1444	4.351	5.02	3.9	1.1		0.36 (-CH3) + 0.33 (-SiMe3)

*synthesized by Aurelie Doira. †Quantity of N_2 adsorbed at P/P0 = 0.8

5.3. Conclusion

We synthesized MCM-41-type nanoporous materials with different levels of hydrophobicity. The nanopores are cylindrical, organized in a 2D-hexagonal arrangement, and with a well-defined pore diameter. The hydrophobicity is given by the presence of different densities of organic groups at the surface. The modified materials are divided into two groups: amphiphilic and hydrophobic.

The amphiphilic materials were synthesized using the co-condensation of tetraethoxysilane with alkyl-triethoxysilanes. Their hydrophobicity comes from the methyl, ethyl, or phenyl groups integrated into the materials' framework. These groups are distributed between the pore surface and the pore walls inside. The amphiphilic materials present high water vapor adsorption capacity and resistance to hydrolysis. The percentage of organic groups that can be incorporated using this synthesis is limited to less than 20 mol% in the precursors' mixture. Beyond this value, we obtained an inhomogeneous pore structure, not suitable for our confinement studies. The study of the effect of amphiphilic confinement in water's density, freezing, and melting is presented in Chapter 6.

The hydrophobic materials were achieved by performing a post-synthesis modification with chlorotrimethylsilane to amphiphilic materials C18-M7-Me and C18-M15-Me. The grafting density was 0.56 nm^{-2} for C18-M7-Me $SiMe_3$ and 0.33 nm^{-2} for C18-M15-Me $SiMe_3$. Due to their high level of hydrophobicity, these nanopores cannot be filled by water vapor adsorption, and we need high pressures to force liquid water's intrusion. This subject will be addressed in Chapter 7, together with the study of water confinement in hydrophobic nanopores at high pressures.

References

(1) Llusar, M.; Monrós, G.; Roux, C.; Pozzo, J. L.; Sanchez, C. One-Pot Synthesis of Phenyl- and Amine-Functionalized Silica Fibers through the Use of Anthracenic and Phenazinic Organogelators. *J Mater Chem* **2003**, *13* (10), 2505–2514. https://doi.org/10.1039/B304479N.

(2) Inagaki, S.; Guan, S.; Fukushima, Y.; Ohsuna, T.; Terasaki, O. Novel Mesoporous Materials with a Uniform Distribution of Organic Groups and Inorganic Oxide in Their Frameworks. *J. Am. Chem. Soc.* **1999**, *121* (41), 9611–9614. https://doi.org/10.1021/ja9916658.

(3) Marei, N. N.; Nassar, N. N.; Vitale, G. The Effect of the Nanosize on Surface Properties of NiO Nanoparticles for the Adsorption of Quinolin-65. *Phys. Chem. Chem. Phys.* **2016**, *18*, 6839–6849. https://doi.org/10.1039/C6CP00001K.

(4) Schoeffel, M.; Brodie–Linder, N.; Audonnet, F.; Alba–Simionesco, C. Wall Thickness Determination of Hydrophobically Functionalized MCM-41 Materials. *J Mater Chem* **2012**, *22*, 557–567. https://doi.org/10.1039/C1JM11578B.

(5) Rabbani, M. M.; Oh, W.-T.; Nam, D.-G. Synthesis and Characterization of Methyltriethoxysilyl-Mediated Mesoporous Silicalites. *Trans. Electr. Electron. Mater.* **2011**, *12* (3), 119–122. https://doi.org/10.4313/TEEM.2011.12.3.119.

(6) Frick, B.; Combet, J.; van Eijck, L. New Possibilities with Inelastic Fixed Window Scans and Linear Motor Doppler Drives on High Resolution Neutron Backscattering Spectrometers. *Nucl. Instrum. Methods Phys. Res. Sect. Accel. Spectrometers Detect. Assoc. Equip.* **2012**, *669*, 7–13. https://doi.org/10.1016/j.nima.2011.11.090.

(7) Colmenero, J.; Mukhopadhyay, R.; Alegría, A.; Frick, B. Quantum Rotational Tunneling of Methyl Groups in Polymers. *Phys. Rev. Lett.* **1998**, *80* (11), 2350–2353. https://doi.org/10.1103/PhysRevLett.80.2350.

(8) Zorn, R.; Frick, B.; Fetters, L. J. Quasielastic Neutron Scattering Study of the Methyl Group Dynamics in Polyisoprene. *J. Chem. Phys.* **2002**, *116* (2), 845–853. https://doi.org/10.1063/1.1424319.

(9) Burkett, S. L.; Sims, S. D.; Mann, S. Synthesis of Hybrid Inorganic–Organic Mesoporous Silica by Co-Condensation of Siloxane and Organosiloxane Precursors. *Chem. Commun.* **1996**, *11*, 1367–1368.

(10) Thommes, M.; Morell, J.; Cychosz, K. A.; Fröba, M. Combining Nitrogen, Argon, and Water Adsorption for Advanced Characterization of Ordered Mesoporous Carbons (CMKs) and Periodic Mesoporous Organosilicas (PMOs). *Langmuir* **2013**, *29* (48), 14893–14902. https://doi.org/10.1021/la402832b.

(11) Kocherbitov, V.; Alfredsson, V. Hydration of MCM-41 Studied by Sorption Calorimetry. *J. Phys. Chem. C* **2007**, *111* (35), 12906–12913. https://doi.org/10.1021/jp072474r.

(12) Getahun, Z.; Huang, C.-Y.; Wang, T.; De León, B.; DeGrado, W. F.; Gai, F. Using Nitrile-Derivatized Amino Acids as Infrared Probes of Local Environment. *J. Am. Chem. Soc.* **2003**, *125* (2), 405–411. https://doi.org/10.1021/ja0285262.

(13) Zhao, X.; Lu, G.; Whittaker, A.; Millar, G.; Zhu, H. Comprehensive Study of Surface Chemistry of MCM-41 Using 29Si CP/MAS NMR, FTIR, Pyridine-TPD, and TGA. *J. Phys. Chem. B 1997, 101, 33, 6525–6531*. 1997.

(14) Zhao, X. S.; Lu, G. Q. Modification of MCM-41 by Surface Silylation with Trimethylchlorosilane and Adsorption Study. *J. Phys. Chem. B* **1998**, *102* (9), 1556–1561. https://doi.org/10.1021/jp972788m.

CHAPTER 6

PROPERTIES OF WATER UNDER AMPHIPHILIC CONFINEMENT

Water confined in amphiphilic conditions is ubiquitous, but the effect of amphiphilic confinement on the universal solvent is not well understood yet. Several groups have investigated the effect of the pore wall hydrophobicity on the freezing and melting of water.[1–3] However, the conditions chosen for such studies (large pore sizes or low pore filling) did not reveal reliable differences in the melting point depression and structure of water with respect to hydrophilic confinement.

Deschamps *et al.* (2010)[4] addressed this issue differently, by confining water in highly hydrophobic, small nanopores (D ~3 nm). In the modified samples, they obtained a larger melting point depression than in hydrophilic materials with the same pore size. The downside of this approach is that they needed high pressure to force water intrusion. Therefore, the conditions of pore-filling were not the same as for hydrophilic nanopores, and the results cannot be directly compared.

The missing piece of this puzzle was to be able to confine water in small nanopores with a certain degree of hydrophobicity at atmospheric pressure. This is why the synthesis and characterization of amphiphilic nanoporous materials using a direct synthesis approach were presented in previous chapters. These materials contain organic groups (methyl, ethyl, or phenyl) incorporated into their framework. Even though their level of hydrophobicity is significantly higher than in MCM-41, water can still penetrate the nanopores by vapor adsorption and by imbibition of the liquid.

This chapter is dedicated to the effect of the pore wall hydrophobicity on the properties of confined water at atmospheric pressure. We will discuss the observed changes in water's density, freezing and melting point, and crystalline structure of confined ice.

6.1. Density of confined water

As the confining material becomes increasingly hydrophobic, the interactions between the surface and water molecules become less attractive. If the hydrophobicity of the nanopores is high enough, one may observe changes in the density of confined water.[5,6]

Here we present the results of the density of H_2O adsorbed in amphiphilic nanoporous organosilica at 298 K (Figure 6.1). The values for the density were obtained using the data from the water adsorption experiments introduced in the previous chapter. The density of confined water was calculated using the total quantity of water adsorbed at a relative pressure (P/P_0 = 0.8), divided by the pore volume from nitrogen adsorption isotherms at that same relative pressure. Table 6.1 shows the resulting values for the density of the nanoconfined water, together with relevant physical-chemical properties of the confining material, such as the pore diameter and the surface density of hydroxyl and organic groups.

Figure 6.2 shows the values of water density found here, compared to previous results obtained by our group, using the same method. In this earlier work, water vapor adsorption experiments were performed in calcined MCM-41 materials. At that time, the pore size was determined using the BET method. Here, we have approximated the D_{SAXS} as D_{BET} + 0.6 nm (Chapter 3), which allowed the comparison with our materials. A clear trend was found for the calcined materials: The density of confined water is almost constant for nanopores bigger than 3 nm (~31 molecules/nm^3). For smaller pore sizes, the density decreases sharply.

Table 6.1: Relevant physical-chemical properties of the nanopores and density of confined water.

Material	D_{SAXS} (nm)	n_{OH} (nm^{-2})	n_{Org} (nm^{-2})	Water density (molecules/nm^3)	Water density (g/cm^3)
MCM-41 C18	4.5	3.0	0	27.9	0.83
C18-M7-Me	4.4	2.4	0.18 (CH_3)	25.0	0.75
C18-M15-Me	4.3	2.2	0.34 (CH_3)	25.6	0.77
C18-M7-Ph	4.3	1.7	0.20 (C_6H_6)	26.3	0.79
C12-M7-Me	3.0	2.2	0.18 (CH_3)	26.5	0.79

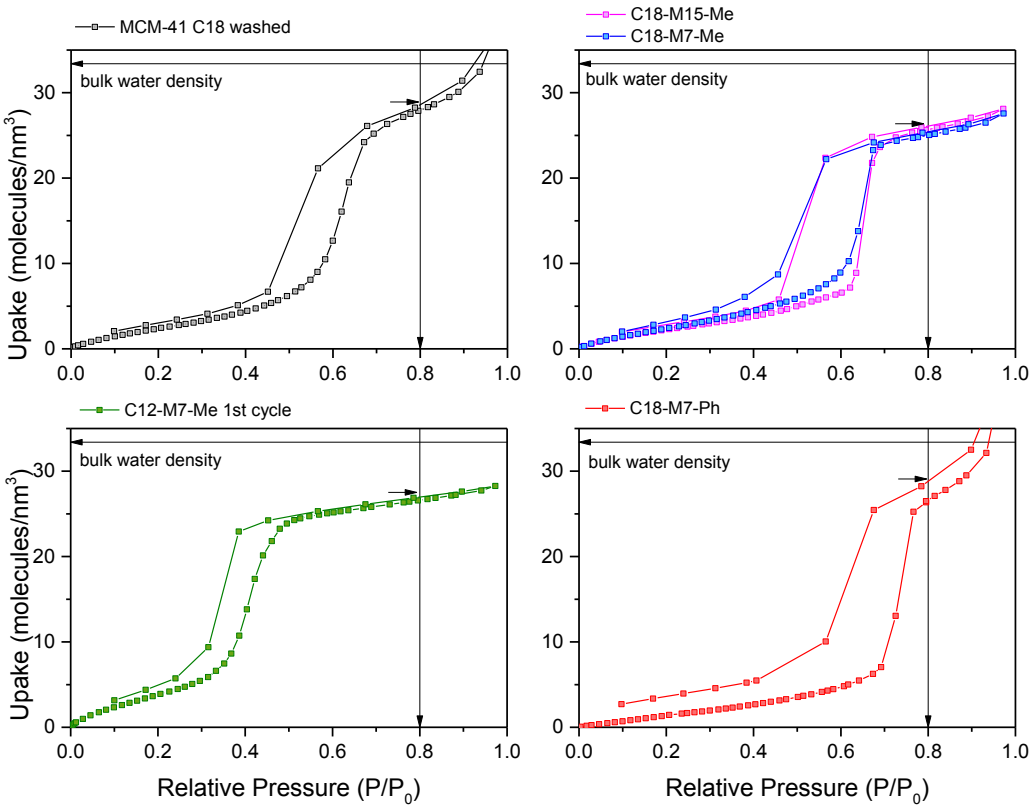

Figure 6.1: Water adsorption-desorption isotherms normalized by the pore volume for the determination of the density of confined water. (P_0 =0.0317 bar at 298.15 K). These data are already shown in Figure 5.11 (Chapter 5) for the characterization of the materials.

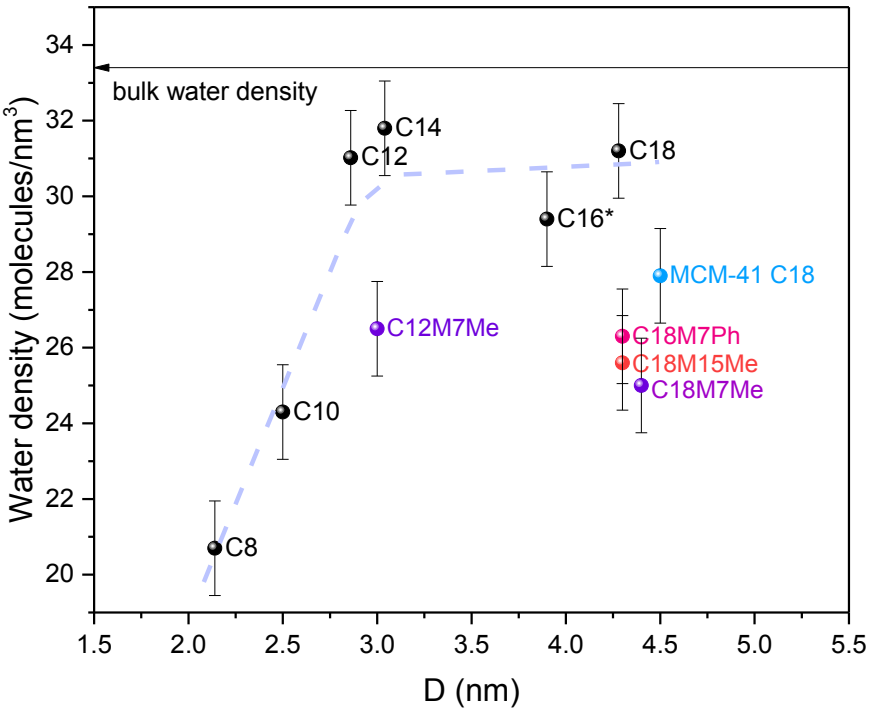

Figure 6.2: Density of confined water. The black dots represent water density values determined by our group using water vapor adsorption in MCM-41 calcined materials of different pore sizes (Pore size estimated as D_{BET} + 0.6 nm).*MCM-41 C16 taken from Kocherbitov et al. (2007)[7]. In color, the density of water

confined in our synthesized hydrophilic and amphiphilic materials. The arrow indicates the density of bulk H_2O at 298.15 K. The dashed line is a guide for the eye.

The obtained values for the density of confined water are significantly smaller than the density of bulk water (33.34 molecules/nm^3 or 0.997 g/cm^3). We also find that the density of water is significantly lower in all the amphiphilic nanopores than in hydrophilic ones (calcined and washed) at the same pore size. However, we did not find a correlation between the number of silanol or organic groups at the surface and the density.

On the shape of the isotherms

As already mentioned in the previous chapter, these are type IV isotherms with H1 hysteresis loops. The soft transition observed for all isotherms (especially for C18-M7-Ph) between the knee of the isotherm (concave section at small P/P_0) and the middle, almost linear section denotes an important overlap between the monolayer and multilayer formation.[8]

The presence of this monolayer-multilayer overlap could be a sign of the formation of water clusters in the early stages of the adsorption, as some water molecules prefer to adsorb on other water molecules instead of on the surface. However, using this technique alone, it is not possible to know if, after capillary condensation, water molecules are homogeneously distributed within the pore or if there are zones of higher density than others.

Source of error

The source of this error comes mainly from the selection of the value of P/P_0. In fact, the quantity of water adsorbed continues to increase after capillary condensation, and the isotherm slope in this region varies depending on the material. Those with an exceptionally high adsorption post-condensation are MCM-41 C18 and C18-M7-Ph (see Figure 6.1).

For example, in the case of C18-M7-Ph, for a slight variation in the selected relative pressure of $\Delta P/P_0 = 0.02$ (between $P/P_0 = 0.80$ and 0.82), the quantity of water adsorbed increases by 2.39 %.

There are two possible explanations for this late adsorption of water. The first one is based on the dynamics of water adsorption: if the confined water slowly rearranges itself to accommodate more water molecules, this would produce an augmentation on the quantity of water adsorbed in every subsequent step of the isotherm. However, our experimental method was intended to avoid this kind of error by allowing a long stabilization time at constant pressure for each point of the isotherm (see details in Chapter 3).

The second possible explanation is that this increase in adsorbed water could be due to water condensation in the intergranular cavities. The intergranular condensation in the range of $0.8 < P/P_0 < 1$ is especially large in the intergranular porosity formed by small grains under 100 nm. This is precisely the case of MCM-41 C18 and C18-M7-Ph, as observed by transmission electron microscopy (Chapter 5)

One should not discard a scenario where both processes, densification of the confined water and condensation in the intergranular cavities, happen simultaneously when approaching the saturation pressure ($P/P_0 = 1$).

The value of relative pressure that we have chosen for the determination of the quantity of adsorbed water was $P/P_0 = 0.8$ because, at this relative pressure, the capillary condensation has taken place for all our materials, and the external water condensation for our small grain samples (MCM-41 C18 and C18-M7-Ph) has not taken place.

6.2. Water freezing and melting in amphiphilic nanopores

The liquid-solid phase transition of water confined in our amphiphilic nanopores was studied by differential scanning calorimetry (DSC). Figure 6.3 shows four examples of DSC curves obtained for H_2O confined in selected materials using a scan rate of 2 K min^{-1} for cooling and heating.

In the case of water confined in MCM-41 C18 (D_{SAXS} = 4.5 nm), an endothermic peak centered at 271.8 K corresponds to the melting of excess water outside the nanopores, the small difference with respect to the value of Tm of bulk water (273.15 K) is expected, given that the excess water is also geometrically restraint by the porosity formed between the nanoporous particles. The second peak, centered at 245 K, corresponds to the water confined in the hydrophilic nanopores of MCM-41 C18.

The four curves shown in Figure 6.3 present an endothermic peak around 270 K that corresponds to the excess water, as in the case of MCM-41. From now, we will rather focus on the second peak that corresponds to the melting of confined water.

Water confined in smaller hydrophilic nanopores, such as MCM-41 C12 (D_{SAXS} = 3.2 nm), presents a wider melting peak, centered at a lower temperature (232 K). This is 13 K lower than in the larger pores of MCM-41 C18.

For water confined in C18-M15-Me (D_{SAXS} = 4.3 nm), we observe again a relatively narrow melting peak, centered at quite a lower temperature (231 K) even though the pore size is very similar to MCM-41 C18. The main difference between the two materials is the pore surface hydrophobicity, modified by the methyl groups at the surface of C18-M15-Me.

The last curve corresponds to the extreme case of water confined in C12-M7-Me (D_{SAXS} = 3.0 nm). Due to the combination of a small pore size and the hydrophobicity given by the methyl groups at the surface, no confined melting peak is detected in this curve. Seemingly, water in C12-M7-Me is confined beyond the thermodynamic limit of crystallization that has been reported in the literature.[4]

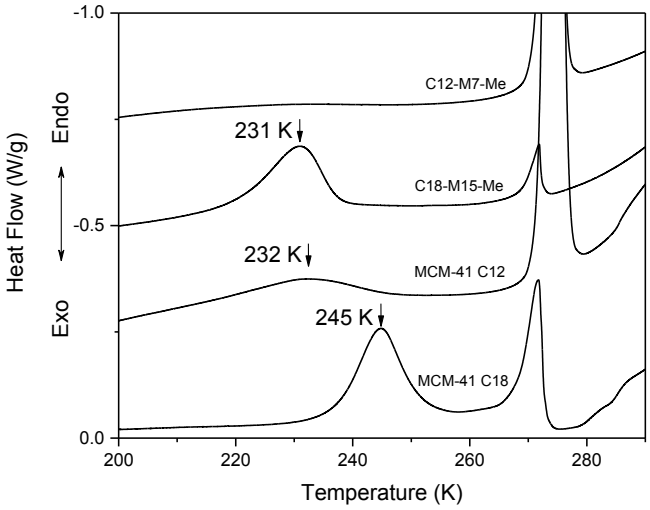

Figure 6.3: Examples of differential scanning calorimetry curves (2 K min^{-1}) of the melting process of water confined in four selected materials: Two hydrophilic cases: MCM-41 C18 (D_{SAXS} = 4.5 nm) and MCM-41 C12 (D_{SAXS} = 3.2 nm) and two amphiphilic cases: C18-M15-Me (D_{SAXS} = 4.3 nm) and C12-M7-Me (D_{SAXS} = 3.0 nm).

Figure 6.4 shows the melting temperature of confined water (maximum of the endothermic peak) as a function of the pore diameter. [5–8]

The melting of water confined in the hydrophilic nanopores of MCM-41 C18 and C12 decreases with decreasing pore size, following the Gibbs-Thomson equation (detailed in Chapter 1), represented as the dashed line. This relationship between the pore size and the melting temperature of confined water in the cylindrical, hydrophilic nanopores of silica materials has been broadly investigated[4,9–11]and it is not the aim of this thesis. These two materials, MCM-41 C12 and MCM-41 C18, are provided here for effects of comparison with amphiphilic nanopores of similar pore size.

The study of the effect of the pore surface chemistry of the pore in the melting temperature of water has been possible because we have used the direct synthesis approach. This approach does not change the pore size significantly, and because the hydrophobicity of the pores is weak enough to let water adsorb in the nanopores at atmospheric pressure. For this reason, there was no need to apply a high intrusion pressure that could affect the density and structure of the confined water.

The results show a significant decrease in the melting temperature of water in all the

amphiphilic materials compared to their hydrophilic homologous MCM-41 C18.

In the series of methyl-modified materials: C18-M7-Me, C18-M10-Me, and C18-M15-Me, the melting temperature of water decreases systematically with an increase of methyl groups present in the material. At its highest value (in C18-M15-Me), the melting temperature of water is surprisingly low, being comparable to water confined in much smaller nanopores, like those of MCM-41 C12.

By changing the organic group to a more voluminous one, like ethyl or phenyl, one would expect a greater effect on the melting temperature of the confined water. This is evidenced in the case of the phenyl-modified material, C18-M7-Ph, with a difference of almost -5 K with respect to C18-M7-Me. However, the case of C18-M7-Et is not significantly different from C18-M7-Me.

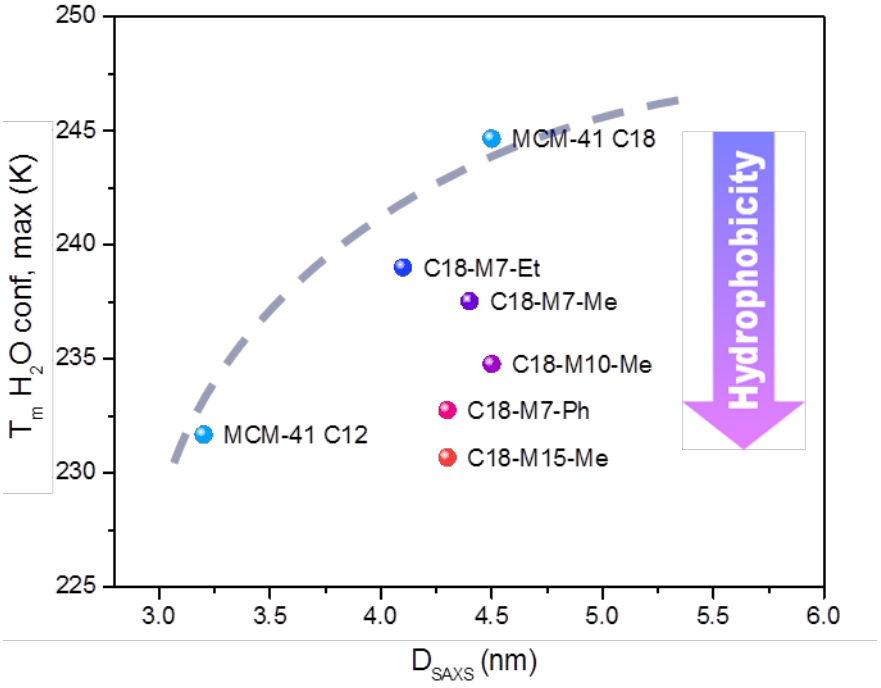

Figure 6.4: Melting temperature of confined H_2O as a function of the pore size. The dashed line is a guide for the eye corresponding to the expected values for hydrophilic MCM-41 materials. P = 1 bar.

The reproducibility of the synthesis method was tested when another chemist (A. Doira, during her master's internship) synthesized additional amphiphilic materials (Figure 6.5, data in Table 6.2). The results show that there is no significant difference between the different syntheses of C18-M15-Me. Nevertheless, in the case of C18-M7-Me, a variation of more than 6 K indicates an important difference in the surface of C18-M7-Me and C18-M7-Me*. From an experimental point of view, this is explained by the fact that the relative error to add the small volume of MTES needed for the precursors' mixture of C18-M7-Me is much higher than for C18-M15-Me. Therefore, the surface properties of C18-M15-Me are more reproducible than those of C18-M7-Me, and this clearly affects the melting point

of confined water.

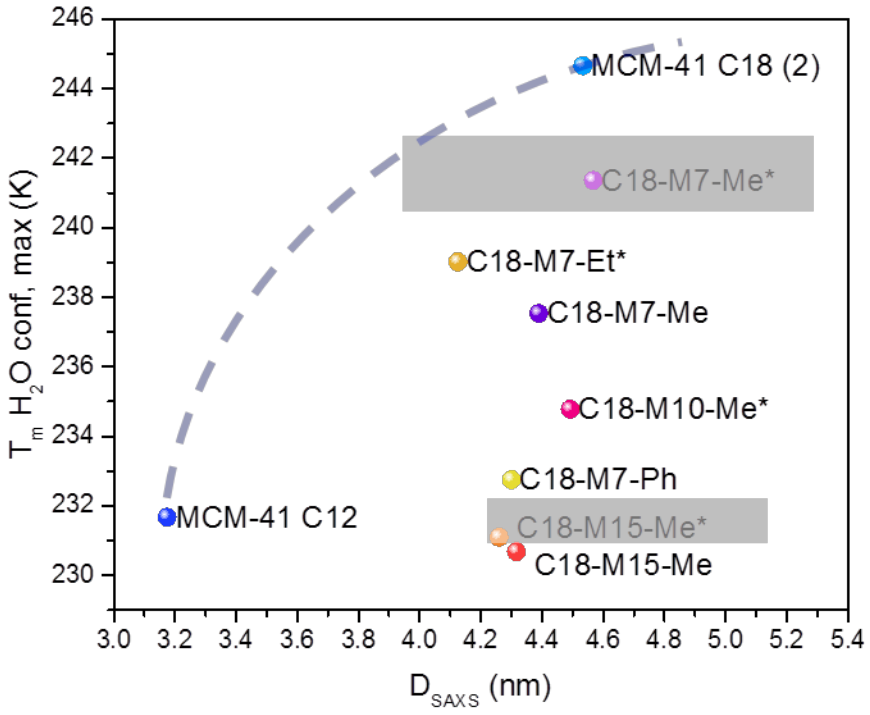

Figure 6.5: Effect of the reproducibility of the synthesis. Materials synthesized by A. Doira are designated with an asterisk (*).

Table 6.2: Pore sizes, reciprocal pore radius, melting temperatures, and melting temperature depletion of confined H_2O and D_2O.

Sample	D_{SAXS} (nm)	$1/R_{SAXS}$ (nm^{-1})	$T_{m\ H2O,\ conf}$ (K)	$T_{m\ D2O,\ conf}$ (K)	$\Delta T_{m\ H2O,\ conf}$ (K)	$\Delta T_{m\ D2O,\ conf}$ (K)
MCM-41 C18	4.5	0.44	245	248	28.5	29.2
MCM-41 C12	3.2	0.63	232	NA[a]	41.5	NA[a]
C18-M7-Et*	4.1	0.48	239	NA[a]	34.1	NA[a]
C18-M7-Me	4.4	0.46	238	NA[a]	35.6	NA[a]
C18-M10-Me*	4.5	0.45	235	NA[a]	38.4	NA[a]
C18-M7-Ph	4.3	0.47	233	237	40.4	40.2
C18-M15-Me	4.3	0.47	231	234	42.5	43.2
C12-M7-Me	3.0	0.67	NA[b]	NA[b]	NA[b]	NA[b]

*Synthesized by A. Doira during her internship. NA[a]: not measured. NA[b]: no crystallization detected by DSC.

Figure 6.6 shows the values of the melting temperature depletion as a function of the inverse of the pore radius. This representation gives a straight line in the case of hydrophilic materials, as denoted by the dashed line. For selected materials (those that

were later used for neutron diffraction experiments, namely MCM-41 C18, C18-M15-Me, C18-M7-Ph, and C12-M7-Me), additional calorimetry experiments have been performed using D_2O. This allowed us to confirm that the melting temperature depletion is independent of the isotopic composition.

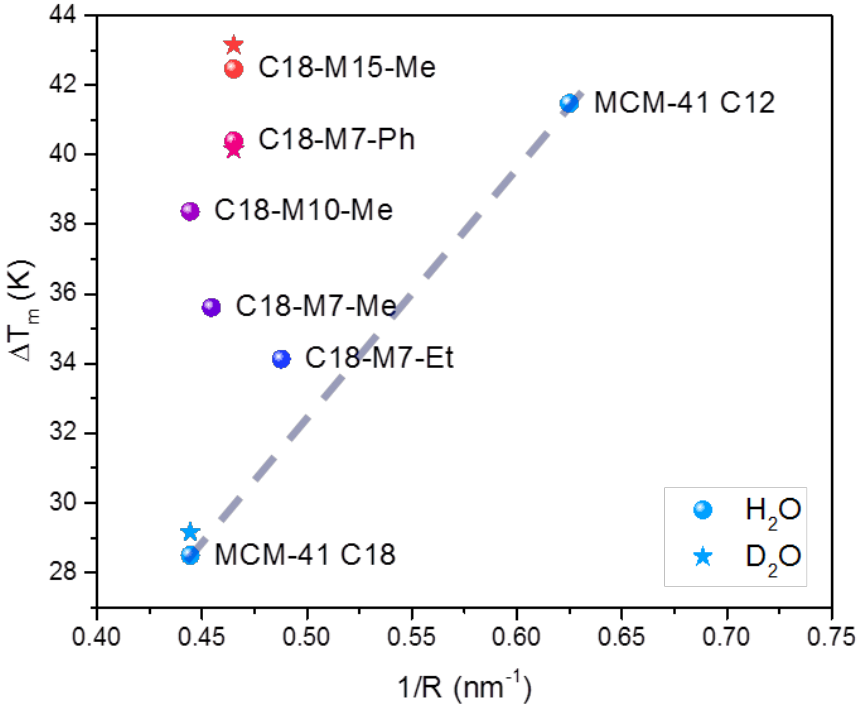

Figure 6.6: Melting point depletion of H_2O (circles) and D_2O (stars) as a function of the reciprocal pore radius. The dashed line is a guide for the eye corresponding to the expected values for hydrophilic MCM-41 materials, in agreement with the Gibbs-Thomson equation. P = 1 bar.

Table 6.3 shows the values of the freezing temperature of water in the nanopores and its difference with respect to the melting temperature (freezing-melting hysteresis). The freezing temperature is susceptible to change with the scan rate, filling factor, and presence of external water. Thus, these parameters were kept constant for the experiment. The scan rate was fixed at 2 $Kmin^{-1}$, the filling factor was f~0.8, assuring no excess water outside of the nanopores.

The thermodynamic limit of crystallization has been related to the point where the freezing-melting hysteresis becomes null. The analysis of this property has allowed us to assess if water confined in the amphiphilic nanopores is closer to, or further away from this limit. From Figure 6.7, it is clear that water confined in the amphiphilic materials presents a significantly lower melting temperature while maintaining a large freezing-melting hysteresis. This means that by using amphiphilic surfaces, one could maintain water in its liquid state at much lower temperatures than established for hydrophilic nanopores[4] of similar pore size.

Table 6.3: Melting temperatures, freezing temperatures, and melting-freezing hysteresis of water confined in

hydrophilic and amphiphilic nanopores. Heating and cooling scan rates = 2 K/min.

Sample	D_{SAXS} (nm)	$T_{m\ H2O,\ conf}$ (K)	$T_{f\ H2O,\ conf}$ (K)	$T_{m\ H2O,\ conf}$ - $T_{f\ H2O,\ conf}$ (K)
MCM-41 C18	4.5	245	235	10
MCM-41 C12	3.2	232	226	6
C18-M7-Et	4.1	239	226	13
C18-M7-Me	4.4	238	229	9
C18-M10-Me	4.3	235	225	10
C18-M7-Ph	4.3	233	224	9
C18-M15-Me	4.3	231	223	8

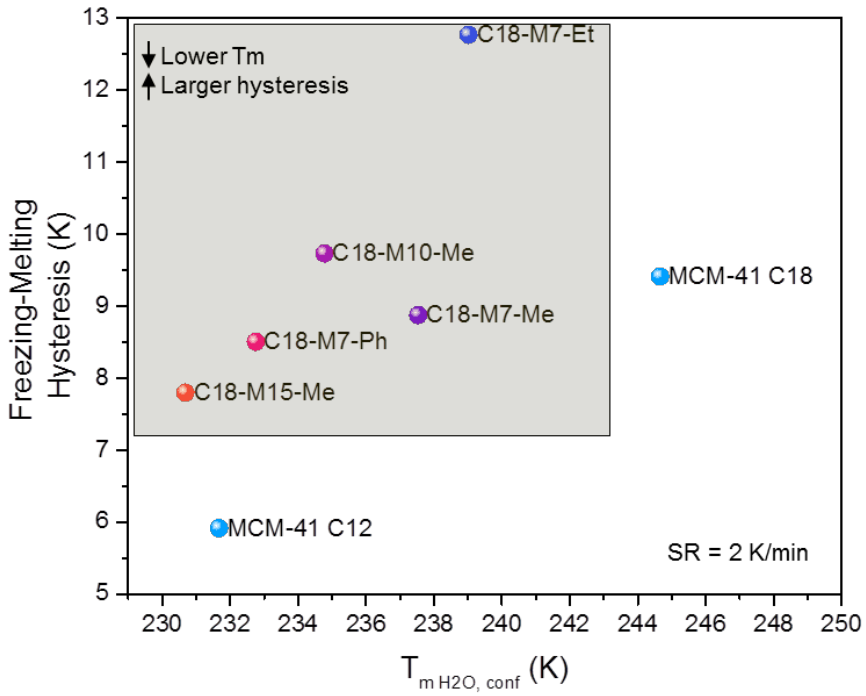

Figure 6.7: Freezing-melting temperature hysteresis as a function of the melting temperature of confined water. The yellow square delimits the values obtained for water confined in amphiphilic materials, where lower Tm, yet larger hysteresis are observed. SR = Scan rate = 2 K/min.

When we analyze the confined water's fusion peak area and divide it by the total amount of confined water, a molar enthalpy of fusion is obtained for the confined material. As shown in Table 6.4, these results are always lower than the molar enthalpy of fusion of bulk water. Same as the melting temperature, this quantity decreases with the hydrophobicity of the material.

A diminution of the enthalpy of fusion has already been observed in the literature for decreasing pore sizes[12,13]. It has been established that the fraction of water crystalized in the nanopore ($\%_{Crystal}$) can be calculated as the apparent molar enthalpy of fusion ($\Delta H_{f,\ Ic}$*) divided by the enthalpy of fusion of the bulk ice (6.05 kJ/mol, for cubic ice formed from

H_2O and 6.16 kJ/mol when formed from D_2O):

$$\%_{Crystal\ H2O,\ i} = \frac{\Delta H_{f,Ic*,i}}{6.05\ kJ/mol} \quad (6.1)$$

$$\%_{Crystal\ D2O,\ j} = \frac{\Delta H_{f,Ic*,j}}{6.16\ kJ/mol} \quad (6.2)$$

For example, the apparent enthalpy of melting in the nanopores of MCM-41 C18 corresponds to 42% of the bulk value, indicating that only such a fraction of the confined ice can be formed in the pore. This value is in agreement with previous simulations and experiments[10,12,13].

The fraction of ice in the nanopores with respect to the total amount of confined water decreases to 26% for C18-M7-Ph and 18% for C18-M15-Me. The percentage of ice formed in the nanopores of C12-M7-Me was not high enough to be detected by the DSC.

Figure 6.8 shows the percentage of ice formed in our amphiphilic nanopores compared with the results obtained by Kittaka *et al.* (2006)[12] for standard SBA-15 and MCM-41 materials of different pore sizes. In this experiment, we have carefully prepared four samples: MCM-41 C18, C18-M7-Ph, C18-M15-Me, and C12-M7-Me, adding approximately 80% of the corresponding pore volume of the material with D_2O. Heavy water was selected to further analyze these samples by neutron diffraction, and a relatively large sample was prepared each time (~500 mg of dry powder + D_2O). Additionally, careful mixing of the sample and at least one hour of equilibration time in a hermetic glass container was needed for all the water to penetrate the nanopores. Such conditions of sample preparation, and a subsequent measurement by thermogravimetric analysis (TGA) to confirm the amount of confined water right after the DSC measurements, allowed us to obtain reliable values of ΔH_f that we can compare with the literature.

Table 6.4: Apparent enthalpy of fusion of confined H D_2O and percentage of frozen D2O calculated from calorimetry experiments

Sample	Molecule	D (nm)	1/R (nm^{-1})	$\Delta H_{f,\ Ic}^{*}$ ($kJ/mol_{Total,\ conf}$)	Crystal by DSC (%)
Bulk H_2O	**H_2O**	-	-	6.05	100
Bulk D_2O	**D_2O**	-	-	6.16	100
MCM-41 C18	**D_2O**	4.5	0.44	2.69	42
C18-M7-Ph	**D_2O**	4.3	0.49	1.64	26
C18-M15-Me	**D_2O**	4.3	0.46	1.12	18

C12-M7-Me	**D_2O**	3.0	0.67	NA	NA
MCM-41 C22[12**]	**H_2O**	4.2	0.48	3.27	54
MCM-41 C18[12**]	**H_2O**	3.6	0.55	2.26	37
MCM-41 C16[12**]	**H_2O**	3.1	0.64	1.75	29
MCM-41 C14[12**]	**H_2O**	2.8	0.70	1.34	22
MCM-41 C12[12**]	**H_2O**	2.4	0.84	0.36	5.9

*Enthalpy of fusion of cubic ice $\Delta H_{f,\,Ic} = \Delta H_{f,\,Ih} + \Delta H_{Ic\text{-}Ih}$; where $\Delta H_{Ic\text{-}Ih}$ =35.6 J mol^{-1}.[14]

**Calcined materials.[12]

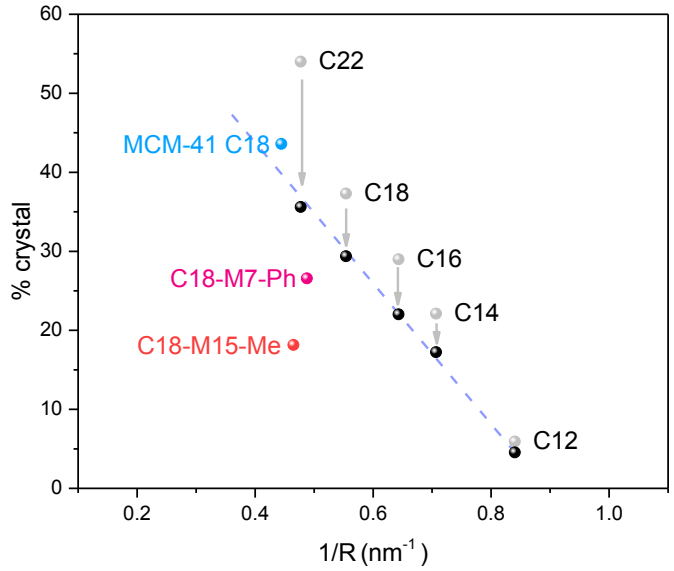

Figure 6.8: Percentage of crystallized water in hydrophilic and amphiphilic nanopores, determined by calorimetry vs. the inverse of the pore radius. Grey dots: data taken from Kittaka et al. (2006)[12]: The pore diameter was calculated using the Dollimore Hill relation, and the value of ΔH_f was calculated from DSC curves, considering the amount of water from capillary condensation, excluding the volume of the monolayer adjacent to the pore wall (approx. 20-30% of the pore volume). Black dots: The %crystal decreases when considering all the pore volume (including the adsorption monolayer). Color dots: Our selected materials MCM-41 C18 (washed), C18-M15-Me, and C18-M7-Ph (water confined in C12-M7-Me does not crystallize). The dashed line is a guide for the eye to differentiate the effect of a decreasing pore size from the effect of an increasing hydrophobicity of the pore wall of our amphiphilic materials.

From figure 6.8, we observe that the percentage of confined water in the nanopores that crystallizes decreases with the nanopore size. This percentage approaches zero at 1/R ~ 0.8, which corresponds to a pore diameter of ~2.5 nm, in close agreement with the values estimated in the literature for the thermodynamic limit of crystallization of water in MCM-41-type nanopores (D_{KJS} = 2.8 nm[10] and D_{BET} = 2.2 nm in hydrophobic materials using intrusion[4])

Similar to the melting temperature, the percentages of ice obtained in our selected amphiphilic materials deviate from the behavior of water confined in hydrophilic

nanopores. For materials with increasing hydrophobicity C18-M7-Ph and C18-M15-Me, the fraction of water that can form a crystal is significantly lower than expected for ~4 nm nanopores and consistent with a lower T_m.

6.3. Ice structure in amphiphilic confinement

The structure of ice confined in the selected materials (MCM-41 C18, C18-M7-Ph, C18-M15-Me, and C12-M7-Me) was studied using neutron diffraction. As mentioned in the previous section, a filling factor of approximately 80 % (f ~0.8) at room temperature was used to avoid water expulsion from the nanopores upon a decrease in its density during the temperature ramp, cooling down to 180 K. This was verified by the absence of the peak corresponding to the melting of excess water.

The lowest temperature of 180 K was chosen based on our DSC results. This, together with a slow cooling ramp (> 8h from 298 K to 180 K), was to ensure the maximum amount of crystallized water in all samples. Several diffraction curves were measured during the cooling and heating cycles to assess the evolution of the confined water's structure caused by the temperature variation. As in the previous section, we will give special attention to the melting process of confined ice.

The data treatment (detailed in Chapter 4) involves subtracting the signal from the dried confining material. However, this correction does not account for the cross terms between the surface and confined water. For this reason, we will not use these results to attempt to establish a pair correlation function of the confined water.

On the melting process

Figure 6.9 shows several diffraction curves taken during the melting process of D_2O confined in C18-M15-Me. Here, it can be clearly distinguished that the Bragg peaks of ice disappear between 220 and 240 K. From this temperature, the typical diffraction pattern of liquid water appears[15,16].

The evolution of what we considered the most critical features of the diffraction curves versus the temperature is represented in Figure 6.10. Here we can see how the maximum of the structure factor (Q_{max}) and S(Q) intensity, at different relevant wave vector values, such as 1.0 $Å^{-1}$, 1.7 $Å^{-1,}$ and 2.8 $Å^{-1}$, change during the temperature ramp, heating from 180 to 260 K.

The position of the maximum of the structure factor shifts from 1.7 $Å^{-1}$ to 1.85 $Å^{-1}$ between 220 and 250 K (light blue curve). Likewise, the intensity of the Bragg peaks at 1.7 $Å^{-1}$ and 2.8 $Å^{-1}$ decreases sharply in this range of temperature (pink and green curves, respectively).

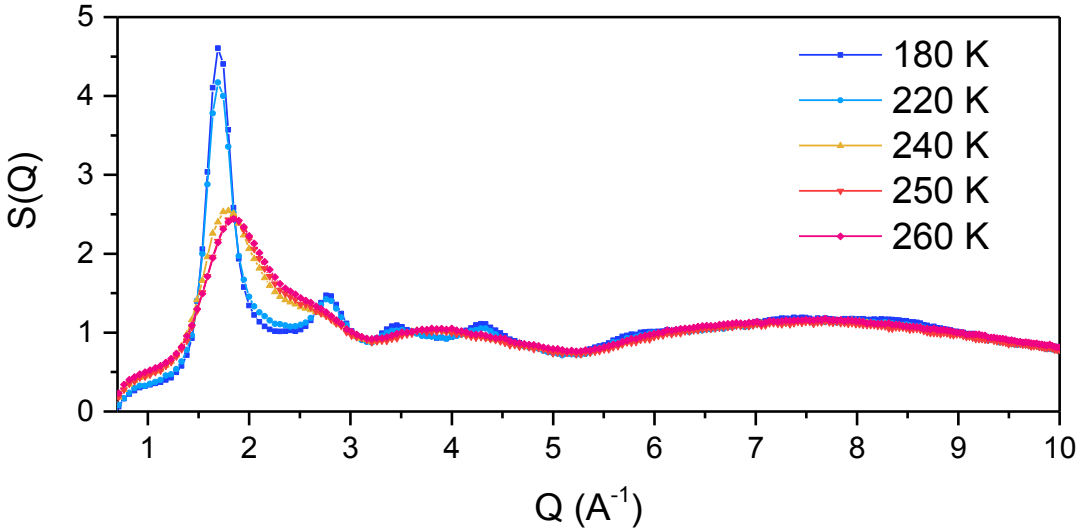

Figure 6.9: Neutron diffraction curves of water confined in C18-M15-Me during the melting process from 180 K to 260 K. The corrections applied to the curves are detailed in section 4.4 of chapter 4.

These changes in the structure factor correspond to the variation of intermolecular terms during the solid-liquid phase transition of confined water. The structure factor of the ice confined in C18-M15-Me is characterized by the Bragg peaks at 1.7, 2.8, 3.4, and 4.3 $Å^{-1}$. This structure is stable for temperatures up to 220 K when the melting process starts, and the ice transforms into liquid water, which is denser and less organized. For this reason, we observe a sudden shift of Q_{max} to larger Q values and the vanishing of the Bragg peaks.

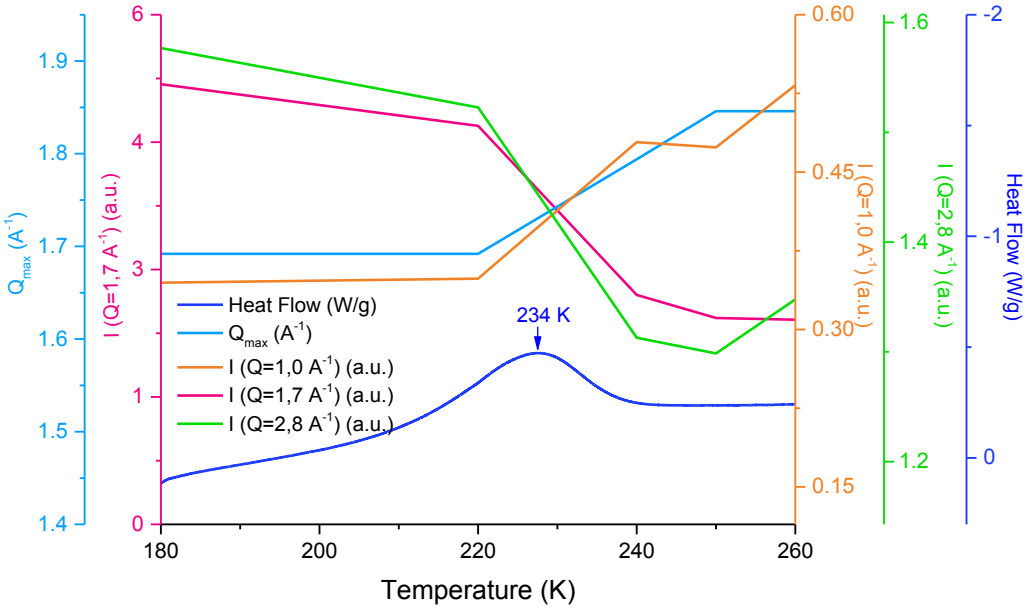

Figure 6.10: Evolution of selected features from the neutron diffraction curves of D_2O confined in C18-M15-Me versus the temperature during the heating ramp from 180 to 260 K at 1 bar. The maximum of the structure factor (Q_{max}) (light blue) and the intensity of S(Q) at Q = 1.0 $Å^{-1}$ (orange), 1.7 $Å^{-1}$ (pink) and 2.8 $Å^{-1}$(green). In dark blue, the DSC curve of D_2O@C18-M15-Me showing the endothermic peak of the melting of confined ice in the same temperature range.

We have also studied the intensity at the smallest Q region of the spectrum, sensitive to variations in the macroscopic compressibility[17]. The relationship between the intensity of S(Q = 0) and this property of the water molecule is given by the equation:

$$S(Q = 0) = \rho_M k_B T \chi_T$$

where ρ_M is the molecular density, k_B is the Boltzman constant, and χ_T is the isothermal compressibility.

Unfortunately, we do not have access to the Q range lower than 0.8, as the curves are significantly altered by the subtraction of the empty matrix and our measurements are also limited by the artifacts caused by the signal coming from the direct beam in the 7C2 spectrometer. Therefore, we have limited our study to Q = 1.0 $Å^{-1}$.

The evolution of S(Q= 1.0 $Å^{-1}$) (orange curve) shows a slight rise from 180 to 220 K, followed by a sudden increase in two steps from 220 to 240 K and 250 to 260 K. This fact remains compatible with an increase in the macroscopic compressibility of liquid water with respect to its solid phase.

The obtained results on the melting behavior captured by neutron diffraction are in complete agreement with the DSC results presented in the previous section (dark blue curve).

Neutron structure factor of confined water at 180 K

Figure 6.11 shows the neutron diffraction patterns of confined ice in the studied nanoporous materials at 180 K and 1 bar.

Our first observation was the absence of several Bragg peaks of hexagonal (bulk) D_2O (at 1.6, 1.8, and 2.35 $Å^{-1}$). This served as confirmation of the DSC experiments, proving that all the water was located inside the nanopores during the recording of the neutron diffraction spectra.

As reported in the literature for water crystals in confined geometry[18], we have found the signature of stacking disorder ice (I_{SD}) in all the C18 samples. This structure consists of randomly mixed cubic and hexagonal planes[19–22], as shown schematically in Figure 6.12. It has been found that only the common peaks of hexagonal and cubic ice (continuous vertical lines at Q = 1.7, 2.8, 3.4, and 4.3 $Å^{-1}$ in Figure 6.11) are observed in the diffraction curves.

However, there is a subtle difference in the case of C18-M7-Ph. Unlike in the rest of the samples, the high order hexagonal peak (102) (dashed vertical line at 2.4 $Å^{-1}$ in Figure 6.11) is noticeable, even though its intensity is relatively weak compared to the rest of the peaks.

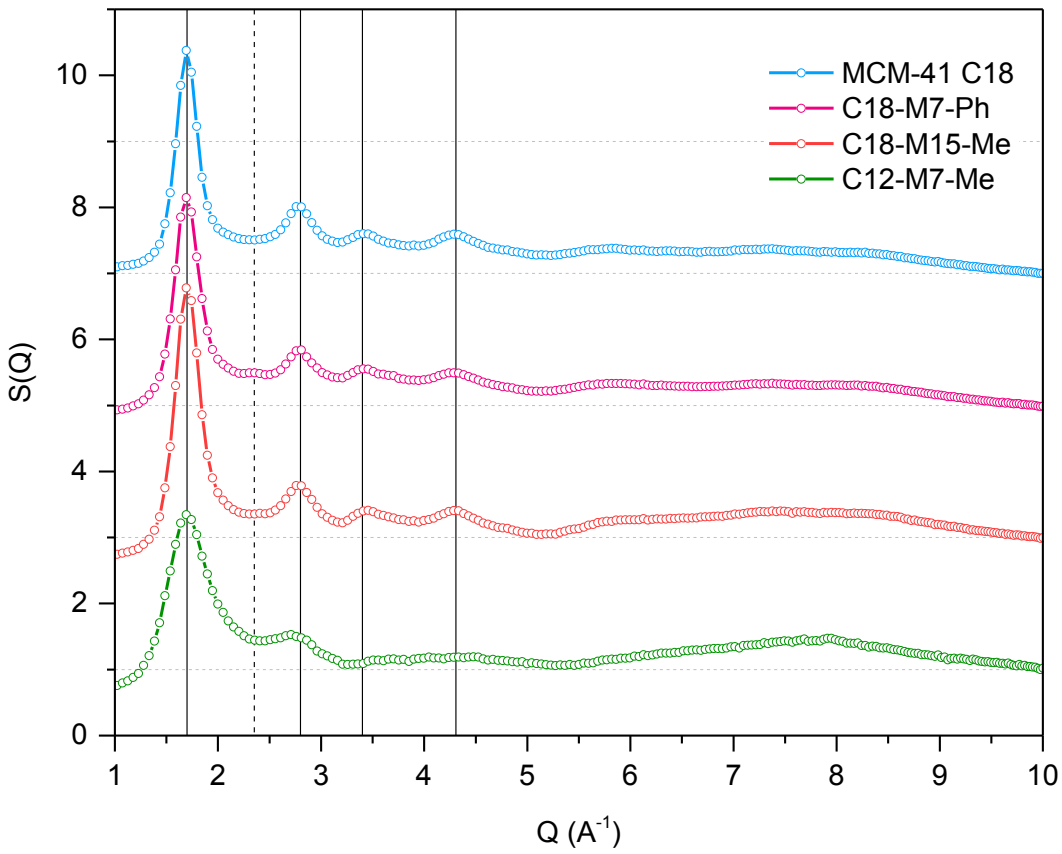

Figure 6.11: Neutron diffraction patterns (7C2@Orphée) of D_2O confined in selected materials with a filling factor of approx. 80% (f = 0.8) at 1 bar and 180 K. The curves are vertically offset for clarity. The vertical lines indicate the position of the (002) peak of hexagonal ice and (111) peak of cubic ice at 1.7 $Å^{-1}$, the (110) peak of hexagonal ice and (220) peak of cubic ice at 2.8 $Å^{-1}$, and the (112) peak of hexagonal ice and (311) peak of cubic ice at 3.4 $Å^{-1}$. 4.3 $Å^{-1}$

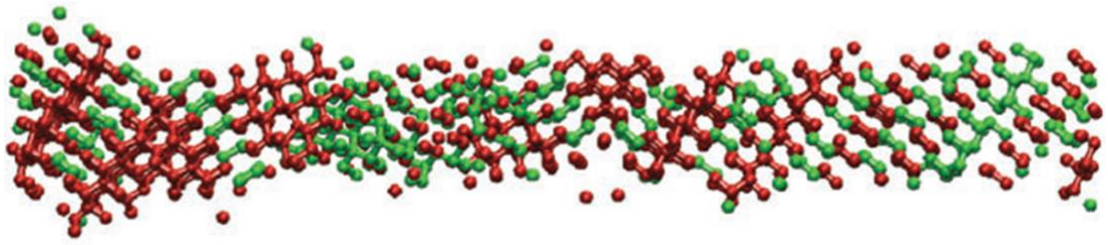

Figure 6.12: Configuration of crystallized water in a 3 nm hydrophilic nanopore at 195 K using molecular dynamics simulations with the mW water model (Tm simulated 225 K). The structure shows a stacking disorder of hexagonal (green) and cubic ice layers (red). Extracted from Moore et al. (2010).[13]

Another remarkable case is C12-M7-Me, where the absence of the peaks located at 3.4 $Å^{-1}$ and 4.3 $Å^{-1}$ indicates a much less structured form of water. This is compatible with the structure found by Yoshida et al. (2008)[16] for D_2O in MCM-41 C10. The signature resembles the low-density amorphous form of water (Figure 6.13). This result is in agreement with the fact that no endothermic peak for the melting of confined water is observed in the DSC curves of this sample, and it serves as a confirmation of the hypothesis that water confined in C12-M7-Me must be beyond the thermodynamic limit of crystallization.

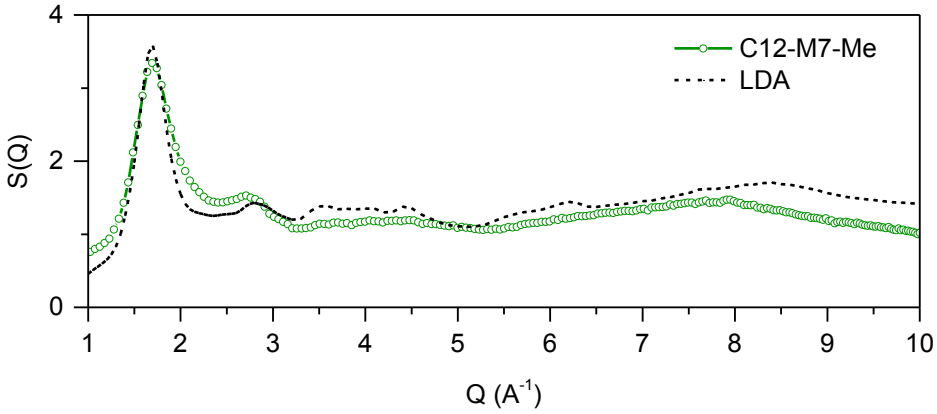

Figure 6.13: Neutron diffraction pattern of D2O confined C12-M7-Me. The structure of water confined in this amphiphilic material with a small pore size (D_{SAXS} = 3 nm) is compared to the low density amorphous of water (courtesy of MC Bellissent-Funel)

For the other three samples (MCM-41 C18, C18-M7-Ph, and C18-M15-Me), the diffraction curves are more structured. So, we performed a more detailed analysis of the structure of confined ice using the crystallographic software FullProf (Figure 6.14). This analysis allowed us to fit the peaks of the diffraction patterns with the structure of hexagonal and cubic ice and estimate the crystallites' size using the Rietveld method.

Table 6.5 summarizes the results of the neutron diffraction fit: the percentage of the crystalline and amorphous phase with respect to the total amount of confined water, the fractions of hexagonal and cubic ice present in the crystalline phase, and the ice crystallite size.

Table 6.5: Physical properties of the confined ice extracted from the fit of the neutron diffraction curves using FullProf.

Sample	D_{SAXS} (nm)	Crystal by DSC (%)	Crystal by ND (%)	Amorphous by ND (%)	I_h in crystal (%)	I_c in crystal (%)	Ice grain size (nm)
MCM-41 C18	4.5	42	55	45	23	77	2.8
C18-M7-Ph	4.1	26	31	69	33	67	1.9
C18-M15-Me	4.3	18	28	72	24	76	1.7

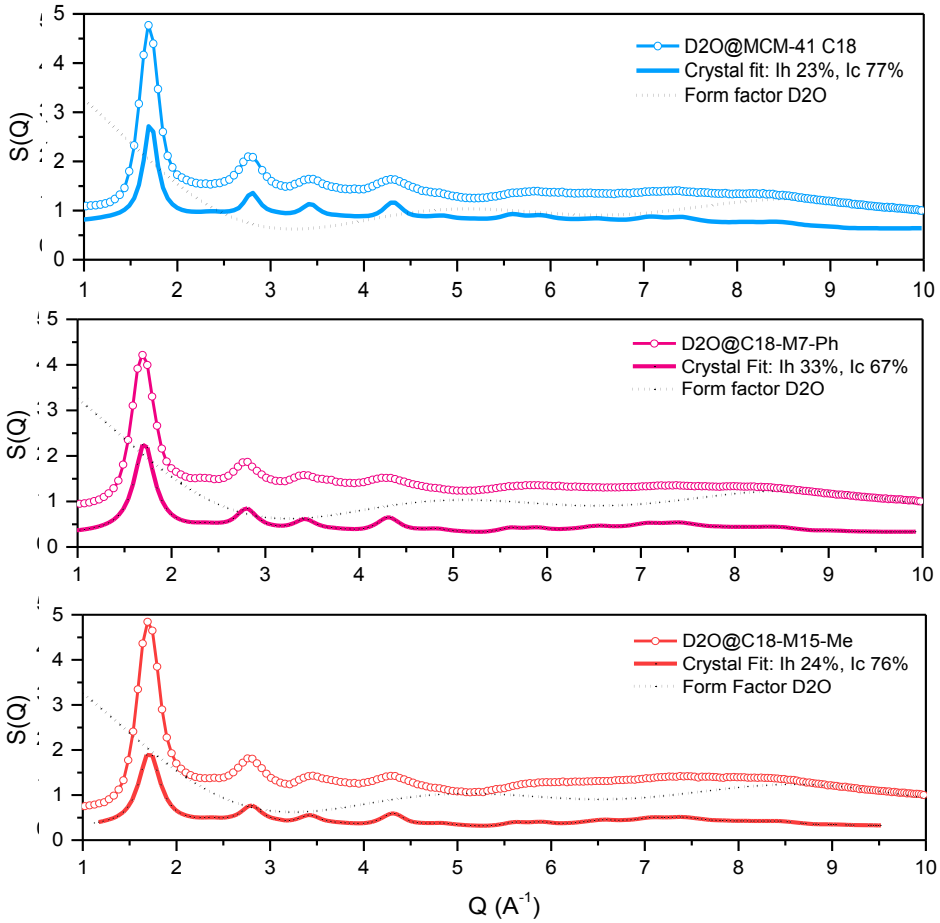

Figure 6.14: Results of the FullProf data fit for D_2O confined in MCM-41 C18, C18-M7-Ph, and C18-M15-Me at 1 bar and 180 K. The dashed line corresponds to the form factor of crystallized D_2O.

We find that the percentage of crystal found by neutron diffraction is always higher than the value obtained from DSC. This variation may partly come from the temperature difference of the measurements. For neutron diffraction, we have used the curves obtained at 180 K, whereas the analysis of the enthalpy by DSC is performed around the melting temperature of the confined water (230 K – 245 K). It is possible that, on one hand, at lower temperatures, confined ice crystals continue to grow and rearrange[23] within the nanopore. On the other hand pre-melting could occur for the smallest grains at higher temperature.

The percentages of hexagonal and cubic ice found are in close agreement with the simulation results of Moore and Molinero (2011)[20]. They predict a proportion of hexagonal to cubic layers of 1:2 (33 % hexagonal vs. 67 % cubic). As expected, the percentage of hexagonal ice is highest in C18-M7-Ph, which was the only diffraction curve with a visible high-order peak at 2.4 $Å^{-1}$. From these results, it seems that the presence of phenyl groups at the surface may favor the growth of hexagonal ice layers.

The Rietveld refinement method was used to estimate the size of the crystallites, taking into account the instrumental resolution of the 7C2 spectrometer. The main idea behind this analysis is that smaller crystallites produce wider diffraction peaks. The results indicate

that the crystallites are significantly smaller than the dimensions offered by the nanopore, and they reduce significantly when there are organic groups present at the surface. The values found here are in close agreement with the critical size of ice nuclei in a 3 nm hydrophilic nanopores estimated by Moore *et al.* (2010)[13], between 75 to 100 water molecules (D = 1.6 - 2.4 nm), and to the value determined experimentally by Moberg *et al.* (2019)[24] using IR spectroscopy (~90 water molecules)[24].

When we plotted the difference between the crystal fit and the overall diffraction pattern (Figure 6.15), we obtained a residual amorphous confined water. It is, however, more difficult to conclude on the structure of the amorphous water. Only for C18-M15-Me, where the percentage of amorphous is the largest, the residual structure is similar to the low density amorphous of water (LDA). However, its location in the pore is not defined and remains difficult to compare to bulk LDA.

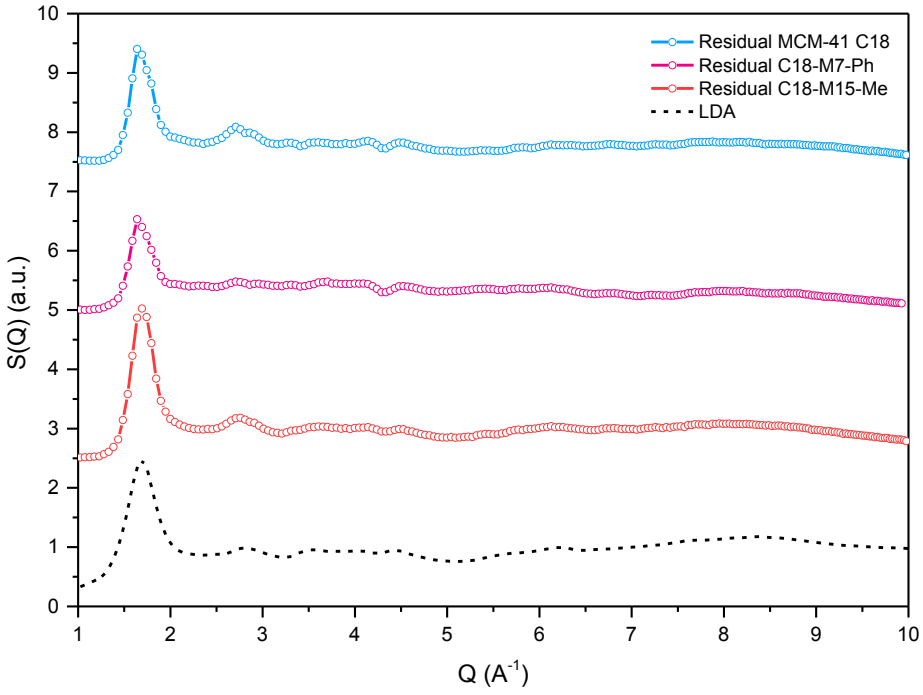

Figure 6.15: Residual (Data – Crystal Fit) for D_2O confined in MCM-41 C18, C18-M7-Ph, and C18-M15-Me at 1 bar and 180 K and structure factor of the low density amorphous (LDA) form of water (courtesy of MC Bellissent-Funel). The curves are shifted for clarity.

6.4. Dynamics of water confined in amphiphilic nanopores

To address the issue of water dynamics when it is confined in amphiphilic materials, we performed neutron spin-echo experiments to determine the relaxation times of D_2O in C18-M7-Ph and C8M15Me. However, experimental complications arose from the fact that the organic groups at the surface contain hydrogen atoms with a large incoherent scatter-

ing cross-section. Incoherent scattering decreases the neutron beam polarization, and thus, the signal of neutron spin echo, especially above 270 K. On the other hand, measurements at lower temperatures (below 250 K) were not successful because the crystallization process had already started.

For these reasons, we were only able to make three exploitable measurements between 270 K and 250 K. Figure 6.16 shows the intermediate scattering functions, and the Kohlrausch–Williams–Watts (KWW) stretched exponential fit. Note that the large error bars and dispersity of the data reflect the limitations of the experiment.

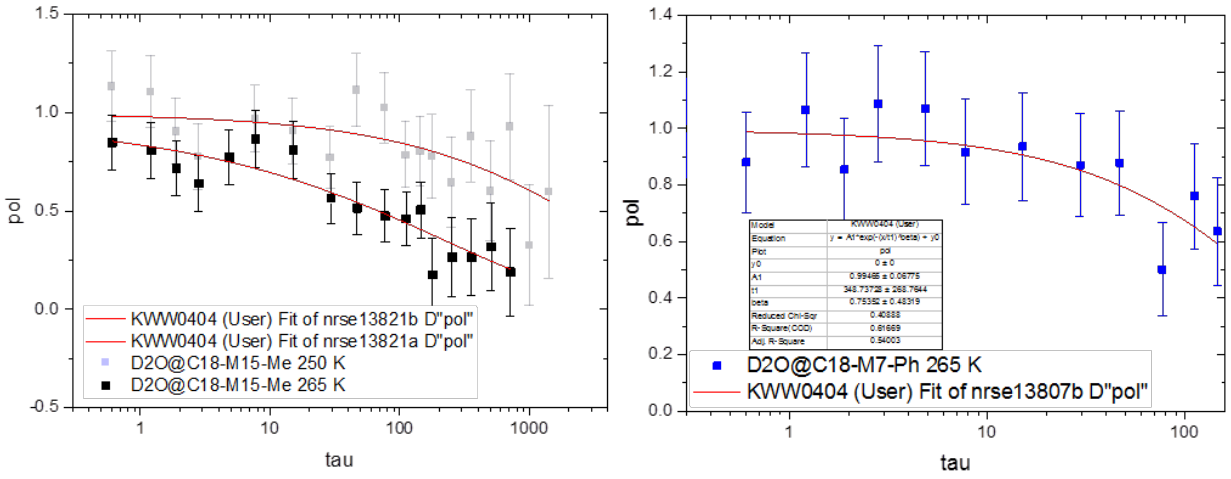

Figure 6.16: Intermediate scattering functions divided by the resolution for D2O confined in amphiphilic nanoporous materials (C18-M15-Me and C18-M7-Ph) at Q = 1.7 $Å^{-1}$. The red lines show the fits with the KWW stretched exponential function.

The obtained relaxation times of liquid water confined in amphiphilic nanopores are represented with stars in Figure 6.17. Here, we compare our results to the dynamics of bulk water[25], water confined in SBA-15, MCM-41 C10, and water intercalated in graphite oxide layers[26]. We compare both confined H_2O and D_2O, bearing in mind that confined water exhibits a much weaker isotope effect than bulk water[27]. We found that water confined in amphiphilic nanopores was two decades ($x10^2$) slower than bulk water and one decade ($x10^1$) slower than water confined in hydrophilic nanopores. The relaxation times found here are similar to those obtained by Cerveny *et al.* (2010)[26] for H_2O (25 wt %) intercalated in graphite oxide (the interlayer distance for the hydrated sample was 0.8 nm).

From our results, it seems that the organic (methyl and phenyl) groups at the surface slow down water molecules, which is in agreement with a reduced ability to form a crystal. However, due to the limitations of the technique, additional measurements need to be performed to confirm this trend. A different result was found by Jani *et al.* (2021) when they compared the dynamics of water confined in hydrophilic MCM-41 and more hydrophobic organosilicas (Divinil-benzene PMO). They found that the largest slowdown were obtained for the hydrophilic silicas.[28]

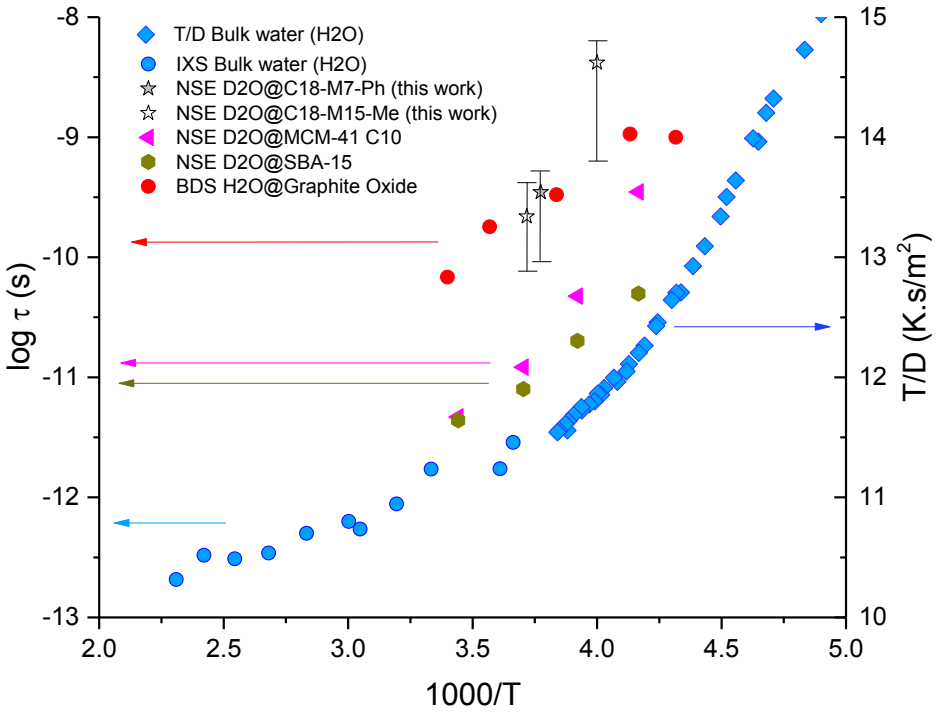

Figure 6.17: Dynamics of bulk and confined water. Relaxation times of Bulk H_2O (blue circles), the continuation of the curve is given by the diffusion coefficient of H_2O[25] (to be read using the right Y scale). Relaxation times of D_2O confined in C18-M7-Ph and C18-M15-Me (stars, this work), D_2O confined in MCM-41 C10 (pink triangles) and SBA-15 (green circles), and H_2O intercalated in graphite oxide layers (red circles)[26].

6.5. Conclusion

The results of this chapter show the marked effect of the surface chemistry on the thermodynamic properties of confined water at atmospheric pressure. We have found significant differences in the density, melting point, percentage of water that crystallizes, and the size of the ice grains formed.

The density of confined water decreases with respect to water confined in hydrophilic MCM-41 when organic groups are present at the surface of the nanopores. However, at 298.15 K, we did not find significant variations among C18-M7-Me, C18-M15-Me, and C18-M7-Ph. Now, when we reduce the system's temperature, we start noticing striking differences among the samples. We found a clear trend in the melting temperature depletion, according to the material's hydrophobicity, and this goes together with a decrease in the percentage of crystal obtained by DSC and neutron diffraction (Figure 6.18). In these amphiphilic materials, ΔT_m is better correlated to the size of the grain of ice formed than to the nanopore size. Another interesting finding was that a decrease in the

melting temperature was also followed by a systematic decrease in the freezing-melting hysteresis.

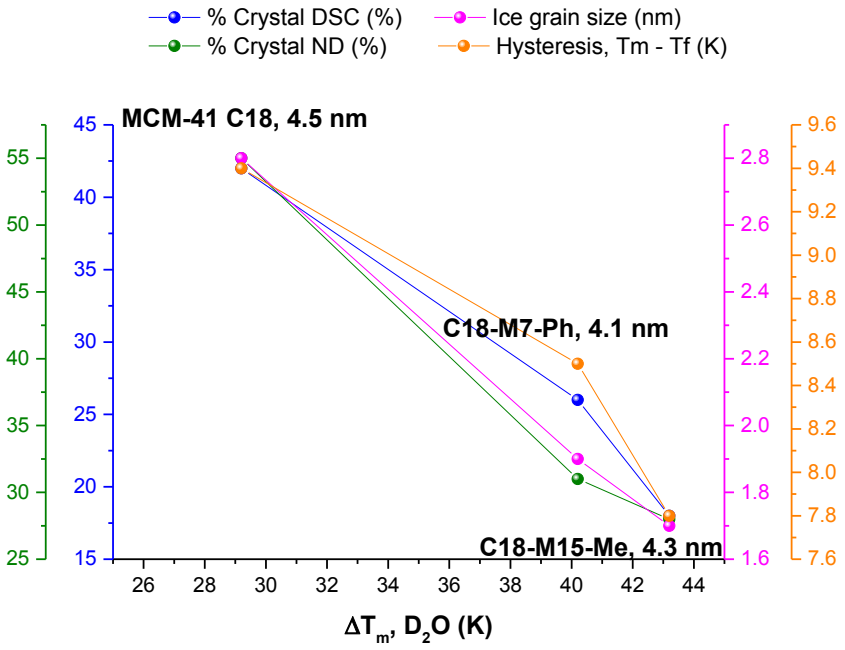

Figure 6.18: Percentage of crystal by DSC and neutron diffraction, ice grain size, and hysteresis as a function of the melting temperature depletion for hydrophilic and amphiphilic nanoporous materials.

The effect of the pore wall hydrophobicity was also studied by Morishige (2018)[1], using DSC and X-ray diffraction to assess the melting point depression and structure of ice confined in ordered mesoporous carbons with pore diameters between 6.4 nm and 16.4 nm. On the structure of confined water at 200 K, they found a good fit for a linear combination of a crystalline and an amorphous component attributed to a non-freezable layer of water between the pore surface and a crystalline ice core. Concerning the melting point depression, he did not find any significant difference with respect to hydrophilic silica of similar pore size (significantly larger pore sizes than in this study).

The results shown in this chapter agree with those of Morishige (2018)[1] in that the structure of confined water at low temperatures contains a crystalline component and an amorphous component coming from non-freezable water. However, a liquid layer next to the pore wall would not be sufficient to explain the small size of ice crystallites. This is why we propose that the liquid-like fraction of water presents a non-homogeneous distribution around the ice grains in the nanopores, and especially neighboring the organic groups at the surface of the amphiphilic materials, as schematized in Figure 7.19.

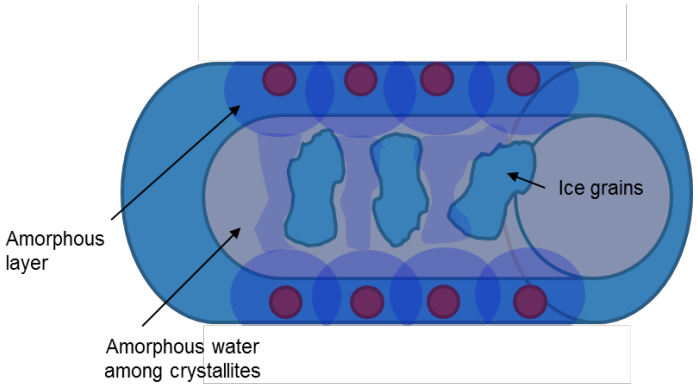

Figure 7.19: Schematic representation of ice in an amphiphilic nanopore. The red circles represent the organic groups at the surface. The ice I_{SD} grains and amorphous liquid-like water exist in a non-homogeneous distribution.

Our results on the marked effect of the pore wall hydrophobicity in the melting point depression of water confined in amphiphilic nanopores (D ~4.5 nm) contrast those of Morishige (2018). In our opinion, this effect was not noticeable in the mesoporous carbons due to their relatively large pore size (6.4 nm to 16.4 nm), which makes the number of water molecules in contact with the surface was relatively small with respect to the bulk-like water in the core of the nanopores.

Based on our observations of the effect of the pore surface chemistry on the fraction of non-freezable water, crystallite size, and dynamics of the confined water, we conclude that the ice confined in our amphiphilic nanoporous materials (C18-M15-Me and C18-M7-Ph) was able to nucleate but not to grow. This is probably due to an environment constrained by organic groups that slow down water molecules in such a way that they cannot contribute to the crystal's growth.

References

1. Morishige, K. Influence of Pore Wall Hydrophobicity on Freezing and Melting of Confined Water. *J. Phys. Chem. C* **122**, 5013–5019 (2018).
2. Jelassi, J. *et al.* Studies of water and ice in hydrophilic and hydrophobic mesoporous silicas: pore characterisation and phase transformations. *Phys. Chem. Chem. Phys.* **12**, 2838 (2010).
3. Hirama, Y., Takahashi, T., Hino, M. & Sato, T. Studies of Water Adsorbed in Porous Vycor Glass. *Journal of Colloid and Interface Science* **184**, 349–359 (1996).
4. Deschamps, J., Audonnet, F., Brodie-Linder, N., Schoeffel, M. & Alba-Simionesco, C. A thermodynamic limit of the melting/freezing processes of water under strongly hydrophobic nanoscopic confinement. *Phys. Chem. Chem. Phys.* **12**, 1440–1443 (2010).
5. Takei, T. *et al.* Changes in density and surface tension of water in silica pores. *Colloid & Polymer Science* **278**, 475–480 (2000).
6. Rother, G. *et al.* Water Uptake by Silica Nanopores: Impacts of Surface Hydrophilicity and Pore Size. *J. Phys. Chem. C* **124**, 15188–15194 (2020).
7. Kocherbitov, V. & Alfredsson, V. Hydration of MCM-41 Studied by Sorption Calorimetry. *J. Phys. Chem. C* **111**, 12906–12913 (2007).
8. Thommes, M. *et al.* Physisorption of gases, with special reference to the evaluation of surface area and pore size distribution (IUPAC Technical Report). *Pure and Applied Chemistry* **87**, 1051–1069 (2015).
9. Schreiber, A., Ketelsen, I. & Findenegg, G. H. Melting and freezing of water in ordered mesoporous silica materials. *Physical Chemistry Chemical Physics* **3**, 1185–1195 (2001).
10. Jähnert, S. *et al.* Melting and freezing of water in cylindrical silica nanopores. *Phys. Chem. Chem. Phys.* **10**, 6039 (2008).
11. Findenegg, G. H., Jähnert, S. & Schreiber, A. Freezing of Water in Cylindrical Nanopores. in *Poromechanics V* 693–700 (American Society of Civil Engineers, 2013). doi:10.1061/9780784412992.082.
12. Kittaka, S., Ishimaru, S., Kuranishi, M., Matsuda, T. & Yamaguchi, T. Enthalpy and interfacial free energy changes of water capillary condensed in mesoporous silica, MCM-41 and SBA-15. *Physical Chemistry Chemical Physics* **8**, 3223 (2006).
13. Moore, E. B., de la Llave, E., Welke, K., Scherlis, D. A. & Molinero, V. Freezing, melting and structure of ice in a hydrophilic nanopore. *Physical Chemistry Chemical Physics* **12**, 4124 (2010).

14. Yamamuro, O., Oguni, M., Matsuo, T. & Suga, H. Heat capacity and glass transition of pure and doped cubic ices†. *Journal of Physics and Chemistry of Solids* **48**, 935–942 (1987).

15. Bellissent-Funel, M. -C., Lal, J. & Bosio, L. Structural study of water confined in porous glass by neutron scattering. *The Journal of Chemical Physics* **98**, 4246–4252 (1993).

16. Yoshida, K., Yamaguchi, T., Kittaka, S., Bellissent-Funel, M.-C. & Fouquet, P. Thermodynamic, structural, and dynamic properties of supercooled water confined in mesoporous MCM-41 studied with calorimetric, neutron diffraction, and neutron spin echo measurements. *The Journal of Chemical Physics* **129**, 054702 (2008).

17. Morineau, D. & Alba-Simionesco, C. Hydrogen-bond-induced clustering in the fragile glass-forming liquid *m* -toluidine: Experiments and simulations. *The Journal of Chemical Physics* **109**, 8494–8503 (1998).

18. Dore, J., Webber, B., Hartl, M., Behrens, P. & Hansen, T. Neutron diffraction studies of structural phase transformations for water–ice in confined geometry. *Physica A: Statistical Mechanics and its Applications* **314**, 501–507 (2002).

19. Morishige, K. & Uematsu, H. The proper structure of cubic ice confined in mesopores. *The Journal of Chemical Physics* **122**, 044711 (2005).

20. Moore, E. B. & Molinero, V. Is it cubic? Ice crystallization from deeply supercooled water. *Physical Chemistry Chemical Physics* **13**, 20008 (2011).

21. Malkin, T. L., Murray, B. J., Brukhno, A. V., Anwar, J. & Salzmann, C. G. Structure of ice crystallized from supercooled water. *Proceedings of the National Academy of Sciences* **109**, 1041–1045 (2012).

22. Malkin, T. L. *et al.* Stacking disorder in ice I. *Physical Chemistry Chemical Physics* **17**, 60–76 (2015).

23. Thurmer, K. & Nie, S. Formation of hexagonal and cubic ice during low-temperature growth. *Proceedings of the National Academy of Sciences* **110**, 11757–11762 (2013).

24. Moberg, D. R. *et al.* The end of ice I. *Proc Natl Acad Sci USA* **116**, 24413–24419 (2019).

25. Xu, Y., Petrik, N. G., Smith, R. S., Kay, B. D. & Kimmel, G. A. Growth rate of crystalline ice and the diffusivity of supercooled water from 126 to 262 K. *Proc Natl Acad Sci USA* **113**, 14921–14925 (2016).

26. Cerveny, S., Barroso-Bujans, F., Alegría, Á. & Colmenero, J. Dynamics of Water Intercalated in Graphite Oxide. *J. Phys. Chem. C* **114**, 2604–2612 (2010).

27. Agapov, A., Novikov, V. N., Kisliuk, A., Richert, R. & Sokolov, A. P. Role of quantum fluctuations in structural dynamics of liquids of light molecules. *The Journal of Chemical Physics* **145**, 234507 (2016).

28. Jani, A. *et al.* Dynamics of water confined in mesopores with variable surface interaction. *J. Chem. Phys.* **154**, 094505 (2021).

CHAPTER 7

HYDROPHOBIC WATER CONFINEMENT USING HIGH PRESSURE

In the previous chapters, we have seen how nanoporous silica materials with different levels of hydrophobicity (hydrophilic, amphiphilic, and hydrophobic) have been synthesized. In addition, we have seen that remarkable differences in water behavior (including the decrease in its melting point, percentage of crystallized water, and slower dynamics) can be triggered by introducing a small number of organic groups in the confining material's framework.

This time, we will focus on water confined in highly hydrophobic materials. For this purpose, we have used the recently synthesized post-grafted organosilicas C18-M15-Me $SiMe_3$ and C18-M7-Me $SiMe_3$. We have also used a sample of post-grafted C14 MCM-41 $SiMe_3$ previously synthesized by our group for effects of comparison.

This chapter is divided into three sections. The first one is dedicated to water vapor adsorption on hydrophobic nanopores. This technique was used to confirm the hydrophobic character and the stability of the material before embarking on neutron experiments.

Second, we will discuss the study of water intrusion in hydrophobic nanopores at high pressures, followed by neutron imagery. This macroscopic technique allowed the determination of the intrusion pressure and the estimation of the quantity of water introduced into the nanopores.

Finally, we will discuss the structure of water at the nanoscale by presenting neutron diffraction results to determine the phase of confined ice formed. These last results are essential for the construction of a new phase diagram of water under hydrophobic confinement.

7.1. Water vapor adsorption on hydrophobic nanopores

In order to determine if a nanoporous material is hydrophobic, a systematic analysis of the surface-water interaction must be performed. For non-porous materials, one would perform contact angle measurements to assess the level of hydrophobicity. This analysis is not suitable for nanoporous materials because the external surface roughness would modify the wetting characteristics of the material.[1]

Another alternative, more adequate to nanoporous materials, is to perform water adsorption experiments and to evaluate the hydrophobicity by the amount of water adsorbed at a specific temperature and pressure and the shape of the obtained isotherm[2].

In this work, hydrophobic nanoporous materials were defined as those in which water does not condense at pressures lower than the saturation pressure of water, P_0 (0.0317 bar at 298.15 K); instead, a much higher pressure (several hundreds of bar) is needed for water intrusion to occur (see section 7.2).

Figures 7.1 and 7.2 show the results of the water vapor adsorption experiments on hydrophobic materials, carried out at 298.15 K. The small amount of adsorbed water and the absence of a condensation step confirm the hydrophobic character of the nanopores. The total amount of water that penetrates the hydrophobic nanopores is less than nine molecules per nm^3 for C18-M7-Me $SiMe_3$ and C14 MCM-41 $SiMe_3$ and much lower (<2.8 molecules/nm^3) for C18-M15-Me $SiMe_3$ (Table 7.1). These values are very small compared to the density of bulk liquid H_2O (33.4 molecules/nm^3), and it should not be assumed that water inside the hydrophobic nanopores is homogeneously distributed with this reduced density.

Table 7.1: Physical properties and maximum quantity of water adsorbed ($N_{ads,\ max}$) for the hydrophobic materials. The available pore volume V_{pore} was determined by nitrogen adsorption.

Material	D_{SAXS} (nm)	D_{BET} (nm)	V_{pore} (cm^3/g)	$N_{ads,\ max}$ (molecules/nm^3)	Uptake (mg_{H2O}/g)
C18-M7-Me $SiMe_3$	4.02	2.52	0.547	8.5	139
C18-M15-Me $SiMe_3$	3.89	1.76	0.539	2.8	45
C14 MCM-41 $SiMe_3$	2.45	3.18	0.194	8.1	47

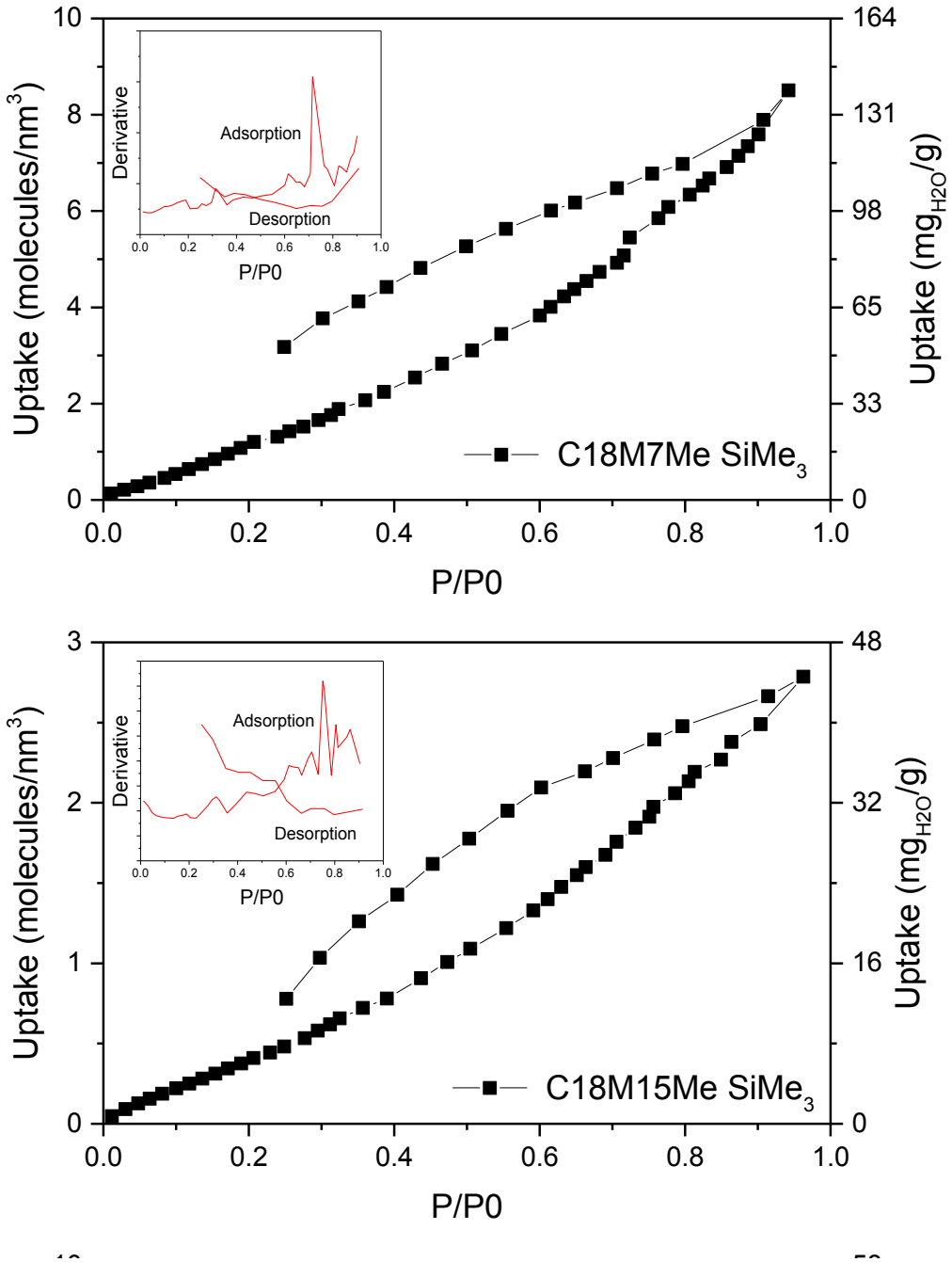

Figure 7.1: Water adsorption/desorption isotherms of C18-M7-Me $SiMe_3$ and C18-M15-Me $SiMe_3$ at 298.15 K. Insert: Derivative of the uptake vs. P/P0

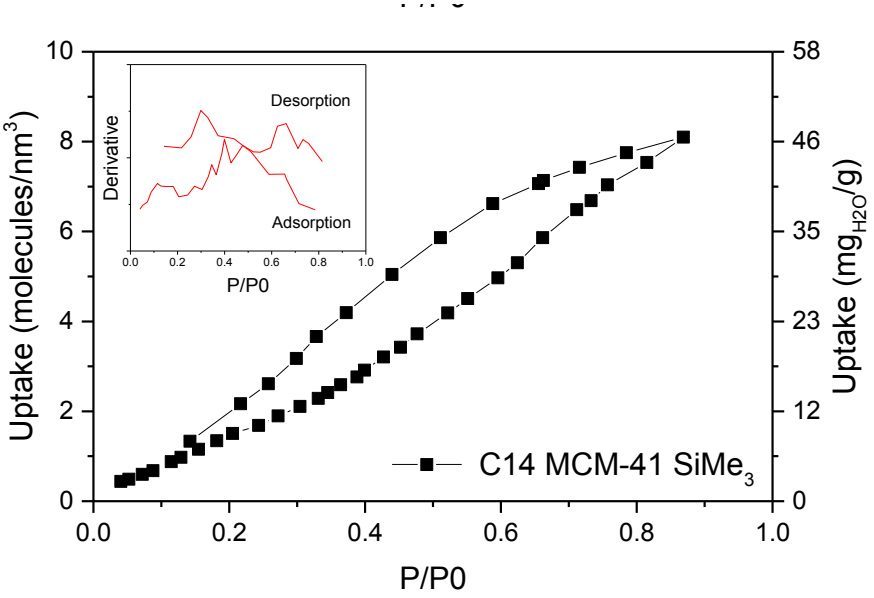

Figure 7.2: Water adsorption/desorption isotherms of C14 MCM-41 SiMe3 at 298.15 K. Insert: Derivative of the uptake vs. P/P0.

Valuable information about the water-surface interaction can be extracted from the analysis of the shape of the isotherms. Even though they are difficult to categorize according to the IUPAC classification[3], we observe similarities to a type III isotherm. The lack of a "knee of the isotherm" (*i.e.*, a sharp convex section at the beginning of the adsorption) denotes the absence of an identifiable monolayer formation. Instead, the water molecules are clustered around the most favorable sites of adsorption[4], the few silanol groups present at the surface.

Type III isotherms are mainly found in non-porous or macroporous solids, and they do not tend to present an adsorption-desorption hysteresis, as those presented here. The existence of this hysteresis is indicative of a partial nanopore filling[4]. However, the pore-filling process is quite different from that seen in Chapter 6, where a sharp capillary condensation step was observed. Instead, here we observe small jumps on the water adsorption.

Analyzing the uptake derivative vs. the relative pressure (Inserts in Figures 7.1 and 7.2), we find that the most significant jumps (maxima of the derivative) are at P/P0 = 0.72 for C18-M7-Me $SiMe_3$, P/P0 = 0.75 for C18-M15-Me $SiMe_3$, and P/P0 = 0.4 for C14 MCM-41 $SiMe_3$. Such sudden increases in the quantity of water adsorbed can be interpreted as the formation of water pockets around silanol hydrophilic sites.

On the duration of the experiments

Another important observation from these experiments is that the time required for an adsorption-desorption cycle was around three days on the hydrophobic materials. Such

long duration contrasts with water vapor adsorption-desorption isotherms on hydrophilic or amphiphilic materials, which took ~1.5 days to be completed. What we have seen is that the adsorption of a few water molecules on the hydrophobic nanopores at pressures lower than the saturation pressure of water, at 298.15 K, is a very slow process.

Comparison with other types of materials

When we compare to other nanoporous materials (Figure 7.3), we find that these results in water vapor adsorption are more similar to hydrophobic zeolites than to amphiphilic nanoporous silica. Indeed, hydrophobic zeolitic imidazole frameworks (ZIF) of the type ZIF-8 share the same type of adsorption isotherm (Type III). However, the level of water vapor adsorbed in ZIF-8 is significantly lower (~1.3 molecules/nm^3) and the convex shape of the isotherm is more pronounced.[2] Whereas water adsorbs much more readily in amphiphilic C18 materials. In this last case, it is easy to obtain filled amphiphilic nanopores with a density of ~29 molecules/nm^3 (Chapter 6).

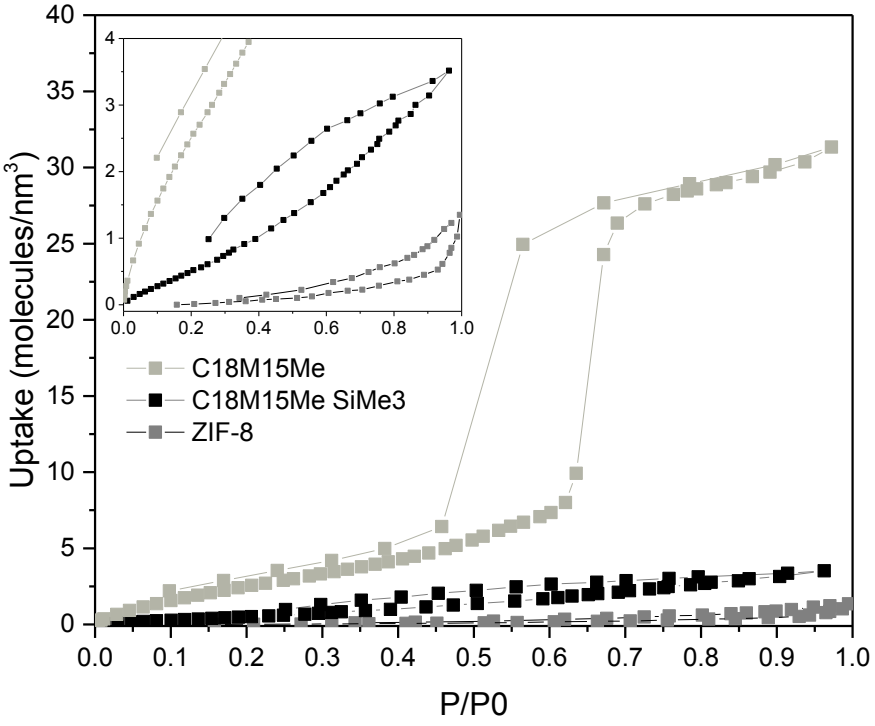

Figure 7.3: Comparison of water vapor adsorption isotherms on amphiphilic organosilica C18-M15-Me (Chapter 6), hydrophobic organosilica C18-M15-Me $SiMe_3$ hydrophobic zeolite ZIF-8 (identified as MAF-4 in reference 2)[2]. Insert : Zoom at low uptake to compare the shape of the adsorption isotherms.

Stability towards hydrolysis

In the case of C18-M15-Me $SiMe_3$, three water adsorption-desorption cycles were performed (Figure 7.4) to study the change of the surface upon contact with water. Results show that the first two isotherms are almost identical, evidencing that the material's sur-

face remains essentially unchanged. However, a noticeable increase in the quantity of water adsorption was observed in the third cycle, from 2.8 molecules/nm^3 to 2.94 molecules/nm^3. This additional adsorption can be explained by the opening of Si-O-Si bridges present in the surface, forming two silanol groups (Si-OH) where additional water molecules can be adsorbed.

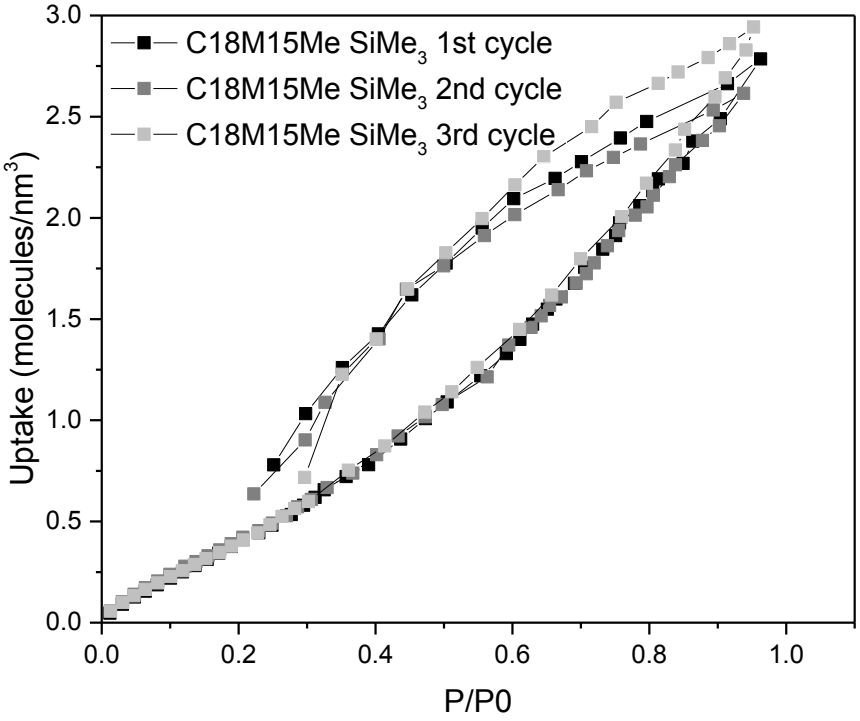

Figure 7.4: Three consecutive cycles of water adsorption/desorption on C18-M15-Me $SiMe_3$ at 298.15 K. The material was dried under vacuum at 90 °C for 24 h after each isotherm.

Nitrogen adsorption experiments performed before and after water adsorption allowed studying the changes in the surface. Figure 7.5 shows that the pore volume decreases by 8.5% (from 0.539 cm^3/g to 0.493 cm^3/g) due to the water molecules that have been integrated, thickening the material's framework. Furthermore, the C value changed from C = 19 to C = 23 after the three water adsorption-desorption cycles. The increase of the C value, which is correlated with an increase of the surface polarity, agrees with the hypothesis of some Si-O-Si bridges opening into more polar silanol groups.

In summary, the results of water vapor adsorption allowed us to confirm the highly hydrophobic character of the nanomaterials and to understand the limits of water entrance into hydrophobic nanopores at low pressures. Under such conditions, only a few water molecules will make their way into the nanopores in an extremely slow process that involves the formation of water clusters around the available silanol groups. We were also able to assess the stability of the materials towards hydrolysis using N_2 adsorption, and we have seen that their structure is preserved, with minor modifications due to the

incorporation of water molecules into the material's framework.

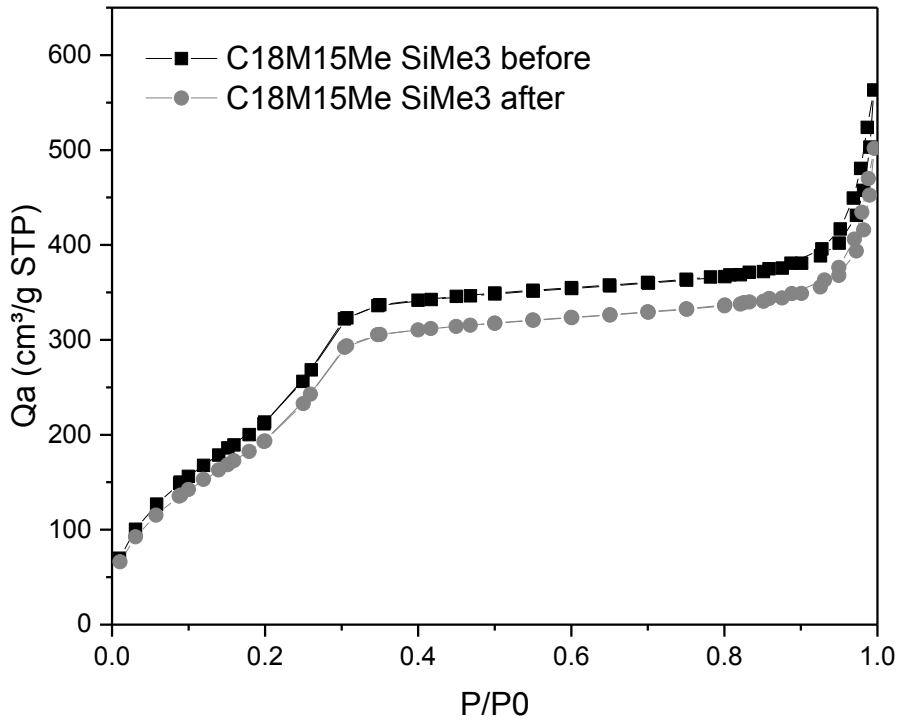

Figure 7.5: Nitrogen adsorption/desorption isotherms on C18-M15-Me SiMe3 at 77K before and after three water adsorption and desorption cycles.

7.2. Water intrusion followed by Neutron Imaging

Since water will not fill the hydrophobic nanopores through water vapor adsorption, the next logical step if one wants to study water confinement in hydrophobic conditions is to gather the hydrophobic powder and water, increase the pressure and observe. When put together, these two components form a heterogeneous lyophobic system (HLS). This kind of system is known for its energy storage and dissipation properties and is characterized by the intrusion and extrusion processes. [5–10]

Here, we used neutron imaging to observe the different types of materials submitted to high water pressures. In particular, we followed the process of forced water intrusion into hydrophobic nanopores using this technique.

The principle behind this technique is that, as water absorbs neutrons, the intensity of a selected area of the neutron radiography can be correlated to the amount of water in the sample.[11] When the moment of intrusion arrives, then water will occupy the available pore volume, which translates into a sudden decrease in the total intensity of the radiography. Likewise, when the pressure of water decreases during the decompression cycle, the extrusion process can be observed due to a sudden increase in the intensity of the images. Section 4.6 contains the details on the experimental setting and data treatment.

An example of the series of images obtained during this process is shown in Figure 7.6. At the beginning of the experiment, the capsule is full of hydrophobic powder at atmospheric pressure (a). The pressure is then increased to 1.7 bar (b). This causes the compaction of the powder towards the bottom of the cell. Then, the first droplet of water appears in the picture and makes contact with the surface of the hydrophobic material (c); the fact that there is no wetting confirms the hydrophobic character of the material. At 2.6 bar (d), water infiltrates between the metallic capsule and the powder. Only at 2.75 bar (e), the material and water start mixing; this is the pressure needed for inter-grain intrusion. The mixing evolves with pressure (f), and at 337.5 bar, the beginning of the intrusion process is detected, and the intensity suddenly decreases until the pressure arrives at 475 bar (h). In this experiment, the pressure continued to be increased up to 2000 bar, and then it was slowly released. At the end of the first compression-decompression cycle, the system is back at atmospheric pressure (i), and one can observe how the hydrophobic material aggregates back together. Such aggregation slowly evolves in time due to inter-grain water expulsion (j).

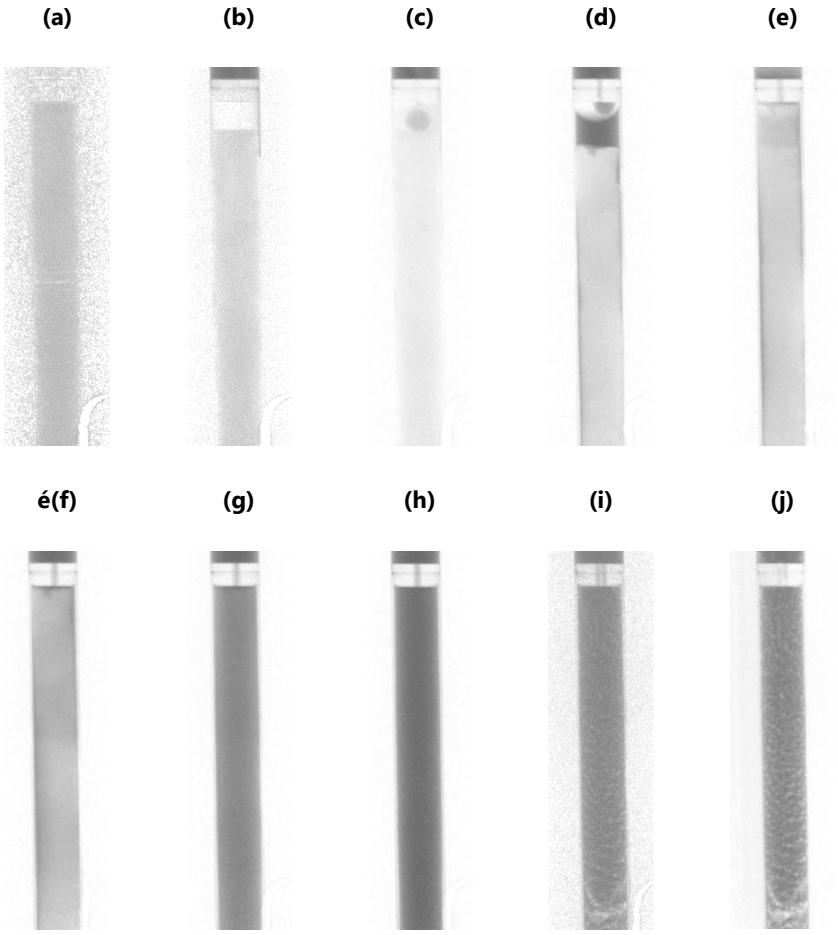

Figure 7.6: Neutron images of a capsule containing 178.9 mg of C18-M7-Me $SiMe_3$. Relevant images of the compression-decompression cycle are shown: (a) P = 1 bar (Dry powder), (b) P = 1.7 bar (Compressed powder), (c) P = 2.2 bar (First water droplet), (d) P = 2.6 bar (water penetrates the space between the metallic

capsule and the material), (e) P = 2.75 bar (Inter-grain intrusion), (f) P = 5.85 bar, (g) P = 337.5 bar (Start of the intrusion of water in the nanopores), (h) P = 475 bar (End of the intrusion), (i) P = 1 bar (Back to atmospheric pressure), (j) P = 1 bar (elapsed time after the end of decompression, t = 10 min). The brightness of the images here presented has been adjusted to facilitate visibility; therefore, the total intensity is not normalized.

A quantitative analysis was performed to determine the amount of water introduced in the nanopores after intrusion (Figures 7.7 to 7.9). The mass of water in the pores was calculated from the difference between the total quantity of water and the external water (the amount of external water also increases on account of its densification with pressure). This last one is estimated by extrapolating the quantity of external water present before the intrusion, taking into account the water densification with pressure (black line). Then, the mass of water in the pores, Δm, was converted in volume using the density of bulk water at the given pressure. Finally, the obtained water volume was divided by the total available pore volume to obtain a percentage of the pore occupancy. However, it is important to keep in mind that the density of water inside the hydrophobic nanopores may significantly differ from the density of bulk water and that the percentage shown is merely a way to compare the available pore volume with the increase in the amount of water in the system.

Figure 7.7 shows the calculated mass of water in a capsule containing 178.9 mg of C18-M7-Me $SiMe_3$ versus the pressure. During the compression cycle, the mass of water raises abruptly (from point (1) to point (2)) due to water intrusion. The intrusion pressure is related to the inflection point of the curve (380 bar). We estimated only 58% of pore occupancy in this stage, which corresponds to an average density of 17.8 molecules/nm^3 over the whole accessible volume.

In a second step (from point (2) to (3)), the mass of water keeps increasing. The densification of the external water accounts only for a part of this increase; the rest is due to the intrusion of additional water molecules in the nanopores. At 2000 bar, 68% of pore occupancy was obtained, which corresponds to an average density of 24.3 molecules/nm^3.

During the decompression, a steady decrease in the mass of water is observed until the extrusion pressure (32.5 bar). The intrusion-extrusion hysteresis observed here (347.5 bar difference between the intrusion and extrusion pressures) is characteristic of shock absorber systems and results from the different mechanisms followed by the intrusion and extrusion processes. The intrusion process has been described in the literature as a function of the pore radius using the Laplace-Washburn equation (Section 1.2), while the extrusion process mechanism requires the formation of a vapor bubble within the nanopore.[5]

Figure 7.8 shows the results for a sample containing 122 mg of C14 MCM-41 $SiMe_3$. The

intrusion pressure, in this case, is found at 450 bar. The amount of water is higher than expected for the available pore volume. In the first intrusion step, 107 % of the pore volume measured by nitrogen adsorption is occupied, and at 1000 bar, this value increases to 152 %. However, the scenario of a higher average density in the nanopores is not consistent with the literature or with the values for water intrusion in the other samples. Then, a possible explanation for this observation is that the water pressure could have opened some blocked nanopores present in the material or simply that its pore volume has been underestimated.

The range of pressures at which the intrusion process takes place is wider or narrower depending on the material. For C14 MCM-41 $SiMe_3$, the intrusion process is spread in a wider range (from 300 bar to 500 bar) than for C18-M7-Me $SiMe_3$ (from 337 bar to 475 bar). This could be a consequence of the uniform pore size and grafting density of C18-M7-Me $SiMe_3$ and possible pore blockage in C14 MCM-41 $SiMe_3$.

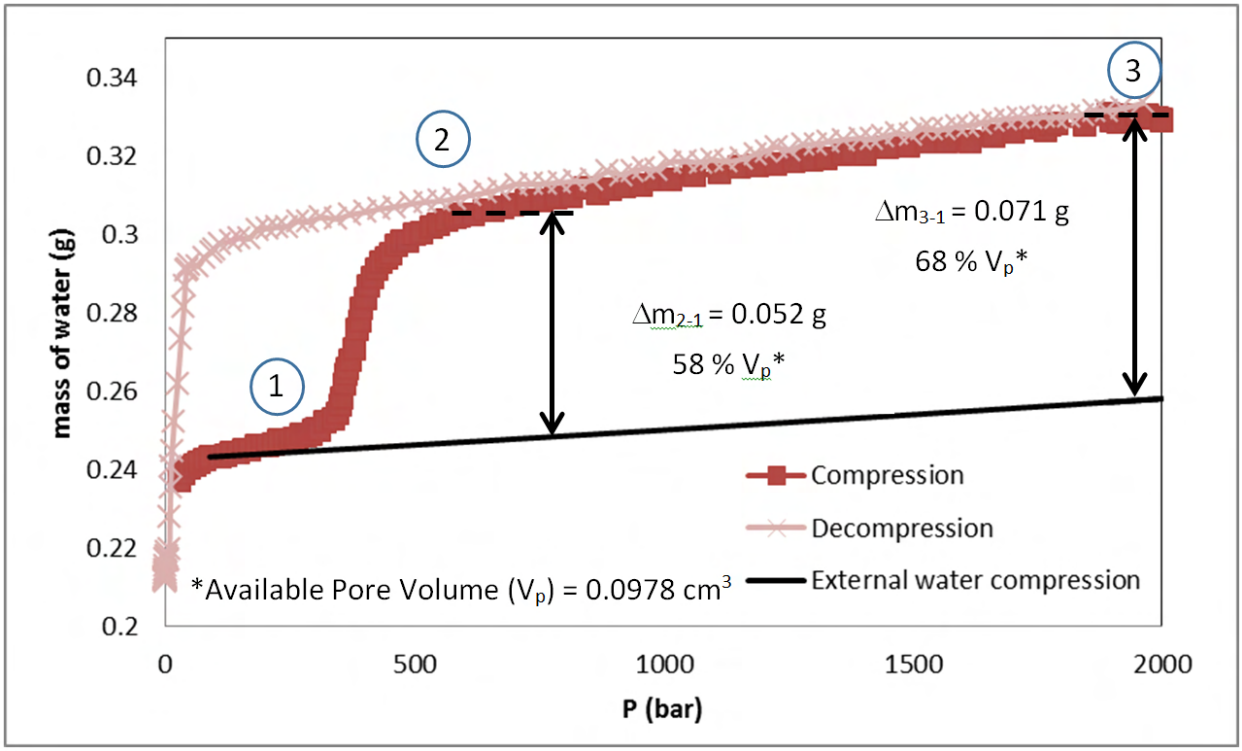

Figure 7.7: Mass of water as a function of the pressure for a sample with 179 mg of C18-M7-Me $SiMe_3$ (Vp = 0.547 cm^3/g).

On the duration of the experiments

The results mentioned above can be compared because the scan rate used for both samples was approximately the same (~10 bar/min). For the third sample, C18-M15-Me $SiMe_3$ (Figures 7.9 and 7.10), the pressure of water was kept at 109 bar for nearly one hour. After this, we steadily increased the pressure up to 1000 bar with a scan rate of ~50 bar/min.

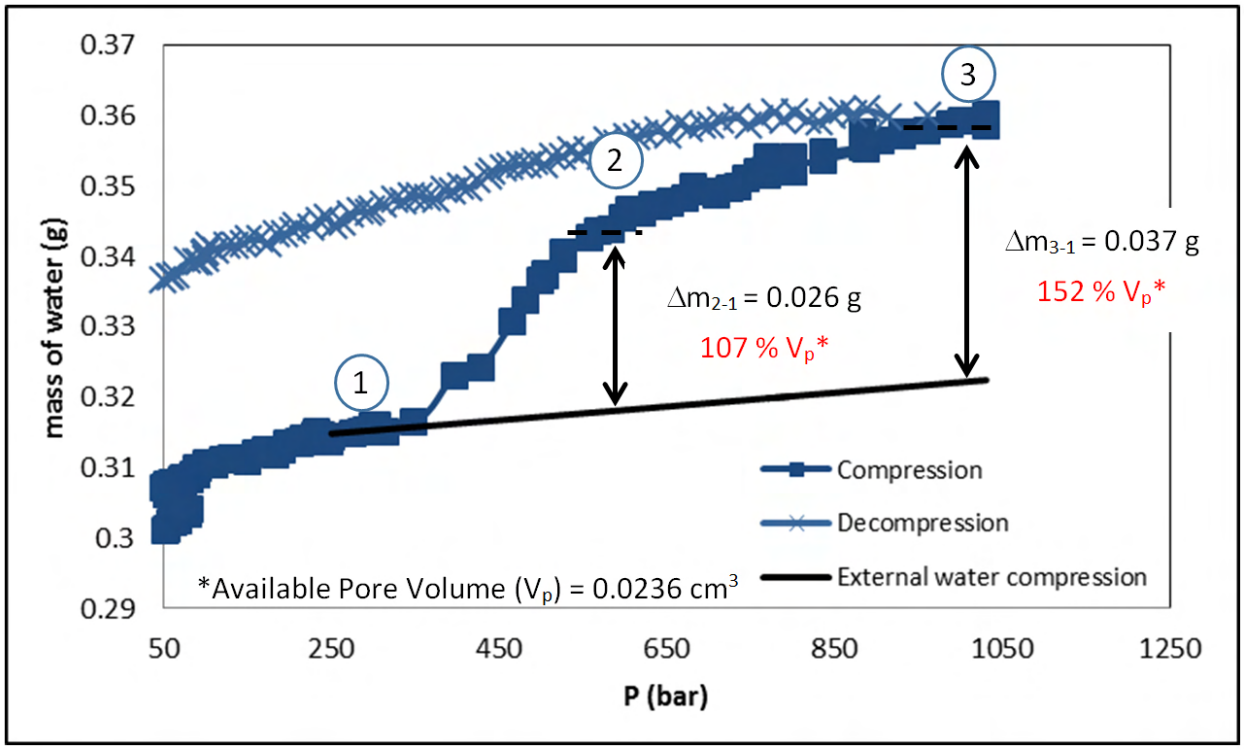

Figure 7.8: Mass of water as a function of the pressure for a sample with 122 mg of C14 MCM-41 $SiMe_3$ (Vp = 0.194 cm^3/g).

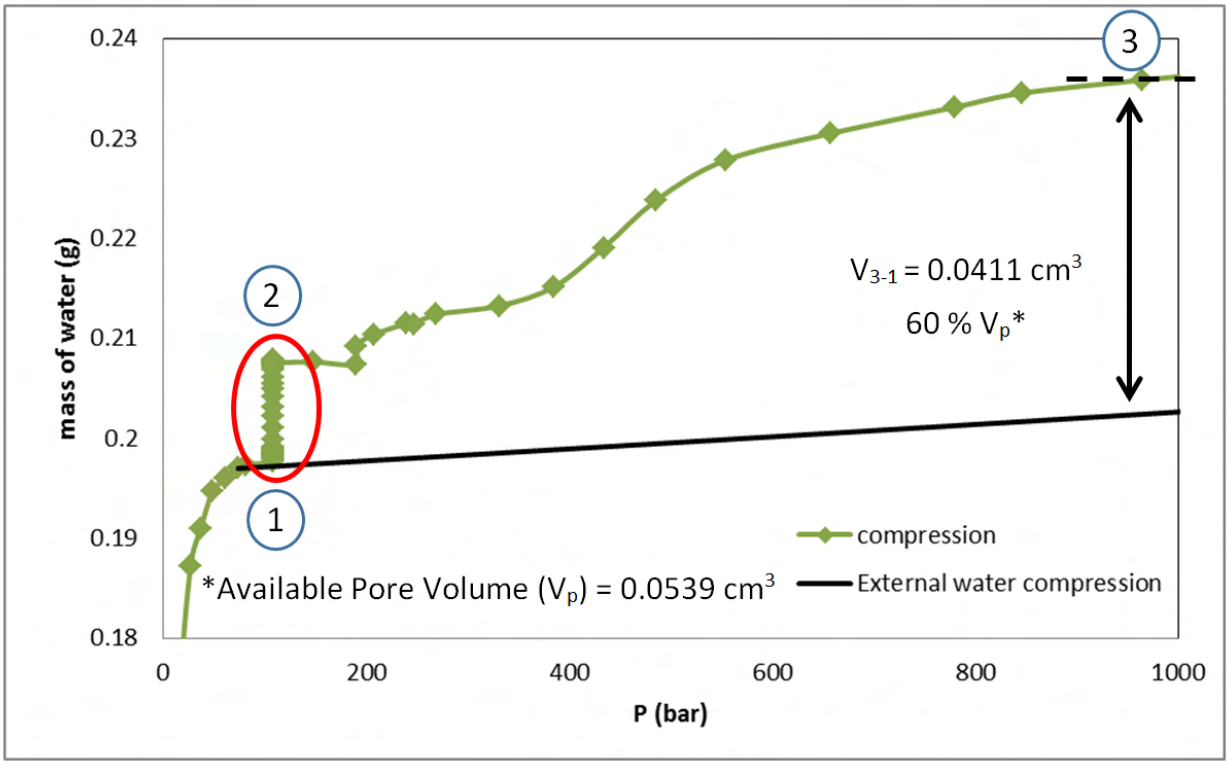

Figure 7.9 : Mass of water as a function of the pressure for a sample with 100 mg of C18-M15-Me $SiMe_3$ (Vp = 0.539 cm^3/g).

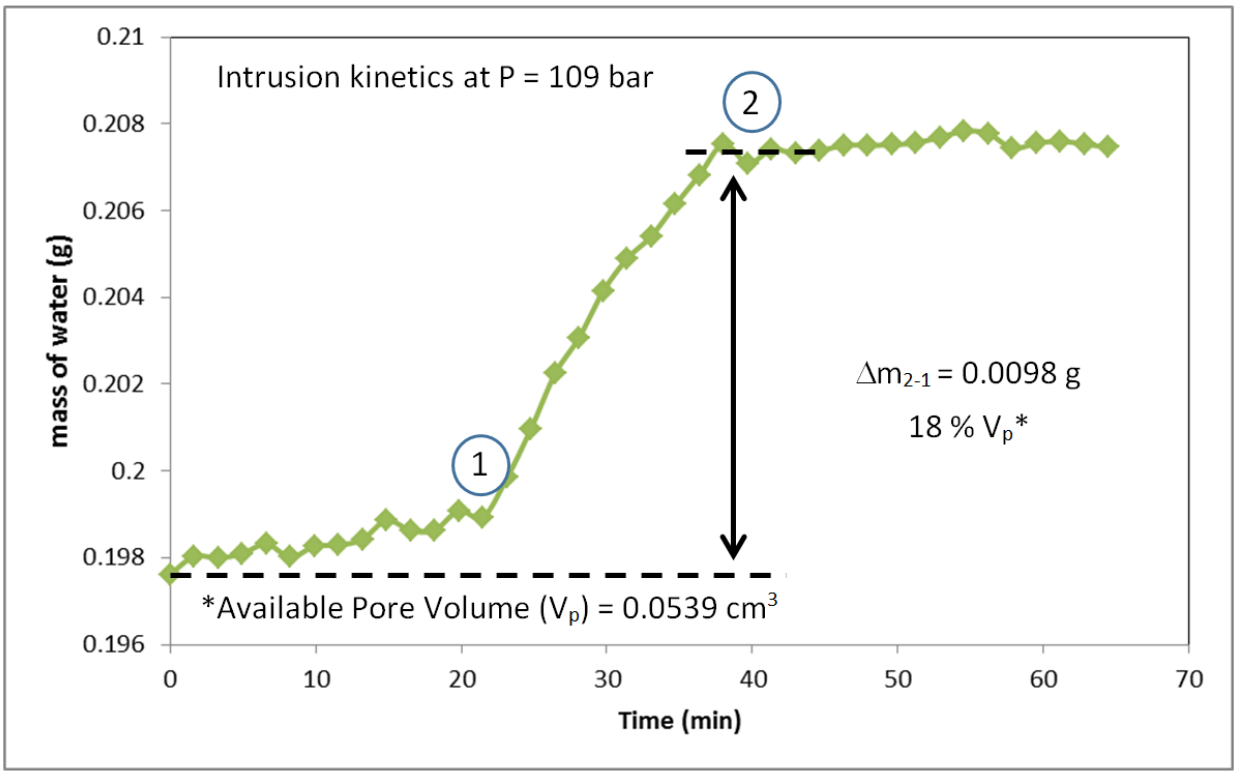

Figure 7.10: Mass of water as a function of time for a sample with 100 mg of C18-M15-Me $SiMe_3$ (Vp = 0.539 cm^3/g). Isobaric conditions at 109 bar during 64 minutes. End of intrusion around 40 min.

At constant pressure = 109 bar (Figure 7.10), results show that the intrusion process starts at 21 minutes and arrives at a plateau at minute 38. According to this result, water penetrates the nanopores with a limit of 18 % of the pore volume, corresponding to an average water density of 6 molecules/nm^3. This result shows that water's forced intrusion into the hydrophobic nanopores is a slow-kinetics process; this is in agreement with the dynamics found by Picard *et al.* (2021) in hydrophobically modified PMOs (using much faster rates)[12].

Once elapsed this time in isobaric conditions, the pressure continued to be increased. A significant intrusion step was observed at 450 bar. At 1000 bar, around 60 % of pore occupancy was obtained; this is 25.5 molecules/nm^3.

Table 7.2 shows the obtained intrusion pressures for the different materials.

Table 7.2: Water intrusion pressure and pore size for the different post-grafted organosilica materials.

Material	D_{SAXS} (nm)	P_{int} (bar)
C18-M7-Me $SiMe_3$	4.02	380
C18-M15-Me $SiMe_3$	3.89	450
C14 MCM-41 $SiMe_3$	2.45	450

The intruded water volume found here for C18-M7-Me $SiMe_3$, as for C18-M15-Me $SiMe_3$, was found lower than the available pore volume in the material, which would lead to a lower average water density inside the nanopores. This apparent lower density of hydrophobically confined water agrees with the simulations of H_2O in silicalite-1, performed by Desbiens *et al.* (2005)[13].

Unfortunately, the data obtained for the decompression of water in C18-M15-Me $SiMe_3$ did not conduct a quantitative analysis due to the substantial loss of material upon decompression and the small volume of the sample compared to the volume of the capsule (Figure 7.11).

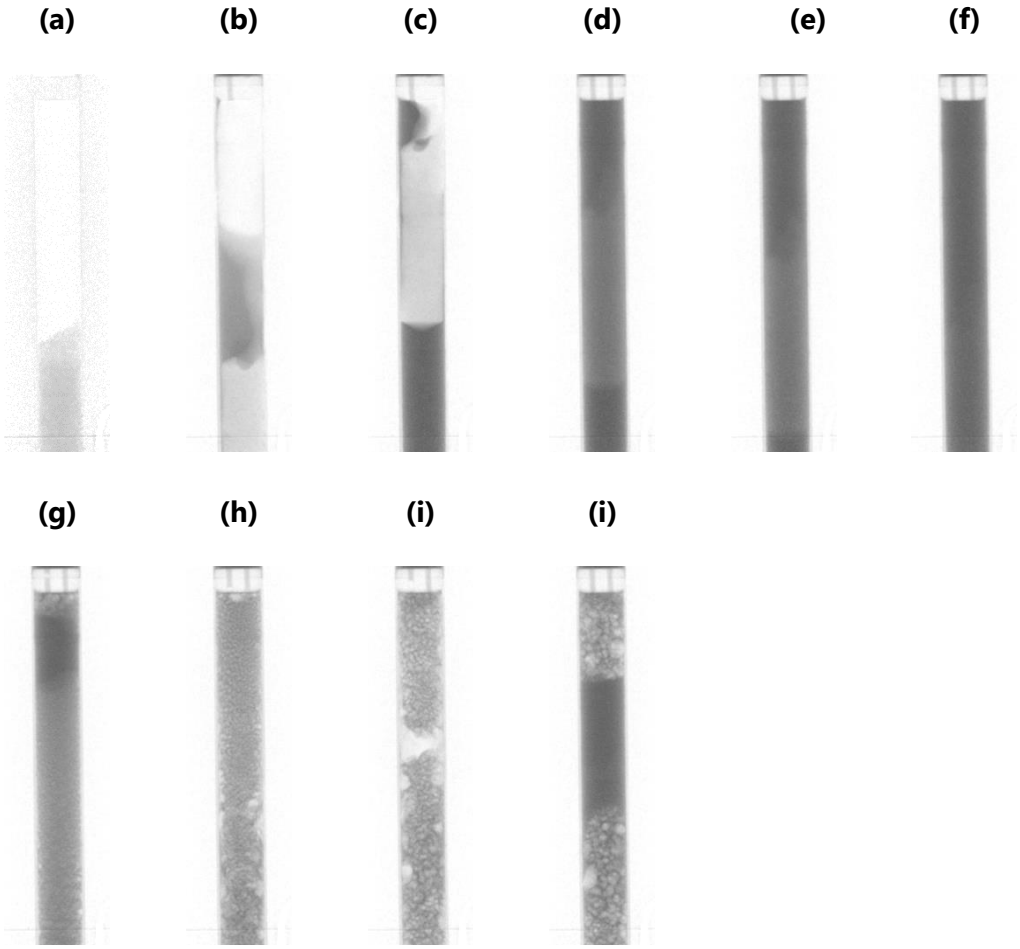

Figure 7.11: Neutron images of a capsule containing 100 mg of C18-M15-Me $SiMe_3$. Relevant images of the compression-decompression cycle are shown: (a) P = 1 bar (Dry powder), (b) P = 1.6 bar , (c) P = 2.1 bar (Flotation of the material on water), (d) P = 109 bar, elapsed time t = 8 min, (e) P = 109 bar, elapsed time t = 16.5 min, (f) P = 486 bar, (g) back to P = 3.15 bar (Loss of part of the material), (h) P = 1.8 bar (Aggregation), (i) P = 1 bar (Back to atmospheric pressure), (j) P = 1 bar (elapsed time after the end of decompression, t = 8 min). The brightness of the images here presented has been adjusted to facilitate visibility; therefore, the total intensity is not normalized.

Comparison with other types of materials

In figure 7.12, our results on the intrusion pressure of water in hydrophobic nanopores are presented in the context of the analysis made by Fraux *et al.* (2017). Their review[8] compares the results obtained for water intrusion in micelle templated post-grafted silicas (MTS, blue squares)[5] and in zeolites of the AFI, DDR, MEL, and MFI-types (red squares)[14,15]. In the first group, the nanopores are cylindrical and independent, similar to post-grafted MCM-41 and to our materials. The second group (red squares) corresponds to all-silica frameworks zeosils with smaller, interconnected cavities. The value obtained by Michel *et al.* (2019)[9] for ZIF-8 (black square) seems to fall in the same linear trend as the zeosil frameworks.

In both cases, linear relationships between the intrusion pressure and the inverse of the pore radius were found, as described by the Laplace-Washburn equation (Section 1.2) for a given series of materials. It is important to note that the linear trend is found in the selected zeolites only when the radius of the largest cavity of the framework (and not the entrance of the pore radius) is used.[8]

The different slope found in the two cases was attributed to different surface chemistry in the two types of materials. In the case of grafted MCM-41, the hydrophobicity comes from the organic groups at the surface, whereas for the zeosils, it comes from an all-silica surface.[8] In this context, it is expected that our results fall in the same category as the grafted MCM-41.

From these data and assuming that confined water has the same surface tension as bulk water, an apparent advancing angle of ~120° was found for the hydrophobic MTS and ~100° for the zeolites[8]. The estimated advancing angle for our materials is ~127° for C18-M7-Me $SiMe_3$ and C18-M15-Me $SiMe_3$ and ~111° for C14 MCM-41 $SiMe_3$.

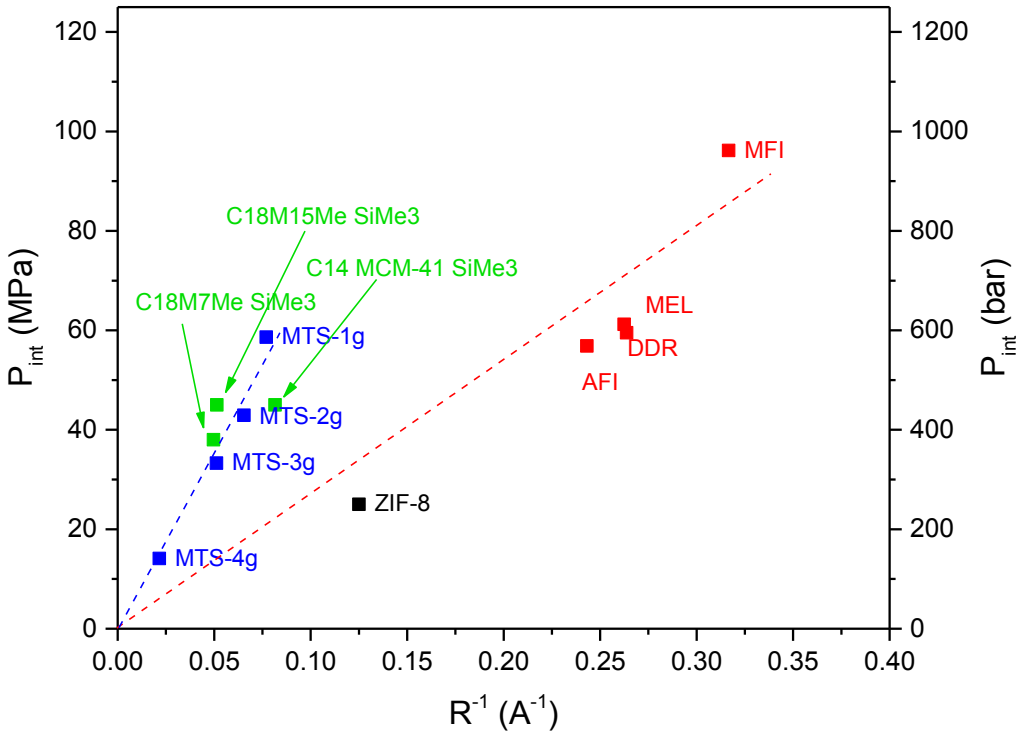

Figure 7.12: Water intrusion pressure as a function of the inverse of the pore radius, adapted from Fraux *et al.* (2017)[8]. Blue squares correspond to grafted hydrophobic mesoporous silica of the MCM-41 type (Micelle Templated Silicas, MTS, grafted)[5], red squares correspond to zeosil frameworks with interconnected pores, and the black square corresponds to the zeolitic imidazole framework ZIF-8[9]. The dashed lines are a guide for the eye. Additional highly confining zeolites (MTW, FER, and TON, not represented here) are considered by Fraux *et al.* (2017)[8].

As a qualitative comparison, Figures 7.13 and 7.14 show the images of a cell filled with amphiphilic and hydrophilic powders (C12M7Me and C12 MCM-41, respectively) upon increasing water pressure. Here we observe that the powder and water immediately mix, and an imbibition front can be identified, although the amphiphilic sample seems to be more heterogeneous upon decompression.

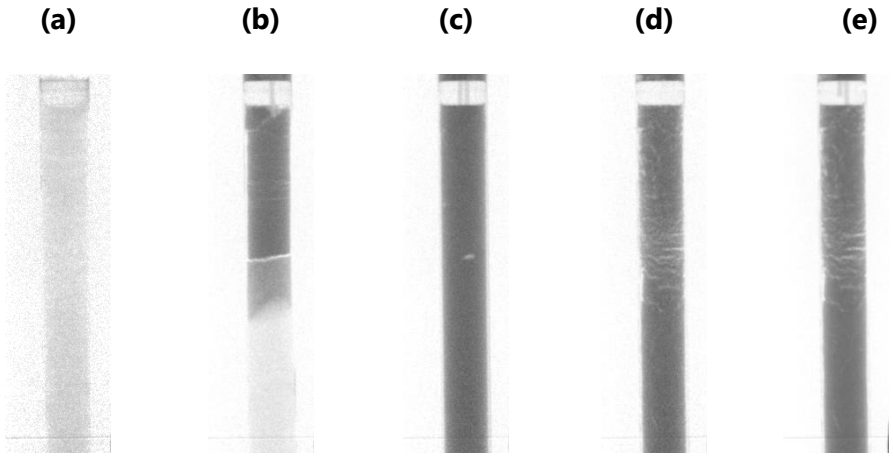

Figure 7.13: Neutron images of a capsule containing 250 mg of the amphiphilic sample C12-M7-Me. Relevant images of the compression-decompression cycle are shown: (a) P = 1 bar (Dry powder), (b) P = 7

bar, (c) P = 118.5 bar, (d) back to P = 1.1 bar, (e) P = 1 bar (Back to atmospheric pressure). The brightness of the images presented here has been adjusted to facilitate visibility; therefore, the total intensity is not normalized.

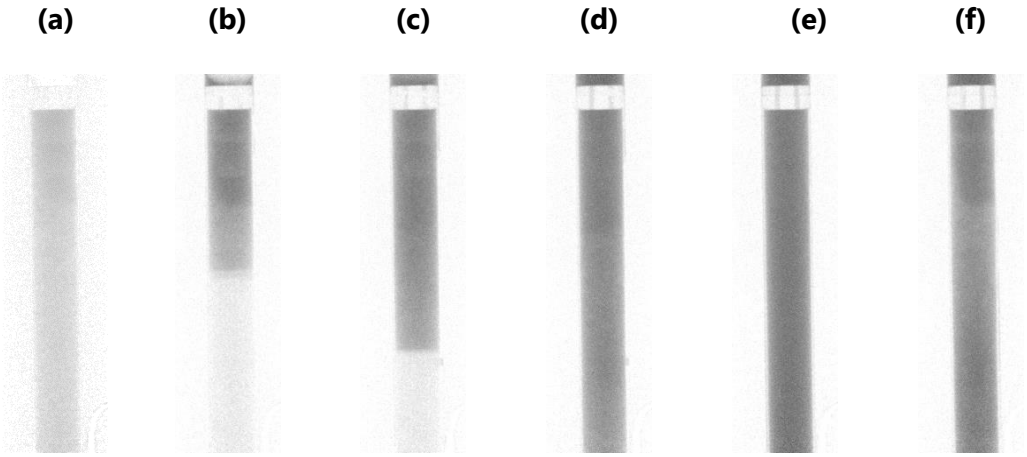

Figure 7.14: Neutron images of a capsule containing 300 mg of the hydrophilic C12 MCM-41. Relevant images of the compression-decompression cycle are shown: (a) P = 1 bar (Dry powder), (b) P = 4 bar, (c) P = 91.1 bar, (d) P = 1901 bar, (e) back to P = 529 bar, and (f) P = 1 bar (Back to atmospheric pressure). The brightness of the images here presented has been adjusted to facilitate visibility; therefore, the total intensity is not normalized.

7.3. Structure of water under hydrophobic confinement

The structure of confined ice at high pressure was studied using the high-resolution diffractometer G4.4 (@LLB). In order to do so, the high-pressure cell was filled with the selected sample (C18-M15-Me $SiMe_3$) and introduced in a cryostat. This setup allowed us to increase the pressure of water to a certain point, cool down the sample from room temperature to 180 K, reheat the sample, further increase the pressure inside the cell, and repeat this process until 4400 bar. Neutron diffraction measurements were performed at selected temperature-pressure points during the cooling and heating cycles in order to study the hysteresis of the phase transitions.

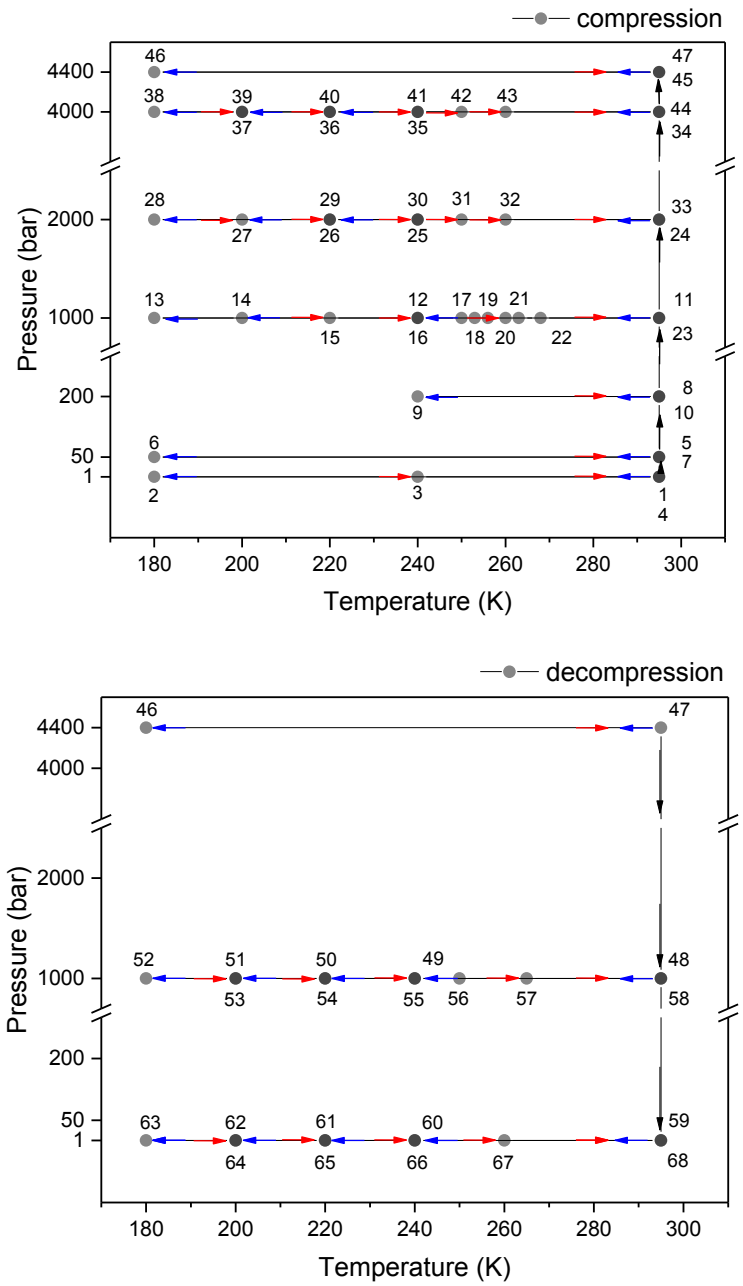

Figure 7.15: Thermodynamic pathway for the neutron diffraction experiment to study D_2O freezing and melting in the hydrophobic nanopores of C18-M15-Me $SiMe_3$. The numbers denote the order of the different diffraction measurements performed. Blue and red arrows symbolize cooling and heating temperature ramps, respectively. (10 bar = 1 MPa)

We stopped at 1000 bar and 1 bar during the decompression and measured the diffraction patterns along a cooling-heating cycle each time. The reason for this was to study the thermodynamic state of water inside the nanopores before and after the application of high pressure.

The thermodynamic pathway of the experiment, as well as the temperature-pressure points where neutron measurements were performed, are shown in Figure 7.15.

Figure 7.16 shows the spectra at different pressures, all taken at the minimum temperature, 180 K. Note that no diffraction peaks other than the background from the high-pressure cell are visible at pressure 200 bar and lower. This agrees with the previously discussed neutron radiography results that water has not entered the beam region for lower pressures. We will now center on the analysis of the heating curves for P ≥ 1000 bar.

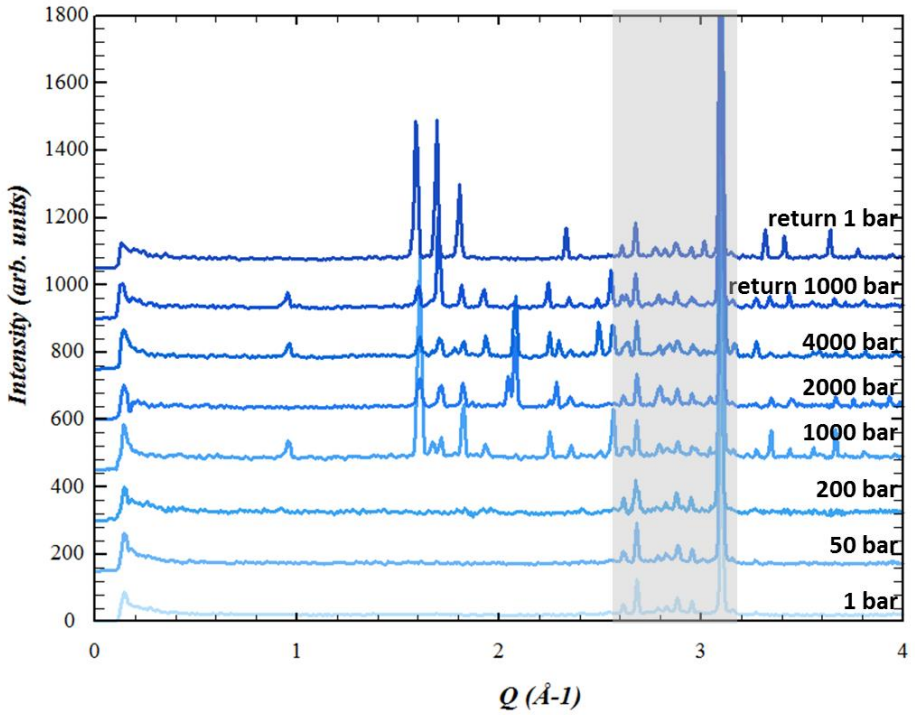

Figure 7.16: C18-M15-Me $SiMe_3$ comparison at different pressures and 180 K. Presence of water in the beam area from 1000 bar. At 200 bar, no significant amount of water was detected inside the nanopores nor among the grains. The grey zone corresponds to the high-pressure cell diffraction. The contribution of the empty matrix at atmospheric pressure (1 bar) is negligible compared to the intensity of the Bragg peaks of the cell. The main (10) peak of the materials at 0.14 $Å^{-1}$ is not detected (see Figure 5.16). The increase in intensity at low Q is due to instrumental background on G44. The thermal expansivity of the cell in this range is very low (~1.5. 10^{-4} K^{-1}).

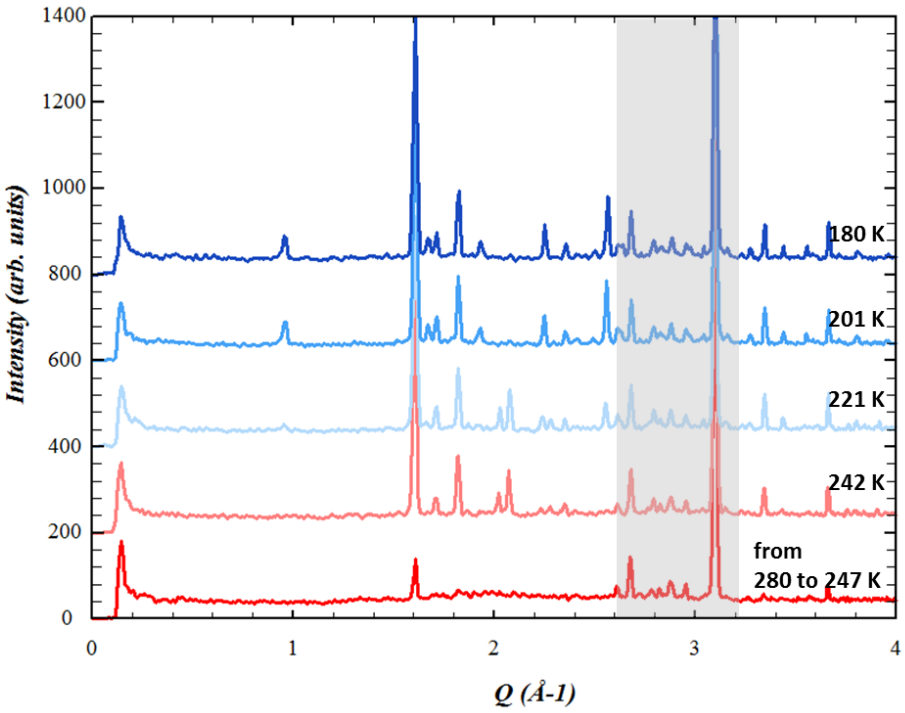

Figure 7.17: C18-M15-Me SiMe3. Cooling cycle at P = 1000 bar. Diffraction measurements were performed during the cooling ramp, from 280 to 247 K (red curve). For the rest of the curves, the temperature was stable with a precision of ±2 K. The external hexagonal ice emerges, as well as the confined Ice III (peaks around 2 $Å^{-1}$). Confined phase ice III transforms into ice II (signature peak at ~1 $Å^{-1}$) between 221 and 201 K.

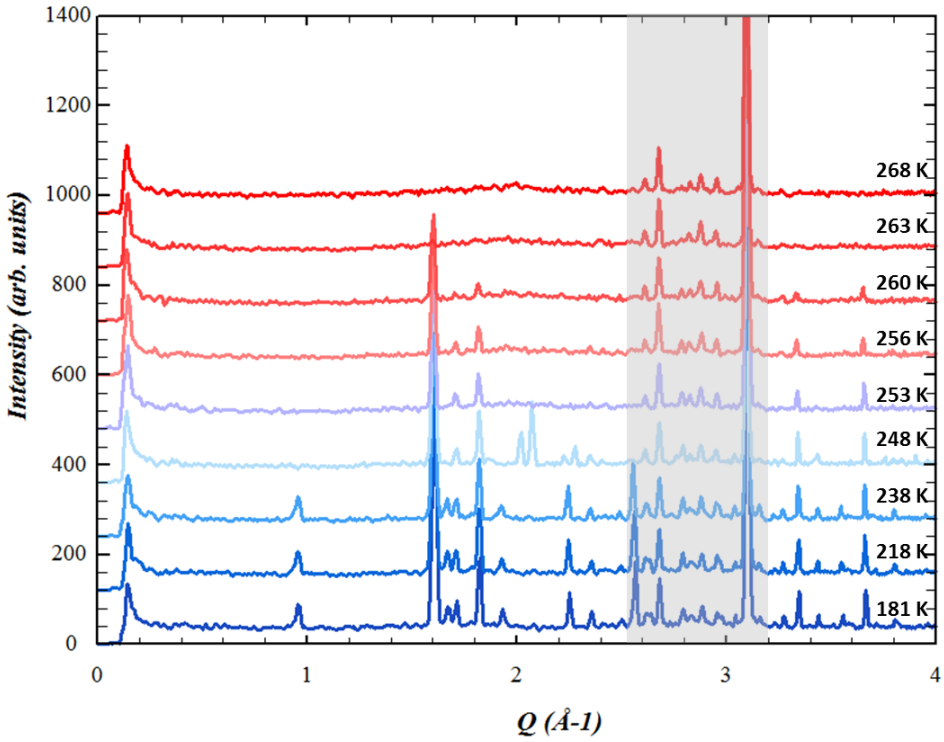

Figure 7.18: C18-M15-Me $SiMe_3$. Heating cycle at P = 1000 bar. Confined phase ice II transforms into ice III between 240 and 248 K. Confined ice III melts between 250 and 253 K. External phase I_h remains for the whole range of temperatures from 180 to 260 K.

Figure 7.17 shows the diffraction curves taken in the *cooling cycle* at 1000 bar (100 MPa). During the cooling ramp at T > 247 K, The most intense peaks from hexagonal ice are observed. At 240 K, the diffraction curve shows peaks at 1.6 $Å^{-1}$, 1.7 $Å^{-1}$, and 1.8 $Å^{-1}$ from hexagonal ice and two additional peaks at 2.03 $Å^{-1}$ and 2.08 $Å^{-1}$, indexable to ice III. At 221 K, the intensity of the peaks from ice III starts to decrease, while several peaks from ice II (0.96 $Å^{-1}$, 1.67 $Å^{-1}$, 1.94 $Å^{-1}$, and 2.25 $Å^{-1}$) start to appear. At 201 K and 180 K, the spectra show peaks from Ih and ice II.

Figure 7.18 shows the diffraction curves taken in the *heating cycle* at 1000 bar. The presence of the diffraction pattern of hexagonal ice is observed in all curves below 260 K. Besides Ih, some curves show additional peaks corresponding to the same phases observed during the cooling cycle. From 180 K to 240 K, these additional peaks correspond to ice II. The additional peaks at 248 K correspond to ice III. At 253 K, only the peaks from I_h remain. Then, at 263 K, all the diffraction peaks from the sample disappear; the only peaks visible are those from the cell.

Our analysis shows that the hexagonal phase is located outside of the nanopores (this is the expected crystal phase for bulk D_2O), and the additional peaks correspond to the D_2O confined in the hydrophobic nanopores. Therefore, we have identified a confined phase transition at 1000 bar from ice III to ice II during the cooling between 221 K and 201 K. From the observed transformation during the heating cycle (Ice II to ice III between 238 K and 248 K), we know that the phase transition is reversible with a freezing-melting hysteresis of approximately 20 K. Then, confined ice III melts between 250 K and 253 K, and the external hexagonal phase melts between 260 and 263 K.

Ice II and ice III are high-density phases that are only present in the phase diagram of bulk D_2O at pressures higher than 2000 bar. Although Ice II might be maintained down to atmospheric pressure, it converts rapidly into cubic ice between 120 K and 160 K.[16] To the best of our knowledge, Ice II at such low pressures and high temperatures has not been found before.

Ice II is 27% more dense than I_h, it has an ordered hydrogen bonding, and it is not stable in the presence of liquid water.[17] Whereas ice III is 24% more dense than I_h, it has a disordered hydrogen bonding and can exist in the presence of liquid water.[18] Figure 7.19 shows the diffraction patterns and representations of ices Ih, II, and III, reconstructed from the crystallographic data[17–19].

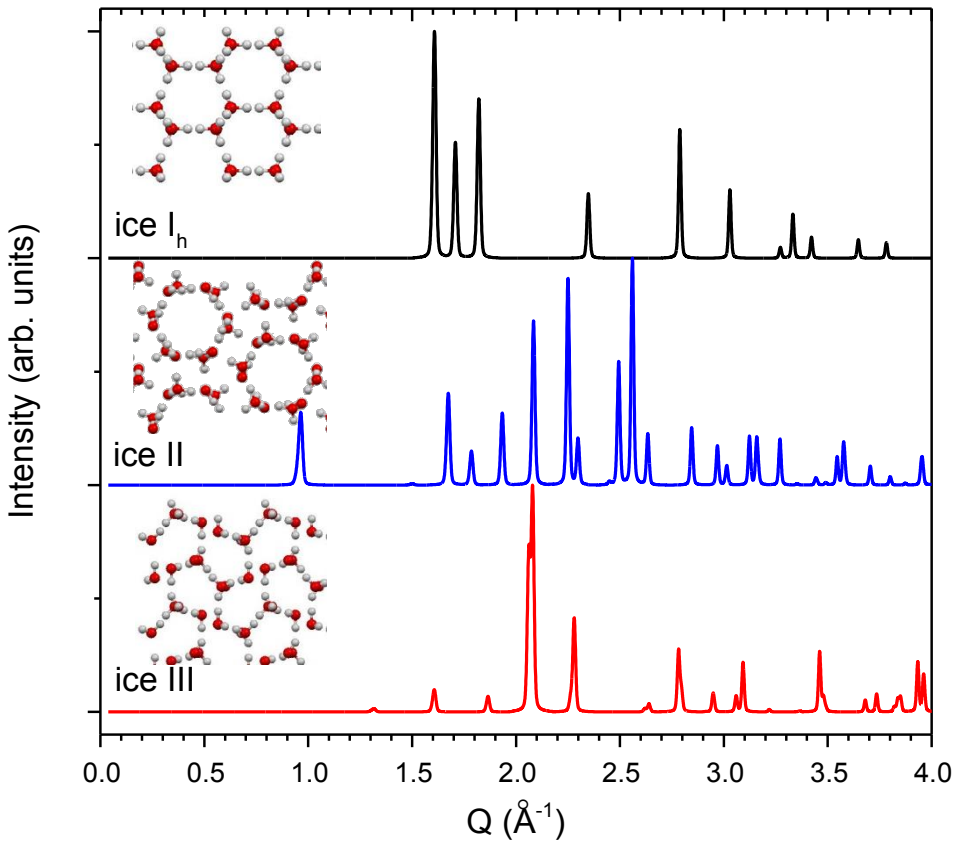

Figure 7.19: Neutron diffraction simulations and representation of ice Ih[19](black), ice II[17](blue), and ice III[18] (red), from crystallographic data.

It is then surprising to find such dense phases of ice at 1000 bar (half the pressure needed for their appearance in bulk water) and high temperatures. A possible implication of this is that water seems to perceive a much higher pressure inside the nanopores than outside them.

Figure 7.20 shows the diffraction patterns during the cooling and heating cycles at 2000 bar. In this case, we observe diffraction peaks from hexagonal ice and ice III. However, the peaks from I_h are quite less intense than those found at 1000 bar.

During the cooling cycle, the peaks from I_h from D_2O outside of the pores and confined ice III are observed from 240 K to 180 K, and the position of one of the peaks from ice III progressively shifts with temperature from 2.02 A^{-1} at 240 K to 2.04 A^{-1} at 180 K. During the heating cycle, confined phase ice III and external phase Ih are both present up to 248 K. Then they both melt before 258 K (The expected melting temperature for bulk D_2O at 2000 bar is 257 K).

Figures 7.21 and 7.22 show the neutron diffraction results during the decompression, at 1000 bar and atmospheric pressure, respectively.

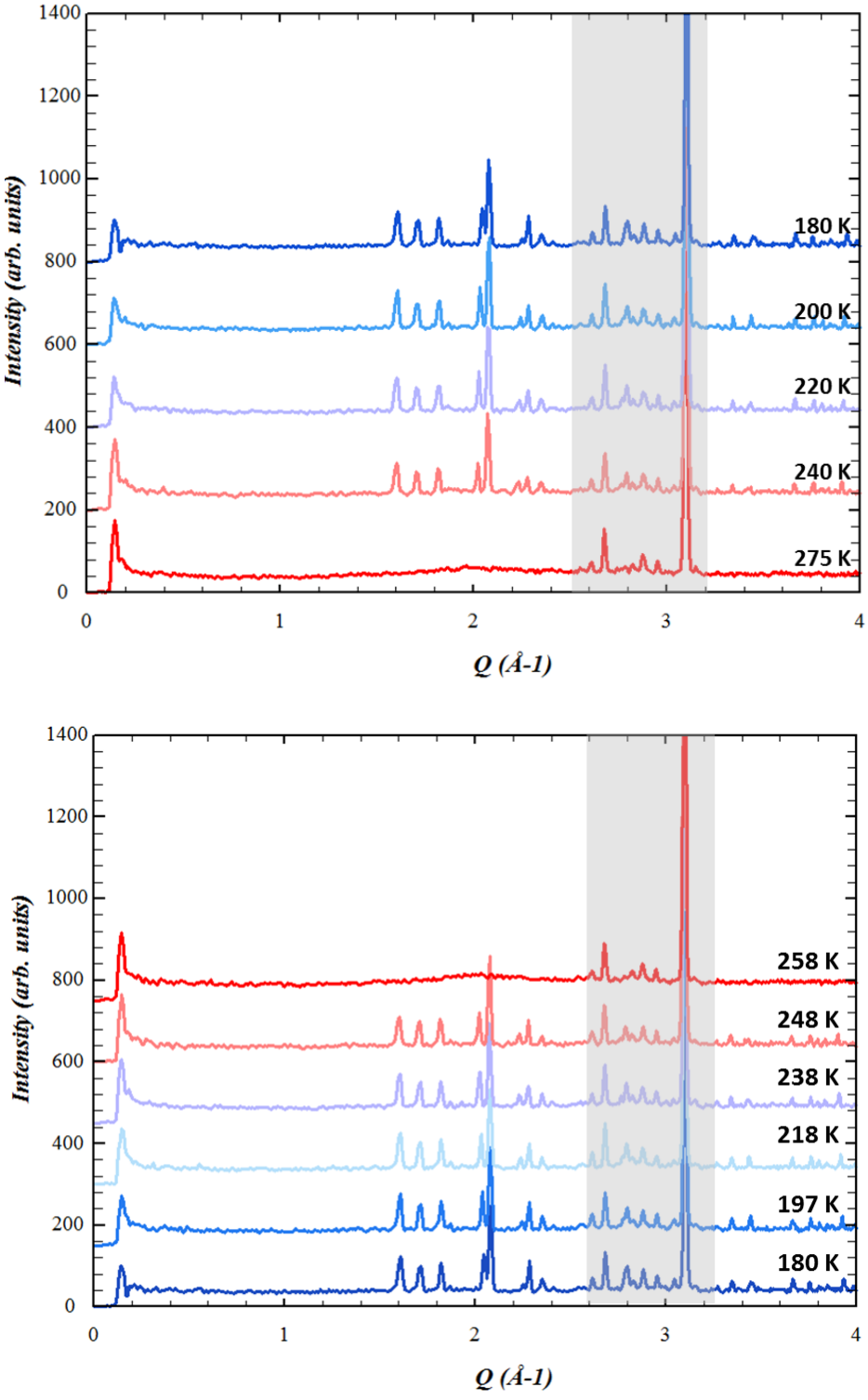

Figure 7.20: Diffraction curves of D_2O@C18-M15-Me $SiMe_3$ at P = 2000 bar. Up: Cooling cycle, Down: Heating cycle.

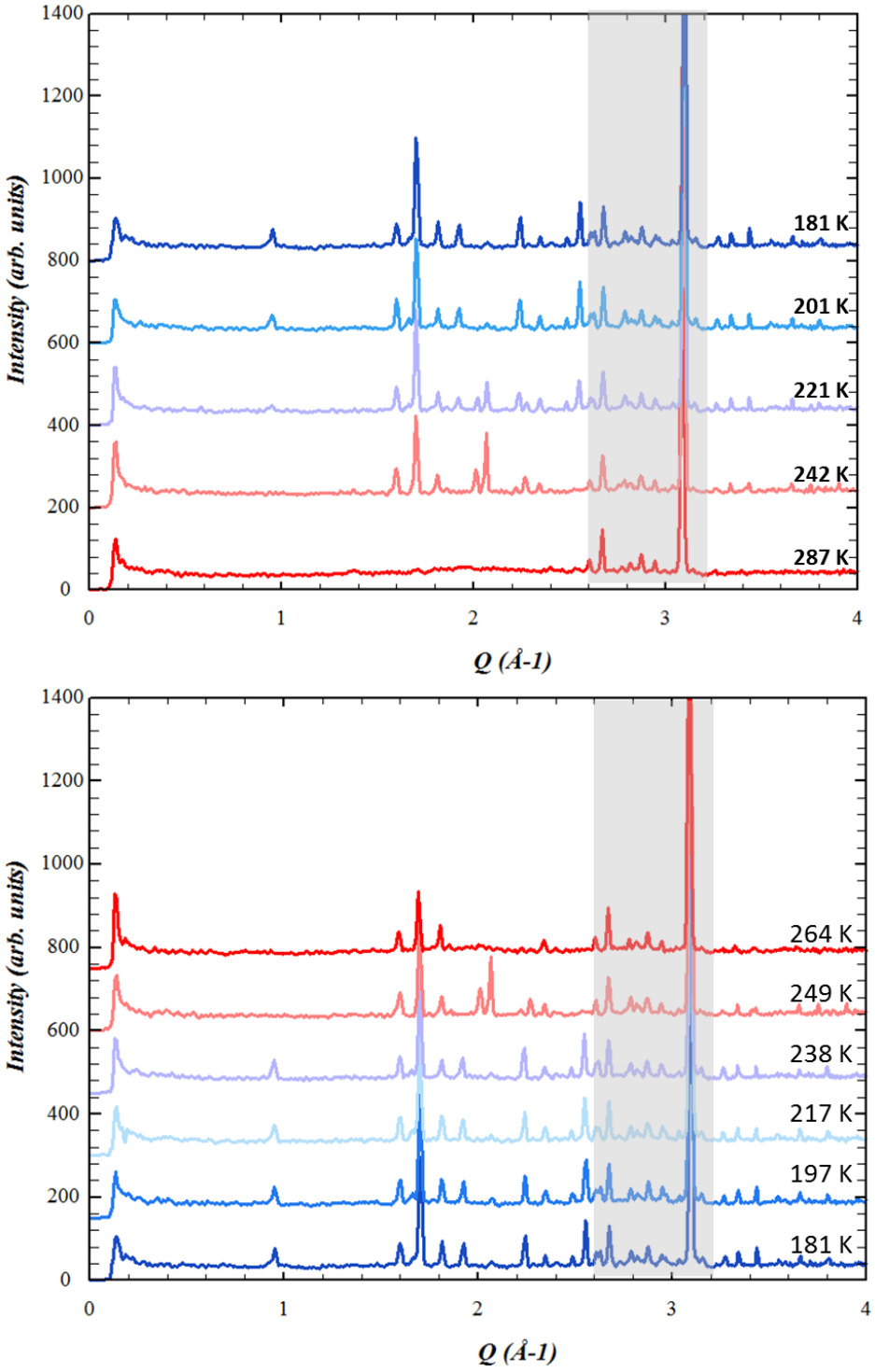

Figure 7.21: C18-M15-Me $SiMe_3$. Heating cycle back at P = 1000 bar. Up: Cooling cycle, Down: Heating cycle. Confined phase ice II transforms into ice III between 240 and 249 K. Confined ice III melts between 249 and 264 K. External phase I_h remains for the whole range of temperatures from 181 to 264 K.

Despite that the sample has been submitted to high pressure (up to 4400 bar), these results at 1000 bar during the decompression cycle (Figure 7.21) show the same phases and phase transitions as observed during the compression cycle. Upon cooling, a transformation of confined ice III to ice II is observed between 221 K and 201 K. Ice II transforms to ice III between 238 K and 249 K. The confined ice III melts before the external

hexagonal phase, between 249 K and 264 K. These results confirm that the confined phase transition at 1000 bar is reproducible and reversible in temperature and pressure.

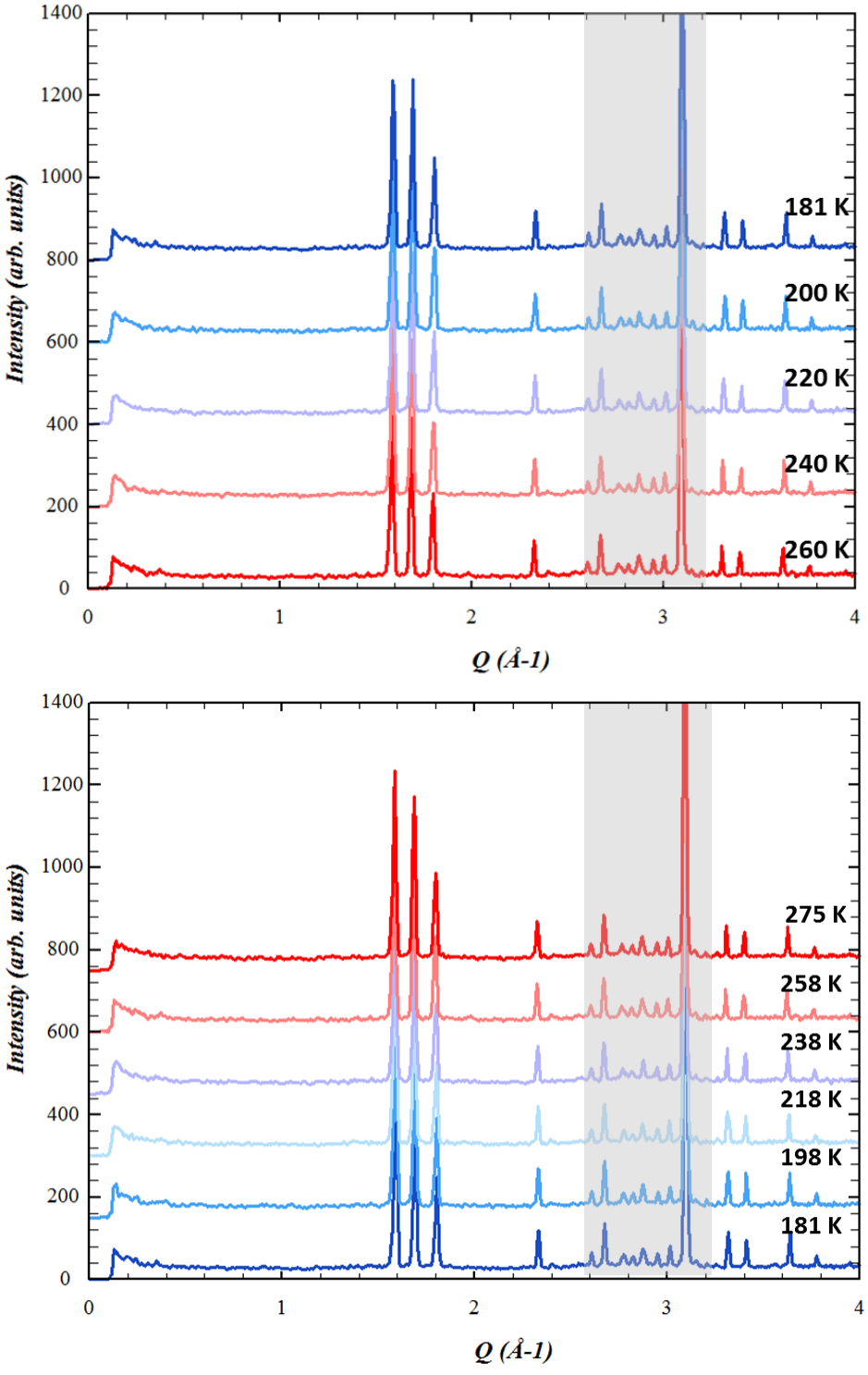

Figure 7.22: C18-M15-Me $SiMe_3$. Heating cycle back at P = 1 bar. Up: Cooling cycle, Down: Heating cycle. Only the external I_h phase is observed.

The results at the end of the decompression cycle (Figure 7.22) show that only the hexagonal phase, expected for bulk D_2O, is present upon cooling and heating cycles. The absence of high-pressure phases in these spectra agrees with our neutron imaging results,

where we observed that, at atmospheric pressure, water had been expulsed from the hydrophobic nanopores.

7.4. Conclusion

In this chapter, we have discussed the results related to the hydrophobic confinement of water in grafted organosilica nanopores. The experimental techniques used for this study were nitrogen and water vapor adsorption, neutron imaging, and high-resolution neutron diffraction.

On the water vapor adsorption in hydrophobic nanopores, we found that the high hydrophobicity of the synthesized materials makes it impossible for water to condense at $P < P_0$. However, our analysis revealed that only a few water molecules can be adsorbed on hydrophobic nanopores via a slow process that occurs in small jumps where water clusters might form around silanol groups.

The intrusion pressure, determined by neutron imaging, ranges between 380 bar and 450 bar, depending on the material. A significant hysteresis was found for the extrusion, which occurred at nearly atmospheric pressure. The values of the intrusion pressure versus the inverse of the pore radius (Laplace-Washburn representation) were compared to the available literature, and we found that our results are in agreement with those obtained by Lefevre *et al.* (2004)[5] for the intrusion of pure water in similar grafted nanoporous silica.

However, we have observed that, even at lower pressures (109 bar for C18-M15-Me $SiMe_3$), it is possible to introduce a reduced amount of water in the hydrophobic nanopores (6 molecules/nm^3, on average) if enough time (at least 40 minutes) is elapsed at isobaric conditions.

Our results also show that water molecules continue to enter the hydrophobic nanopores after the intrusion pressure. In C18-M7-Me $SiMe_3$, for instance, the amount of water in the nanopores increases from 17.8 molecules/nm^3 at the end of the intrusion (582 bar) to 24.3 molecules/nm^3 at the end of the experiment, at 2000 bar.

On the study of the phases of ice formed inside the nanopores, we found that the hydrophobically confined water forms higher-density ice forms. More precisely, the phases ice II and ice III were found at 1000 bar (half of the pressure needed to observe such phases in bulk water), and we observed reversible and reproducible phase transitions from ice II to ice III and then to liquid water.

Considering that the average density of water inside the nanopores was found to be lower than bulk liquid water, but still, higher-density ices are formed, we conclude that the local organization of water at the nanoscale consists of high-density water pockets surrounding the available hydrophilic sites, and empty, forbidden zones where the organic

groups repulse and compress water.

Finally, from our observations, we have drawn new transition lines (Figure 7.23) to the Pressure-Temperature phase diagram of heavy water confined in the hydrophobic nanopores of C18-M15-Me $SiMe_3$.

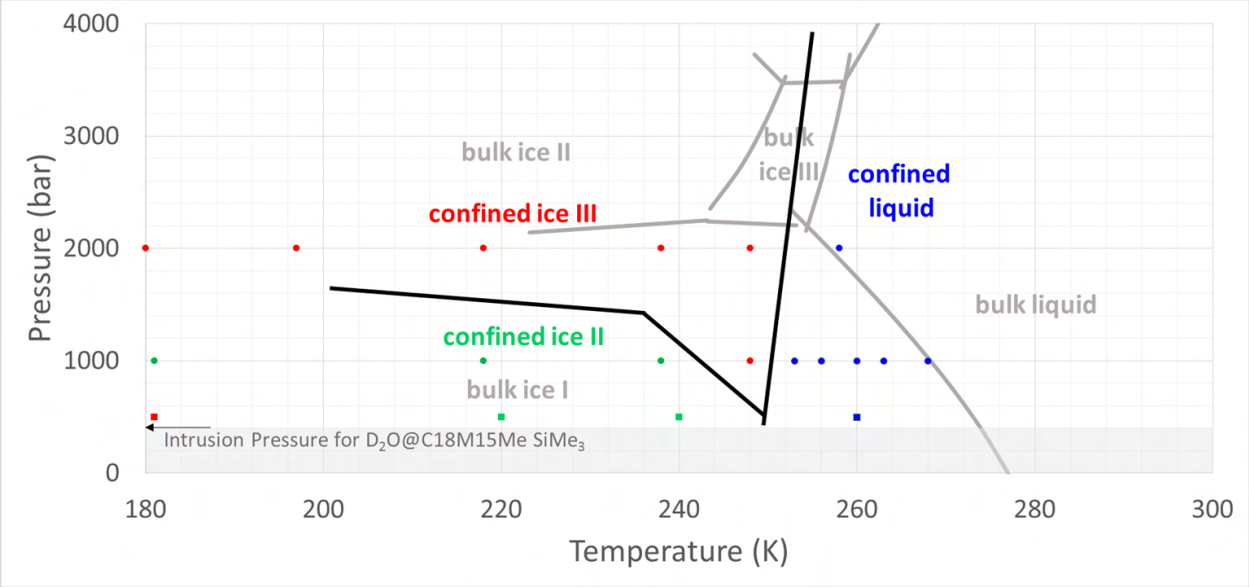

Figure 7.23: Phase diagram of bulk D_2O (Bridgeman, 1935, in grey)[20] and schematic transition lines of confined D_2O (this work, black lines). Neutron diffraction results are symbolized by dots. Red dots: confined ice III, green dots: confined ice II and blue dots: confined liquid.

References

1. Wenzel, R. N. Surface Roughness and Contact Angle. *J. Phys. Chem.* **53**, 1466–1467 (1949).
2. Zhang, J.-P., Zhu, A.-X., Lin, R.-B., Qi, X.-L. & Chen, X.-M. Pore Surface Tailored SOD-Type Metal-Organic Zeolites. *Adv. Mater.* **23**, 1268–1271 (2011).
3. Sing, K. S. W. Reporting physisorption data for gas/solid systems with special reference to the determination of surface area and porosity (Recommendations 1984). *Pure and Applied Chemistry* **57**, 603–619 (1985).
4. Thommes, M. *et al.* Physisorption of gases, with special reference to the evaluation of surface area and pore size distribution (IUPAC Technical Report). *Pure and Applied Chemistry* **87**, 1051–1069 (2015).
5. Lefevre, B. *et al.* Intrusion and extrusion of water in hydrophobic mesopores. *The Journal of Chemical Physics* **120**, 4927–4938 (2004).
6. Eroshenko, V. & Grosu, Y. Thermodynamic and operational properties of heterogeneous lyophobic systems. *Int. J. Thermo* **16**, 1–9 (2012).
7. Grosu, Y. G. Thermodynamics and operational properties of nanoporous heterogeneous lyophobic systems for mechanical and thermal energy storage/dissipation. (2015).
8. Fraux, G., Coudert, F.-X., Boutin, A. & Fuchs, A. H. Forced intrusion of water and aqueous solutions in microporous materials: from fundamental thermodynamics to energy storage devices. *Chem. Soc. Rev.* (2017) doi:10.1039/C7CS00478H.
9. Loic, M. Etude macroscopique dynamique et microscopique des systèmes hétérogènes lyophobes. (2019).
10. Michelin-Jamois, M., Picard, C., Vigier, G. & Charlaix, E. Giant Osmotic Pressure in the Forced Wetting of Hydrophobic Nanopores. *Phys. Rev. Lett.* **115**, 036101 (2015).
11. Kang, M. *et al.* Water calibration measurements for neutron radiography: Application to water content quantification in porous media. *Nuclear Instruments and Methods in Physics Research Section A: Accelerators, Spectrometers, Detectors and Associated Equipment* **708**, 24–31 (2013).
12. Picard, C., Gérard, V., Michel, L., Cattoën, X. & Charlaix, E. Dynamics of heterogeneous wetting in periodic hybrid nanopores. *J. Chem. Phys.* **154**, 164710 (2021).
13. Desbiens, N. *et al.* Water Condensation in Hydrophobic Nanopores. *Angew. Chem. Int. Ed.* **44**, 5310–5313 (2005).

14. Tzanis, L., Trzpit, M., Soulard, M. & Patarin, J. High pressure water intrusion investigation of pure silica 1D channel AFI, MTW and TON-type zeolites. *Microporous and Mesoporous Materials* **146**, 119–126 (2011).

15. Trzpit, M. *et al.* The Effect of Local Defects on Water Adsorption in Silicalite-1 Zeolite: A Joint Experimental and Molecular Simulation Study. *Langmuir* **23**, 10131–10139 (2007).

16. Fortes, A. D., Wood, I. G., Alfredsson, M., Vočadlo, L. & Knight, K. S. The incompressibility and thermal expansivity of D_2O ice II determined by powder neutron diffraction. *J Appl Crystallogr* **38**, 612–618 (2005).

17. Kamb, B., Hamilton, W. C., LaPlaca, S. J. & Prakash, A. Ordered Proton Configuration in Ice II, from Single-Crystal Neutron Diffraction. *The Journal of Chemical Physics* **55**, 1934–1945 (1971).

18. Kamb, B. & Prakash, A. Structure of ice III. *Acta Crystallogr B Struct Crystallogr Cryst Chem* **24**, 1317–1327 (1968).

19. Goto, A., Hondoh, T. & Mae, S. The electron density distribution in ice I_h determined by single-crystal x-ray diffractometry. *The Journal of Chemical Physics* **93**, 1412–1417 (1990).

20. Bridgman, P. W. The Pressure-Volume-Temperature Relations of the Liquid, and the Phase Diagram of Heavy Water. *The Journal of Chemical Physics* **3**, 597–605 (1935).

CONCLUSION

This work addresses the phase behavior of water confined in organosilica nanopores (MCM-41-type) with different levels of hydrophobicity. Our research contributes to the state-of-the-art of several critical issues in water confinement, such as the synthesis of amphiphilic and hydrophobic confining materials, the study of water vapor adsorption and its density in the nanopores, water intrusion/extrusion in hydrophobic materials, the determination of freezing and melting temperatures of confined water as a function of surface chemistry, and the investigation of the crystal structure of confined ice. Two main findings can be highlighted from this thesis: First, we observed that the surface hydrophobicity enhances the effects of confinement on the density and freezing/melting behavior of water in small amphiphilic nanopores (D < 4.5 nm). Second, we found that water confined in highly hydrophobic nanopores (D ~4 nm) crystallizes into higher density ice forms (ices II and III) at significantly lower pressures than expected.

On the synthesis of amphiphilic nanomaterials, a co-condensation approach allowed us to obtain cylindrical nanopores, similar to MCM-41, but with a degree of hydrophobicity given by the presence of different densities (from 0.18 to 0.34 nm^{-2}) and types of organic groups (methyl, ethyl, or phenyl) integrated into the materials' framework. Even though these materials are less hydrophilic than template-extracted (washed) MCM-41, they still present a high water adsorption capacity at low pressures ($P < P_0$).

We found that the density of water confined in amphiphilic nanopores (~26 molecules/nm^3) is significantly lower than in hydrophilic MCM-41 (~28 molecules/nm^3). Furthermore, in the selected range of pore sizes (D < 4.5 nm), the surface hydrophobicity causes an increase in the melting temperature depletion, a decrease in the percentage of crystalized water, and a reduction of the ice grains size. The crystalline structure of confined ice, determined by neutron diffraction, corresponds to stacking-disordered ice (I_{SD}) with around 30 % hexagonal (I_h) and 70 % cubic (I_c) layers. The non-freezable fraction of water, determined by differential scanning calorimetry and neutron diffraction, goes from 45 % to nearly 80 %, depending on the hydrophobicity level. We propose that this liquid-like, amorphous water presents a non-homogeneous distribution around the ice grains, especially around the organic groups at the surface of the amphiphilic nanopores. From our preliminary results on water dynamics, we conclude that the organic groups at the surface might be responsible for slowing down the water molecules that surround them, hindering the ice grain growth.

Later, we post-grafted additional organic groups to the surface of two amphiphilic materials yielding highly hydrophobic nanopores. Their characterization by TGA revealed a grafting density of 0.33 nm^{-2} and 0.56 nm^{-2}, in addition to the pre-existent organic groups. Adsorption experiments showed that water does not condense at low pressures in such nanopores, and higher pressures are required to force water intrusion.

The intrusion pressure, determined by neutron imaging, was around 400 bar (D ~ 4 nm). However, it was possible to introduce a reduced amount of water (6 molecules/nm^3, on average) in the hydrophobic nanopores at lower pressures (109 bar) if enough time (at least 40 minutes) is elapsed at isobaric conditions. It was also observed that water molecules continue to enter the hydrophobic nanopores after the intrusion pressure. A significant hysteresis was found for the extrusion, which occurred at nearly atmospheric pressure.

On the study of the phases of ice formed inside the nanopores, we found that the hydrophobically confined water forms higher-density ice forms. Ice II and III phases were found at 1000 bar (half of the pressure needed to observe such phases in bulk water). The phase transitions from confined ice II to ice III and then to liquid water are reversible and reproducible. These results allowed us to draw new transition lines to the Pressure-Temperature phase diagram of heavy water confined in hydrophobic nanopores.

In hydrophobic nanopores, the juxtaposition between the lower average density of confined water and the formation of higher-density forms of ice might be the result of a local organization in which high-density water pockets surround the available hydrophilic sites, and there are empty, forbidden zones where the organic groups repulse and compress water.

As a perspective, it would be interesting to explore new applications for the amphiphilic and hydrophobic nanoporous materials to confine other systems, such as water-glycerol mixtures and ionic solutions, to study the simultaneous effect of soft and hard amphiphilic confinement. In the research of the phase diagram of confined water at high pressures, it is essential to address the ice phases formed using hydrophilic and amphiphilic materials.

APPENDICES

APPENDIX 1:

A HANDS-ON GUIDE TO POST-GRAFTING NANOPOROUS MATERIALS

In previous experiments, we have successfully synthesized mesoporous organosilica by the direct synthesis method. We have obtained materials similar to SBA-15 and MCM-41 with a homogeneous distribution of small organic groups (methyl, ethyl, and phenyl) at the surface and within the pore walls. Our group has developed optimal methods for the synthesis and template removal of these materials. Results show increased resistance to hydrolysis and an increase in hydrophobicity compared to the standard material. This is evidenced by a systematic decrease in the melting point of water inside the pores.

However, the degree of hydrophobicity obtained by direct synthesis is limited if we aim to obtain an ordered hexagonal pore structure. Therefore, in this experiment, we have decided to modify the surface of the methyl-containing mesoporous materials C18-M7-Me and C18-M15-Me with trimethylsilane groups.

This guide contains a detailed procedure to perform post-synthesis modifications to nanoporous materials to transform them into highly hydrophobic materials.

Substances:

- C18-M7-Me and C18-M15-Me
- $CHCl_3$
- $ClSi(CH_3)_3$
- $N(CH_2CH_3)_3$
- Molecular Sieve 0.3 nm, Merk

Equipment:

- Distillation apparatus
- Round bottomed flask (rbf) (2-neck or 3 neck)
- Oval magnetic stir bar
- Vacuum / gas double ramp
- Septuml
- Glass wool
- 3 Syringes glass/inox 20, 10, 5 ml

Reaction:

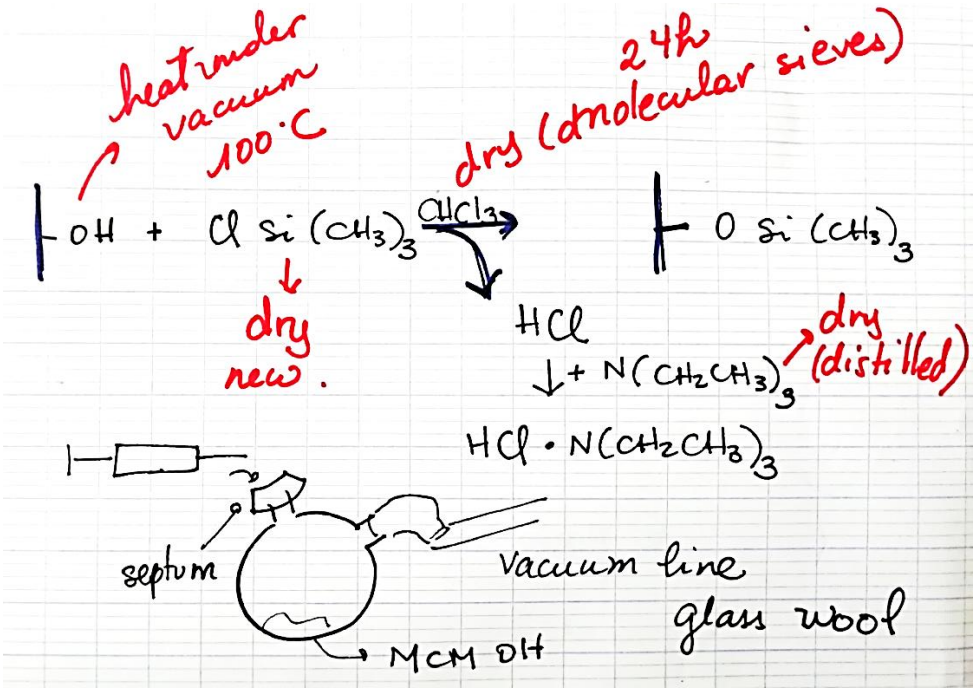

The primary source of error for this reaction: If any of the substances are not properly dry, the remaining water will react $ClSi(CH_3)_3$, which will reduce the amount of $ClSi(CH_3)_3$ available for reaction at the surface and form secondary products inside and outside of the pore network.

Preparation Steps:

- **Round bottom flask (rbf) and Stirrer**: Rinse consecutively with acetone, cyclohexane, and chloroform. Make sure to withdraw any residues from previous reactions. Dry at 110 °C. Place some glass wool securely in the connection to avoid loss of powder and contamination of the line.
- **Syringes:** Rinse with chloroform and let them dry at ambient temperature.
- **Dry silica/organosilica materials** at 110 °C for at least 24 h.
- **Activate molecular sieves** (0.3 nm, Merck) by heating them to 110 °C in the oven for 24h. Then place them with the CHCl3 in a container with a screw cap for 24 h before commencing the reaction.
- **Distill $N(CH_2CH_3)_3$.**
- Double manifold **vacuum line**: Degreasing and greasing (only necessary after cleaning or after a long period of non-usage). Remove ramp from support. Remove all valves and wash them in cyclohexane. Remove old grease and any other residue inside the ramp. Use a wash bottle to economize solvent. Then add a small amount of Apiezon grease on all joints and assemble as shown in **Figure 1.**

Figure 1: Apparatus for reaction under inert atmosphere.

Step 1: Outgassing

⚠ Before opening the Argon flow, make sure all valves from the entry to the bubbler are open.

1. Slowly introduce Argon to the line. Control the speed by looking at the bubbler: One to two bubbles per second (bps) **(Figure 2).**
2. Purge the rbf: Pump out the air by slowly opening the vacuum. You should hear a noise from the vacuum pump while the air is being extracted; close the valve after the noise has stopped.
3. Increase the argon flow to 3 – 4 bps. Fill the rbf with Argon. This will require *carefully* opening and closing the rbf valve several times, avoiding the suction of oil from the bubbler into the line. An optimal Argon rate can be found where rbf filling is rapid.
4. If you have a second balloon in the line, close the valve of the first balloon to change pressure in the second one. Repeat 2 and 3. Reduce the argon flow to the initial rate.
5. Introduce the powder: Ensure there is Argon pressure in the line and the rbf by verifying that the pertinent valves are open. Remove one septum *(Bubbling in oil bubbler stops immediately!)* and introduce the powder with the help of a plastic funnel, close the rbf. *Remember to close the valve to the first rbf before repeating the procedure for the second one*.
6. Carefully open the vacuum for the first sample, close the valve and repeat for the second sample. Then, re-open the vacuum for the first sample and increase the bath temperature to 100 °C.
7. Seal the septum with parafilm. Close Argon and let it outgas all night at 100 °C.

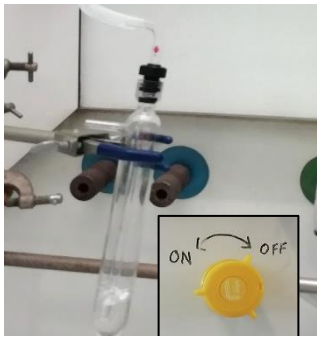

Figure 2: Argon rate control.

Step 2: Silylation Reaction

1. Remove the oil bath and let it cool down for one hour.
2. Introduce Argon into the rbfs (See **Step 1.3**).
3. Connect the Schlenk flask containing triethylamine into the third line and put it under Argon flow **(Figure 3).**
4. Confirm there is Argon pressure in the line and in both reaction flasks before starting the additions.
5. Now the solvent and reagents will be added in this order: chloroform, triethylamine and chlorotrimethylsilane. For each addition before introducing the syringe in the bottles, purge them with Argon three times, the last time take the volume you wish to collect from the reactant's or solvent's flask, release the argon inside the bottle and take the same volume of liquid. Then, remove one septum *(Bubbling should stop immediately!)* and introduce the chloroform making circular movements to drag all the powder left around the flask's neck, close the rbf and stir at 230 rpm, let it stir for 5 minutes **(Figure 4).**
6. Add the triethylamine dropwise for both reactions.
7. Add the chlorotrimethylsilane dropwise for both reactions. The formation of HCl (gas) and subsequent neutralization with the triethylamine is expected.
8. Rinse the syringes with ethanol immediately after the additions.
9. Cover the flasks with aluminum foil, seal the septum with parafilm **(Figure 5)** and let them stir for at least one hour under Argon flow. Close valve and close the Argon bottle. Leave the reaction to stir overnight.

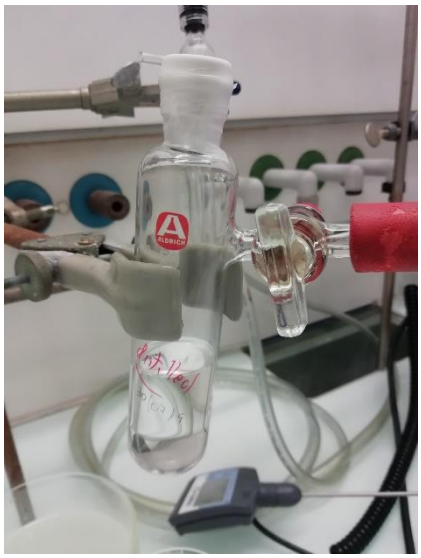

Figure 3: Schlenk flask containing distilled triethylamine.

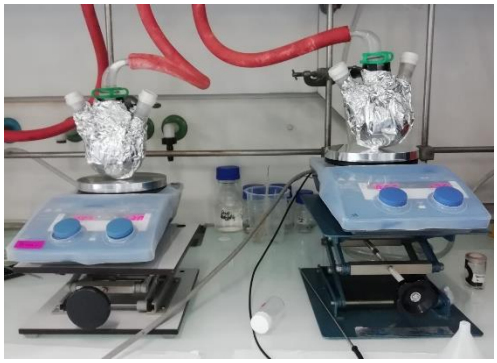

Figure 4: Aluminum foil.

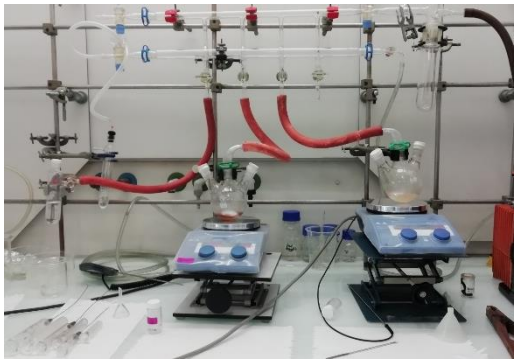

Figure 5: After solvent addition.

Step 3: End of reaction and filtration

1. After one day, the reaction is complete (Figure 6). An inert atmosphere is no longer needed. Register any change of color.
2. Add 50 ml of chloroform and stir vigorously for one hour to dissolve sub-products. Be careful: Formation of HCl when opening flask **(Figure 7)** from excess $ClSi(CH_3)_3$**.**
3. Proceed to filtration with a Buchner funnel (Porosity 4). Rinse three times with chloroform **(Figure 8)** and let the product dry overnight **(Figure 9)**, placing a filter paper on the top of the filter to avoid material loss.
4. Collect the material, transfer to a glass recipient and dry it in the oven at 80 °C. Proceed to characterize the material.

Figure 8: Final chloroform addition.

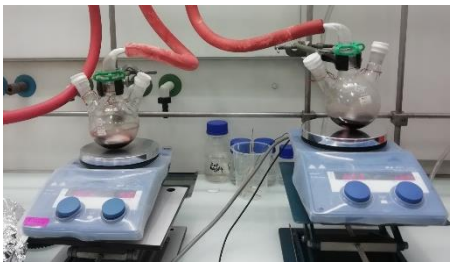

Figure 7: Reaction after 24 h.

Figure 6: Filtration.

Figure 9: Materials before (left) and after (middle) drying. At the right, samples as they have been storage. The obtained powders do not disperse in water, only in ethanol.

Characterization

Chapter 3 describes the techniques for the characterization of the post-grafted materials.

APPENDIX 2:
H_2O VS. D_2O

Replacing ^1H atoms for its isotope ^2H (D) generates a number of differences in the properties of liquid and crystalline water. This is mainly attributed to quantum differences between H_2O and D_2O. For example, D_2O vibrate less and has stronger hydrogen bonds than H_2O, therefore heavy water has been found to be more structured (tetrahedral) than light water (at 25 °C).[19] This explains the slightly larger molar volume of the liquid and the solid (Ih) forms.

D_2O plays an important role in this thesis, as it was used for the neutron diffraction experiments, due to its larger coherent neutron scattering cross section and lower incoherent scattering cross section.

Table 1 shows a comparison between the most important properties of light and heavy water for the purposes of this work.

Table 1: Physical properties of H_2O and D_2O.

Properties	H2O	D2O
Melting Temperature 101.325 kPa (K)	273.152 519 K (0.00 °C) [22]	276.972 519 K (3.82 °C)
Molar Volume of liquid at 25 °C ($cm^3\ mol^{-1}$)	18.0685 cm^3	18.1331 cm^3
Molar Volume of I_h ($cm^3\ mol^{-1}$)	19.66 cm^3 (ice Ih, 0 °C)	19.679 cm^3 (3.81 °C)
Density maximum	3.984 °C , 999.972 kg × m^{-3}	11.185 °C, 1105.3 kg × m^{-3}
Specific heat capacity at 25 °C, Cp	75.338 J × mol^{-1} × K^{-1}	84.67 J × mol^{-1} × K^{-1}
Enthalpy of fusion at 0 °C, 101.325 kPa	6.00678 kJ × mol^{-1}	6.132 kJ × mol^{-1} (3.68 °C)
Translational diffusion coefficient	0.2299 $Å^2$ × ps^{-1} (25 °C)[24], 0.0187 $Å^2$ × ps^{-1} (-31 °C)	0.2109 $Å^2$ × ps^{-1} (25 °C)[21]
Isothermal compressibility	0.4599 GPa^{-1} (25 °C)[25]	0.4763 GPa^{-1} (25 °C)[25]
Coherent neutron scattering length (fm)	H, -3.7409 fm O, +5.805 fm	^{2}H (D), +6.674 fm O, +5.805 fm
Incoherent neutron scattering cross section (b) (1 b = 100 fm^2)	H, 80.26 ^{16}O 0.0	^{2}H (D) 2.05 ^{16}O 0.0

APPENDIX 3

WATER ANOMALIES

The melting point of ice reduces with pressure

In a simple liquid, an increase of pressure promotes freezing, which causes a shift of the melting point towards higher temperatures. In the temperature-pressure phase diagram, this is noted in phase diagrams as a positive slope in the solid-liquid transition line.

In water at pressures up to 2 kbar (200 MPa), this transition line presents a negative slope (Figure 1a). In fact, as the pressure increases, water collapses into clusters of higher density and entropy, causing a shift of the melting point towards lower temperatures. At higher pressures, water crystallizes in the form of ice III, V, VI or VII (Figure 2).[1]

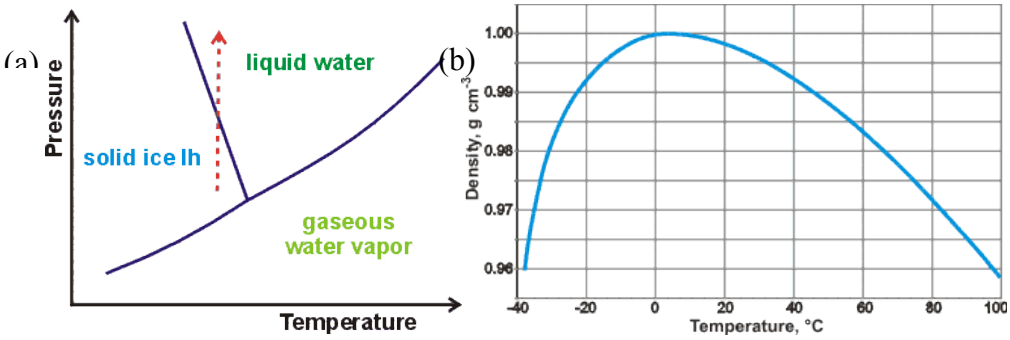

Figure 1: (a) Schematic representation of water's phase diagram in linear scale.[1] (b) Water's density as a function of the temperature, at P = 1 bar, in the range (-40°C < T < 100°C)[1].

Liquid water has a density maximum

The density of most liquids decreases upon heating at any temperature. Instead, the density of liquid water increases from the supercooled domaine to nearly 4°C (Figure 1b). After this temperature, liquid water starts to expand when heated. This phenomenum is the product of two competing mechanisms: structural collapses and thermal expansion.[1] The temperature of maximum density shifts to lower temperatures with increasing pressure up to 2 kbar, when it desappears.[2]

Water has a large number of crystalline and amorphous structures

This phenomenum is also called *water polymorphism* or *polyamorphism*, in the case of amorphous structures. To this day, we know eighteen stable and metastable crystalline ice phases, and three amorphous ice phases. Each of these structures can be understood as (distorded) tetrahedral networks of water molecules where each molecule donates two hydrogen bonds and accepts two of them from/to its neighbors, producing four-coordinated systems. The way in which these units links together, gives rise to the different structures of ice. Even amorphous phases of ice keep a local coordination with four neighbors, with the difference that, unlike crystalline phases, there is no repetition of a unit cell that can recreate the whole structure. [3,4]

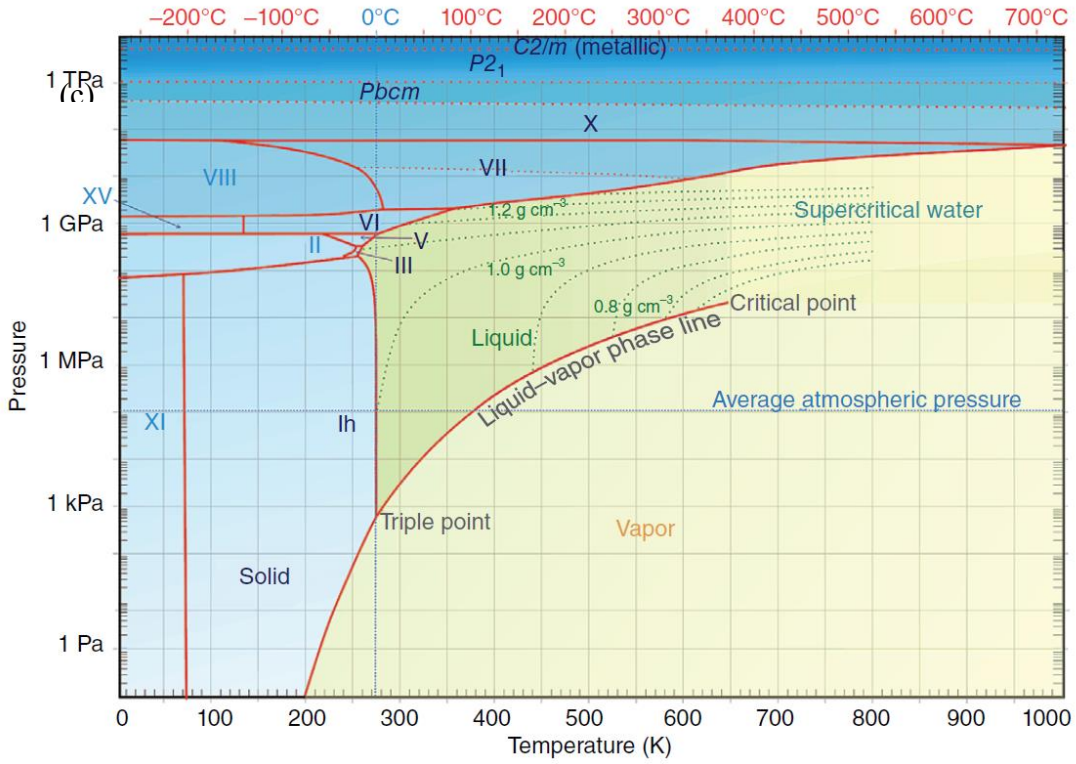

Figure 2: Log-lin pressure-temperature water phase diagram showing the stable ice crystalline phases.5

As it is shown in Figure 3, at low pressure (1 bar) bulk water generally forms stable hexagonal ice (I_h) with O···O···O angle of 109.47° (an exception will be discussed later), as pressure increases, denser crystalline structures are formed by modifications in the network structure and distortions in the O···O···O angles. In ice II these angles vary between 80° and 129° and the decrease in volume with respect to ice I_h is $\Delta V = 3.92$ cm^3 mol^{-1}. The difference between ice II and ice V is $\Delta V = 0.7$ cm^3 mol^{-1}, this last structure has a wide range of angles going from 82 to 135°. The same value (0.7 cm^3 mol^{-1}) corresponds to the difference between ice V and ice VI, with O···O···O angles in the range of 77 to 128°. At

higher pressures, the empty space cannot be filled by a simple distortion of the hydrogen bonds, therefore, ice VII consists in two interpenetrating, four-coordinated networks. The ΔV associated to the change of ice VI to ice VII is 1.05 cm^3 mol^{-1}.[1,3,5]

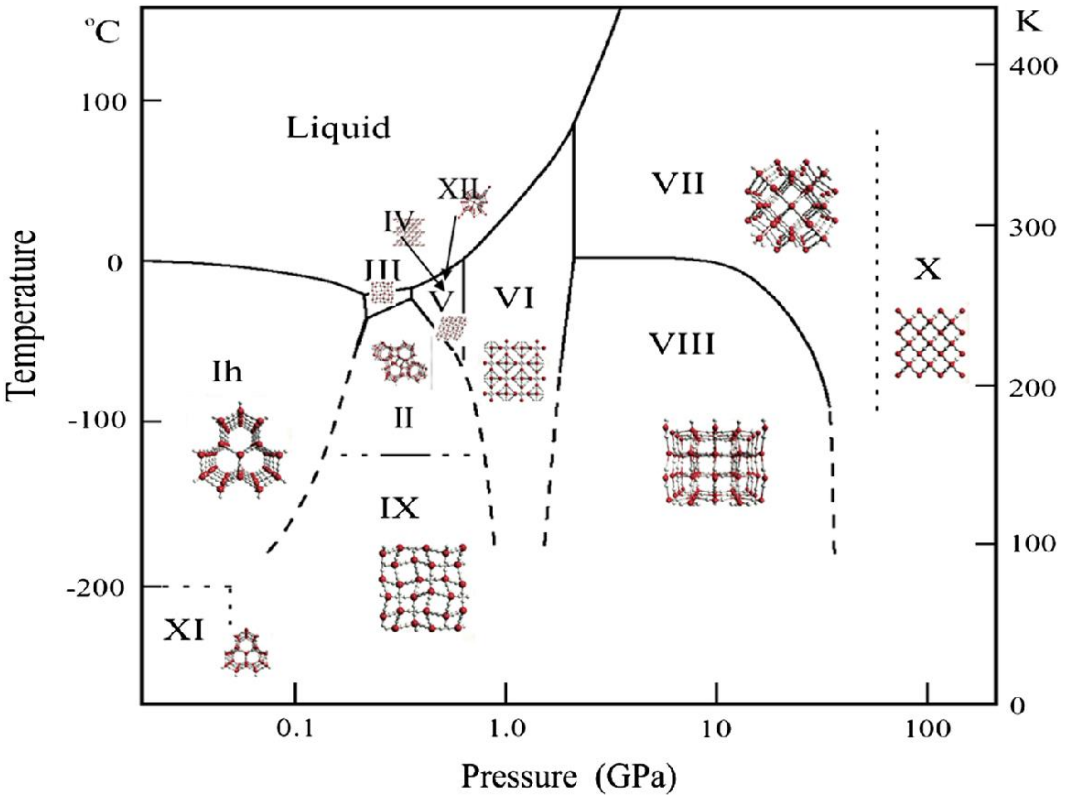

Figure 3: The solid-liquid phase diagram of water.[3]

Under particular conditions,[6] water can also form an structure combining hexagonal ice and cubic ice (I_c). This structure, consisting on randomly mixed I_h and I_c planes receives the name of stacking-disordered ice I_{SD}[7–9]. It is worth noting that a pure crystal of cubic ice (I_c) has not been prepared[11], but the proposed structure is that of a face-centered cubic lattice (space group $P3m_1$)[10,11]. These three possible structures of ice I (I_h, I_c and I_{SD}) have similar densities[11] but different relative stabilities hexagonal ice being the most stable, followed by I_{SD} and lastly I_c. In geometrically confined systems, I_{SD} seems to be the preferred structure of water at ambient pressure.[12]

This wide variety of crystalline structures that change upon conditions of temperature and pressure, are what makes water the ultimate probe for nanoenvironments. Indeed, subtle changes in the pressure perceived by water, can produce the transformation of its crystalline structure. A simpler substance, as olefins or even alcohols, would not be as useful as water to gather information about nanopores, simply because their crystalline

structure remains almost unchanged in the temperature and pressure ranges of this study.

No man's land

Supercooled liquid water can be studied down to the limit of homogeneous nucleation (T_H) at around 232 K and below the glass transition temperature (T_g) at around 160 K, at 1 bar. This "experimentally unaccesible" area (Figure 2) has been called "no man's land". It has been hipothisized that, by extrapolating the transition line between low density amorphous (LDA) and high density amorphous (HDA) glassy water, the obtained line (grey line in Figure 2) would be the border line of a liquid-liquid phase transition between a low density and a high density liquid, with a second critical point lying under the T_H transition line.[13]

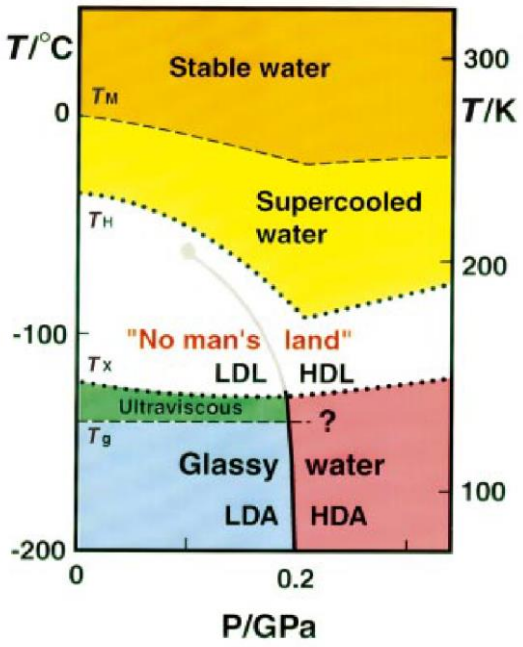

Figure 4: Phase diagram of water at low temperature[13]

Ultrafast spectroscopy[14], the use of micro- (and nano-) droplets and water confinement are some of the methods used to circumvent the problem of "no man's land".

References

(1) Martin, C. Water Structure and Properties. Http://Www1.Lsbu.Ac.Uk/Water/. 2000.

(2) Kumar, P. ANOMALIES OF BULK, NANOCONFINED AND PROTEIN-HYDRATION WATER. 210.

(3) Bartels-Rausch, T.; Bergeron, V.; Cartwright, J. H. E.; Escribano, R.; Finney, J. L.; Grothe, H.; Gutiérrez, P. J.; Haapala, J.; Kuhs, W. F.; Pettersson, J. B. C.; Price, S. D.; Sainz-Díaz, C. I.; Stokes, D. J.; Strazzulla, G.; Thomson, E. S.; Trinks, H.; Uras-Aytemiz, N. Ice Structures, Patterns, and Processes: A View across the Icefields. *Rev. Mod. Phys.* **2012**, *84* (2), 885–944. https://doi.org/10.1103/RevModPhys.84.885.

(4) Fuentes-Landete V.; Mitterdorfer C.; Handle P.H.; Ruiz G.N.; Bernard J.; Bogdan A.; Seidl M.; Amann-Winkel K.; Stern J.; Fuhrmann S.; Loerting T. Crystalline and Amorphous Ices. *Proc. Int. Sch. Phys. LdquoEnrico Fermirdquo* **2015**, *187* (Water: Fundamentals as the Basis for Understanding the Environment and Promoting Technology), 173–208. https://doi.org/10.3254/978-1-61499-507-4-173.

(5) *Encyclopedia of Water: Science, Technology, and Society*, 1st ed.; Maurice, P., Ed.; Wiley, 2019. https://doi.org/10.1002/9781119300762.

(6) Murray, B. J.; Bertram, A. K. Formation and Stability of Cubic Ice in Water Droplets. *Phys Chem Chem Phys* **2006**, *8* (1), 186–192. https://doi.org/10.1039/B513480C.

(7) Moore, E. B.; Molinero, V. Is It Cubic? Ice Crystallization from Deeply Supercooled Water. *Phys. Chem. Chem. Phys.* **2011**, *13* (44), 20008. https://doi.org/10.1039/c1cp22022e.

(8) Malkin, T. L.; Murray, B. J.; Brukhno, A. V.; Anwar, J.; Salzmann, C. G. Structure of Ice Crystallized from Supercooled Water. *Proc. Natl. Acad. Sci.* **2012**, *109* (4), 1041–1045. https://doi.org/10.1073/pnas.1113059109.

(9) Malkin, T. L.; Murray, B. J.; Salzmann, C. G.; Molinero, V.; Pickering, S. J.; Whale, T. F. Stacking Disorder in Ice I. *Phys. Chem. Chem. Phys.* **2015**, *17* (1), 60–76. https://doi.org/10.1039/C4CP02893G.

(10) König, H. Eine kubische Eismodifikation. *Z. Für Krist. - Cryst. Mater.* **1943**, *105* (1–6), 279–286. https://doi.org/10.1524/zkri.1943.105.1.279.

(11) Dowell, L. G.; Rinfret, A. P. Low-Temperature Forms of Ice as Studied by X-Ray Diffraction. *Nature* **1960**, *188* (4757), 1144–1148. https://doi.org/10.1038/1881144a0.

(12) Moore, E. B.; de la Llave, E.; Welke, K.; Scherlis, D. A.; Molinero, V. Freezing, Melting

and Structure of Ice in a Hydrophilic Nanopore. *Phys. Chem. Chem. Phys.* **2010**, *12* (16), 4124. https://doi.org/10.1039/b919724a.

(13) Stanley, H. E.; Buldyrev, S. V.; Canpolat, M.; Mishima, O.; Sadr-Lahijany, M. R.; Scala, A.; Starr, F. W. The Puzzling Behavior of Water at Very Low Temperature. *Phys. Chem. Chem. Phys.* **2000**, *2* (8), 1551–1558. https://doi.org/10.1039/b000058m.

(14) Nilsson, A.; Schreck, S.; Perakis, F.; Pettersson, L. G. M. Probing Water with X-Ray Lasers. *Adv. Phys. X* **2016**, *1* (2), 226–245. https://doi.org/10.1080/23746149.2016.1165630.

APPENDIX 4
RÉSUMÉ EN FRANÇAIS

Chapitre 1

Dans cette thèse, nous avons sélectionné des matériaux de type MCM-41, modifiés par synthèse directe ou par greffage post-synthèse pour contrôler le niveau d'hydrophobie à l'intérieur des pores. Ceci a permis l'étude expérimentale des transitions de phase de l'eau confinée, non seulement dans des nano-environnements hydrophiles et hydrophobes mais aussi dans des nano-environnements amphiphiles. La synthèse et la caractérisation de ces matériaux de confinement (chapitres 2, 3 et 5) ont constitué une partie importante de cette thèse.

Les études mentionnées dans ce chapitre montrent que le point de fusion de l'eau dans les nanopores hydrophiles diminue avec la taille des pores, ce comportement peut être ajusté avec le modèle de Gibbs-Thomson et la structure de la glace confinée dans ces nanopores hydrophiles correspond à un empilement de glace désordonnée. Cette thèse aborde l'effet de différents niveaux d'hydrophobie sur le point de fusion de l'eau et sa structure cristalline (chapitre 6).

Nous avons également vu les avancées des récentes investigations sur les processus d'intrusion et d'extrusion de l'eau dans les nanopores hydrophobes à haute pression. Cependant, une étude expérimentale utilisant la diffraction des neutrons sur la structure de la glace à l'intérieur des nanopores à haute pression n'a pas été rapportée auparavant. Nos résultats sur l'intrusion de l'eau dans les nanopores hydrophobes et la structure cristalline de l'eau confinée à haute pression sont exposés dans le chapitre 7.

En résumé, les objectifs de ce travail étaient :

- D'étudier l'effet de l'hydrophobie de la paroi du pore sur les propriétés de l'eau confinée (densité, Tm, structure cristalline de la glace...).

- D'étudier la structure de l'eau intrudée dans des nanopores hydrophobes à haute pression.

Chapitre 2

Dans ce chapitre, nous avons abordé le mécanisme et les méthodes utilisées pour synthétiser des organosilices nanoporeuses de type MCM-41 et l'élimination des gabarits. Deux approches de modification de surface pour contrôler l'hydrophobie des matériaux ont été exposées : la synthèse directe et le post rafting. La méthode de synthèse directe ou de co-condensation a été utilisée pour préparer les matériaux amphiphiles. L'utilisation de la méthode d'extraction par solvant nous a permis de préparer les produits de synthèse directe sans risque de brûler les groupes organiques à la surface.

Notre approche pour la synthèse des matériaux hydrophobes a consisté en une combinaison de co-condensation et de post-greffage.

Chapitre 3

Une détermination précise des propriétés physiques et chimiques des matériaux nouvellement synthétisés était nécessaire avant les études de confinement. Par conséquent, dans ce chapitre, nous avons présenté les techniques expérimentales qui ont permis une caractérisation complète de ces matériaux.

Les méthodes utilisées pour étudier leur chimie de surface, le volume et la surface spécifiques des pores, la géométrie des pores et leur taille ont été discutées. Les résultats de la caractérisation sont présentés dans le chapitre 5.

La détermination de ce dernier paramètre a fait l'objet d'une attention particulière en raison de la grande variété des méthodes disponibles. Ici, nous avons présenté les arguments derrière notre sélection de la valeur de D_{SAXS} à partir de la méthode de Kruk-Jaroniec-Sayari.

Nous avons inclus l'étude de la surface des matériaux par adsorption de vapeur d'eau dans ce chapitre car cette méthode a permis de déterminer la densité de groupements hydroxyles en surface, et elle a été utile pour évaluer l'hydrophobie des matériaux. Cependant, nous verrons dans le chapitre suivant comment les mêmes expériences ont été

utilisées pour déterminer la densité de l'eau confinée.

Chapitre 4

Les différentes techniques utilisées dans cette thèse pour étudier l'eau confinée, ses mécanismes d'entrée dans les nanopores, ses transitions de phase, sa structure et sa dynamique ont été présentées dans ce chapitre. L'utilisation de l'adsorption d'eau et de l'imagerie neutronique nous a permis de suivre le remplissage des nanopores par l'eau via l'adsorption de vapeur, l'imbibition et l'intrusion. La calorimétrie différentielle à balayage a été utilisée pour déterminer la congélation et la fusion de l'eau confinée à la pression atmosphérique, tandis que la diffraction des neutrons a servi à déterminer la structure de l'eau liquide et de la glace à des pressions allant de 1 à 4000 bars. De plus, l'écho de spin neutronique a été utilisé pour étudier la dynamique d'échantillons sélectionnés d'eau confinée dans des nanopores amphiphiles.

Chapitre 5

Nous avons synthétisé des matériaux nanoporeux de type MCM-41 avec différents niveaux d'hydrophobie. Les nanopores sont cylindriques, organisés selon un arrangement 2D-hexagonal, et avec un diamètre de pore bien défini. L'hydrophobie est donnée par la présence de différentes densités de groupes organiques à la surface. Les matériaux modifiés sont divisés en deux groupes : amphiphiles et hydrophobes.

Les matériaux amphiphiles ont été synthétisés en utilisant la co-condensation du tétraéthoxysilane avec des alkyl-triéthoxysilanes. Leur hydrophobie provient des groupes méthyle, éthyle ou phényle intégrés dans la structure des matériaux. Ces groupes sont répartis entre la surface des pores et les parois intérieures des pores. Les matériaux amphiphiles présentent une grande capacité d'adsorption de la vapeur d'eau et une résistance à l'hydrolyse. Le pourcentage de groupes organiques pouvant être incorporés par cette synthèse est limité à moins de 20 % molaire dans le mélange des précurseurs. Au-delà de cette valeur, nous avons obtenu une structure de pore inhomogène, non adaptée à nos études de confinement. L'étude de l'effet du confinement amphiphile sur la densité, la congélation et la fusion de l'eau est présentée au chapitre 6.

Les matériaux hydrophobes ont été obtenus en effectuant une modification post-synthèse avec du chlorotriméthylsilane sur les matériaux amphiphiles C18-M7-Me et C18-M15-Me. La densité de greffage était de 0,56 nm-2 pour le C18-M7-Me SiMe3 et de 0,33 nm-2 pour le C18-M15-Me SiMe3. En raison de leur haut niveau d'hydrophobie, ces

nanopores ne peuvent pas être remplis par adsorption de vapeur d'eau, et nous avons besoin de hautes pressions pour forcer l'intrusion d'eau liquide. Ce sujet sera abordé dans le chapitre 7, ainsi que l'étude du confinement de l'eau dans les nanopores hydrophobes à haute pression.

Chapitre 6

Les résultats de ce chapitre montrent l'effet marqué de la chimie de surface sur les propriétés thermodynamiques de l'eau confinée à la pression atmosphérique. Nous avons trouvé des différences significatives dans la densité, le point de fusion, le pourcentage d'eau qui cristallise, et la taille des grains de glace formés.

La densité de l'eau confinée diminue par rapport à l'eau confinée dans le MCM-41 hydrophile lorsque des groupes organiques sont présents à la surface des nanopores. Cependant, à 298,15 K, nous n'avons pas trouvé de variations significatives entre C18-M7-Me, C18-M15-Me et C18-M7-Ph. Lorsque nous réduisons la température du système, nous commençons à remarquer des différences frappantes entre les échantillons. Nous avons trouvé une claire diminution de la température de fusion, en fonction de l'hydrophobie du matériau (Figure 6.4), et cela va de pair avec une diminution du pourcentage de cristal obtenu par DSC et par diffraction neutronique (Figure 6.8).

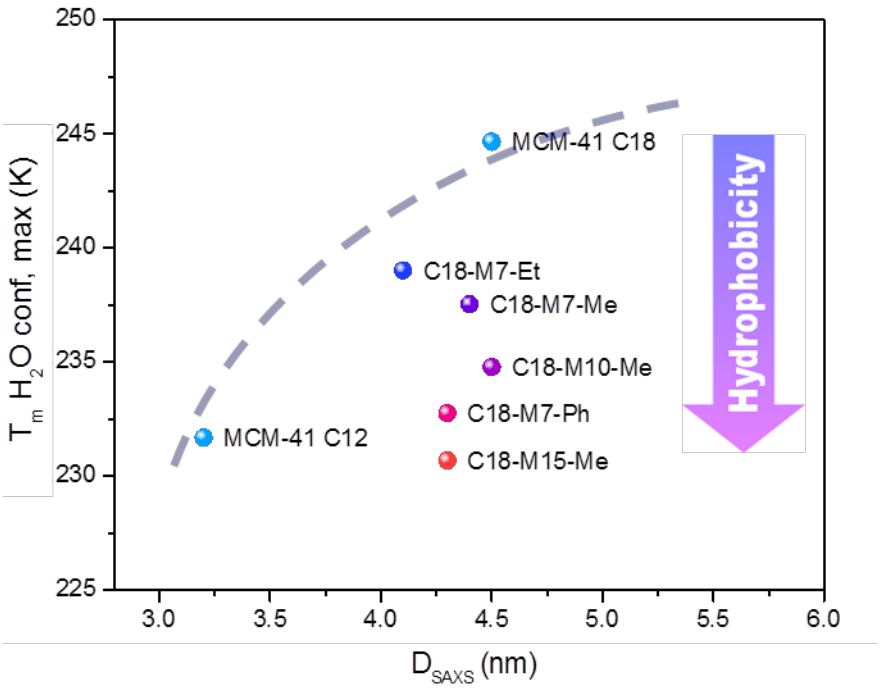

Figure 6.10: Température de fusion du H2O confiné en fonction de la taille des pores. La ligne pointillée est un guide pour l'œil correspondant aux valeurs attendues pour les matériaux MCM-41 hydrophiles. P = 1 bar.

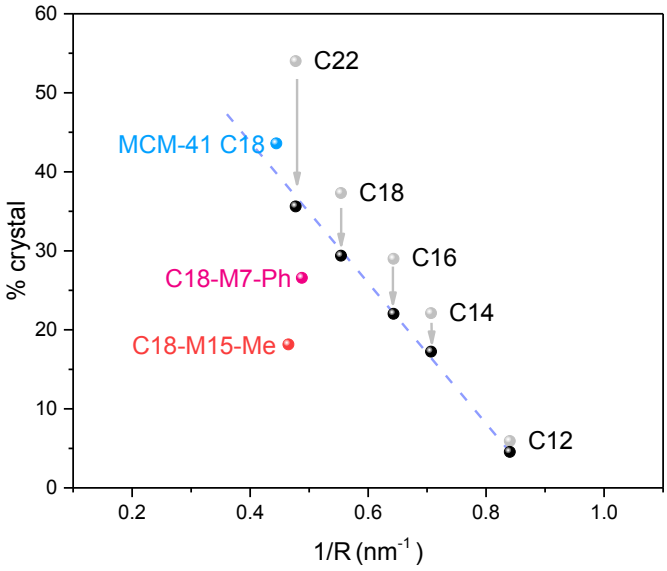

Figure 6.11: Pourcentage d'eau cristallisée dans les nanopores hydrophiles et amphiphiles, déterminé par calorimétrie en fonction de l'inverse du rayon des pores. Points gris : données tirées de Kittaka et al. (2006)12 : le diamètre des pores a été calculé à l'aide de la relation de Dollimore Hill, et la valeur de Hf a été calculée à partir des courbes DSC, en considérant la quantité d'eau provenant de la condensation capillaire, à l'exclusion du volume de la monocouche adjacente à la paroi du pore (environ 20-30% du volume du pore). Points noirs : Le % de cristaux diminue en considérant tout le volume des pores (y compris la monocouche d'adsorption). Points de couleur : Nos matériaux sélectionnés : MCM-41 C18 (lavé), C18-M15-Me, et C18-M7-Ph (l'eau confinée dans le C12-M7-Me ne cristallise pas). La ligne pointillée est un guide pour l'œil qui permet de différencier l'effet d'une diminution de la taille des pores de l'effet d'une augmentation de l'hydrophobie de la paroi des pores de nos matériaux amphiphiles.

La figure 6.9 montre plusieurs courbes de diffraction prises pendant le processus de fusion de D2O confiné dans C18-M15-Me. On peut y distinguer clairement que les pics de Bragg de la glace disparaissent entre 220 et 240 K. A partir de cette température, le schéma de diffraction typique de l'eau liquide apparaît.

L'évolution de ce que nous avons considéré comme les caractéristiques les plus critiques des courbes de diffraction en fonction de la température est représentée sur la figure 6.10. Nous pouvons y voir comment le maximum du facteur de structure (Qmax) et l'intensité S(Q), à différentes valeurs pertinentes du vecteur d'onde, telles que 1,0 Å-1, 1,7 Å-1, et 2,8 Å-1, changent pendant la rampe de température, en passant de 180 à 260 K.

La position du maximum du facteur de structure se déplace de 1,7 Å-1 à 1,85 Å-1 entre 220 et 250 K (courbe bleu clair). De même, l'intensité des pics de Bragg à 1,7 Å-1 et 2,8 Å-1 diminue fortement dans cette gamme de température (courbes rose et verte, respectivement).

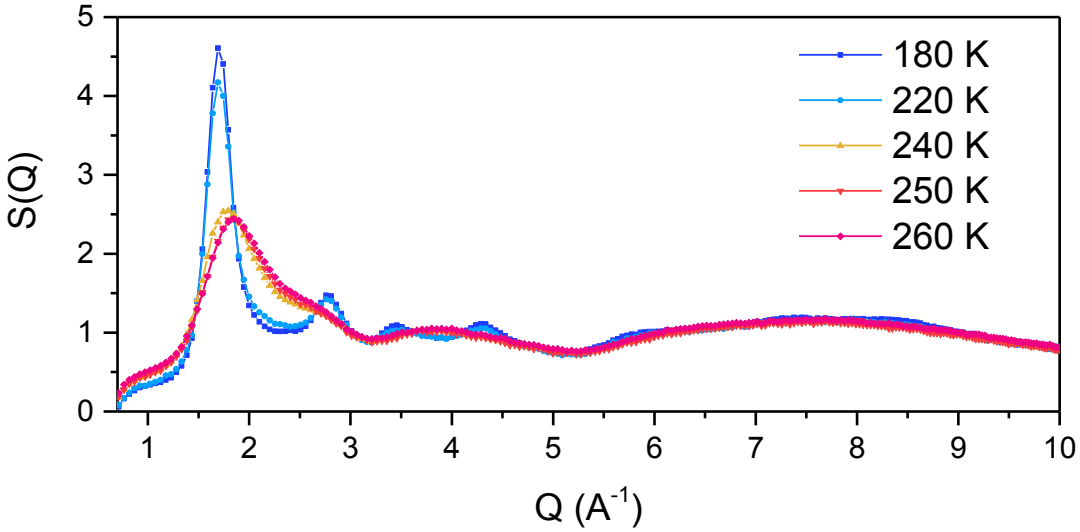

Figure 6.12: Neutron diffraction curves of water confined in C18-M15-Me during the melting process from 180 K to 260 K. The corrections applied to the curves are detailed in section 4.4 of chapter 4.

Ces changements dans le facteur de structure correspondent à la variation des termes intermoléculaires pendant la transition de phase solide-liquide de l'eau confinée. Le facteur de structure de la glace confinée dans C18-M15-Me est caractérisé par les pics de Bragg à 1,7, 2,8, 3,4 et 4,3 Å-1. Cette structure est stable pour des températures allant jusqu'à 220 K, lorsque le processus de fusion commence, et que la glace se transforme en eau liquide, qui est plus dense et moins organisée. Pour cette raison, nous observons un déplacement soudain de Qmax vers des valeurs de Q plus grandes et la disparition des pics de Bragg.

Dans ces matériaux amphiphiles, le Tm est mieux corrélé à la taille du grain de glace formé qu'à la taille des nanopores (Figures 6.18). Un autre résultat intéressant est qu'une diminution de la température de fusion est également suivie d'une diminution systématique de l'hystérésis de congélation-fusion.

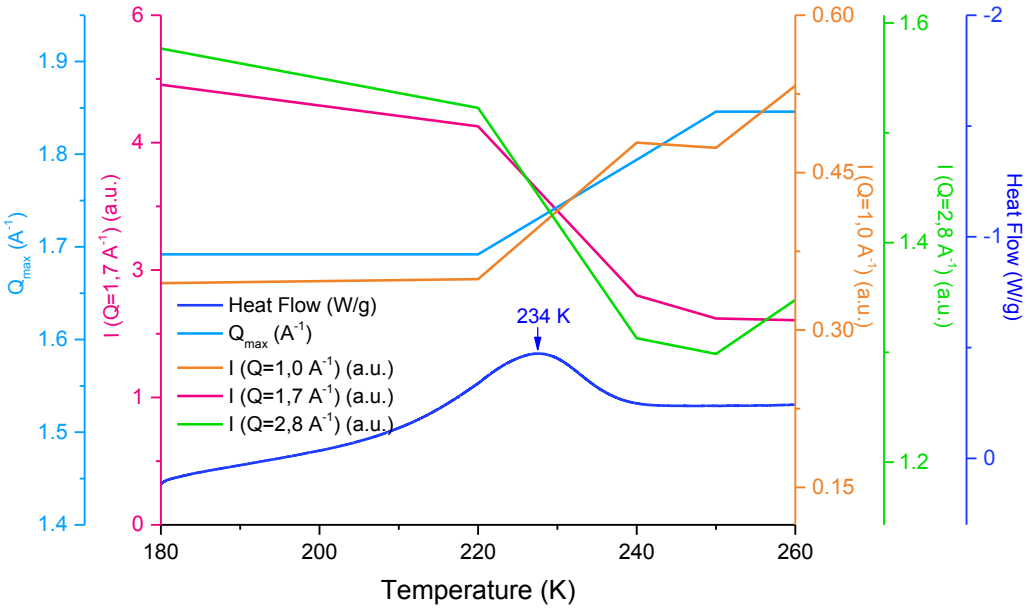

Figure 6.13: Évolution de certaines caractéristiques des courbes de diffraction des neutrons de D2O confiné dans C18-M15-Me en fonction de la température pendant la rampe de chauffage de 180 à 260 K à 1 bar. Le maximum du facteur de structure (Qmax) (bleu clair) et l'intensité de S(Q) à Q = 1,0 Å-1 (orange), 1,7 Å-1 (rose) et 2,8 Å-1(vert). En bleu foncé, la courbe DSC de D2O@C18-M15-Me montrant le pic endothermique de la fusion de la glace confinée dans la même plage de température.

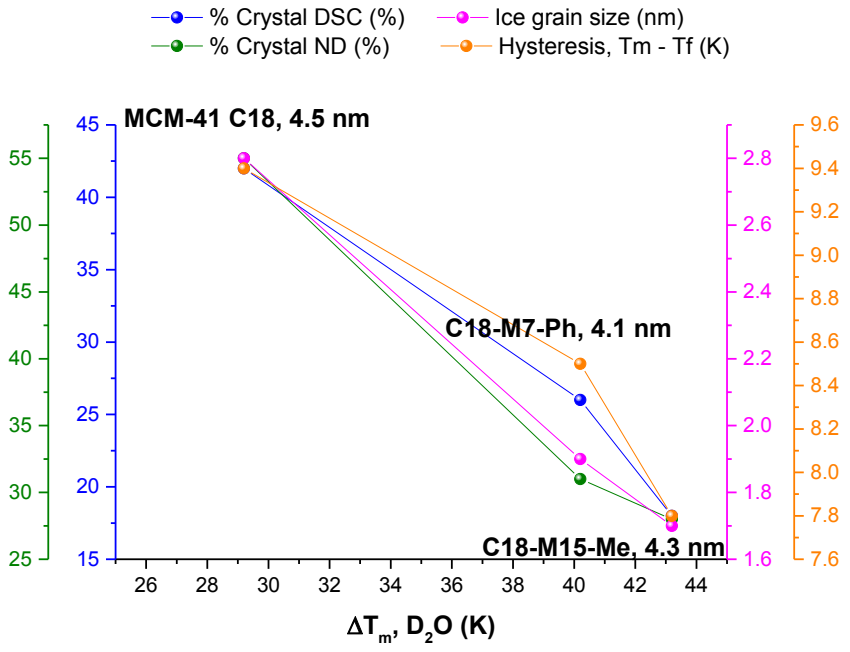

Figure 6.18 : Pourcentage de cristal par DSC et diffraction neutronique, taille du grain de glace et hystérésis en fonction de l'abaissement de la température de fusion pour des matériaux nanoporeux hydrophiles et amphiphiles.

L'effet de l'hydrophobie de la paroi des pores a également été étudié par Morishige (2018), en utilisant la DSC et la diffraction des rayons X pour évaluer l'abaissement du point de fusion et la structure de la glace confinée dans des carbones mésoporeux ordonnés avec des diamètres de pores compris entre 6,4 nm et 16,4 nm. Concernant la structure de l'eau confinée à 200 K, ils ont trouvé un bon ajustement pour une combinaison linéaire d'un composant cristallin et d'un composant amorphe attribué à une couche d'eau non congelable entre la surface des pores et un noyau de glace cristallin. Concernant la dépression du point de fusion, il n'a pas trouvé de différence significative par rapport à la silice hydrophile de taille de pore similaire (tailles de pore significativement plus grandes que dans cette étude).

Les résultats présentés dans ce chapitre concordent avec ceux de Morishige (2018) en ce sens que la structure de l'eau confinée à basse température contient un composant cristallin et un composant amorphe provenant de l'eau non congelable. Cependant, une couche liquide à côté de la paroi du pore ne serait pas suffisante pour expliquer la petite taille des cristallites de glace. C'est pourquoi nous proposons que la fraction liquide de l'eau présente une distribution non homogène autour des grains de glace dans les nanopores, et surtout à proximité des groupes organiques à la surface des matériaux amphiphiles, comme schématisé dans la Figure 6.19.

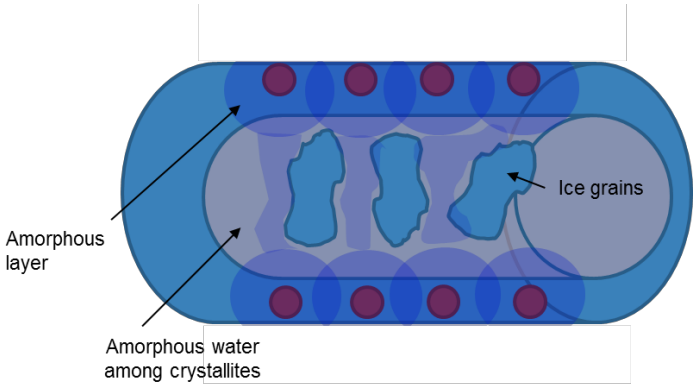

Figure 6.19 : Représentation schématique de la glace dans un nanopore amphiphile. Les cercles rouges représentent les groupes organiques à la surface. Les grains de glace ISD et l'eau amorphe de type liquide existent dans une distribution non-homogène.

Nos résultats sur l'effet marqué de l'hydrophobie de la paroi du pore dans la dépression du point de fusion de l'eau confinée dans des nanopores amphiphiles (D ~4,5 nm) contrastent avec ceux de Morishige (2018). Selon nous, cet effet n'était pas perceptible dans les carbones mésoporeux en raison de la taille relativement importante de leurs pores

(6,4 nm à 16,4 nm), ce qui fait que le nombre de molécules d'eau en contact avec la surface était relativement faible par rapport à l'eau en volume dans le cœur des nanopores.

Sur la base de nos observations de l'effet de la chimie de surface des pores sur la fraction d'eau non congelable, la taille des cristallites et la dynamique de l'eau confinée, nous concluons que la glace confinée dans nos matériaux nanoporeux amphiphiles (C18-M15-Me et C18-M7-Ph) était capable de nucléer mais pas de croître. Ceci est probablement dû à un environnement contraint par des groupes organiques qui ralentissent les molécules d'eau de telle sorte qu'elles ne peuvent pas contribuer à la croissance du cristal.

Chapitre 7

Dans ce chapitre, nous avons discuté des résultats relatifs au confinement hydrophobe de l'eau dans les nanopores d'organosilice greffés. Les techniques expérimentales utilisées pour cette étude étaient l'adsorption d'azote et de vapeur d'eau, l'imagerie neutronique et la diffraction neutronique à haute résolution.

Concernant l'adsorption de vapeur d'eau dans les nanopores hydrophobes, nous avons constaté que la forte hydrophobie des matériaux synthétisés rend impossible la condensation de l'eau à $P < P0$. Cependant, notre analyse a révélé que seules quelques molécules d'eau peuvent être adsorbées sur les nanopores hydrophobes via un processus lent qui se produit par petits sauts où des clusters d'eau pourraient se former autour des groupes silanol.

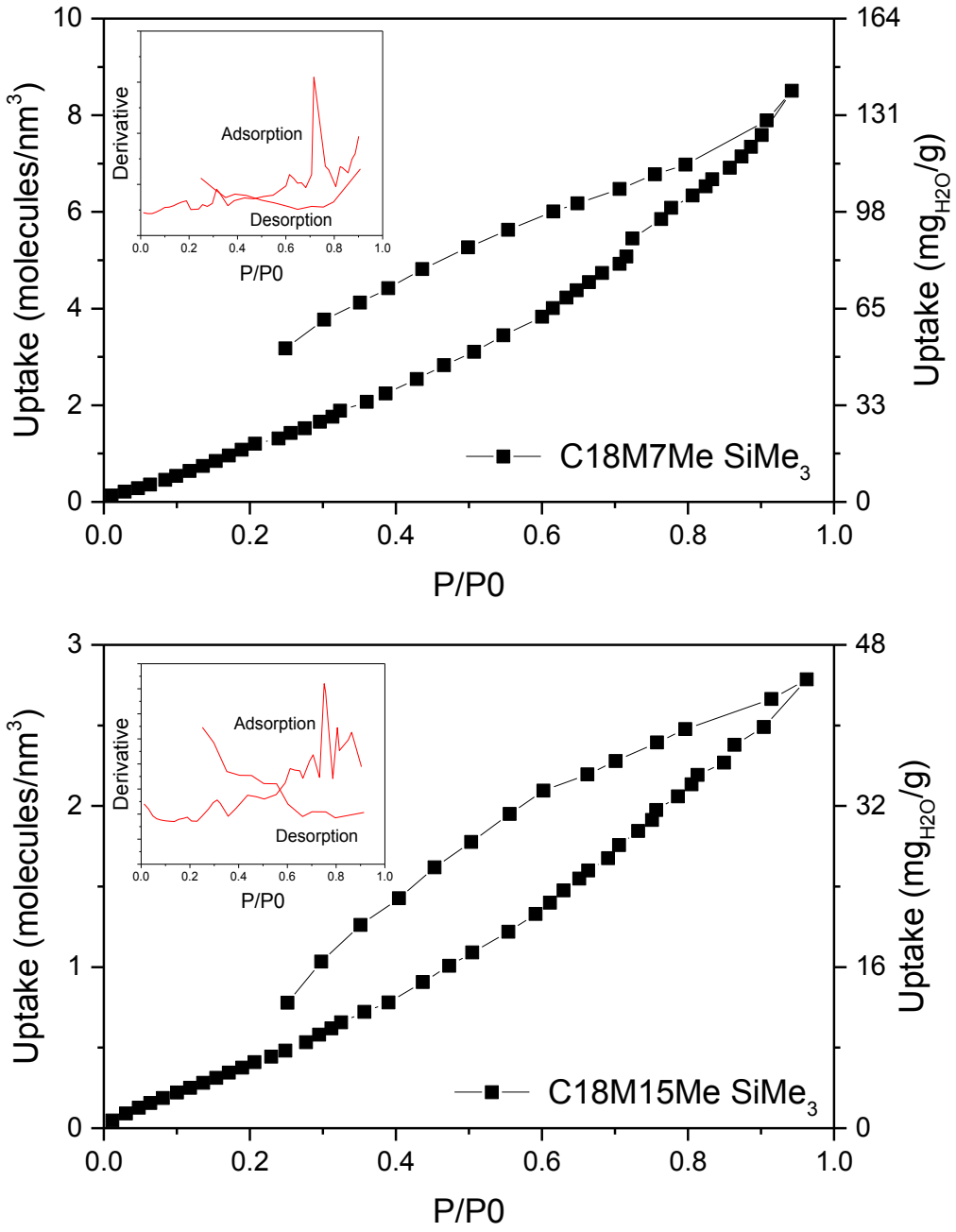

Figure 7.14: Isothermes d'adsorption/désorption d'eau de C18-M7-Me SiMe3 et C18-M15-Me SiMe3 à 298,15 K. Insert : Dérivée de l'absorption en fonction de P/P0.

Une autre observation importante de ces expériences est que le temps nécessaire pour un cycle d'adsorption-désorption était d'environ trois jours sur les matériaux hydrophobes. Cette longue durée contraste avec les isothermes d'adsorption-désorption de la vapeur d'eau sur les matériaux hydrophiles ou amphiphiles, qui ont pris ~1,5 jours pour être complétés. Ce que nous avons vu, c'est que l'adsorption de quelques molécules d'eau sur les nanopores hydrophobes à des pressions inférieures à la pression de saturation de l'eau, à 298,15 K, est un processus très lent.

Lorsque nous comparons avec d'autres matériaux nanoporeux (Figure 7.3), nous constatons que ces résultats en matière d'adsorption de vapeur d'eau sont plus similaires aux zéolithes hydrophobes qu'à la silice nanoporeuse amphiphile. En effet, les cadres zéolitiques imidazoles (ZIF) hydrophobes de type ZIF-8 partagent le même type d'isotherme d'adsorption (Type III). Cependant, le niveau de vapeur d'eau adsorbé dans les ZIF-8 est significativement plus faible (~1.3 molécules/nm3) et la forme convexe de l'isotherme est plus prononcée.2 Alors que l'eau s'adsorbe beaucoup plus facilement dans les matériaux amphiphiles C18. Dans ce dernier cas, il est facile d'obtenir des nanopores amphiphiles remplis avec une densité de ~29 molécules/nm3 (Chapitre 6).

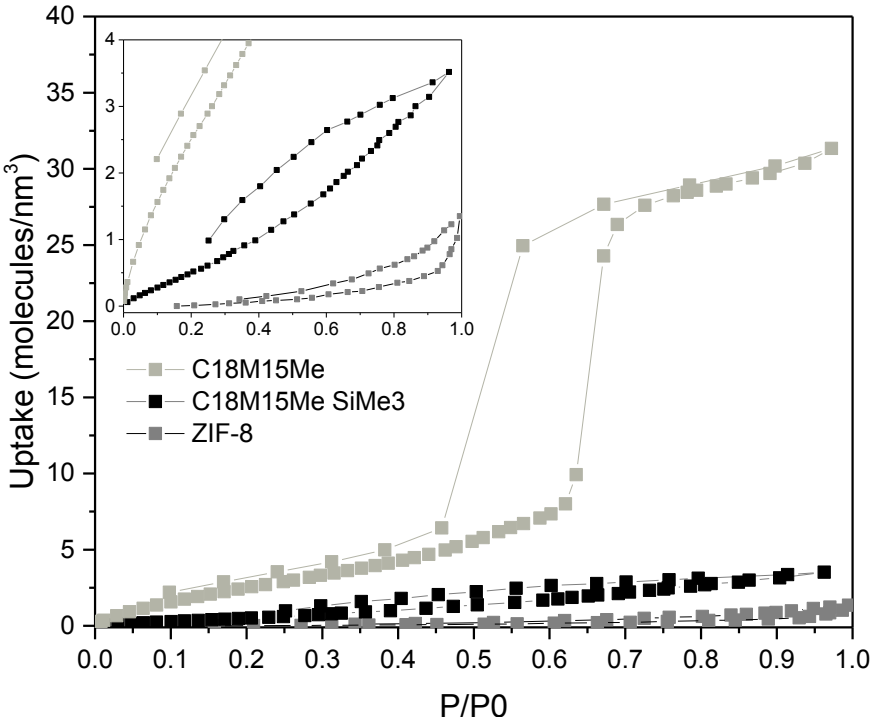

Figure 7.15: Comparaison des isothermes d'adsorption de la vapeur d'eau sur l'organosilice amphiphile C18-M15-Me (chapitre 6), l'organosilice hydrophobe C18-M15-Me SiMe3 et la zéolite hydrophobe ZIF-8 (identifiée comme MAF-4 dans la référence 2). Insert : Zoom à faible absorption pour comparer la forme des isothermes d'adsorption.

La pression d'intrusion, déterminée par imagerie neutronique (Figures 7.6 et 7.7), se situe entre 380 bar et 450 bar, selon le matériau. Une hystérésis significative a été trouvée pour l'extrusion, qui s'est produite à une pression presque atmosphérique. Les valeurs de la pression d'intrusion en fonction de l'inverse du rayon des pores (représentation de Laplace-Washburn) ont été comparées à la littérature disponible, et nous avons constaté que nos résultats sont en accord avec ceux obtenus par Lefevre et al. (2004) pour l'intrusion d'eau pure dans une silice nanoporeuse greffée similaire.

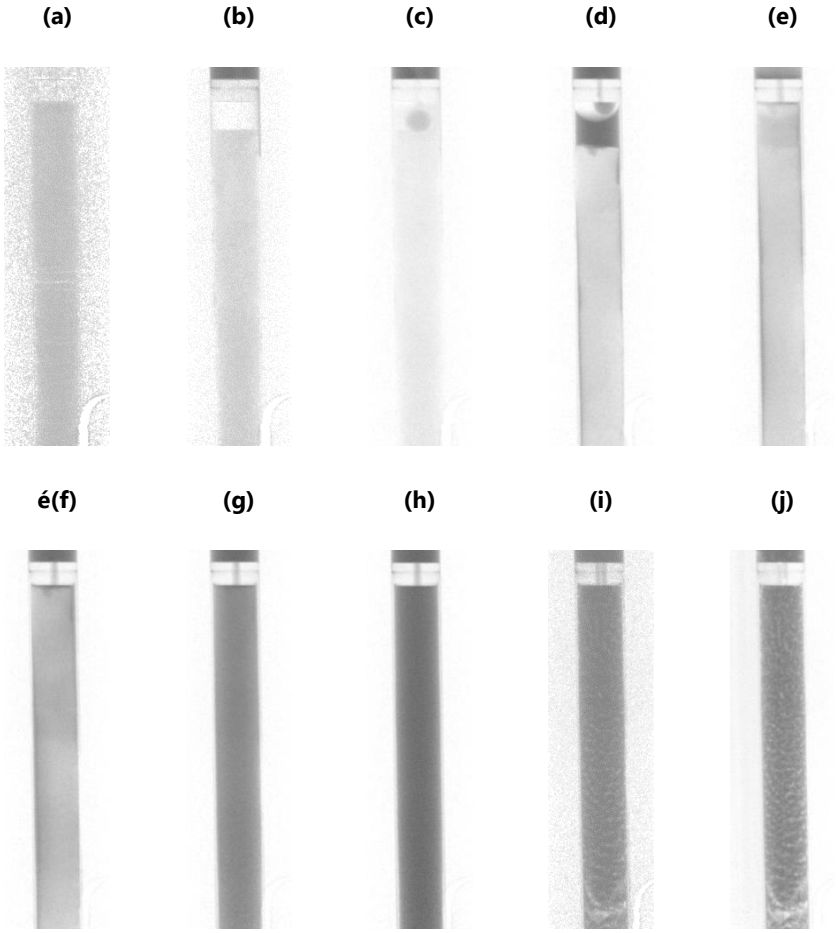

Figure 7.16: Images neutroniques d'une capsule contenant 178,9 mg de C18-M7-Me SiMe3. Les images pertinentes du cycle de compression-décompression sont montrées : (a) P = 1 bar (poudre sèche), (b) P = 1,7 bar (poudre comprimée), (c) P = 2,2 bar (première goutte d'eau), (d) P = 2,6 bar (l'eau pénètre dans l'espace entre la capsule métallique et le matériau), (e) P = 2,75 bar (intrusion inter-grain), (f) P = 5. 85 bar, (g) P = 337.5 bar (Début de l'intrusion de l'eau dans les nanopores), (h) P = 475 bar (Fin de l'intrusion), (i) P = 1 bar (Retour à la pression atmosphérique), (j) P = 1 bar (temps écoulé après la fin de la décompression, t = 10 min). La luminosité des images présentées ici a été ajustée pour faciliter la visibilité ; par conséquent, l'intensité totale n'est pas normalisée.

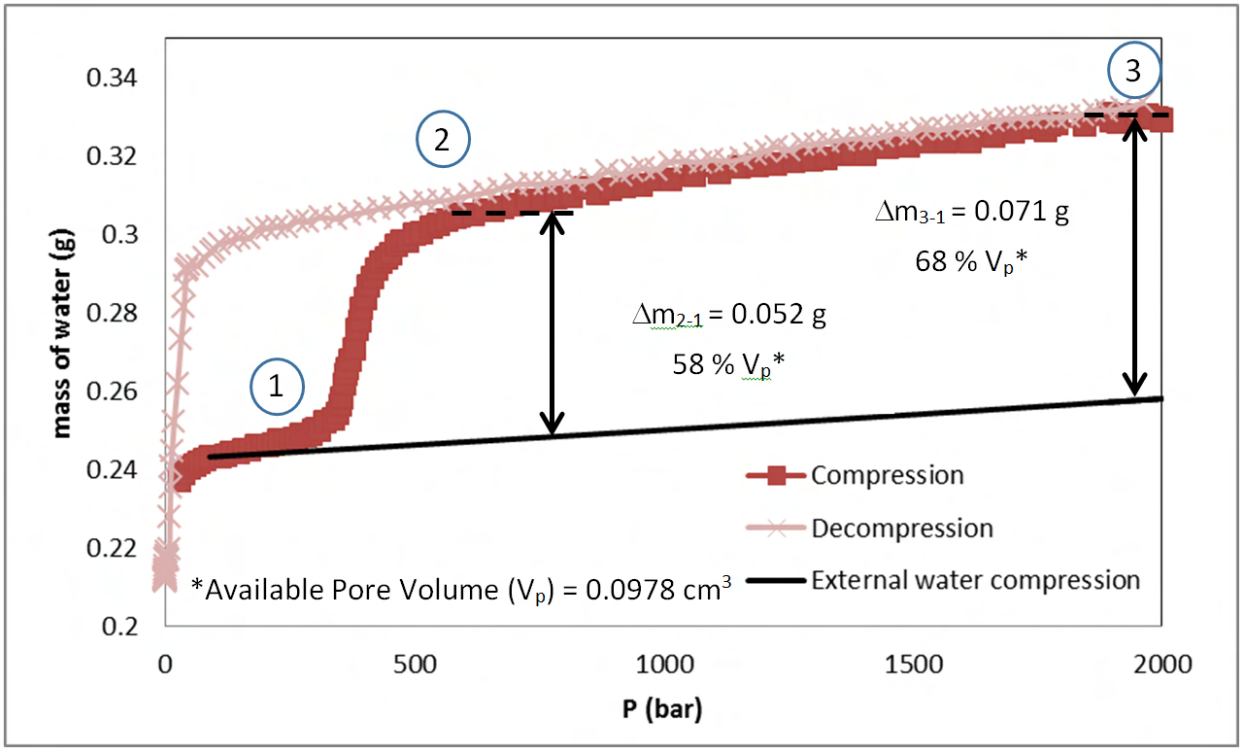

Figure 7.17: Masse d'eau en fonction de la pression pour un échantillon contenant 179 mg de C18-M7-Me SiMe3 (Vp = 0,547 cm3/g).

Cependant, nous avons observé que, même à des pressions plus faibles (109 bar pour C18-M15-Me SiMe3, Figure 7.10), il est possible d'introduire une quantité réduite d'eau dans les nanopores hydrophobes (6 molécules/nm3, en moyenne) si un temps suffisant (au moins 40 minutes) est écoulé dans des conditions isobares.

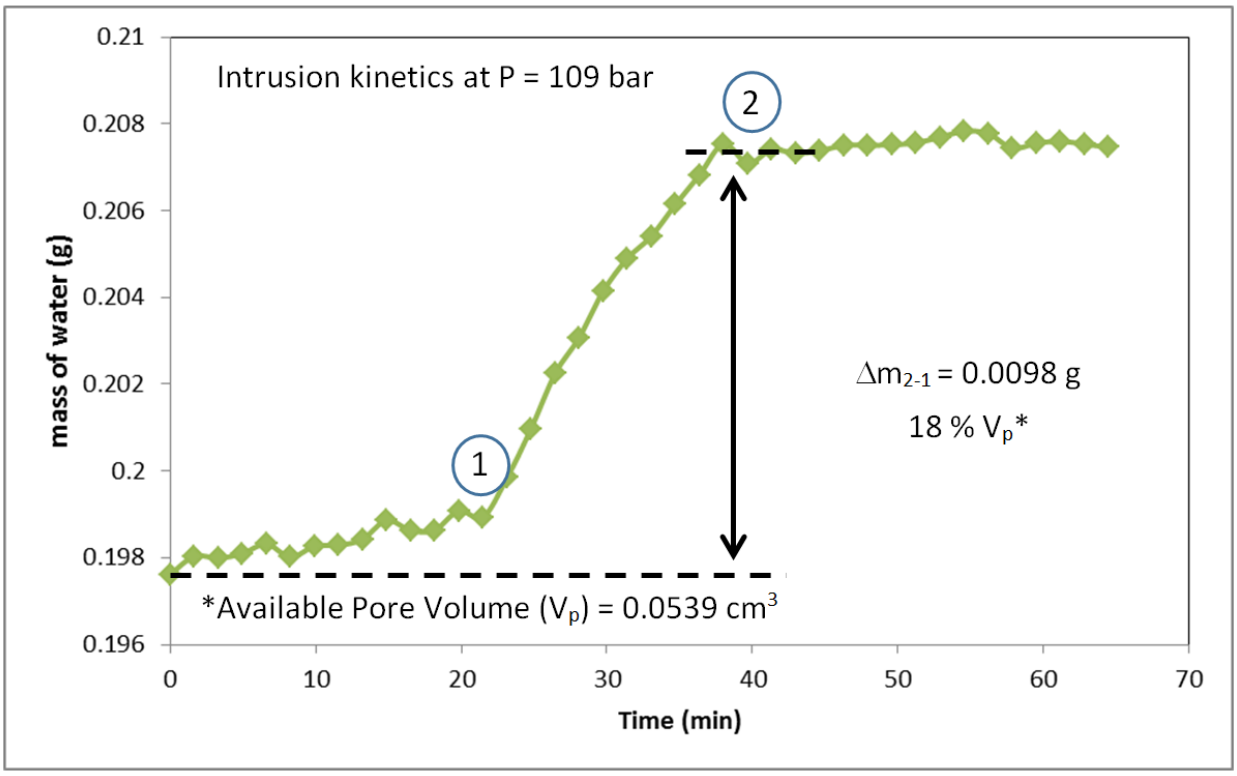

Figure 7.18: Masse d'eau en fonction du temps pour un échantillon contenant 100 mg de C18-M15-Me SiMe3 (Vp = 0,539 cm3/g). Conditions isobares à 109 bar pendant 64 minutes. Fin de l'intrusion vers 40 min.

Nos résultats montrent également que les molécules d'eau continuent de pénétrer dans les nanopores hydrophobes après la pression d'intrusion. Dans le C18-M7-Me SiMe3, par exemple, la quantité d'eau dans les nanopores passe de 17,8 molécules/nm3 à la fin de l'intrusion (582 bars) à 24,3 molécules/nm3 à la fin de l'expérience, à 2000 bars.

En étudiant les phases de glace formées à l'intérieur des nanopores, nous avons constaté que l'eau confinée de manière hydrophobe forme des formes de glace de plus haute densité. Plus précisément, les phases glace II et glace III ont été trouvées à 1000 bar (la moitié de la pression nécessaire pour observer de telles phases dans l'eau en volume), et nous avons observé des transitions de phase réversibles et reproductibles de la glace II à la glace III, puis à l'eau liquide.

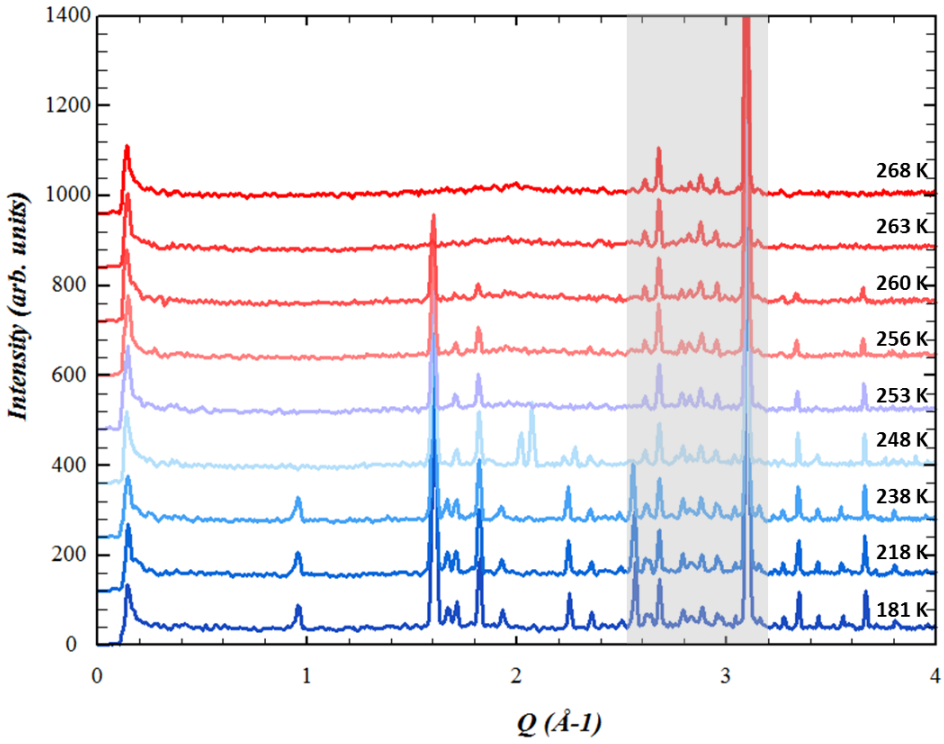

Figure 7.19: C18-M15-Me SiMe3. Cycle de chauffage à P = 1000 bar. La glace II en phase confinée se transforme en glace III entre 240 et 248 K. La glace III confinée fond entre 250 et 253 K. La phase externe Ih reste pour toute la gamme de températures de 180 à 260 K.

Si l'on considère que la densité moyenne de l'eau à l'intérieur des nanopores est inférieure à celle de l'eau liquide, mais que des glaces de densité supérieure se forment malgré tout, nous concluons que l'organisation locale de l'eau à l'échelle nanométrique consiste en des poches d'eau de haute densité entourant les sites hydrophiles disponibles, et en des zones vides et interdites où les groupes organiques repoussent et compriment l'eau.

Enfin, à partir de nos observations, nous avons tracé de nouvelles lignes de transition (Figure 7.23) au diagramme de phase pression-température de l'eau lourde confinée dans les nanopores hydrophobes de C18-M15-Me SiMe3.

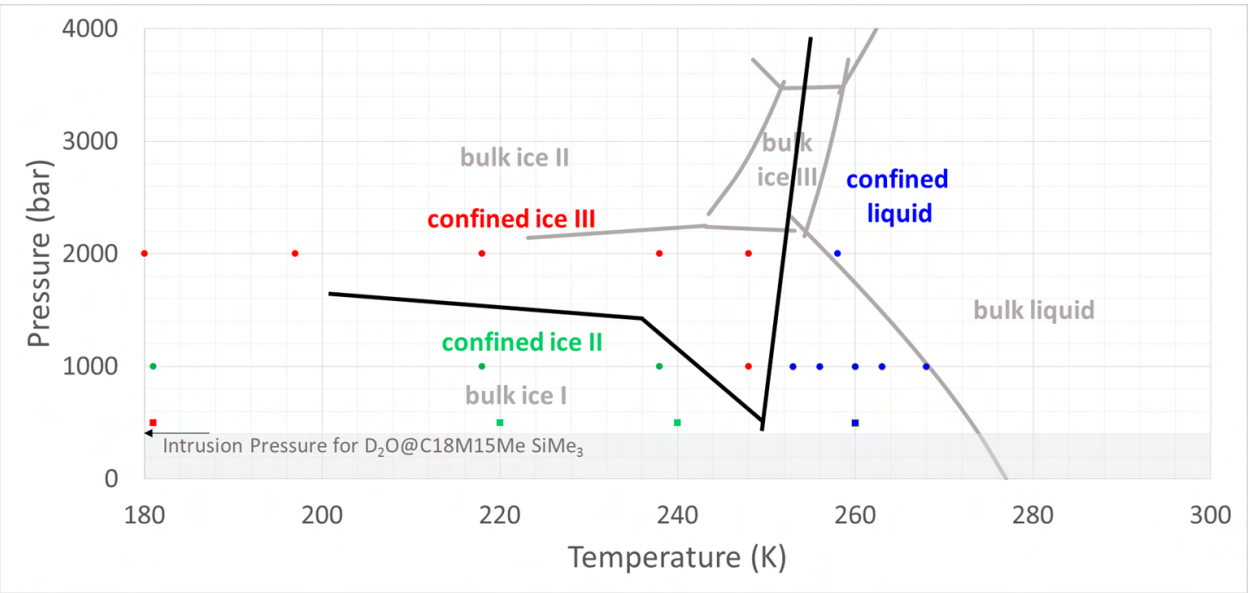

Figure 7.23 : Diagramme de phase du D2O en volume (Bridgeman, 1935, en gris)20 et lignes de transition schématiques du D2O confiné (ce travail, lignes noires). Les résultats de la diffraction des neutrons sont symbolisés par des points. Points rouges : glace confinée III, points verts : glace confinée II et points bleus : liquide confiné.

Conclusion générale

Ce travail traite du comportement de phase de l'eau confinée dans des nanopores d'organosilice (type MCM-41) avec différents niveaux d'hydrophobie. Notre recherche contribue à l'état de l'art dans plusieurs domaines critiques du confinement de l'eau, tels que la synthèse de matériaux de confinement amphiphiles et hydrophobes, l'étude de l'adsorption de la vapeur d'eau et de sa densité dans les nanopores, l'intrusion/extrusion d'eau dans des matériaux hydrophobes, la détermination des températures de congélation et de fusion de l'eau confinée en fonction de la chimie de surface, et l'étude de la structure cristalline de la glace confinée. Deux résultats principaux peuvent être mis en évidence dans cette thèse : Premièrement, nous avons observé que l'hydrophobie de surface renforce les effets du confinement sur la densité et le comportement de congélation/fusion de l'eau dans de petits nanopores amphiphiles (D < 4,5 nm). Deuxièmement, nous avons constaté que l'eau confinée dans des nanopores hautement hydrophobes (D ~4 nm) cristallise en formes de glace de densité plus élevée (glaces II et III) à des pressions significativement plus basses que prévu.

Concernant la synthèse de nanomatériaux amphiphiles, une approche de co-condensation nous a permis d'obtenir des nanopores cylindriques, similaires au MCM-41, mais avec un degré d'hydrophobie donné par la présence de différentes densités (de 0,18 à 0,34 nm-2) et types de groupes organiques (méthyle, éthyle ou phényle) intégrés dans la charpente des matériaux. Bien que ces matériaux soient moins hydrophiles que le MCM-41

extrait du gabarit (lavé), ils présentent toujours une capacité d'adsorption d'eau élevée à basse pression (P < P0).

Nous avons constaté que la densité de l'eau confinée dans les nanopores amphiphiles (~26 molécules/nm3) est significativement plus faible que dans la MCM-41 hydrophile (~28 molécules/nm3). En outre, dans la gamme sélectionnée de tailles de pores (D < 4,5 nm), l'hydrophobie de surface entraîne une augmentation de l'appauvrissement de la température de fusion, une diminution du pourcentage d'eau cristallisée et une réduction de la taille des grains de glace. La structure cristalline de la glace confinée, déterminée par diffraction neutronique, correspond à une glace désordonnée par empilement (ISD) avec environ 30 % de couches hexagonales (Ih) et 70 % de couches cubiques (Ic). La fraction non congelable de l'eau, déterminée par calorimétrie différentielle à balayage et par diffraction des neutrons, va de 45 % à près de 80 %, selon le niveau d'hydrophobie. Nous proposons que cette eau liquide et amorphe présente une distribution non-homogène autour des grains de glace, en particulier autour des groupes organiques à la surface des nanopores amphiphiles. D'après nos résultats préliminaires sur la dynamique de l'eau, nous concluons que les groupes organiques à la surface pourraient être responsables du ralentissement des molécules d'eau qui les entourent, entravant ainsi la croissance des grains de glace.

Par la suite, nous avons post-greffé des groupes organiques supplémentaires à la surface de deux matériaux amphiphiles pour obtenir des nanopores hautement hydrophobes. Leur caractérisation par TGA a révélé une densité de greffage de 0,33 nm-2 et 0,56 nm-2, en plus des groupes organiques préexistants. Les expériences d'adsorption ont montré que l'eau ne se condense pas à basse pression dans ces nanopores, et que des pressions plus élevées sont nécessaires pour forcer l'intrusion d'eau.

La pression d'intrusion, déterminée par imagerie neutronique, était d'environ 400 bars (D ~ 4 nm). Cependant, il a été possible d'introduire une quantité réduite d'eau (6 molécules/nm3, en moyenne) dans les nanopores hydrophobes à des pressions inférieures (109 bar) si un temps suffisant (au moins 40 minutes) est écoulé dans des conditions isobares. Il a également été observé que les molécules d'eau continuent de pénétrer dans les nanopores hydrophobes après la pression d'intrusion. Une hystérésis significative a été trouvée pour l'extrusion, qui s'est produite à une pression presque atmosphérique.

Lors de l'étude des phases de la glace formée à l'intérieur des nanopores, nous avons constaté que l'eau confinée par l'hydrophobie forme des formes de glace de plus haute densité. Les phases de glace II et III ont été trouvées à 1000 bars (la moitié de la pression

nécessaire pour observer de telles phases dans l'eau en volume). Les transitions de phase de la glace II confinée à la glace III puis à l'eau liquide sont réversibles et reproductibles. Ces résultats nous ont permis de tracer de nouvelles lignes de transition au diagramme de phase Pression-Température de l'eau lourde confinée dans des nanopores hydrophobes.

Dans les nanopores hydrophobes, la juxtaposition entre la densité moyenne plus faible de l'eau confinée et la formation de formes de glace de plus haute densité pourrait être le résultat d'une organisation locale dans laquelle des poches d'eau de haute densité entourent les sites hydrophiles disponibles, et il existe des zones vides et interdites où les groupes organiques repoussent et compriment l'eau.

Dans une perspective, il serait intéressant d'explorer de nouvelles applications pour les matériaux nanoporeux amphiphiles et hydrophobes afin de confiner d'autres systèmes, tels que les mélanges eau-glycérol et les solutions ioniques, pour étudier l'effet simultané du confinement amphiphile mou et dur. Dans la recherche du diagramme de phase de l'eau confinée à haute pression, il est essentiel d'aborder les phases de glace formées à l'aide de matériaux hydrophiles et amphiphiles.

PUBLICATION

ACS OMEGA

http://pubs.acs.org/journal/acsodf

Article

Direct Synthesis of Mesoporous Organosilica and Proof-of-Concept Applications in Lysozyme Adsorption and Supported Catalysis

Oriana Osta,* Marianne Bombled, David Partouche, Florian Gallier, Nadège Lubin-Germain, Nancy Brodie-Linder, and Christiane Alba-Simionesco

Cite This: *ACS Omega* 2020, 5, 18842−18848

Read Online

ACCESS | Metrics & More | Article Recommendations | Supporting Information

ABSTRACT: Mesoporous materials represent a useful alternative for exploiting the effects of confinement on molecular trapping and catalysis. Their efficiency often depends on the interactions between the surface and the targeted molecules. One way to enhance these interactions is to adjust the hydrophobic/hydrophilic balance of the surface. In the case of mesoporous silica, the incorporation of organic groups is an efficient solution to adapt the material for specific applications. In this work, we have used the co-condensation method to control the hydrophobicity of mesoporous organosilica. The obtained materials are methyl- or phenyl-containing silica with a pore size between 3 and 5 nm. The surface chemistry control has shown the enhanced performance of the materials in two proof-of-concept (PoC) applications: lysozyme adsorption and supported catalysis. The lysozyme adsorption is observed to be over 3 times more efficient with the phenyl-functionalized material than MCM-41, due to $\pi-\pi$ interactions. For the catalysis, copper(II) was immobilized on the organosilica surface. In this case, the presence of methyl groups significantly enhanced the product yield for the catalyzed synthesis of a triazole derivative; this was attributed to the enhanced hydrophobic surface−reactant interactions. It was also found that the materials have a higher water adsorption capacity and an improved resistance to hydrolysis. The modulation of water properties in confinement with hydrophobic surfaces, consistently with the water as tuneable solvent (WaTuSo) concept, is a crucial aspect in the efficiency of mesoporous materials for dedicated applications.

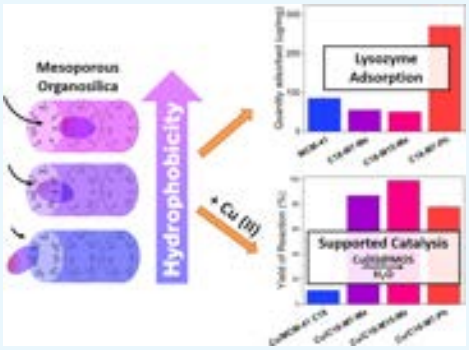

INTRODUCTION

Molecular trapping and supported catalysis are applications of mesoporous materials with great industrial and scientific impact. A key parameter for their efficiency is the hydrophobicity of the surface, accompanied by a large surface area and the appropriate pore size.[1] Classic examples for applications in molecular trapping are the encapsulation followed by controlled drug delivery in nanomedicine,[2] the effective removal of the low concentrations of pollutants,[3] and molecular confinement studies,[1,4−6] to mention a few. In the area of catalysis, mesoporous silica-supported reactions have been investigated, for example, in wastewater treatment,[7] in reducing the amount of certain compounds in the mainstream of tobacco smoke,[8] and in product yield improvement for organic reactions,[9−11] among other applications. In a particular case, copper-doped nanoporous silica has been found to be a reusable, regioselective catalyst for the cycloaddition reaction between a terminal alkyne and an azide through click chemistry.[10,12] However, in some cases, the yields of reaction are very low and this is attributed to the low interaction between the hydrophobic reactants and the hydrophilic materials.

In this context, MCM-41 offers high surface area, ordered structure, and thermal stability but fails in providing the correct hydrophobic/hydrophilic balance for efficient interaction with most organic molecules. Frequently, even after postgrafting hydrophobic groups on the surface, this balance is not met due to a total transformation of the surface from hydrophilic to hydrophobic. A partial functionalization with this method has shown to produce inhomogeneous, rough surfaces with the majority of the grafted groups on the external surface or at the extremes of the pores.[9,13,14]

The co-condensation method has been conceived as an alternative to introducing hydrophobic groups to mesoporous silica materials yielding a more uniform functionalization.[9,15] In this case, a silica precursor is condensed together with an organosilane. This method has been studied to introduce acid, basic and unsaturated groups in the walls of MCM-41-like materials so that they can be directly used for catalytic applications.[14,16−18]

Received: April 30, 2020
Accepted: July 13, 2020
Published: July 24, 2020

https://dx.doi.org/10.1021/acsomega.0c01996
ACS Omega 2020, 5, 18842−18848

According to recent studies, the hydrophobicity of the nanoenvironment has an impact on the properties of confined water, which is the solvent used for both the applications studied. Indeed, under hydrophobic nanoconfinement, water undergoes changes in its H-bond network, lowering its polarity and providing enhanced solvation of nonpolar solutes. This concept has been called water tuneable solvent (WaTuSo).[19] Some consequences of this phenomenon have been, for example, enhanced gas storage[20] and dramatic improvement of catalytic efficiency.[21]

In this context, our aim was to control the hydrophobicity of organosilica materials for specific applications by introducing methyl or phenyl groups through co-condensation with methyltriethoxysilane (MTES) or phenyltriethoxysilane (PTES), acting directly on water properties tuning its polarity for the specific applications.

Herein, we present a proof-of-concept (PoC) (i.e., evidence that demonstrates the suitability of these materials) for applications in protein adsorption and supported catalysis. Lysozyme was chosen as a model to study the effect of hydrophobicity in protein uptake. In addition, the supported copper (click) catalysis of the cycloaddition reaction between two hydrophobic reactants, benzyl azide and 4-bromo-1-butyne, in aqueous media instead of an organic solvent, was tested with the synthesized materials.

During the direct synthesis of mesoporous organosilica, we focused on obtaining a stable material with a highly ordered pore structure. To avoid the disruption of the honeycomb-like structure and based on previous research,[22,23] the percentage of organosilane in the precursor mixture was kept under 20 mol %. The conditions of template washing by ethanol extraction were adjusted to obtain clean material without causing damages to the surface.

Samples were named according to the template used and their fraction of MTES or PTES in the precursor mixture: C18-M7-Me for 0.93 tetraethyl orthosilicate (TEOS)/0.07 MTES, C18-M15-Me for 0.85 TEOS/0.15 MTES, and C18-M7-Ph for 0.93 TEOS/0.07 PTES, all of them using C_{18}TAB as a template, and C12-M7-Me for 0.93 TEOS/0.07 MTES using C_{12}TAB as a template. Standard MCM-41 C18 and C12 were synthesized and washed under the same conditions for comparison. Here, we mainly focus on the materials C18-M7-Ph and C18-M15-Me materials, which showed an optimal performance in lysozyme trapping and as support for the click catalysis, respectively. A comprehensive characterization (Fourier transform infrared (FTIR), nitrogen and water adsorption, small-angle X-ray scattering (SAXS), transmission electron microscopy (TEM), INS) has been performed and is discussed herein; the details are provided in the Supporting Information.

RESULTS AND DISCUSSION

In Figure 1, the standard characterization of the materials is shown.

Template removal and incorporation of the organic groups in the mesoporous silica were verified by means of FTIR (Figure 1A). In all samples, the typical absorption bands at 1060, 796, and 445 cm^{-1} associated with Si−O stretching and bending modes of condensed silica were found, as well as a band at 953 cm^{-1} associated with the Si−OH groups at the surface.[24] In the spectra of samples C18-M7-Me and C18-M15-Me, an absorption band at 1276 cm^{-1} is present; this band is attributed to the C−H bending of the carbon bonded

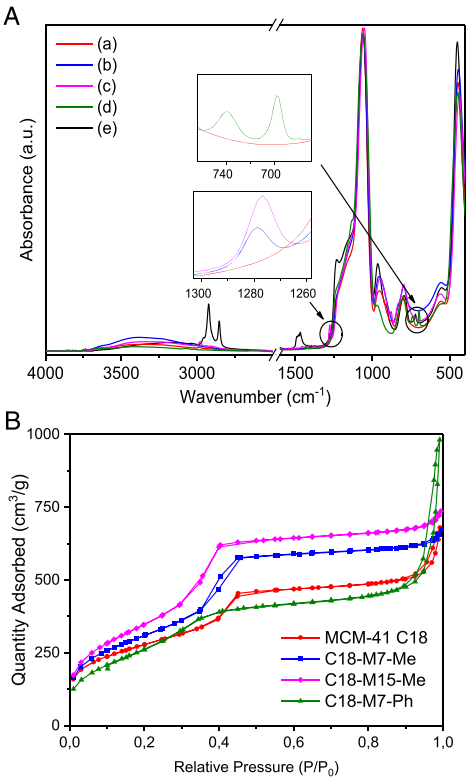

Figure 1. (A) FTIR spectra of (a) MCM-41 C18, (b) C18-M7-Me, (c) C18-M15-Me, (d) C18-M7-Ph, and (e) MCM-41, as synthesized. 1(B) Nitrogen adsorption−desorption isotherms of MCM-41 C18 and mesoporous organosilica materials at 77 K.

to a Si atom, confirming the incorporation of the methyl group in the framework. The intensity of this band increases when the fraction of MTES used is larger. The incorporation of the phenyl group in sample C18-M7-Ph was identified by the peaks at 695−740 cm^{-1}, from the aromatic C−H bend. The absorption bands at 2921, 2852, and 1480 cm^{-1}, from C−H stretching and bending of the alkyl chain of C_{18}TAB, are only present in the as-synthesized material, indicating that the washing method has been efficient in removing the template.

Nitrogen adsorption and desorption isotherms of these samples at 77 K are shown in Figure 1B. For standard and methyl-modified MCM-41 C18, results show a regular type IV adsorption isotherm. In the case of co-condensation of TEOS with MTES, an increase in surface area and pore volume with respect to MCM-41 C18 was observed (see Table 1). On the other hand, the co-condensation with PTES produced a less organized material, evidenced by a spread capillary con-

Table 1. Mean Physical Properties of Selected Materials

sample	S_{BET} (m^2/g)	V_{pore} (cm^3/g)[a]	d_{10} (nm)[b]	D_{pore} (nm)[c]	C
MCM-41 C18	1007	0.712	4.45	4.22	112
C18-M7-Me	1130	0.899	4.48	4.43	77.7
C18-M15-Me	1284	0.982	4.31	4.32	57.2
C18-M7-Ph	989	0.628	4.65	4.30	44.1

[a]Single point adsorption total pore volume at $P/P_0 = 0.5$. [b]Calculated from SAXS curves. [c]Calculated using the KJS model taking into account the lattice plane spacing (d_{10}).[26]

https://dx.doi.org/10.1021/acsomega.0c01996
ACS Omega 2020, 5, 18842−18848

densation and slightly lower surface area and pore volume than those of MCM-41 C18.

The late condensation at P/P_0, higher than 0.9 in samples MCM-41 C18 and C18-M7-Ph, was attributed to condensation in the interparticle cavities when the size of the mesoporous silica grains are few tens of nanometers[25] as evidenced for C18-M7-Ph by TEM (Figure S2).

It is worth noting that the affinity constant, C, calculated from the BET equation, decreased 49 and 61% with respect to the value of MCM-41 C18 (C = 112) for C18-M15-Me and C18-M7-Ph, respectively. This parameter decreases with a decrease in the strength of the adsorbent−adsorbate affinity. Since induced dipole−dipole interactions govern this adsorption, the introduction of organic groups decreases the affinity of nitrogen toward the surface. Then, the observed drop in the C value within the same family of materials is another evidence of their increasing hydrophobicity.

These results indicate that, upon the introduction of MTES at percentages up to 15%, the obtained organosilica maintains an ordered pore structure while increasing their hydrophobic character; this was also confirmed by SAXS (Figure S1 in the Supporting Information).

By inelastic neutron scattering experiments (Figure S3), looking for the ability of the methyl groups to freely rotate, we are able to distinguish the populations of methyl groups trapped in the walls and those at the surface. The quantification of the two populations leads to an estimation of 30−35% of methyl groups trapped into the walls, while the rest 70−65% are at the surface. Besides the characterization aspect, this information about the distribution of methyl groups and the temperature range where the motions are active should help further investigation on the mobility of confined fluids.

Lysozyme Adsorption. The selected organosilica materials were placed in contact with a 0.5 mg/mL solution of lysozyme at pH 7.4 at room temperature for 4 h; then, they were filtered and the decrease in the concentration of the protein in a solution was measured by ultraviolet (UV) adsorption at 280 nm. This allowed the calculation of the amount of lysozyme adsorbed per milligram of the molecular sieve. In the case of methyl-modified materials C18-M7-Me and C18-M15-Me, the quantities adsorbed per milligram of organosilica (55 ± 1 and 50 ± 5 μg/mg, respectively) were lower than those for the reference MCM-41 C18 (85 ± 10 μg/mg). Remarkably, in the case of the phenyl-modified sample, C18-M7-Ph, a 3.2 times higher adsorption was observed (270 ± 30 μg/mg).

Lysozyme adsorption is driven by electrostatic interactions between the Si−OH groups and the positively charged protein at pH 7.4. Therefore, the presence of $-CH_3$ instead of −OH groups on the surface could be one of the reasons for the lower quantity adsorbed by the methyl-modified silica. On the other hand, the high amount of lysozyme adsorbed by C18-M7-Ph is attributed to its ability to interact with the protein via electrostatic as well as $\pi-\pi$ interactions.

FTIR spectra (Figure 2) show peaks centered at 1656 and 1535 cm^{-1} corresponding to the amide I and amide II bands of lysozyme, respectively. The small peak at 1594 cm^{-1} comes from the aromatic C−C stretching of the phenyl functionalization. The amide I band consists of C═O stretching coupled with N−H bending and C−H stretching components. As these stretching modes are affected by the hydrogen bonds present in the different conformations (α-helix, parallel and antiparallel

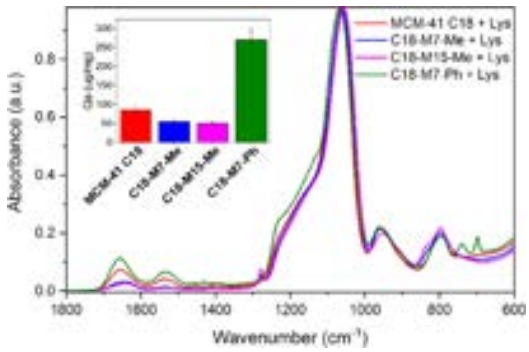

Figure 2. FTIR (ATR) spectra of the lysozyme adsorbed on the materials. Inset: quantities of lysozyme (μg) adsorbed per milligram of material.

β-sheets, etc.), the shape of the amide I band gives information about the secondary structure of the protein.[27] It is then possible to perform studies of protein structure under different confined conditions using these new molecular sieves.

Catalysis of the Alkyne−Azide Cycloaddition Reaction. The homogeneous azide−alkyne Huisgen cycloaddition reaction in solution is known to be very efficient, but it requires a copper(I) species as a catalyst. This species is prompt to disproportionate, making it necessary to add an auxiliary reducing species, as an ascorbate. Additionally, an extraction or filtration step has to be performed to purify the product.[28]

The alternative here proposed is to use the synthesized nanoporous organosilica as support for copper(II) to perform the heterogeneous catalysis of this reaction.

This method has been used before for a variety of reactants, using mesoporous silica (SBA-15) as support. High conversion rates were obtained when the reactants were hydrophilic, but the yield of reaction decreased significantly for hydrophobic reactants; this was attributed to the hydrophilic character of the pores.[12]

The azide−alkyne cycloaddition reaction tested here between two hydrophobic reactants at ambient temperature, is shown in Figure 3.

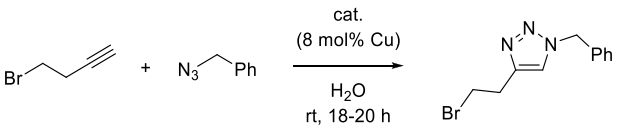

Figure 3. Cycloaddition reaction between bromobutyne and benzyl azide in the presence of a copper catalyst in water.

Copper(II) was immobilized on the materials using the method developed by Brodie-Linder et al.[29] The materials were tested as catalysts for this reaction, with no addition of reducing agents or further ligands. It is worth noting that both reactants are not miscible in water. When the supported catalyst is added, the formation of a Pickering emulsion was observed for all of the reactions.

Figure 4 shows the yields of reaction obtained by means of NMR spectroscopy. A vast increase in the yield of the reaction is observed for the methyl- and phenyl-modified samples Cu/C18-M7-Me, Cu/C18-M15-Me, and Cu/C18-M7-Ph (87, >99, and 78% respectively) with respect to the yield of 11% obtained when Cu/MCM-41 C18 is used as a catalyst. The

https://dx.doi.org/10.1021/acsomega.0c01996
ACS Omega 2020, 5, 18842−18848

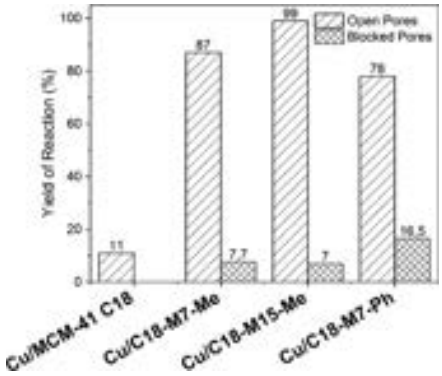

Figure 4. Yields of the cycloaddition reaction between bromobutyne and benzyl azide in water for different silica-supported copper catalysts with open and blocked pores.

formation of a Pickering emulsion was observed for all of the reactions.

These results confirm that the presence of methyl or phenyl groups enhances the adsorption of the organic reactants. The total transformation of the reactants on Cu/C18-M15-Me indicates that this material provides an optimum nanoenvironment for this particular reaction in water.

Next, we checked if the catalysis takes place inside the nanopores by performing a control experiment, using copper-doped materials with pores blocked by surfactant. The procedure involved doping the as-synthesized nanoporous materials, i.e., without template removal by washing or calcination. The FTIR spectra of these materials are shown in Figure S4, where the peaks that correspond to the C−H stretching and bending modes of the carbonated chain of the surfactant at 2921, 2852, and 1480 cm^{-1} can be observed.

Even though the molar percentage of copper in the reaction was maintained at 8 mol %, the yield of reaction obtained with blocked pores was much lower than the corresponding yield obtained with open pores (Figure 4), indicating that great part of the catalysis takes place inside the pores of the organosilica materials.

A photograph of an example of the catalytic mixture in the form of a Pickering emulsion and a schematic representation is shown in Figure S5. The copper-doped mesoporous particles acted not only as catalysts, providing nanopores with the proper hydrophobic/hydrophilic balance for the diffusion of reactants and products but also as an emulsifier. A higher local concentration, obtained by the Pickering emulsion process instead of simple dispersion in an organic solvent, could have enhanced the adsorption of the reactant molecules on the surface of the amphiphilic nanopores.

Furthermore, this method allows the substitution of organic solvents by water and the biphasic reaction system simplifies the recuperation of the catalyst by filtration. Such a reaction system could be extended to other sets of reactants, where one or both are water-immiscible, to take full advantage of the mass transport properties of Pickering emulsions.[30,31]

Role of Confined Water. We have seen so far, how, introducing a small percentage of methyl- or phenyltriethoxysilane in the reaction mixture can cause drastic effects in the performance of the mesoporous silica in key applications like molecular uptake and catalysis. We have attributed these results, mainly, to the adjustment of the surface chemistry.

Now, as both of the studied applications involve suspension of the material in water, we decided to investigate the behavior of the materials when they interact with water. We have investigated this by performing water vapor adsorption into the materials and a subsequent nitrogen adsorption experiment to evaluate the surface properties of the materials after interacting with water.

Water adsorption isotherms (Figure 5) show that the total quantity of water increases when the pore volume of the

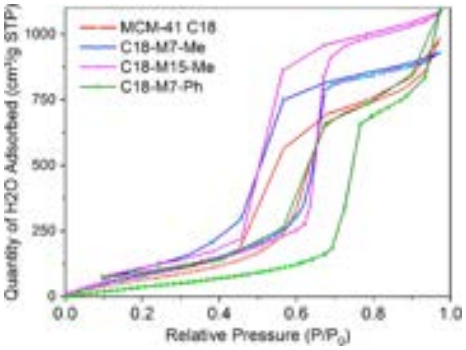

Figure 5. Water adsorption and desorption isotherms at 298.15 K.

material is higher, regardless of their organic functionalization. These results show that the hydrophobicity of the materials is not strong enough to avoid water vapor condensation in the pores. It is well known that this is not the case for postgrafted hydrophobic organosilica, where the amount of water that can enter the pores, at atmospheric pressure, is negligible. The high water uptake found here seems to be a key parameter of the efficiency of the materials in the studied applications.

Recent studies show that, under hydrophobic nanoconfinement, water undergoes changes in its H-bond network, lowering its polarity and obtaining enhanced solvation of nonpolar solutes. This concept has been called Water Tuneable Solvent (WaTuSo).[19] Some consequences of this phenomenon are, for example, enhanced gas storage[20] and dramatic improvement of catalytic efficiency.[21] Thus, it is arguable that the hydrophobic/hydrophilic materials used in this work have the ability not only to adsorb a large quantity of water but also to modulate the properties of water in confinement to match the polarity requirements for a dedicated application. The properties of water confined in these amphiphilic nanopores are currently under investigation and these will be treated in future publications.

Hydrothermal Resistance. It is known that mesoporous silica such as MCM-41 presents a low hydrothermal resistance,[32−34] and this is one of the main disadvantages of this material for applications in aqueous media. For this reason, we have studied the surface degradation of the organosilica materials after contact with water.

During water adsorption experiments, the materials were in contact with water at neutral pH and 25 °C. Afterward, they were heated to 90 °C under vacuum for 24 h to assure the elimination of any residual water molecule.

Even though soft conditions of pH and temperature were used, it was possible to compare the effects of this controlled exposure to water for the different materials.

Figure 6 shows nitrogen adsorption−desorption isotherms for the same organosilica samples before and after water adsorption (and desorption). The total quantity of N_2

https://dx.doi.org/10.1021/acsomega.0c01996
ACS Omega 2020, 5, 18842−18848

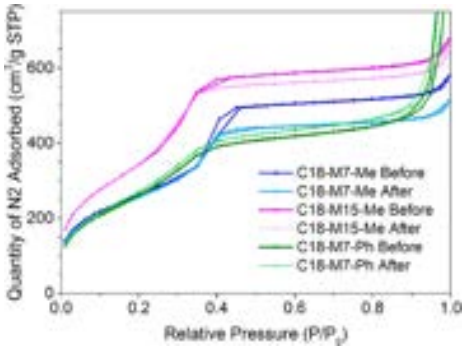

Figure 6. Nitrogen adsorption−desorption isotherms of selected materials at 77 K before and after water adsorption.

adsorbed after capillary condensation is directly related to the pore volume. This quantity decreases due to the pore structure degradation upon contact with water. In the case of C18-M7-Me, the quantity of N_2 adsorbed at P/P_0 = 0.5 decreases by 11.8% of its initial value. A smaller difference (4.22%) is observed in the case of C18-M15-Me, while the pore volume of C18-M7-Ph is roughly constant (a small negative value of 3.16%, attributable to the experimental error).

These results indicate that there is an increased stabilization of the surface toward hydrolysis when the hydrophobicity of the surface increases due to the presence of methyl or phenyl groups. Such resistance allows the material to be efficient in the time required for the local mechanism of the applications.

CONCLUSIONS

Using a direct synthesis of TEOS with MTES or PTES, mesoporous organosilica materials were produced for testing their applications in lysozyme adsorption and supported copper catalysis. A complete characterization confirmed the large surface area, ordered pore structure, and organic functionalization of the materials, providing a partial hydrophobic environment that depends on the percentage of organosilane present in the precursor mixture. It was observed that such a difference in the nanoenvironment had a significant impact on the performance of the materials in the selected applications.

The quantity of lysozyme adsorbed decreased for all of the methyl-modified materials, with respect to the original MCM-41 C18. In contrast, the lysozyme uptake by the phenyl-modified sample, C18-M7-Ph, was more than three times higher than that by the reference MCM-41. This enhancement is attributed to the $\pi-\pi$ interactions between the organosilica and the protein.

The copper-doped materials were proven to be active for regiospecific catalysis of the cycloaddition reaction between 4-bromo-1-butyne and benzyl azide, using water as a solvent. In particular, C18-M15-Me provided an ideal surface for this reaction, with an obtained yield of the reaction of >99%.

Finally, we found that the high capacity for water uptake and modulations of its properties in hydrophobic nanoconfinement, together with better resistance to hydrolysis, were certainly important factors for the performance of C18-M7-Ph in lysozyme adsorption and for C18-M15-Me in the catalysis experiments.

EXPERIMENTAL SECTION

For the direct synthesis of mesoporous organosilica, we focused on obtaining a stable material with a highly ordered pore structure. To avoid the disruption of the honeycomb-like structure and based on previous research,[22] the percentage of organosilane in the precursor mixture was kept under 20 mol %.

Materials. Octadecyltrimethylammonium bromide ($C_{21}H_6NBr$), dodecyltrimethylammonium bromide ($C_{15}H_6NBr$), tetraethyl orthosilicate (TEOS), methyltriethoxysilane (MTES), phenyltriethoxysilane (PTES), ammonia (30%), hydrochloric acid (37%), and ethanol (99.98%) were purchased from Sigma-Aldrich.

Direct Synthesis of Mesoporous Organosilica. MCM-41-type materials with different percentages of MTES or PTES were prepared. For each one, 4 mmol of the cationic surfactant C_nTAB was dissolved in 72.0 mL of ultrapure water at 50 °C and stirred vigorously for 1.5 h for complete dissolution; then, the temperature was decreased to 35 °C and 4.8 mL of ammonia (30%) was added. The mixture was stirred for further 5 min. After, the precursors' mixture was added keeping the number of moles of the alkylethoxy and ethoxysilane (26.33 mmol) constant. The final molar composition of the reaction mixture was $(1 - x)$ TEOS/x MTES (or PTES)/2.4 NH_3/0.15 C_nTAB/152 H_2O, where x is the fraction of methyl- or phenyltriethoxysilane that goes from 0 to 0.15 and n is the length of the alkyl chain of the surfactant. The reaction was allowed to stir at a rate of 300 rpm for 3.5 h. The obtained white solid was washed twice with 40 mL of HCl 2% v/v and then with ultrapure water until reaching a neutral pH.

The conditions of template removal were adjusted to obtain clean material without causing damages to the surface. For this purpose, two steps were needed: first, an acidification step, followed by an ethanol extraction step. The procedure was as follows: 100 mL of the aqueous solution of HCl (2% v/v) was added per gram of the product and the mixture stirred for 25 min at room temperature. The solid was filtered and redispersed in a mixture of 200 mL of ethanol 99% and 10 mL of ultrapure water. This mixture was stirred at 50 °C for 3 h; then, the solid was filtered and dried for 24 h in an oven at 60 °C. The key parameters for a successful washing were the concentration and time of exposure to the acidic solution, as well as the presence of 5% v/v of water mixed with ethanol in the extraction step. The template extraction was verified by means of FTIR. An extra thermal treatment to accomplish total surfactant removal was only needed for the sample C18-M7-Ph. This sample was additionally heated at 350 °C for 1 h under a nitrogen atmosphere.

The samples were named according to the template used and their fraction of MTES or PTES in the precursor mixture: C18-M7-Me for 0.93 TEOS/0.07 MTES, C18-M15-Me for 0.85 TEOS/0.15 MTES, and C18-M7-Ph for 0.93 TEOS/0.07 PTES, all of them using C_{18}TAB as a template, and C12-M7-Me for 0.93 TEOS/0.07 MTES using C_{12}TAB as a template. The standard MCM-41 C18 and C12 were synthesized and washed under the same conditions for comparison.

Characterization. The FTIR spectra of the samples were taken with a Bruker TENSOR equipped with a Platinum ATR from 4000 to 400 cm^{-1}, with a resolution of 2 cm^{-1}. Nitrogen and water vapor adsorption−desorption experiments were performed with an ASAP 2020 surface area and porosity analyzer from Micromeritics. Nanoporous silica samples were

https://dx.doi.org/10.1021/acsomega.0c01996
ACS Omega 2020, 5, 18842−18848

degassed under vacuum at 90 °C for 24 h. Nitrogen adsorption isotherms were taken at 77 K and the water vapor adsorption isotherms at 298.15 K. Thermogravimetric analyses were performed with a Q50 thermonuclear from TA Instruments under a controlled nitrogen gas flow from ambient temperature to 850 °C with a temperature ramp of 10 °C/min. Small-angle X-ray scattering patterns were collected using a Xeuss 2.0 HR SAXS/WAXS instrument from Xenocs with a Cu Kα (5 kV, 0.6 A). TEM images were taken with a JEOL JEM-2010 high-resolution transmission electron microscope operating at 200 kV.

Lysozyme Adsorption. Approximately 10 mg of the selected materials was mixed with 10 mL of a 0.5 mg/mL solution of lysozyme from chicken egg white in a 10 mM phosphate buffer, pH 7.4, for 4 h at room temperature. Then, the suspensions were centrifuged for 10 min at 15 000*g*, and 1 mL of the supernatant was passed through a 0.2 μm filter and transferred to a quartz cell. The UV absorption spectra were taken at 280 nm. The UV absorption spectra of the rinsing water were also taken to discard the loss of weakly bounded lysozyme. The solids were rinsed with water and dried under vacuum. The FTIR spectra of the lysozyme-rich materials were recorded.

Copper Postgrafting. The method of copper postgrafting followed the protocol described by Jlalia et al.[12] One hundred and fifty milligrams of the washed nanoporous silica materials were added to 40 mL of a 0.05 M solution of copper nitrate, previously adjusted to pH 10.5 with ammonia (30%) and stirred vigorously. Immediately after 10 min, the solid was filtered and washed with ultrapure water until neutral pH. The obtained blue material was dried in the oven at 50 °C. The above-mentioned procedure was also applied to the as-synthesized samples (without removing the surfactant from the pores) to obtain materials with copper grafted only on the external surface.

Catalytic Tests. For all samples, benzyl azide (67 μL) and 4-bromo-1-butyne (47 μL) were added to 2 mL of water containing a particular amount of copper-doped materials corresponding to 8 mol % with respect to the benzyl azide reactant. Upon agitation, the mixture forms an O/W Pickering emulsion. The reactions were performed for 20 h. After that time, the mixtures were vacuum filtered with a polyacrylamide membrane and the blue solids were rinsed twice with 2 mL of ethyl acetate each time. After solvent evaporation, the conversion to 1-benzyl-4-bromoethyl-triazole was determined by ^{1}H NMR.

A control experiment was performed with the pores blocked by surfactant molecules (C_{18}TAB) and copper grafted only on the external surface. The rest of the experimental conditions (time, temperature, concentration of reactants, Cu mol % in reaction mixture) were kept constant.

■ ASSOCIATED CONTENT

Supporting Information

The Supporting Information is available free of charge at https://pubs.acs.org/doi/10.1021/acsomega.0c01996.

Additional data on the characterization of the materials is available: mean physical properties of the additional prepared mesoporous organosilica materials, TEM images, small-angle X-ray scattering curves, neutron backscattering experiments, FTIR spectra of the copper-doped materials with the pores blocked with the surfactant, and photograph and schematic representations of the O/W Pickering emulsion formed during catalysis experiments (PDF)

■ AUTHOR INFORMATION

Corresponding Author

Oriana Osta − *Université Paris-Saclay, CEA, CNRS, LLB, 91191 Gif-sur-Yvette, France;* orcid.org/0000-0002-9909-6641; Email: oriana.osta@cea.fr

Authors

Marianne Bombled − *Université Paris-Saclay, CEA, CNRS, LLB, 91191 Gif-sur-Yvette, France*

David Partouche − *Université Paris-Saclay, CEA, CNRS, LLB, 91191 Gif-sur-Yvette, France; Université Paris-Saclay, Synchrotron Soleil, 91190 Saint-Aubin, France*

Florian Gallier − *CY Cergy Paris Université, CNRS, BioCIS, 95000 Cergy-Pontoise, France; Université Paris-Saclay, CNRS, BioCIS, 91190 Châtenay-Malabry, France*

Nadège Lubin-Germain − *CY Cergy Paris Université, CNRS, BioCIS, 95000 Cergy-Pontoise, France; Université Paris-Saclay, CNRS, BioCIS, 91190 Châtenay-Malabry, France;* orcid.org/0000-0003-0713-9286

Nancy Brodie-Linder − *Université Paris-Saclay, CEA, CNRS, LLB, 91191 Gif-sur-Yvette, France; CY Cergy Paris Université, CNRS, BioCIS, 95000 Cergy-Pontoise, France; Université Paris-Saclay, CNRS, BioCIS, 91190 Châtenay-Malabry, France*

Christiane Alba-Simionesco − *Université Paris-Saclay, CEA, CNRS, LLB, 91191 Gif-sur-Yvette, France*

Complete contact information is available at: https://pubs.acs.org/10.1021/acsomega.0c01996

Notes

The authors declare no competing financial interest.

■ ACKNOWLEDGMENTS

The authors thank Veronique Arluison for helpful discussion on the confined lysozyme, Annie Brûlet for the SAXS experiments, and Henriette Wase Hansen and Bernhard Frick for inelastic neutron scattering on IN16B at the ILL (Grenoble, France).

■ REFERENCES

(1) Lei, C.; Shin, Y.; Magnuson, J. K.; Fryxell, G.; Lasure, L. L.; Elliott, D. C.; Liu, J.; Ackerman, E. J. Characterization of Functionalized Nanoporous Supports for Protein Confinement. *Nanotechnology* **2006**, *17*, 5531−5538.

(2) Charnay, C.; Bégu, S.; Tourné-Péteilh, C.; Nicole, L.; Lerner, D. A.; Devoisselle, J. M. Inclusion of Ibuprofen in Mesoporous Templated Silica: Drug Loading and Release Property. *Eur. J. Pharm. Biopharm.* **2004**, *57*, 533−540.

(3) Cashin, V. B.; Eldridge, D. S.; Yu, A.; Zhao, D. Surface Functionalization and Manipulation of Mesoporous Silica Adsorbents for Improved Removal of Pollutants: A Review. *Environ. Sci.: Water Res. Technol.* **2018**, *4*, 110−128.

(4) Dosseh, G.; Xia, Y.; Alba-Simionesco, C. Cyclohexane and Benzene Confined in MCM-41 and SBA-15: Confinement Effects on Freezing and Melting. *J. Phys. Chem. B* **2003**, *107*, 6445−6453.

(5) Azaïs, T.; Laurent, G.; Panesar, K.; Nossov, A.; Guenneau, F.; Sanfeliu Cano, C.; Tourné-Péteilh, C.; Devoisselle, J.-M.; Babonneau, F. Implication of Water Molecules at the Silica−Ibuprofen Interface in Silica-Based Drug Delivery Systems Obtained through Incipient Wetness Impregnation. *J. Phys. Chem. C* **2017**, *121*, 26833−26839.

(6) Brodrecht, M.; Kumari, B.; Breitzke, H.; Gutmann, T.; Buntkowsky, G. Chemically Modified Silica Materials as Model Systems for the Characterization of Water-Surface Interactions. *Z. Phys. Chem.* **2018**, *232*, 1127−1146.
(7) Wu, Q.; Hu, X.; Yue, P. L.; Zhao, X. S.; Lu, G. Q. Copper/MCM-41 as Catalyst for the Wet Oxidation of Phenol. *Appl. Catal., B* **2001**, *32*, 151−156.
(8) Gomis, A. M.; Gómez Siurana, A.; Berenguer Muñoz, D.; Martínez Castellanos, I.; Beltrán, M. Effect of Mesoporous Catalysts on the Mainstream Tobacco Smoke of 3R4F and 1R5F Reference Cigarettes. *Am. J. Chem. Eng.* **2015**, *3*, 1−18.
(9) Mbaraka, I. K.; Shanks, B. H. Design of Multifunctionalized Mesoporous Silicas for Esterification of Fatty Acid. *J. Catal.* **2005**, *229*, 365−373.
(10) Roy, S.; Chatterjee, T.; Pramanik, M.; Roy, A. S.; Bhaumik, A.; Islam, Sk. M. Cu(II)-Anchored Functionalized Mesoporous SBA-15: An Efficient and Recyclable Catalyst for the One-Pot Click Reaction in Water. *J. Mol. Catal. A: Chem.* **2014**, *386*, 78−85.
(11) Rostamnia, S.; Doustkhah, E. Nanoporous Silica-Supported Organocatalyst: A Heterogeneous and Green Hybrid Catalyst for Organic Transformations. *RSC Adv.* **2014**, *4*, 28238−28248.
(12) Jlalia, I.; Gallier, F.; Brodie-Linder, N.; Uziel, J.; Augé, J.; Lubin-Germain, N. Copper(II) SBA-15: A Reusable Catalyst for Azide-Alkyne Cycloaddition. *J. Mol. Catal. A* **2014**, *393*, 56−61.
(13) Wang, X.; Lin, K. S. K.; Chan, J. C. C.; Cheng, S. Direct Synthesis and Catalytic Applications of Ordered Large Pore Aminopropyl-Functionalized SBA-15 Mesoporous Materials. *J. Phys. Chem. B* **2005**, *109*, 1763−1769.
(14) Yokoi, T.; Yoshitake, H.; Tatsumi, T. Synthesis of Amino-Functionalized MCM-41 via Direct Co-Condensation and Post-Synthesis Grafting Methods Using Mono-, Di- and Tri-Amino-Organoalkoxysilanes. *J. Mater. Chem.* **2004**, *14*, 951−957.
(15) Sayari, A.; Hamoudi, S. Periodic Mesoporous Silica-Based Organic-Inorganic Nanocomposite Materials. *Chem. Mater.* **2001**, *13*, 3151−3168.
(16) Shang, F.; Sun, J.; Wu, S.; Yang, Y.; Kan, Q.; Guan, J. Direct Synthesis of Acid−Base Bifunctional Mesoporous MCM-41 Silica and Its Catalytic Reactivity in Deacetalization−Knoevenagel Reactions. *Microporous Mesoporous Mater.* **2010**, *134*, 44−50.
(17) Macquarrie, D. J. Direct Preparation of Organically Modified MCM-Type Materials. Preparation and Characterisation of Amino-propyl−MCM and 2-Cyanoethyl−MCM. *Chem. Commun.* **1996**, 1961−1962.
(18) Fowler, C. E.; Burkett, S. L.; Mann, S. Synthesis and Characterization of Ordered Organo−Silica−Surfactant Mesophases with Functionalized MCM-41-Type Architecture. *Chem. Commun.* **1997**, 1769−1770.
(19) Breynaert, E.; Houlleberghs, M.; Radhakrishnan, S.; Grübel, G.; Taulelle, F.; Martens, J. A. Water as a Tuneable Solvent: A Perspective. *Chem. Soc. Rev.* **2020**, *49*, 2557−2569.
(20) Casco, M. E.; Silvestre-Albero, J.; Ramírez-Cuesta, A. J. Methane hydrate formation in confined nanospace can surpass nature. *Nat. Commun.* **2015**, *6*, No. 6432.
(21) Liu, C.-C.; Chou, H.-J.; Lin, C.-Y.; Janmanchi, D.; Chung, P.-W.; Mou, C.-Y.; Yu, S. S.-F.; Chan, S. I. The Oversolubility of Methane Gas in Nano-Confined Water in Nanoporous Silica Materials. *Microporous Mesoporous Mater.* **2020**, *293*, No. 109793.
(22) Burkett, S. L.; Sims, S. D.; Mann, S. Synthesis of Hybrid Inorganic−Organic Mesoporous Silica by Co-Condensation of Siloxane and Organosiloxane Precursors. *Chem. Commun.* **1996**, 1367−1368.
(23) Putz, A.-M.; Wang, K.; Len, A.; Plocek, J.; Bezdicka, P.; Kopitsa, G. P.; Khamova, T. V.; Ianăşi, C.; Săcărescu, L.; Mitróová, Z. Mesoporous Silica Obtained with Methyltriethoxysilane as Co-Precursor in Alkaline Medium. *Appl. Surf. Sci.* **2017**, *424*, 275−281.
(24) Llusar, M.; Monrós, G.; Roux, C.; Pozzo, J. L.; Sanchez, C. One-Pot Synthesis of Phenyl- and Amine-Functionalized Silica Fibers through the Use of Anthracenic and Phenazinic Organogelators. *J. Mater. Chem.* **2003**, *13*, 2505−2514.
(25) Marei, N. N.; Nassar, N. N.; Vitale, G. The Effect of the Nanosize on Surface Properties of NiO Nanoparticles for the Adsorption of Quinolin-65. *Phys. Chem. Chem. Phys.* **2016**, *18*, 6839−6849.
(26) Kruk, M.; Jaroniec, M.; Sayari, A. Adsorption Study of Surface and Structural Properties of MCM-41 Materials of Different Pore Sizes. *J. Phys. Chem. B* **1997**, *101*, 583−589.
(27) Adams, S.; Higgins, A. M.; Jones, R. A. L. Surface-Mediated Folding and Misfolding of Proteins at Lipid/Water Interfaces. *Langmuir* **2002**, *18*, 4854−4861.
(28) Himo, F.; Lovell, T.; Hilgraf, R.; Rostovtsev, V. V.; Noodleman, L.; Sharpless, K. B.; Fokin, V. V. Copper(I)-Catalyzed Synthesis of Azoles. DFT Study Predicts Unprecedented Reactivity and Intermediates. *J. Am. Chem. Soc.* **2005**, *127*, 210−216.
(29) Brodie-Linder, N.; Besse, R.; Audonnet, F.; LeCaer, S.; Deschamps, J.; Impéror-Clerc, M.; Alba-Simionesco, C. The Key to Control Cu II Loading in Silica Based Mesoporous Materials. *Microporous Mesoporous Mater.* **2010**, *132*, 518−525.
(30) Zhao, Y.; Zhang, X.; Sanjeevi, J.; Yang, Q. Hydroformylation of 1-Octene in Pickering Emulsion Constructed by Amphiphilic Mesoporous Silica Nanoparticles. *J. Catal.* **2016**, *334*, 52−59.
(31) Zhang, M.; Ettelaie, R.; Yan, T.; Zhang, S.; Cheng, F.; Binks, B. P.; Yang, H. Ionic Liquid Droplet Microreactor for Catalysis Reactions Not at Equilibrium. *J. Am. Chem. Soc.* **2017**, *139*, 17387−17396.
(32) Pérez, L. L.; van Eck, E. R. H.; Melián-Cabrera, I. On the Hydrothermal Stability of MCM-41. Evidence of Capillary Tension-Induced Effects. *Microporous Mesoporous Mater.* **2016**, *220*, 88−98.
(33) Jiang, C.; Su, A.; Li, X.; Zhou, T.; He, D. Study on the Hydrothermal Stability of MCM-41 via Secondary Restructure. *Powder Technol.* **2012**, *221*, 371−374.
(34) Prouzet, E.; Kacheff, A.; Aubert, G.; Bentaleb, A.; Backov, R.; Aymonier, C. Toward a Sustainable Preparation of Tunable Mesoporous Silica. *J. Supercrit. Fluids* **2019**, *143*, 139−145.

https://dx.doi.org/10.1021/acsomega.0c01996
ACS Omega 2020, 5, 18842−18848